UNIVERSIDADE DE LISBOA
FACULDADE DE CIÊNCIAS

The impact of Land Surface Model vegetation parameterization on the terrestrial water and carbon cycles

" Documento Definitivo"

Doutoramento em Ciências Geofísicas e da Geoinformação
Especialidade de Meteorologia

David Pierre Ann Stevens

Tese orientada por:
Doutor Emanuel Nemésio de Sousa Dutra
Doutor Pedro Manuel Alberto De Miranda

Documento especialmente elaborado para a obtenção do grau de doutor

2022

UNIVERSIDADE DE LISBOA

FACULDADE DE CIÊNCIAS

The impact of Land Surface Model vegetation parameterization on the terrestrial water and carbon cycles

Doutoramento em Ciências Geofísicas e da Geoinformação

Especialidade de Meteorologia

David Pierre Ann Stevens

Tese orientada por:

Doutor Emanuel Nemésio de Sousa Dutra

Doutor Pedro Manuel Alberto De Miranda

Júri:

Presidente:

- João Manuel de Almeida Serra, Professor Catedrático e Presidente do Departamento de Engenharia Geográfica, Geofísica e Energia da Faculdade de Ciências da Universidade de Lisboa

Vogais:

- Doutor Rui Paulo Vasco Salgado, Professor Associado com Agregação, Escola de Ciências e Tecnologia da Universidade de Évora
- Doutor João Carlos Andrade dos Santos, Professor Catedrático, Departamento de Física da Universidade de Trás os Montes e Alto Douro
- Doutor Emanuel Nemésio de Sousa Dutra, Investigador Principal Instituto Português do Mar e da Atmosfera, IP
- Doutor Pedro Miguel Matos Soares, Professor Auxiliar Faculdade de Ciências da Universidade de Lisboa.

Documento especialmente elaborado para a obtenção do grau de doutor

Trabalho financiado pela Fundação para Ciência e a Tecnologia (PD/BD/135250/2017)

2022

Abstract

The surface-atmosphere turbulent exchanges couple the water, energy, and carbon cycles in the earth system. The biosphere plays an important role in the evaporation process, and vegetation related parameters such as the leaf area index (LAI), vertical root distribution and stomatal resistance are poorly constrained due to sparse observations at the spatial-temporal scales at which land surface models (LSMs) operate. Considering the central role of the land surface vegetation in the climate system, various networks and methods of observational data and processes are used to constrain different ECMWF (European Center for Medium-Range Weather Forecasts) model configurations to better understand underlying conditions of the land surface energy, water and carbon budgets. Observed data from the FLUXNET network are used to perform offline point simulations with a strong emphasis on the representation of evaporation and its link with water stress conditions. The close relationship between LAI and the minimum canopy resistance is investigated and shows some model performance improvements potential but failed to solve other issues such as excessive evaporative drought conditions. However, the replacement of the exponential roots profile by a uniform roots distribution and associated maximum rooting depth reduced the underestimation of evaporation during water stress conditions. This result highlights the importance of root distribution in controlling soil moisture resistance in water stress conditions. The revised uniform root profile also has a positive effect on the model carbon cycle representation and brings model output closer to observations. Moreover, the positive effect of this new root scheme on model performance is intensified when coupled with the A-gs photosynthesis-conductance scheme as opposed to the traditionally used Jarvis approach, which implies that a more physiologically based model vegetation parameterization could benefit land surface models performance. The same findings also apply at the grid scale, where the replacement of the current vegetation types, cover, characteristics and LAI, by a new high resolution remote sensing derived global vegetation dataset did not significantly affect the simulated water budgets. However, the deeper and uniform root scheme allows plants to use soil water more efficiently and induce a more intense and positive response from land surface models. Even if an increase in model resolution could improve the simulations, the core of LSMs discrepancies reflect parameterization uncertainty to represent and capture smaller-scale unresolved processes and integrate them to the model grid-scale.

Key words: Land surface model, vegetation parameterization, earth observation, benchmarking, machine learning.

Resumo

As trocas de água, energia e carbono entre a superfície terrestre e a atmosfera são muito importantes no sistema terrestre. Estes fluxos são fundamentais para compreender a resposta do sistema terrestre ao aumento da concentração de gases de efeito estufa e às mudanças climáticas. O aquecimento global e a intensificação dos extremos climáticos são um risco significativo para a nossa sociedade. Neste contexto, é fundamental que os modelos climáticos tenham uma representação precisa dos processos da superfície terrestre para clarificar de que forma as alterações climáticas poderão afetar a biosfera e como a sociedade poderá antecipar eventos extremos.

Os modelos de superfície terrestre (MST) são a componente dos modelos climáticos responsáveis pela representação dos fluxos de água, energia e carbono entre a superfície terrestre e a atmosfera, e são ferramentas sofisticadas para projetar a evolução da superfície da Terra nos próximos anos, décadas e séculos. A variedade e a complexidade dos processos subjacentes às trocas entre a superfície terrestre e a atmosfera (da turbulência na camada limite à fisiologia das plantas) são um desafio quer para observar quer para modelar. Os desenvolvimentos contínuos da modelação, apoiados por um crescente poder computacional, resultaram numa maior complexidade dos MSTs, apoiada no aumento das fontes de dados de avaliação e impulsionada por novas metodologias (por exemplo técnicas de aprendizagem automática – Machine Learning) e observações da Terra. No entanto, o aumento do nível de complexidade dos modelos não é necessariamente traduzido num melhor desempenho dos modelos, devido a incertezas na compreensão e modelação das interações entre os ramos atmosférico e terrestre do ciclo energético, hidrológico e do carbono. Além disso, o elevado número de componentes que caracterizam estes processos dificulta a atribuição de erros do modelo a processos específicos.

Considerando o papel central que a vegetação da superfície terrestre tem no sistema climático, nesta tese são utilizados vários dados observacionais para desenvolver e avaliar diferentes configurações do modelo de superfície do ECMWF (Centro Europeu de Previsões de Tempo de Médio Prazo). O principal objetivo é de avaliar os processos e componentes do modelo mais relevantes na representação dos fluxos. Numa primeira fase, o trabalho foi desenvolvido para vários locais, utilizando dados de 17 torres FLUXNET para realizar simulações com ênfase na representação da evaporação e sua relação com as condições de stress hídrico. Três restrições de resistência de cobertura vegetal foram avaliadas: (i) o papel das características da vegetação através do uso do índice de área foliar de alta resolução espacial representando as condições da estação local; (ii) o impacto da resistência mínima do coberto vegetal e (iii) o impacto de uma distribuição uniforme das raízes

no stresse da humidade do solo.

A climatologia de alta resolução do índice de área foliar não teve um impacto significativo nos fluxos superficiais e o ajuste entre índice de área foliar e a resistência mínima do coberto vegetal revelou algum potencial para melhorar a variabilidade dos fluxos de evaporação. O modelo do ECMWF, bem outros modelos de superfície terrestre, têm limitações na representação da evaporação em situações de stresse hídrico, devido à depleção da humidade do solo na camada superior, enquanto ainda existe água disponível nas camadas mais profundas. Desta forma, a substituição do atual perfil exponencial de raízes por uma distribuição de raízes mais profunda e uniforme reduziu a subestimação da evaporação em condições de stresse hídrico.

Com o objetivo de integrar os resultados obtidos no ciclo do carbono, os mesmos dados e métodos foram aplicados a duas versões diferentes do modelo de superfície terrestre do ECMWF, representando as duas formulações distintas da condutividade dos estomas: (i) Jarvis e (ii) a abordagem fisiológica da planta A- gs, com um foco nas trocas de carbono (Net Ecosystem Exchange (NEE)). Para obter estimativas confiáveis de NEE e evaporação à superfície é necessária uma representação adequada das trocas de carbono e água entre a vegetação e a atmosfera, sendo esses fluxos ligados pela condutividade do estoma. Os dados de observações terrestres de alta resolução não melhoraram significativamente o desempenho do modelo. No entanto, a abordagem fisiológica da planta para representar a fotossíntese no modelo, a formulação A-gs, teve um impacto positivo nas estações que sofrem com a seca evaporativa e a subestimação da evaporação durante períodos de stresse hídrico. Como anteriormente, a humidade no solo e a distribuição das raízes também demonstrou potencial para melhorar o desempenho do ciclo de carbono no modelo e reduzir a diferenças entre os resultados do modelo e as observações. Demonstrou-se que a combinação da abordagem fisiológica da planta e da distribuição de raízes mais profundas e uniformes tem um impacto positivo nas simulações. Ainda que a escolha das estações FLUXNET abranja uma ampla gama de diferentes tipos de clima e vegetação, estes resultados estão limitados pela amostragem das estações utilizadas.

O trabalho foi expandido para todo o globo terrestre, para testar (i) o impacto da alteração da climatologia do índice de área folear, (ii) da caracterização da cobertura do solo e (iii) e as raízes mais profundas e uniformes. Os resultados das várias configurações do modelo foram confrontados com três conjuntos de dados independentes obtidos através do treino de algoritmos de aprendizagem automática com observações pontuais: escoamento, humidade do solo e evaporação. Considerando a escala espacial da simulação global, foi necessário recorrer a uma metodologia nova e classificação climática, para analisar o desempenho das várias configurações do modelo de uma forma consistente. A simulação global utilizando a mais recente climatologia de índice de área foliar e os diferentes

tipos e características da vegetação não melhorou as simulações do modelo. Estes resultados foram consistentes com o trabalho inicial nas 17 estações FLUXNET. A profundidade e uniformidade das raízes levou a uma resposta mais intensa do modelo. No entanto, os resultados foram variáveis, havendo regiões com impactos positivos, e outras regiões com impactos negativos. As zonas tropicais e áridas são as que mais beneficiaram, uma vez que o modelo mais com raízes mais profundas e com distribuição uniforme diminuiu a situações de seca precoce, que é observada principalmente em regiões caracterizadas por stresse hídrico. Os resultados também revelaram o potencial para a otimização dos parâmetros do modelo. No entanto, não é possível descartar que as parametrizações do modelo devam ser mais focadas na avaliação global das estratégias de uso de água das plantas ao nível do ecossistema, em detrimento da atual afetação dos parâmetros ao tipo de vegetação dominante. O aumento da resolução espacial do modelo ou a otimização de parâmetros poderá contribuir para melhorar o modelo. No entanto, continuaram a existir incertezas nos modelos, associados à representação dos processos biofísicos. Estas incertezas são propagadas nas várias escalas temporais e espaciais, e diferentes em cada modelo. Desta forma, o atual estado da arte que aconselha a utilização da informação de vários modelos na interpretação das projeções climáticas continuará a ser fundamental.

Palavras-chave: Modelos de Superfície Terrestre (MST), parametrização da vegetação, observação da terra, benchmarking, machine learning.

Acknowledgments

First of all I would like to be grateful to my two Supervisors Emanuel Dutra and Pedro Miranda, for their help, guidance and support toward my PhD. Thanks to Emanuel Dutra I was able to overcome the different issues that I encountered during my research. In four years of PhD under the supervision of Emanuel Dutra I learned more than during all my previous years of study and research.

I would like to thanks the Fundação para a Ciência e a Tecnologia for their financial and administrative support.

Thank you to Célia Lee who allowed me to handle my administrative failures.

I also would like to thank my family and Soon Joo for their support during this long journey. A special thanks to Ceu and Armenio Martins from the Cafe "Flor da Sera" who provided me with the internet during the last stage of my PhD.

Contents

1 Introduction - The land surface as a key component of the earth system 1

1.1 The land surface and the role of vegetation in climate processes . . . 2

1.1.1 The energy cycle . . . 2

1.1.2 The terrestrial water cycle . . . 2

1.1.3 The terrestrial carbon cycle . . . 3

1.2 Land Surface Models . . . 3

1.3 Research questions and organization of the thesis . . . 4

2 Role of remote sensed leaf area index, albedo and roots distribution on ECMWF land surface model - offline evaluation against flux tower measurements 6

2.1 Introduction . . . 6

2.2 Data and Methods . . . 8

2.2.1 Data . . . 8

2.2.2 CHTESSEL model . . . 10

2.2.3 Simulations setup . . . 12

2.2.4 Evaluation . . . 13

2.3 Results . . . 14

2.3.1 Comparison of LAI and Albedo . . . 14

2.3.2 Fluxes evaluation . . . 16

2.3.3 Soil moisture stress . . . 19

2.4 Discussion . . . 23

2.5 Conclusions . . . 24

3 CTESSEL and CHTESSEL heat fluxes and carbon exchanges offline evaluation against flux tower measurements 26

3.1 Introduction . . . 26

3.2 Data and Methods . . . 27

3.2.1 Data . . . 27

3.2.2 CTESSEL land surface model . . . 28

3.2.3 Simulation setup . . . 29

3.2.4 Evaluation . . . 30

3.3 Results . . . 31

3.3.1 CTESSEL sensible and latent heat flux evaluation . . . 31

3.3.2 Carbon fluxes in CHTESSEL and CTESSEL . . . 37

3.3.3 Discussion . . . 37
3.3.4 Conclusions . . . 39

4 Confronting different ECMWF land surface model configurations against global scale machine learning gridded datasets 40
4.1 Introduction . . . 40
4.2 Data and Methods . . . 41
4.2.1 Data . . . 41
4.2.2 Model and simulation setup . . . 43
4.2.3 Evaluation . . . 45
4.3 Results . . . 47
4.3.1 Performance of CHTESSEL control configuration . . . 47
4.3.2 Impact of land cover, LAI and rooting depth . . . 49
4.3.3 Regional evaluation . . . 53
4.4 Discussion . . . 55
4.5 Conclusion . . . 57

5 Conclusion 58

A Supporting material of Chapter 2. 60

B Supporting material of Chapter 3. 89

C Supporting material of Chapter 4. 120

Bibliography 123

List of Tables

2.1 *FLUXNET* tower flux stations used in this study 9
2.2 Model simulations acronyms and detailed configuration 13
2.3 Comparison between CTR and MODIS ALB (MALB) for each tower. The root mean square difference is computed for the mean annual cycle. 15
2.4 Comparison between CTR and MODIS LAI (MLAI) for each tower. The root mean square difference is computed for the mean annual cycle. 16
2.5 CTR r_{smin} and optimal r_{smin} and R_{DMAX} used in MLAI_RSMIN and MLAI_ROOT, respectively. 19

3.1 Model simulations acronyms and detailed configuration 30
3.2 Station vegetation types (L define low and H high vegetation types), and optimal rooting depth considering one variable (NEE), two varibales (Qle and Qh) and three variables (NEE, Qle, Qh). 31

4.1 Model simulations acronyms and detailed configuration for grid-scale evaluation . . . 45

A.1 CHTESSEL vegetation types and associated parameters. R_1 to R_4 denote the root fraction in layers 1 to 4 (with depths of 0.07, 0.21, 0.72 and 1.89 m). The Final 4 lines indicate the root fraction when considering an uniform rooting depth with maximum rooting depth R_{DMAX} of 0.5, 1, 2 and 2.89 meters. 62

List of Figures

2.1 Latent (a-d top panels) and sensible (bottom panels) heat flux evaluation in terms of MBE, SD, NME and r for CTR, MLAI, MLAI_RSMIN and MLAI_ROOT. The boxplots represent each metric's distribution for the 17 towers showing the percentiles 25, 50 and 75. Symbols denote outliers for values further than 1.5 times the interquartile range from the nearest 25th or 75th percentile. 18

2.2 Latent heat flux (Qle) and soil moisture in Amplero (a), Blodgett (b) and Espirra (c). For Qle (left axis) observations are in grey, and the simulations from MLAI in blue and from MLAI_NOSM in orange. The soil moisture (right axis) for MLAI simulation is shown for the top 3 layer (red solid) and deep layer (red dashed). The light dotted red and blue lines represent soil moisture at field capacity and wilting point, respectively. 20

2.3 Simulated and observed latent heat flux during one example year with a 14 days running mean smoothing. Observations are in grey, CTR in black, MLAI in blue, MLAI_ROOT in green and MLAI_RSMIN in red. 22

3.1 Latent (a-d top panels) and sensible (bottom panels) heat flux evaluation in terms of MBE, SD, NME and r for C_CTR, C_MLAI and C_MLAI_ROOT. The boxplots represent each metric's distribution for the 17 towers showing the percentiles 25, 50 and 75. Symbols denote outliers for values further than 1.5 times the interquartile range from the nearest 25th or 75th percentile. 32

3.2 Budyko classification of the 17 Fluxnet stations. 33

3.3 Latent heat flux (Qle) and soil moisture in Amplero (a), Blodgett (b), Espirra (c), Mopane (d), and Palang (e). For the Qle (left axis), the observations are in black and the simulation for CTESSEL CTR (C_CTR) in grey, for CTESSEL MODIS LAI (C_MLAI) in light blue, for CHTESSEL MODIS LAI (MLAI) in blue and for CTESSEL without soil moisture stress (C_MLAI_NOSMS) in orange. The soil moisture (right axis) for MLAI simulation is shown for the top 3 layers (red solid) and deep layer (red dashed). The light dotted red and blue lines represent soil moisture at field capacity and the wilting point, respectively. 34

3.4 Simulated and observed latent heat flux during one example year of summer evaporative drought (14 day running mean smoothing average). Observations are in black, C_CTR in grey, C_MLAI in light blue, MLAI in blue and C_MLAI_ROOT in light green and MLAI_ROOT in dark green. 36

3.5 Net Ecosystem Exchange evaluation in terms of mean bias error (MBE), standard deviation (SD), normalized mean error (NME) and correlation (r) for CHTESSEL CTR (CTR), CTESSEL CTR (C_CTR), CHTESSEL MODIS LAI (MLAI), CTESSEL MODIS LAI (C_MLAI), CHTESSEL MODIS LAI with root optimization (MLAI_ROOT) and CTESSEL MODIS LAI with root optimization (C_MLAI_ROOT) 38

4.1 Köppen-Geiger four main climate classifications used. The IPCC regions selected are framed with red polygons and light grey area represents masked regions 47

4.2 Evaluation of the CTR setup against GRUN (a), FLUXCOM (b), SoMo (c) and CTR mean Soverall score (f). 48

4.3 4 Köppen-Geiger classes evaluation of the CTR setup. The first number below the barplots represents the % of points in each Köppen-Geiger region. The score below is the median of the grid-points score. The third number is the spatial score ($S_{overall}$). The fourth number is the distance score (S_{dist}). 49

4.4 $S_{overall}$ score evaluation of the CLAI setup against CTR. (a) GRUN CLAI $S_{overall}$ vs GRUN CTR $S_{overall}$, (b) FLUXCOM CLAI $S_{overall}$ vs FLUXCOM CTR $S_{overall}$, (c) SoMo CLAI $S_{overall}$ vs SoMo CTR $S_{overall}$ and (f) CLAI mean $S_{overall}$ vs CTR mean $S_{overall}$ score (f). 50

4.5 4 Köppen-Geïger classes evaluation of the CLAI setup. The first number below the barplots represents the % of points in each Köppen-Geïger region. The score below is the median of the grid-points $S_{overall}$ score. 50

4.6 $S_{overall}$ score evaluation of the CTR_RD setup against CTR. (a) GRUN CTR_RD $S_{overall}$ vs GRUN CTR $S_{overall}$, (b) FLUXCOM CTR_RD $S_{overall}$ vs FLUXCOM CTR $S_{overall}$, (c) SoMo CTR_RD $S_{overall}$ vs SoMo CTR $S_{overall}$ and (f) CTR_RD mean $S_{overall}$ vs CTR mean $S_{overall}$ score (f). 51

4.7 4 Köppen-Geïger classes evaluation of the CTR_RD setup. The first number below the barplots represents the % of points in each Köppen-Geïger region. The score below is the median of the grid-points $S_{overall}$ score. 52

4.8 $S_{overall}$ score evaluation of the CLAI_RD setup against CTR. (a) GRUN CLAI_RD $S_{overall}$ vs GRUN CLAI $S_{overall}$, (b) FLUXCOM CLAI_RD $S_{overall}$ vs FLUXCOM CLAI $S_{overall}$, (c) SoMo CLAI_RD $S_{overall}$ vs SoMo CLAI $S_{overall}$ and (f) CLAI_RD mean $S_{overall}$ vs CLAI mean $S_{overall}$ score (f). 52

4.9 4 Köppen-Geïger classes evaluation of the CLAI_RD setup. The first number below the barplots represents the % of points in each Köppen-Geïger region. The score below is the median of the grid-points $S_{overall}$ score. 53

4.10 IPCC region evaluation Southeast Asia (EAS) and Central Africa (CAF) runoff, evaporation, precipitation and soil moisture (10cm and 50cm depth) mean annual cycle. . 54

4.11 IPCC region evaluation Northeast America (ENA) and Northeast Africa (NEAF) runoff, evaporation, precipitation and soil moisture (10cm and 50cm depth) mean annual cycle. 55

A.1 Time series of Sensible heat flux, latent heat flux, soil moisture and LAI in Palang. The turbulent fluxes time series compare the observations (gray) with the simulations: CTR (black), MLAI (blue), MLAI_RSMIN (red), MLAI_ROOT (green) and MLAI_NOSMS (dashed blue). The soil moisture time series shows the CTR top 3 layers meter soil moisture (top meter solid back) and the bottom layer soil moisture (dashed black) as well as the soil moisture at wilting point (blue) and field capacity (red). The LAI time series compares CTR (black) with the high resolution MODIS LAI time series (dotted blue), the high resolution MLAI (blue), the climatology of MODIS considering the 0.25° bounding box (dashed blue) and CGLS LAI climatology (grey). 63
A.2 As Figure A.1 but for Sylvania station. 64
A.3 As Figure A.1 but for Espirra station. 65
A.4 As Figure A.1 but for Kruger station. 66
A.5 As Figure A.1 but for Amplero station. 67
A.6 As Figure A.1 but for Howard station. 68
A.7 As Figure A.1 but for Mopane station. 69
A.8 As Figure A.1 but for Blodgett station. 70
A.9 As Figure A.1 but for Bugac station. 71
A.10 As Figure A.1 but for Fort Peck station. 72
A.11 As Figure A.1 but for Harvard station. 73
A.12 As Figure A.1 but for Hesse station. 74
A.13 As Figure A.1 but for Howlandm station. 75
A.14 As Figure A.1 but for Hyytiala station. 76
A.15 As Figure A.1 but for Loobos station. 77
A.16 As Figure A.1 but for Palang station. 78
A.17 As Figure A.1 but for Tumbarumba station. 79
A.18 As Figure A.1 but for University of Michigan station. 80
A.19 Sensible heat flux MBE in the 17 stations for each simulation: CTR, MLAI, MLAI_RSMIN and MLAI_ROOT. 81
A.20 Latent heat flux MBE in the 17 stations for each simulation: CTR, MLAI, MLAI_RSMIN and MLAI_ROOT. 82
A.21 Sensible heat flux NME in the 17 stations for each simulation: CTR, MLAI, MLAI_RSMIN and MLAI_ROOT. 83
A.22 Latent heat flux NME in the 17 stations for each simulation: CTR, MLAI, MLAI_RSMIN and MLAI_ROOT. 84
A.23 Sensible heat flux SD in the 17 stations for each simulation: CTR, MLAI, MLAI_RSMIN and MLAI_ROOT. 85
A.24 Sensible heat flux SD in the 17 stations for each simulation: CTR, MLAI, MLAI_RSMIN and MLAI_ROOT. 86
A.25 Sensible heat flux correlation in the 17 stations for each simulation: CTR, MLAI, MLAI_RSMIN and MLAI_ROOT. 87
A.26 Latent heat flux correlation in the 17 stations for each simulation: CTR, MLAI, MLAI_RSMIN and MLAI_ROOT. 88

B.2 As Figure B.1 but for Sylvania station. 90
B.1 Time series of Sensible heat flux, latent heat flux, soil moisture and LAI in Palang. The turbulent fluxes time series compare the observations (grey) with the simulations: C_CTR (black), C_MLAI (light blue), MLAI (blue), C_MLAI_ROOT (green) and C_MLAI_NOSMS (dashed red). The soil moisture time series shows the CTR top 3 layers meter soil moisture (top meter solid back) and the bottom layer soil moisture (dashed black) as well as the soil moisture at wilting point (blue) and field capacity (red). The LAI time series compares CTR (black) with the high resolution MODIS LAI time series (dotted blue), the high resolution MLAI and C_MLAI (blue), the climatology of MODIS considering the 0.25° bounding box (dashed blue) and CGLS LAI climatology (grey). 91
B.3 As Figure B.1 but for Espirra station. 92
B.4 As Figure B.1 but for Kruger station. 93
B.5 As Figure B.1 but for Amplero station. 94
B.6 As Figure B.1 but for Howard station. 95
B.7 As Figure B.1 but for Mopane station. 96
B.8 As Figure B.1 but for Blodgett station. 97
B.9 As Figure B.1 but for Bugac station. 98
B.10 As Figure B.1 but for Fort Peck station. 99
B.11 As Figure B.1 but for Harvard station. 100
B.12 As Figure B.1 but for Hesse station. 101
B.13 As Figure B.1 but for Howlandm station. 102
B.14 As Figure B.1 but for Hyytiala station. 103
B.15 As Figure B.1 but for Loobos station. 104
B.16 As Figure B.1 but for Palang station. 105
B.17 As Figure B.1 but for Tumbarumba station. 106
B.18 As Figure B.1 but for University of Michigan station. 107
B.19 Sensible heat flux MBE in the 17 stations for each simulation: CTR, MLAI, MLAI_RSMIN and MLAI_ROOT. 108
B.20 Latent heat flux MBE in the 17 stations for each simulation: CTR, MLAI, MLAI_RSMIN and MLAI_ROOT. 109
B.21 Sensible heat flux SD in the 17 stations for each simulation: CTR, MLAI, MLAI_RSMIN and MLAI_ROOT. 110
B.22 Sensible heat flux NME in the 17 stations for each simulation: CTR, MLAI, MLAI_RSMIN and MLAI_ROOT. 111
B.23 Latent heat flux NME in the 17 stations for each simulation: CTR, MLAI, MLAI_RSMIN and MLAI_ROOT. 112
B.24 Latent heat flux correlation in the 17 stations for each simulation: CTR, MLAI, MLAI_RSMIN and MLAI_ROOT. 113
B.25 Sensible heat flux SD in the 17 stations for each simulation: CTR, MLAI, MLAI_RSMIN and MLAI_ROOT. 114
B.26 Sensible heat flux SD in the 17 stations for each simulation: CTR, MLAI, MLAI_RSMIN and MLAI_ROOT. 115

B.27 Sensible heat flux SD in the 17 stations for each simulation: CTR, MLAI, MLAI_RSMIN and MLAI_ROOT. 116
B.28 Sensible heat flux correlation in the 17 stations for each simulation: CTR, MLAI, MLAI_RSMIN and MLAI_ROOT. 117
B.29 Latent heat flux correlation in the 17 stations for each simulation: CTR, MLAI, MLAI_RSMIN and MLAI_ROOT. 118
B.30 Sensible heat flux correlation in the 17 stations for each simulation: CTR, MLAI, MLAI_RSMIN and MLAI_ROOT. 119

C.1 Ilamb metrics evaluation of the CTR model setup. 121
C.2 Evaluation of the CTR setup against GRUN. (a) Sbias, (b) Srmse, (c) Sphase, (d) Siav. 121
C.3 Evaluation of the CTR setup against SoMo. (a) Sbias, (b) Srmse, (c) Sphase, (d) Siav. 122
C.4 Evaluation of the CTR setup against Fluxcom. (a) Sbias, (b) Srmse, (c) Sphase, (d) Siav. 122

Chapter 1

Introduction - The land surface as a key component of the earth system

The climate earth system consists of five major coupled components: (i) the atmosphere, (ii) the hydrosphere, (iii) the cryosphere, (iv) the land surface and (v) the biosphere. Each of these earth system climate components are forced and influenced by several external forcing mechanisms. The land surface comprises soil, snow, vegetation, urban area, rivers, lakes and glaciers. Located at the boundary between the atmosphere and the lithosphere, it controls the land surface energy, water and carbon balances. A wide range of biogeochemical and biogeophysical interactions with the atmosphere, referred as land surface processes, influence both the climate and changes in key land surface variables (e.g., surface albedo, surface roughness length, soil moisture, land surface temperature, land cover...). In terms, those changes affect all of the other interconnected components of the earth system (A. J. Pitman, 2003).

Considering the prime role of the land surface in the climate system, different networks (FLUXNET, World Meteorological Organization...) and methods (remote sensing, machine learning...) of land surface observation are established and used to better understand the conditions of the land surface radiative, hydrological, biogeochemical and ecological processes. Considering the interconnected and coupled nature of the land surface, it is important to capture and perceive the interaction among processes and their effect on the climate (A. K. Betts et al., 1996; Zhao and Li, 2015). The development of land surface models (LSM) since the first generation "bucket model" (Manabe, 1969) help us understand the complex interactions between the land surface and the atmosphere from the micro to mesoscales to the continental scale when coupled with large-scale atmospheric models (A. J. Pitman, 2003; Zhao and Li, 2015). LSMs are also a key component in understanding Earth's carbon cycle (A. J. Pitman, 2003; Prentice et al., 2014). Therefore, in order to project the future climate, LSMs must be able to represent the impact of both human activities and natural processes on the surface-atmosphere interactions.

1.1 The land surface and the role of vegetation in climate processes

At regional to global scales, changes in the land surface influence climate at a range of time scales, from seconds to millions of years (Pielke et al., 1998; A. J. Pitman, 2003; Sellers et al., 1996). The vegetation plays a key role in the exchange of water, energy momentum and carbon.

1.1.1 The energy cycle

Shortwave radiation emitted by the sun is reflected, absorbed or transmitted by the atmosphere. A fraction of the solar radiation reaches the land surface and some is reflected back depending on the albedo. The rate of infrared radiation received or emitted by the Earth's surface depends on the temperature and emissivity of the land surface. The energy entering the global climate system is then exchanged as sensible and latent heat fluxes (A. J. Pitman, 2003). The net radiation (R_n) is therefore balanced between the sensible heat flux (Q_h), the latent heat flux (Q_{le}), and the soil heat flux (G). in thermal equilibrium the energy balance at the land surface is given by:

$$R_n = Q_h + Q_{le} + G \tag{1.1}$$

A fraction of incoming solar radiation is reflected back by the albedo, therefore changes in albedo affect the energy budget and thus Q_{le} and Q_h. The albedo is at the center of complex feedback mechanisms between the land surface and some elements of the climate boundary-layer, and changes in clouds or precipitation feedback could modify the initial perturbation of the albedo. Human activities, seasonal vegetation changes, rainfall and snowfall have also a direct impact on albedo (Hall, 2004; A. J. Pitman, 2003). For instance, an increase in albedo would probably reduce the tendency for vegetation growth and plant evapotranspiration rates. Vegetation plays a prime role in the land-atmosphere interactions since plant processes depend on environmental conditions such as amount of radiation, water, CO_2, soil nutrients, temperature, air and soil humidity to grow properly. Changes in leaf area index (LAI, define as the surface area of leaf per surface area of ground) can influence the exchange of both Q_h and Q_{le} and the balance between fluxes from the soil and vegetation. For instance, a decrease in LAI will reduce the canopy shading and increase solar radiation at soil surface. The increase net radiation at the soil surface means an increase in soil evaporation rate (A. J. Pitman, 2003). Roots distribution dictates the amount of soil moisture available for plant transpiration and the existence of positive feedbacks between reduced root water uptake, rainfall and further reduction of the root distribution has an impact on vegetation growth and therefore the energy cycle. A decrease in root depth lowers the amount of water available for evapotranspiration which increase canopy and boundary layer temperature.

1.1.2 The terrestrial water cycle

The latent heat flux energy is used to convert liquid water into vapour (or solid snow to vapour in case of sublimation), therefore the term Qle establishes the link between the energy and water cycle. The land surface partitions available precipitation (P) between evapotranspiration (E), runoff (R) and infiltration (I).

$$P = E + R + I \tag{1.2}$$

The term evapotranspiration represents the total evaporation from the land surface and is the sum of the interception layer evaporation (precipitation retained by the canopy), soil evaporation and transpiration which is the evaporation through the leaves of the water that is absorbed from the roots. Change in vegetation nature and distribution affect evapotranspiration and transpiration and therefore the water cycle.

1.1.3 The terrestrial carbon cycle

The earth's biosphere constitutes a carbon sink that could absorb approximately 2000 Gt of carbon (Prentice et al., 2001). Photosynthesis converts atmospheric CO_2 into it's organic form in order to build up biomass (roots, leaves and stems). The Gross Primary Production (GPP) is defined by the amount of carbon assimilated by plants. Some of this carbon is expelled during plant respiration or autotrophic respiration (R_α). The net plant carbon uptake called net primary productivity is defined as the GPP minus R_α. The ground decomposition of dead vegetation litter releases CO_2 in a process called soil respiration. The heterotrophic respiration (R_h) includes all carbon losses by organisms other than plants. The Net Ecosystem Exchange (NEE) is give by the following equation:

$$NEE = R_h - NPP = R_{eco} - GPP \tag{1.3}$$

where the sum of autotrophic and heterotrophic respiration is the ecosystem respiration, $R_{eco} = R_\alpha + R_h$.

1.2 Land Surface Models

Land Surface Models were primarily developed to numerically simulate the evolution of the land surface, providing boundary conditions to the atmosphere, on time-scale ranging from short-range forecasts (few days) to climate change projections (centuries). LSMs also provide ocean models with discharges of water, sediments and solutes. Originally the land surface models were designed to capture the essential features of land-atmosphere interactions. However, land-atmosphere interaction and the land surface state is also a very important source of information in many applications other than numerical weather prediction or climate change projections. Therefore LSMs have been re-casted to help us make decisions on environment management in order to build resilience to a changing climate (Blyth et al., 2021). Here the focus is on the descriptions of LSMs representation of processes related to the energy, water and carbon cycle.

Land Surface Models simulate the partitioning of surface net radiation at the land surface into the emission of thermal infrared radiation to the atmosphere, latent heat flux associated with evaporation and transpiration, sensible heat flux and ground heat flux. They need to solve the surface energy balance (equation 1.1) and the water budget (equation 1.2). In order to do so, a common approach of LSMs is to consider the land surface as an electrical analogue where the rate of exchange between the land surface and the atmosphere are controlled by a number of resistance parameters, depending

on the local climate and the internal properties of the land surface and vegetation (Boussetta et al., 2012; Manrique-Suñén, 2016; A. J. Pitman, 2003).

Land Surface Models have evolved considerably since the first "bucket" model by Manabe (Manabe, 1969), and despites caveats and simplifications it was a key step in the representation of land surface processes in climate models (A. J. Pitman, 2003). Today's models have considerably evolved in resolution and complexity as they include representations of numerous processes that are known to impact the earth system

Second generation models implemented a revised physical representation of the vegetation, soil temperature and soil moisture representation. The major advances of third-generation LSMs is the inclusion of an explicit canopy conductance in order to improve evaporation simulation and carbon uptake by the plants. These more physically based LSMs (second and third generation models) are able to capture the complexity of energy and moisture exchange between the soil, the vegetation, the water cycle and the carbon cycle. Today's LSMs play a crucial role in our ability to assess the remaining carbon emission humanity could emit to limit climate change to international targets (Blyth et al., 2021). LSMs represent a unique and powerful tool at the intersections of the fields of physics, biochemistry, physiology, ecology, hydrology, geography, statistics, mathematics and high-performance computing. They are in a state of constant evolution and current development tries to address the issues related to ecosystem resilience under a range of environmental and anthropogenic pressures. In order to resolve the heterogeneity of the land surface across a multitude of scales, most of the LSMs use the "tiling" approach. Each grid box is divided into fractions of different types of land use with independent solutions of the surface energy budget (Manrique-Suñén, 2016).

1.3 Research questions and organization of the thesis

The objective of this thesis is to advance our understanding of the role of the coupling between the water and the carbon cycles in the Earth System. It also aims at identifying relevant surface processes related with the water and carbon cycles at weather and climate time-scales. Sensitivity analysis, calibration and tuning of key parameters need to be performed in order to fulfill those objectives. This requires the need for land surface model simulations with the incorporation of the latest earth observation and global gridded datasets. Satellite products helped to redefine more up-to-date model parameters and monthly climatology (LAI and Albedo). Datasets based on machine learning algorithms are used here to evaluate model simulations with gridded observation on a global scale. This use of high-resolution state-of-the-art observations provides a trustable base to perform land surface model parameters sensitivity analysis and thus identify key surface processes or parameters associated with the LSMs representation of the water and carbon cycles.

The thesis is organized in 5 chapters:

- Chapter 1 presented an overview of the land surface role within the earth system;
- Chapter 2 includes the research published in Stevens et al., 2020 where the main objective was to evaluate the representation of canopy resistance in the ECMWF LSM CHTESSEL by testing (i) the added value of the high resolution LAI and albedo to represent local station conditions and (ii) the impact of the roots distribution on soil moisture stress;

- Chapter 3 extends the work of the second chapter by comparing two formulations for evaporation in the ECMWF LSM (CHTESSEL and CTESSEL) in terms of both water (Qle), energy (Qh/Qle) and carbon (NEE) fluxes as well as the role of roots distribution on soil moisture stress on both model formulations;
- Chapter 4, build on the previous chapters work, moves from a point-scale to a global scale assessing the impact of updating the land cover and roots distribution in the ECMWF LSM, and evaluating it against several global datasets of runoff, evaporation and soil moisture based on machine learning algorithms;
- Chapter 5 resumes the main conclusion of the thesis.

Chapter 2

Role of remote sensed leaf area index, albedo and roots distribution on ECMWF land surface model - offline evaluation against flux tower measurements

2.1 Introduction

The water, energy, and carbon exchanges between the land surface and the atmosphere are a key component of the Earth system. These exchanges are crucial for the understanding of the Earth System response to the increase in greenhouse gases concentration and climate change. The variety and complexity of the underlying processes driving these exchanges (from boundary layer turbulence to plant physiology) are challenging both to observe and to model. From a modelling perspective, these fluxes provide boundary conditions to Numerical Weather Prediction models (NWP) and Earth System Models (ESM). The longer time scales of some of the land surface processes (Carvalhais et al., 2014; Orth and Seneviratne, 2012), when compared with the atmosphere, are crucial for sub-seasonal to seasonal predictability (Koster et al., 2010; Koster et al., 2011; Koster and Walker, 2015) and to represent climate feedbacks (Seneviratne et al., 2010; Woodward, 1998).

The turbulent exchanges of latent heat flux (Q_{le}), or evaporation, couples the surface water, energy and carbon budgets. Evaporation requires available water and energy (Denissen et al., 2020). Additionally, a significant part of evaporation is due to plant transpiration (Coenders-Gerrits et al., 2014; D. M. Lawrence et al., 2007; Schlesinger and Jasechko, 2014) which is coupled with vegetation photosynthesis and carbon exchanges, with a key role for soil moisture (X. Liu et al., 2020). From an atmospheric perspective, the partition of the net surface energy into Q_{le} and sensible heat flux (Q_h) modulate the atmospheric boundary layer evolution with implications ranging from convection

and clouds evolution Gentine et al., 2013 to amplification of extremes (Teuling et al., 2013; Vogel et al., 2017). Vegetation transpiration and carbon uptake for photosynthesis are mediated by stomatal opening. Therefore, stomatal conductance is an essential component in the representation of evaporation in land surface models (LSM). Stomatal conductance is modulated by environmental factors (e.g. water stress) (Damour et al., 2010), and the leaf-to-canopy upscaling dependent on vegetation characteristics (Sprintsin et al., 2012).

This chapter focus on the impact of the representation of canopy resistance on Q_{le} and Q_h fluxes in the European center for Medium-Range Weather Forecasts (ECMWF) Land Surface model (LSM) CHTESSEL (Balsamo et al., 2009; Boussetta, Balsamo, Beljaars, Kral, et al., 2013). It is motivated by the results of the Land Surface Model Benchmarking Evaluation Project (PLUMBER Best et al., 2015), in which CHTESSEL participated, and by Ukkola et al., 2016 that focused on seasonal-scale evaporative droughts. These studies compared the performance of several LSMs using atmospheric forcing from several FLUXNET towers. Best et al., 2015 benchmarked the LSMs against simple physically based models and empirical relationships. The striking results showed that all participating LSMs were outperformed by an out-of-sample linear regression against downward shortwave radiation for the simulation of sensible heat flux, and by three-variable nonlinear regression that uses instantaneous atmospheric humidity and temperature in addition to downward shortwave radiation for the simulation of latent heat flux. Another key finding in PLUMBER was that LSMs had difficulties in simulating latent heat flux in sites with low annual precipitation, suggesting that this could be associated with the representation of water stress conditions in the models. The follow-up study of Ukkola et al., 2016 found systematic biases across the LSMs, including CHTESSEL, in simulation of energy and water fluxes under water-stressed conditions. Despite these limitations, Best et al., 2015 also found that LSMs perform well, compared with the empirical benchmarks, when considering metrics for the extremes of the distributions. Therefore, the physical constraints in the LSMs and their continued development are paramount to simulate conditions outside of training conditions as is the case for climate change scenarios (Sungmin et al., 2020).

Canopy resistance in CHTESSEL follows an empirical multiplicative formulation describing the effects of different environmental variables (Jarvis, 1976), which is a common approach in several LSMs. Another approach is to couple net photosynthesis with canopy resistance (C. M. Jacobs et al., 1996). CHTESSEL also has a module to compute natural land carbon exchanges, but the carbon exchanges are decoupled from evaporation due to conflicting results in NWP (Boussetta, Balsamo, Beljaars, Panareda, et al., 2013) justifying the focus on Q_{le} and Q_h in this study. In the resistance approach used by CHTESSEL, vegetation characteristics are considered via the use of the Leaf Area Index (LAI). The environmental factors account for water stress, which is dependent on soil moisture content varying linearly between unstressed vegetation and wilting point. In this study, we address these two components of the canopy resistance formulation in CHTESSEL: (i) vegetation characteristics and (ii) water stress.

Vegetation characteristics are investigated by testing the use of a high-resolution LAI climatology based on the Moderate Resolution Imaging Spectroradiometer (MODIS) product. The impact of a high-resolution Albedo climatology is also investigated. The use of this high-resolution data is mo-

tivated by the increased quality and amount of available Earth Observations (EO) (Balsamo et al., 2018). Here we aim at evaluating the impact of using location specific LAI data when compared with the common LAI data has been spatially aggregated to a coarse grid for NWP applications. The water stress representation is investigated by testing a uniform roots distribution with an associated maximum rooting depth. This is compared with the current formulation in CHTESSEL that assumes an exponential roots distribution (Zeng et al., 1998). Roots distribution defines the maximum amount of water that is reachable by the plants, modulating the response of transpiration to moisture stress (Desborough, 1997; X. Liu et al., 2020).

As in Best et al., 2015, observed data from 17 stations of the FLUXNET global network of micrometeorological flux measurements, are used to carry out offline simulations with CHTESSEL and evaluate sensible and latent heat fluxes, with particular emphasis on the representation of evaporation and its relation with water stressed conditions. The main objective in this chapter is to evaluate the representation of canopy resistance by testing (i) the added value of the high-resolution LAI and albedo to represent local station conditions and (ii) the impact of roots distribution on soil moisture stress. The data and methods are described in the next section, followed by the presentation of the results. The results are discussed in section 4 followed by the main conclusion in section 5.

2.2 Data and Methods

2.2.1 Data

Tower flux data

Observed data from 20 FLUXNET towers were initially considered as in Best et al (Best et al., 2015). These stations are widely used since they present a variety of vegetation types and climates (Best et al., 2015; Cescatti et al., 2012; Haughton et al., 2016). The Spanish stations of ElSaler and ElSaler2 were removed due to the presence of large water bodies nearby and irrigated agricultural fields. The Canadian station of Merbleue was also problematic and thus removed since this tower is in the middle of a wetland, which is difficult to correctly model. This corroborates with Haverd et al., 2016 who also removed these 3 stations from their study, resulting in the 17 stations described in Table 2.1. The data includes gap-filled half-hourly driving data for the LSM (air temperature and humidity, surface pressure, windspeed, precipitation and downward solar and thermal radiation), and surface sensible and latent heat flux used for model evaluation.

Table 2.1: *FLUXNET* tower flux stations used in this study

Station	Country	Latitude	Longitude	Plant Functional Type	Time period
Amplero	Italy	41.9041	13.6052	Grassland	2003-06
Blodgett	US	38.8953	-120.633	Evergreen needleleaf	2000-06
Bugac	Hungary	46.6917	19.6017	Grassland	2002-06
Espirra	Portugal	38.6394	-8.6018	Evergreen broadleaf	2001-06
Fort Peck	US	48.3077	-105.102	Grassland	2000-06
Harvard	US	42.5378	-72.1715	Deciduous broadleaf	1994-2001
Hesse	France	48.6742	7.0656	Deciduous broadleaf	1999-2006
Howard	Australia	-12.4943	131.152	Woody Savanna	2002-05
Howlandm	US	45.2041	-68.7402	Evergreen needleleaf	1996-2004
Hyytiala	Finland	61.8474	24.2948	Evergreen needleleaf	2001-04
Kruger	South Africa	-25.0197	31.4969	Savanna	2002-03
Loobos	Netherlands	52.1679	5.744	Evergreen needleleaf	1997-2006
Mopane	Botswana	-19.9165	23.5603	Woody Savanna	1999-2001
Palang	Indonesia	-2.345	114.036	Evergreen broadleaf	2002-03
Sylvania	US	46.242	-89.3477	Mixed forest	2002-05
Tumbarumba	Australia	-35.6557	148.152	Evergreen broadleaf	2002-05
University of Michigan	US	45.5598	-84.7138	Deciduous broadleaf	1999-2003

Satellite Albedo and Leaf Area Index

We use the combined MODIS LAI and Fraction of Photosynthetically Active Radiation (FPAR) product (MCD15A3H.006). This is a 4-day composite dataset with a spatial resolution of 500 m available since July 2002 to present. This MODIS product has been validated in different studies (H. Fang et al., 2012; Sea et al., 2011) reporting uncertainties in the order of 1 m^2/m^2. In addition to the MODIS LAI product, the Copernicus Global Land Service (CGLS) LAI was also used in this study. The product is obtained from SPOT-VGT and PROBA-V satellite observations with 1 km resolution using a neural network algorithm (Verger et al., 2014) and is available since 1999. A comparison between MODIS and CGLS (a new version with 300 m resolution) LAI products with ground based observations over North America reported a root mean square differences of 0.57 for the CGLS product and 0.81 to 0.89 for MODIS (Brown et al., 2020).

In addition to the LAI product, the Combined MODIS Bidirectional Reflectance Distribution Function (BRDF) and Albedo products (MCD43A4.006, Schaaf et al., 2002) were also used. This product has been available since February 2000 with a 500m resolution. Wang et al. (Wang et al., 2014) reported root mean square errors ranging between 0.02 for forest regions and 0.03 for agricultural/grassland regions.

The most restrictive Quality Control (QC) criteria was applied in order to select only the best quality data. In the case of the albedo product, the model requires snow-free albedo. Therefore, the MODIS snow products (MOD10A1.006 and MYD10A1.006) were used to mask the albedo data when snow was present. A less restrictive quality filtering was applied for LAI (H. Fang et al., 2012), and good quality data is also selected (QC>64 - Highest and good quality). A Similar quality

control data filtering was also applied to the CGLS data (only QC=0 (land pixel clear observations) or QC=512 (High latitude -lat >55° and Solar Zenith Angle >70°)).

MODIS LAI and albedo, as well as the CGLS LAI were extracted for the 17 Fluxnet stations (see Table 2.1) by averaging the data of the central pixel with the four other pixels in the direct vicinity. Monthly means were first computed, and the monthly climatology computed excluding months with more than 50% of missing data, for the full available period until 2018 (since 1999 for the CGLS LAI, since 2003 for the MODIS LAI and since 2000 for the MODIS albedo).

The quality based data screening was too restrictive for the northern latitude stations, especially during the winter when satellite products are subjected to cloud contamination. In Hyytiala, Loobos and Palang the MODIS albedo product has a large amount of cloud contamination, and not enough data is available to calculate the monthly climatology. The quality control data filtering was therefore relaxed and changed not only to best quality data but also to good quality data ($QC \leq 1$). After this processing, Hyytiala presented high albedo values in January, associated with snow contamination. January's albedo was replaced by a linear interpolation between December and February. This shows the difficulty to generate snow-free albedo data (Sun et al., 2017), particularly in regions and seasons that are predominantly snow (and cloud) covered. However, this is not expected to influence the model simulations as during January the surface albedo has a small impact due to the reduced amount of available solar radiation in Hyytiala.

2.2.2 CHTESSEL model

CHTESSEL is the land surface scheme of the ECMWF model (Balsamo et al., 2009; Boussetta, Balsamo, Beljaars, Panareda, et al., 2013). In CHTESSEL each grid-box is divided into up to 6 land fractions representing vegetation, soil, snow and interception. Surface fluxes are calculated separately for the different subgrid surface fraction (or "tile") leading to a separate solution of the surface energy balance and skin temperature for each of these tiles, which are then aggregated in each grid-box. In each grid-box two vegetation types can coexist (high and low vegetation) controlled by four parameters: dominant high and low vegetation type and the area fraction for the high and low vegetation. Each vegetation type is characterized by a series of fixed parameters: (i) minimum canopy resistance r_{smin}, (ii) a vegetation coverage density C_{veg}, (iii) a coefficient GD, for the dependence of the canopy resistance on water vapour pressure deficit and the (iv) the roots distribution over the soil layers, specified by an exponential profile modulated by the coefficients a_r and b_r. The numerical values for the parameters (see Table A.1 in the appendix A) are based on literature (Bonan, 1994; Dorman and Sellers, 1989; Giard and Bazile, 2000; Mahfouf et al., 1995; Manzi and Planton, 1994; A. Pitman, 1991; Zeng et al., 1998) and on expert decision in the context of the performance of the model in NWP. For example, the introduction of a seasonal variable LAI was accompanied with a revision of the minimum canopy resistance (Boussetta, Balsamo, Beljaars, Panareda, et al., 2013). A detailed description of CHTESSEL can be found in the integrated forecasting system (IFS) documentation (Chapter 9 in: https://www.ecmwf.int/node/19308, last access: November 2021) and here the details of the evaporation calculation is presented due to its relevance in the results interpretation and discussion.

For high and low vegetation, the turbulent flux of water is given by:

$$E = \frac{\rho_a}{r_a + r_c}(q_L - q_{sat}(T_{sk})), \quad r_a = (|U_L|C_H)^{-1} \tag{2.1}$$

where ρ_a is the air density, U_L, and q_L are the wind speed and humidity at the lowest atmospheric model level, $q_{sat}(T_{sk})$ the saturation humidity at skin temperature (T_{sk}), and C_H the turbulent exchange coefficient (depending on the atmospheric stability). In addition to the aerodynamic resistance (r_a), the canopy resistance (r_c) (Jarvis, 1976) is calculated as:

$$r_c = \frac{r_{smin}}{LAI} * f_1(R_s) * f_2(\theta) * f_3(D_a) \tag{2.2}$$

where r_{smin} is the minimum stomatal resistance (see Table A.1), f_1 is a function of downward short-wave radiation (R_s), f_3 a function of the atmospheric water vapour deficit (D_a) and f_2 the soil moisture resistance given by:

$$1/f_2(\overline{\theta}) = \begin{cases} 0 & \overline{\theta} < \theta_{pwp} \\ (\overline{\theta} - \theta_{pwp})/(\theta_{cap} - \theta_{pwp}) & \theta_{pwp} \leq \overline{\theta} \leq \theta_{cap} \\ 1 & \overline{\theta} > \theta_{cap} \end{cases} \tag{2.3}$$

where θ_{pwp} and θ_{cap} are the soil moisture at permanent wilting point and at field capacity, respectively and $\overline{\theta}$ is a weighted average of the unfrozen soil water computed using the fraction of roots in each layer (R_k) (Zeng et al., 1998) using the a_r and b_r coefficients (in Table A.1):

$$R_k = 0.5\left[exp\left(-a_r z_{k-1/2}\right) + exp\left(-b_r z_{k-1/2}\right) - exp\left(-a_r z_{k+1/2}\right) - exp\left(-b_r z_{k+1/2}\right)\right] \tag{2.4}$$

where $z_{k+1/2}$ is the depth of the bottom layer k in m and $z_{1/2}$ is $= 0$. In CHTESSEL the soil is discretized in four layers with thickness of 0.07, 0.21, 0.72 and $1.89m$, with lower bounds at 0.07, 0.28, 1, $2.89m$.

In CHTESSEL the state of vegetation is given by the LAI, entering the canopy resistance calculation normalizing r_{smin} (equation 2.2). In the current operational NWP configuration, a satellite observation-based climatology is considered for the representation of LAI. It is based on collection 5 of MODIS (product MOD15A2). The climatology was derived from 9 years of data (2000 to

2008) and rescaled to a previous LAI static field used at ECMWF before 2012 (Boussetta, Balsamo, Beljaars, Kral, et al., 2013).

2.2.3 Simulations setup

Offline point simulations were performed using CHTESSEL driven by the meteorological data observed at the towers. The model is initialized with soil moisture at field capacity and runs once for the full length of the available forcing period for each station. The state at the end of the simulation is then used to provide initial conditions to start the main simulation. For most sites this procedure guarantees enough time for spin-up, in particular for the deeper soil moisture. The exceptions are Palang and Kruger with only two years. In both cases, the top meter soil moisture in the two year of simulation does not show a significant drift. In Palang there is an increase of the deep soil moisture during the simulation (see Figure A.16 in appendix A), but still within the inter-annual variability. In each site only one dominant high or low vegetation type is allowed defined according to the plant functional type (PFT). Howard, Kruger and Mopane stations report PFTs that are not available in CHTESSEL (woody savanna and savanna). These stations were set as tall grass vegetation type (see Table 2.5), as this is the closest vegetation type in the vicinity of the stations in the global land cover dataset used by the model.

Several model configurations were tested and resumed in Table 3.1. These configurations aim at investigating the role of (i) high resolution remote sensing LAI and albedo and (ii) model formulation and parameters. The first configuration, labelled as "CTR" for control, used CHTESSEL original input data with ECMWF Integrated Forecasting System (IFS). The monthly climatologies of snow-free albedo and LAI were extracted from the nearest grid-point of operational NWP fields with a 9 km resolution. This model configuration serves as a reference against which other model configurations will be compared, and was the same that was used in Best et al., 2015. The second one, labelled as "MALB" uses the MODIS extracted high resolution albedo monthly climatology over the stations. The third configuration, labelled as "MLAI" uses the MODIS extracted high resolution LAI monthly climatology over the station. In both cases, the albedo and LAI data represent the nearest five MODIS pixels from the station (as described in section 2.2.1).

Two additional model configurations were tested to investigate the role of r_{smin} and roots distribution, both using the MODIS LAI high resolution data. For r_{smin} a set of simulations varying r_{smin} between 25 and 500 with a step of 25 was performed for each site. For the roots distribution, a uniform roots distribution was adopted up to a maximum rooting depth (R_{DMAX} m) changing the computation of the roots fraction in each layer in equation 2.4 to:

$$R_k = \frac{max\left[0, min\left(R_{DMAX, z_{k+1/2}}\right) - z_{k-1/2}\right]}{R_{DMAX}} \tag{2.5}$$

In this configuration, 4 maximum rooting depths are tested: 0.5, 1, 2, and 3 m. The CTR roots distribution for each vegetation type and for the tested uniform rooting depths are given in Table

A.1 (in appendix A). Root density distribution and roots depth is poorly constrained at large spatial scales as it varies between individual species and climate factors (Cabelguenne and Debaeke, 1998; Guswa, 2008; Nielsen and Vigil, 2018). Therefore, a uniform distribution is a simple and straightforward first-order assumption.

An optimal model simulation for each site was then selected and labeled MLAI_RSMIN for the optimal simulations with varying r_{smin} and MLAI_ROOT for the optimal simulations with varying the maximum rooting depth R_{DMAX}. The selection of the optimal configuration is described in the following section. Finally, an idealized experiment removing the soil moisture stress function from the canopy resistance (MLAI_NOSMS, setting $f_2 = 1$ in equation 2.2 when soil moisture is above wilting point) was performed. This idealized experiment provides an estimate of evaporation in a situation of soil moisture at field capacity.

Table 2.2: Model simulations acronyms and detailed configuration

Simulation	**Details**
CTR	Control simulation with default CHTESSEL parameters and input LAI and Albedo
MALB	As CTR but replacing the input Albedo climatology by the new high resolution MODIS climatology
MLAI	As CTR but replacing the input LAI climatology by the new high resolution MODIS climatology
MLAI_NOSMS	As MLAI but removing soil moisture stress function from the canopy resistance (setting $f_2 = 1$) when soil moisture is above wilting point in Eq 2.3
MLAI_RSMIN	As MLAI but selecting the optimal r_{smin} for each station from a set simulations with varying r_{smin} between 25 and 500.
MLAI_ROOT	As MLAI but using an uniform root distribution (Eq. 2.5) and selecting the optimal R_{DMAX} for each station from a set of simulations with R_{DMAX} of 0.5, 1, 2, and 3 m.

2.2.4 Evaluation

The simulated Qle and Qh is compared with the tower measurements using 4 metrics (i) the Mean bias error MBE, standard deviation difference SD, correlation coefficient r, and normalized mean error NME. The SD is computed as the absolute difference between 1.0 and the ratio between simulated and observed standard deviation. The NME is the mean absolute error normalized by the mean absolute observed deviations from the mean. These metrics follow Best et al., (Best et al., 2015) and are detailed in the Appendix (equation A.1 to equation A.4). The calculations are performed on daily simulated and measured fluxes.

For the selection of the optimal simulations with varying r_{smin} or maximum rooting depth a ranking approach considering the four metrics for both Qh and Qle was considered. For each metric and flux each simulation is ranked in ascending order from 1 to 20 in the case of r_{smin} and 1 to 4 in the case of R_{DMAX}. This results in rankings that are then added and the simulation with the lowest rank is selected as the optimal simulation. This process is performed independently for each site, and assumes that the metrics for Qle and Qh are of equal weight, and does not distinguish between larger or smaller differences between metrics in the ranking. The use of the rankings of each metric without considering the actual metric value nor the differences between simulations, is a limitation as simulations ranked differently can be actually very close. This approach can be interpreted as a simple optimization strategy to select the optimal r_{smin} or R_{DMAX} for each site. However, it is not intended to be a proper model calibration as it is site specific and considers the entire set of observations. The search of the optimal simulations on each site by changing r_{smin} or R_{DMAX} is designed to provide an estimate of the upper bound on the best achievable performance of the model. It is a benchmark to determine if the model could be improved just by changing the particular parameter. The reduced number of stations (only 17) and sampling of vegetation types imposes limitations in performing a proper out of sample calibration to provide estimates of r_{smin} and R_{DMAX} for each of the vegetation types.

2.3 Results

2.3.1 Comparison of LAI and Albedo

In this section we compare the LAI and Albedo high resolution (station) with the original CHTESSEL input data. The high resolution MODIS data for each tower is compared with the original CHTESSEL input data in terms of the mean and root mean square differences, which is computed for the mean annual cycle. The MODIS albedo is very close to CTR in all stations (see Table 2.3) with most of the stations with RMSD around 0.03. There are two exceptions, Fort Peck and Loobos with a root mean square difference (RMSD) of 0.07 mostly due to lower values in ALB when compared with CTR during winter, which are associated with snow contamination. Despite the importance of albedo in the surface energy balance, these results suggest that for these 17 stations we should expect a small impact in CHTESSEL simulation due to the update of CTR albedo by the high resolution MODIS albedo.

Table 2.3: Comparison between CTR and MODIS ALB (MALB) for each tower. The root mean square difference is computed for the mean annual cycle.

Station	**Mean CTR**	**Mean MALB**	**RMSD MALB vs CTR**
Amplero	0.16	0.15	0.03
Blodgett	0.13	0.1	0.02
Bugac	0.18	0.16	0.03
Espirra	0.16	0.14	0.02
Fort Peck	0.25	0.18	0.07
Harvard	0.11	0.13	0.03
Hesse	0.13	0.15	0.03
Howard	0.15	0.13	0.02
Howlandm	0.11	0.12	0.01
Hyytiala	0.12	0.11	0.02
Kruger	0.17	0.16	0.03
Loobos	0.17	0.11	0.07
Mopane	0.16	0.17	0.01
Palang	0.14	0.13	0.01
Sylvania	0.11	0.13	0.04
Tumbarumba	0.16	0.12	0.04
University of Michigan	0.11	0.13	0.03
Median	**0.15**	**0.13**	**0.03**

The comparison of CTR and MLAI in Table 2.4 depicts comparatively large differences in several stations with RMSD above 1 in Bugac, Hesse, Howland, and Palang. The time series of the climatological LAI of CTR, MODIS and CGLS are shown for all stations in the appendix A (Figures A.1 to A.18). The large differences in the climatology are mostly in the seasonal cycle amplitude, with MLAI presenting a more pronounced seasonal phenology. These results show some uncertainty in mapping LAI between the different EO products. Despite the differences between MODIS and CGLS, our results show a larger discrepancy between the products and the CTR climatology used in CHTESSEL with a median RMSD of 0.86 between CTR and MLAI when compared with a median RMDS of 0.43 between MODIS and CGLS LAI. While the CTR LAI is also based on MODIS data, it was derived from a shorter time period (2000-2008) and was rescaled to match a previous LAI field used at ECMWF (Boussetta, Balsamo, Beljaars, Kral, et al., 2013). These LAI differences, both in the mean and in the annual cycle are expected to impact the model simulations, which are investigated in the following section.

Table 2.4: Comparison between CTR and MODIS LAI (MLAI) for each tower. The root mean square difference is computed for the mean annual cycle.

Station	**Mean CTR**	**Mean MLAI**	**Mean CGLS**	**RMSD MLAI vs CTR**	**RMSD MODIS vs CGLS**
Amplero	2.43	1.7	1.51	0.9	0.29
Blodgett	3.08	2.28	2.98	0.87	0.47
Bugac	1.93	0.92	1.04	1.04	0.17
Espirra	2.38	1.42	1.13	0.97	0.20
Fort Peck	0.89	0.35	0.34	0.54	0.08
Harvard	3.14	2.45	2.78	0.75	0.58
Hesse	2.35	2.66	2.27	1.65	0.52
Howard	1.76	1.55	1.58	0.28	0.47
Howlandm	3.08	2.40	2.83	1.04	0.82
Hyytiala	2.12	1.69	1.73	0.50	0.51
Kruger	1.76	0.98	0.93	0.80	0.16
Loobos	2.21	1.87	1.87	0.53	0.43
Mopane	1.59	0.87	0.65	0.73	0.25
Palang	5.59	4.42	4.01	1.20	0.40
Sylvania	2.63	1.73	2.24	0.91	0.62
Tumbarumba	3.60	4.31	3.09	0.83	0.72
University of Michigan	2.42	2.11	1.76	0.86	0.25
Median	**2.38**	**1.73**	**1.76**	**0.86**	**0.43**

2.3.2 Fluxes evaluation

The use of the high resolution MODIS albedo had a negligible impact on model performance (not shown). This was expected due to the similarity between the albedo climatologies. Therefore, the MALB simulations are not shown or further explored. Figure 2.1 shows the distribution of the different metrics for Qh and Qle comparing CTR and MLAI simulations (among other model configurations to be discussed in the next section). In the MLAI simulation the Qle MBE is reduced from a median value of -3.02 W/m^2 in CTR to -2.19. Similarly, Qh MBE is reduced from 12.08 W/m^2 in CTR to 8.48 W/m^2 in MLAI. The standard deviation ratio (SD) is also improved with a reduction from 0.26 and 0.17 for Qle and Qh, respectively in CTR to 0.19 and 0.14 in MLAI. This improved variability is also seen in the temporal correlation with an increase from 0.79 to 0.83 in the Qle from CTR to MLAI and from 0.77 to 0.80 in Qh. Finally, the normalized mean error (NME) has a slight reduction in Qh from 0.78 in CTR to 0.75 in MLAI and slightly increase for Qle (0.62 in CTR and 0.64 in MLAI). We note that statistical significance of the changes in the model performance were not assessed because of the small sample size. Despite the small sample, only 17 stations, these results suggest a modest, but positive, impact of replacing CTR LAI by the high resolution MODIS data for the station.

It was not possible to identify a systematic improvement in model performance associated with the use of the high resolution LAI dataset. Each station reacts differently, depending on the time period considered. Some stations in some years benefit from the MODIS product, while other stations or time periods show a deterioration of model performance. Moreover, the impacts of the high resolution LAI dataset on model performance could not be generalized or classified by Plant Functional Type (PFT) as stations within the same PFT do not react similarly to LAI changes. Stations with a good performance in CTR (Fort Peck, Harvard, Howard, Howlandm, Hyytiala, Loobos, University of Michigan), are not impacted by the LAI changes. Additionally, the large differences between the CTR and LAI climatologies are not reflected in changes in model performance in some stations like Hesse or Howlandm. However, some stations suffering from poorer performances in CTR, benefit with MLAI as for example Bugac, Espirra, Palang, Sylvania and Tumba. Considering the four metrics used to characterise model performance, the temporal correlation benefits the most from the use of the high resolution LAI since this product has a larger interseasonal variability than CTR.

LAI enters the canopy resistance formulation normalizing the minimum stomatal resistance (r_{smin} in equation 2.2). It is therefore expected that changes in the LAI climatology would benefit from an adjustment of r_{smin} parameter. Such adjustment could be achieved by constraining r_{smin} so that the ratio r_{smin}/LAI would stay unchanged for each PFT. However, due to the small sample of stations for each PFT such an approach is not feasible. A set of simulations with varying r_{smin} was performed to select an optimal r_{smin} with the best model performance for each station, as described in section 2.4. The optimal r_{smin} for each site is presented in Table 2.5. The simulations with the optimal r_{smin} (MLAI_RSMIN) have a negligible impact on model performance (see Figure 2.1, comparing MLAI and MLAI_RSMIN). The only noteworthy impact is a clear reduction of the SD for Qle (see Figure 2.1 and Figure A.24), with the remaining performance metrics unchanged when compared with MLAI. These results show that r_{smin} acts primarily on the seasonal amplitude of Qle, explaining the large impact on SD, but neutral in the remaining performance metrics for Qle and Qh. In particular, the neutral impact on Qh SD highlights that the improved seasonal variability in Qle does not necessarily lead to an improved Qh seasonality.

There are three sites with a large increase of r_{smin} from CTR to MLAI_RSMIN: Kruger (100 to 300), Mopane (175 to 300) and Sylvania (175 to 400). In all three cases the mean LAI decreased from CTR to MLAI (see Table 2.5). This suggests that an adjustment that would keep the ratio r_{smin}/LAI unchanged with changes in LAI would not be optimal, or an indication that the default r_{smin} parameters were not optimal. In these 3 stations the increased r_{smin} results in a reduction of evaporation, as expected, which is clearly seen in Sylvania (see Figure A.2). However, the Qle reduction in Sylvania is associated with an unusually large r_{smin} of 400 sm^{-1}, suggesting that this might be compensating missing processes in the model and/or errors in the driving/observations data Ukkola et al., 2016 reported that Sylvania was excluded from their study due to precipitation problems). There are three sites with a large decrease of r_{smin}: FortPeck (100 to 25), Blodgett (250 to 150) and Espirra (240 to 75). In these stations there was also a reduction of the LAI from CTR to MLAI. From these three stations, Espirra stands out with the largest reduction of r_{smin}, resulting in an increase of Qle and decrease of Qh, particularly during spring (see Figure A.3). We note that

Qle in Espirra was underestimated in CTR, and was further reduced in MLAI due to the reduction of the LAI (mean LAI changed from 2.38 in CTR to 1.42 in MLAI). The optimal r_{smin} change from 240 to 75 acts to reduce the r_{smin}/LAI ratio from 100 sm^{-1} to 52 sm^{-1}. We also note that the other two evergreen broadleaf tree stations, Palang and Tumba, have a mean LAI of about 4.4 m^2/m^2 with a r_{smin}/LAI ratio of 54 sm^{-1}. These results suggest that the high resolution MODIS LAI extracted for Espirra station underestimates the station vegetation LAI (Rodrigues et al., 2011).

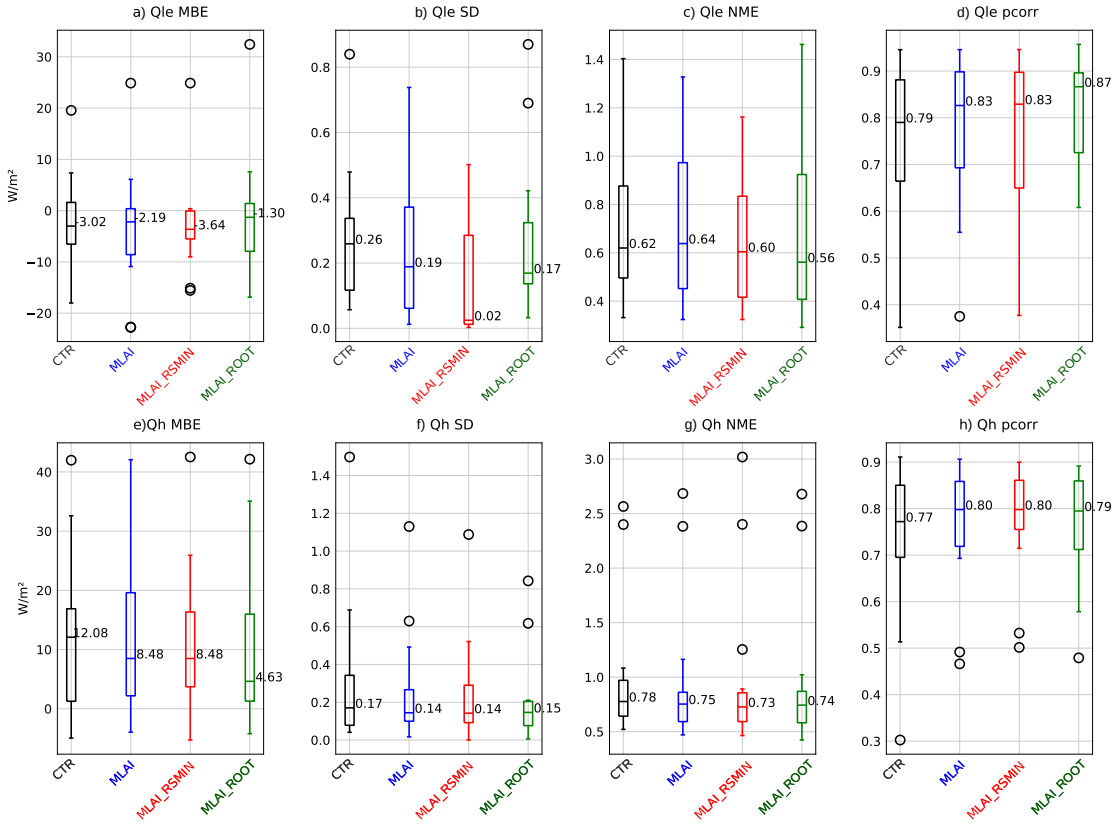

Figure 2.1: Latent (a-d top panels) and sensible (bottom panels) heat flux evaluation in terms of MBE, SD, NME and r for CTR, MLAI, MLAI_RSMIN and MLAI_ROOT. The boxplots represent each metric's distribution for the 17 towers showing the percentiles 25, 50 and 75. Symbols denote outliers for values further than 1.5 times the interquartile range from the nearest 25th or 75th percentile.

The metrics distributions in Figure 2.1 show some dispersion, associated with occurrence of a few outliers. The detailed results for each station and score are presented in the appendix A, in Figures A.19 to A.26. It is possible to identify five stations with recurrent problematic results for Qh/Qle in different metrics: Blodgett, Espirra, Mopane, Palang and Kruger. In Kruger, CHTESSEL overestimates substantially Qle after rainfall events, followed by an underestimation of Qle and overestimation of Qh (see Figure A.4). Kruger is a very dry station with soil moisture below wilting point, and the peak evaporation following rainfall events is mainly driven by bare soil evaporation. The remaining four stations: Blodget, Espirra, Mopane and Palang share a similar problem of an early evaporative reduction associated with dry soil moisture conditions resulting in the overesti-

mation of Qh. Although not seen clearly in the evaluation metrics, Amplero and Tumba also show similar Qle temporal error patterns. This early evaporation reduction, or evaporative droughts, as proposed by Ukkola et al., 2016, is further investigated in the following section.

Table 2.5: CTR r_{smin} and optimal r_{smin} and R_{DMAX} used in MLAI_RSMIN and MLAI_ROOT, respectively.

Station	**Vegetation type**	r_{smin} **CTR**	r_{smin} **optimal**	R_{DMAX} **optimal**
Amplero	L, Short grass	100	100	2
Bugac	L, Short grass	100	175	0.5
Fort Peck	L, Short grass	100	25	0.5
Howard	L, Tall grass	175	125	2
Kruger	L, Tall grass	100	300	2
Mopane	L, Tall grass	175	300	1
Blodgett	H, Evergreen needleleaf	250	150	3
Espirra	H, Evergreen broadleaf	240	75	3
Harvard	H, Deciduous broadleaf	175	250	1
Hesse	H, Deciduous broadleaf	175	175	2
Howlandm	H, Evergreen needleleaf	250	275	0.5
Hyytiala	H, Evergreen needleleaf	250	225	0.5
Loobos	H, Evergreen needleleaf	250	150	2
Palang	H, Evergreen broadleaf	240	275	2
Sylvania	H, Interrupted forest	175	400	3
Tumbarumba	H, Evergreen broadleaf	240	225	2
University of Michigan	H, Deciduous broadleaf	175	400	3

2.3.3 Soil moisture stress

Ukkola et al., 2016 identified a systematic overestimation of evaporative droughts in several LSMs, including CHTESSEL, which is consistent with the results in this chapter mainly in Amplero, Blodget, Espirra, Howard, Mopane, Palang and Tumba. Here evaporative drought refers to the regular dry season evaporation reduction as well as anomalous dry periods as defined by Ukkola et al., 2016. Figure 2.2 shows the time series of Qle and soil moisture for Amplero, Blodgett and Espirra (time series for all stations are provided in appendix A Figures A.1 to A.18). In these three examples it is possible to identify the early reduction of evaporation associated with the drop of soil moisture (Figure 2.2 compare Qle reduction in blue with top soil moisture reduction in red). In these stations, the evaporation starts to diverge from the observations when soil moisture in the top meter (where most of the roots are present in CTR - Table A.1) falls below field capacity and approaches the wilting point. During this period, the deep layer soil moisture (dashed red line in Figure 2.2) is above or close to field capacity. This is further illustrated by comparing the MLAI Qle simulations with MLAI_NOSMS in Figure 2.2 (blue vs dashed-blue line). These idealized simulations, without soil moisture stress, differ from MLAI exactly during the dry-down period, being closer to the observed Qle. The MLAI_NOSMS simulations present some unrealistic Qle variations (see for example 2003 in Amplero in Figure 2.2) associated with the drop of soil moisture below wilting

point (not shown) that stops evaporation to avoid water conservation problems that could result in numerical instabilities. Despite this limitation, the MLAI_NOSMS simulations suggest that the evaporative drought in CHTESSEL is tightly associated with the soil moisture stress formulation. The discrepancy between soil moisture conditions in the top meter versus the bottom layer during the dry-down and associated evaporative drought (Figure 2.2) motivated the exploratory revision of the roots distribution.

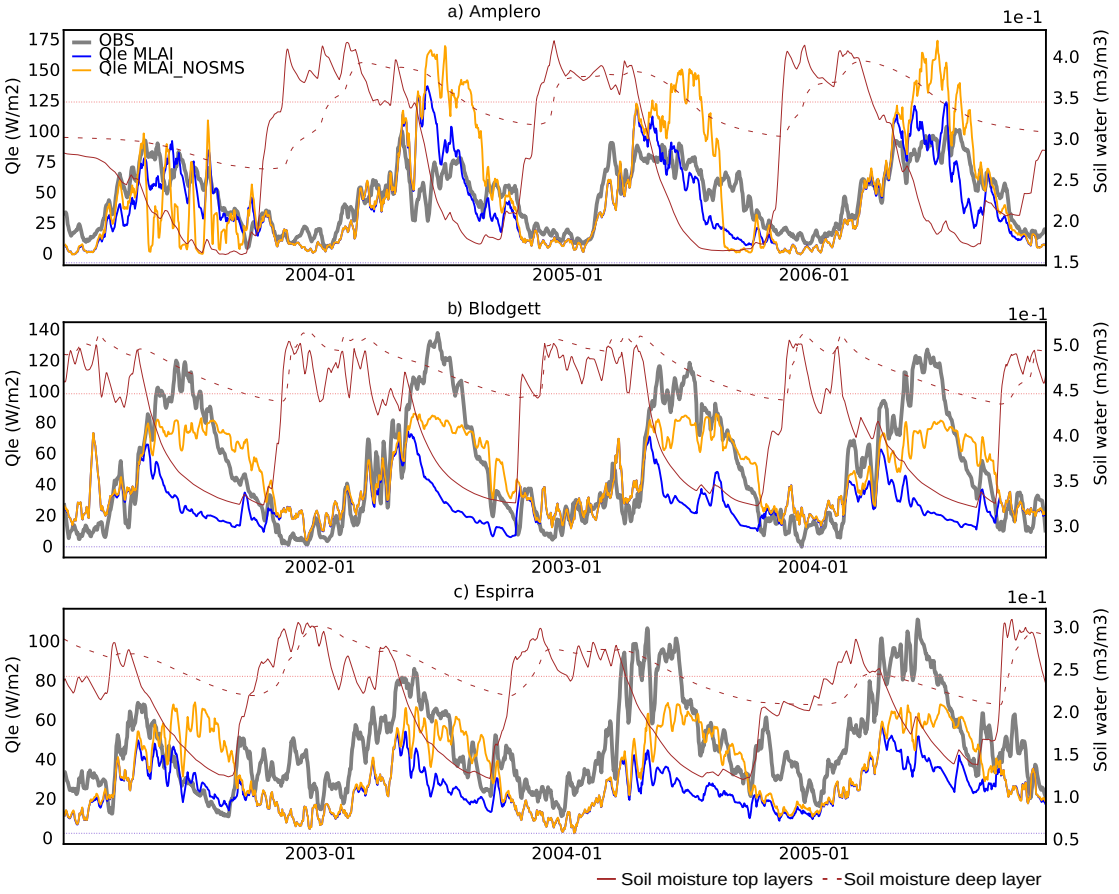

Figure 2.2: Latent heat flux (Qle) and soil moisture in Amplero (a), Blodgett (b) and Espirra (c). For Qle (left axis) observations are in grey, and the simulations from MLAI in blue and from MLAI_NOSM in orange. The soil moisture (right axis) for MLAI simulation is shown for the top 3 layer (red solid) and deep layer (red dashed). The light dotted red and blue lines represent soil moisture at field capacity and wilting point, respectively.

The roots distribution with the uniform formulation (Eq. 2.5) for the different maximum rooting depths (0.5, 1, 2 and 3 m) is presented in Table A.1 allowing the comparison with the CTR roots fraction for each layer and vegetation type. The main change of the uniform rooting depth are a decrease of the roots fraction in the top layer(s) and an increase of root fraction in the deeper layers. This will give more weight to the deeper layers when computing the root zone soil moisture. The optimal maximum rooting depth for each station (see section 2.2.4) in MLAI_ROOT is shown in Table 2.5.

Of the three short grass stations, Bugac and FortPeck show an optimal R_{DMAX} of 0.5 m with negligible differences to MLAI, while Amplero shows a R_{DMAX} of 2 m with an increase of Qle in late spring and summer. The increased Qle in Amplero in August/September 2005 (Figure 2.3) partially reduces the evaporative drought in MLAI, but results is an overestimation of Qle in June/July. A closer investigation of the full time series of simulated fluxes and the high resolution MODIS LAI (Figure A.5) identifies a LAI drop during the 2005 summer which cannot be represented when using a climatology. Similar behavior is also seen in the 2004 summer. Despite the reduction of the evaporative drought in late summer in Amplero with the uniform roots distribution, other factors influence the inter-annual and inter-seasonal variability of Qle and Qh which are not captured by CHTESSEL, as well as observational errors and scale mismatches. Inter-annual variability is also seen in Howard with a negligible impact of the uniform roots distribution in 2005, but with a positive impact in 2002, 2003 and 2004 (see Figure 2.3 for 2004 and Figure A.6 for the full time series). Mopane also displays evaporative drought events, but with very dry soil moisture conditions (see Figure A.7) the impact of the uniform roots distribution was negligible

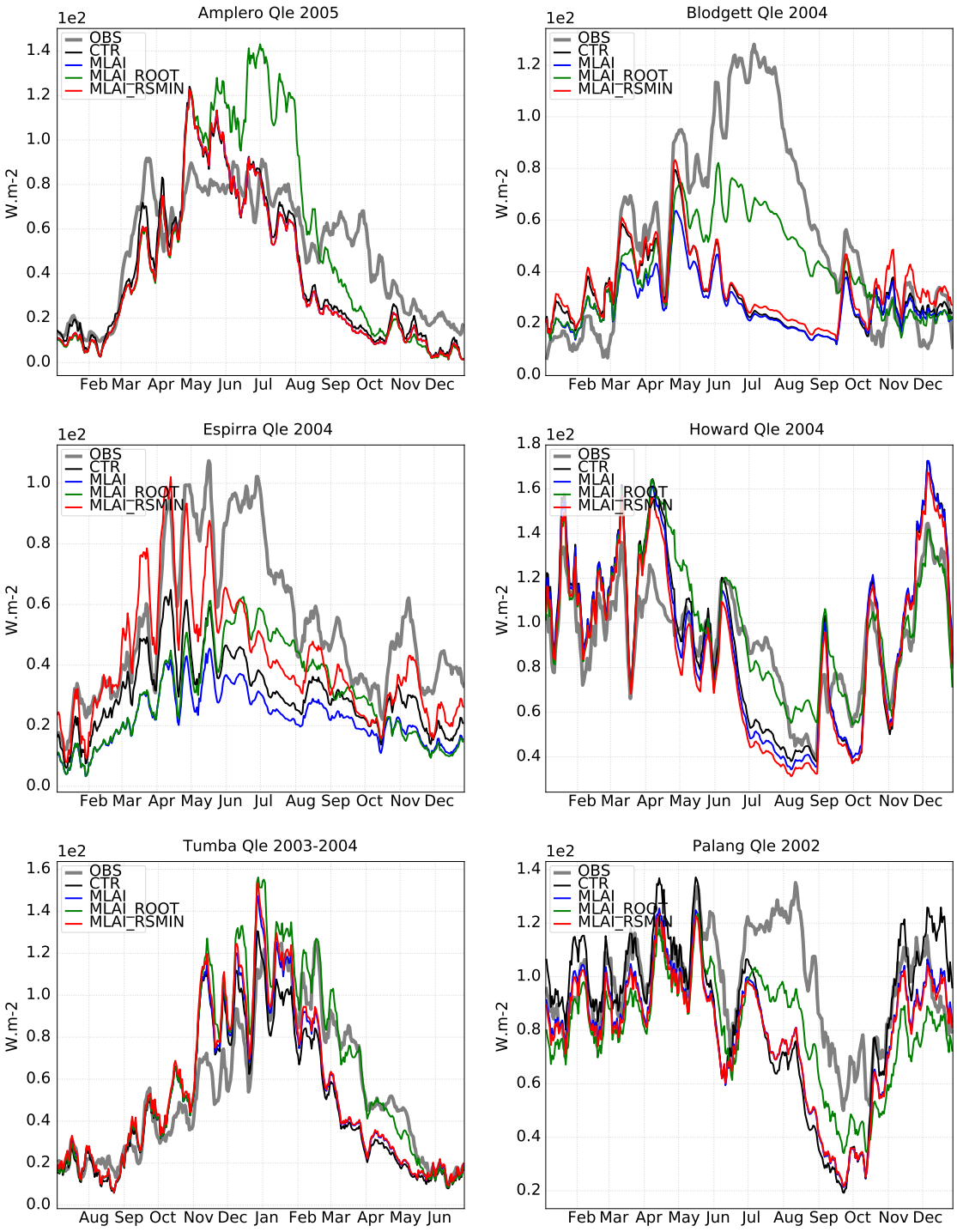

Figure 2.3: Simulated and observed latent heat flux during one example year with a 14 days running mean smoothing. Observations are in grey, CTR in black, MLAI in blue, MLAI_ROOT in green and MLAI_RSMIN in red.

In the forest sites all R_{DMAX} are between 2 and 3 meters, with the exception of Harvard with 1m and Howland and Hyytiala with 0.5m. These three forest sites, plus Loobos and UniMich were

among the best performing in CTR and MLAI. The impact of the uniform roots distribution is small since all these 5 sites have abundant precipitation and soil moisture conditions which are close to field capacity. Hesse station is the only case of a consistent deterioration of Qle with the uniform rooting depth and R_{DMAX} of 2 m, mainly due to a considerable overestimation, contrasting with a reduction of the Qh bias. This mixed effect in the Qh and Qle justifies the use of several metrics and joint Qh and Qle in the model evaluation. Other processes and/or driving/observations limitations are likely responsible for the errors. The remaining four forest sites Blodget, Espirra, Palang and Tumba (see Figure 2.3) all display excessive evaporative drought associated with soil moisture dry-down. In these sites, the experimental formulation of uniform rooting depth with the optimal R_{DMAX} partially reduced the excessive evaporative drought. The largest impact is seen in Palang and Blodgett that were among the sites with the worst Qle and Qh correlations. From these sites shown in Figure 2.3 the uniform root distribution had the largest impact on Qle while r_{smin} and MLAI changes only show minor differences to CTR in Espirra.

2.4 Discussion

The systematic underestimation of Qle and overestimation of Qh in CTR (see Figure 2.1) is opposite from the findings of Martens et al., 2020 who compared ERA5 data against observations from 143 FLUXNET sites. Similar biases in CHTESSEL considering a subset of 51 FLUXNET stations were also found by Nogueira et al., 2021. The differences of these studies to our results are likely associated with the different sampling of stations. It is also worth noting that the energy budget closure of eddy covariance sites can induce systematic errors (Ershadi et al., 2014; Wilson, 2002). Therefore, the interpretation of the systematic biases in the simulated Qle and Qh must be cautious. In this chapter, the use of several evaluation metrics that account for both mean biases and variability, with equal weights, partially mitigate problems that could arise from systematic observation errors.

Despite the availability of long-term EO records of LAI, we considered only the high-resolution LAI climatology. This was driven by two reasons: (i) several stations encompass periods before the EO records availability (before 1999 in the case of CGLS, or 2002 in the case of MODIS), and (ii) we considered that the first step was to evaluate the impact the high-resolution station location conditions, neglecting inter-annual variability. However, our results suggest that the lack of inter-annual variability in the vegetation state might be responsible for some of the model problems. Amplero station is an example where we observe some relation between the time-varying high-resolution LAI (see Figure A.5, bottom panel dotted blue line) and the Qle inter-annual variability. There are robust evidences of the added value of assimilating LAI in land-surface models, enhancing their capabilities to monitor vegetation phenology and fluxes (Albergel et al., 2019; Albergel et al., 2020; Boussetta et al., 2015; Stöckli, Rutishauser, et al., 2008). This is particularly relevant in models that have a prognostic evolution of vegetation phenology.

The soil moisture resistance, or water stress factor, in CHTESSEL has two components: (i) the derivation of the root zone soil moisture content (using an exponential roots distribution) and (ii) a linear transformation between field capacity (unstressed vegetation) and wilting point. This chapter focused only in the derivation of the root zone soil moisture content testing a new uniform

roots distribution and associated maximum rooting depth. There are different approaches to relate root zone soil moisture and the water stress factor, such as curvi-linear relationships or the use of soil matric potential (Egea et al., 2011; Verhoef and Egea, 2014). Such approaches, combined with the rooting depth distribution, are likely to further enhance the model capability to represent root water uptake. Moreover, X. Liu et al., 2020 reported that a dynamical rooting depth evolution improved the performance of the Noah-MP-Crop model under drought-like situations. Additionally, vapour pressure deficit and stem xylem conductance are also known to influence stomatal regulation (Konings et al., 2017; Massmann et al., 2019), but were not considered. The presence of a shallow water table could also influence latent heat flux during drought periods (Pinto et al., 2014). Water table is not represented in CHTESSEL, and we are not aware of such effects in the 17 sites considered.

Finally, the metrics distribution for MLAI_ROOT (in Figure 2.1) showed more potential to reduce Qle and Qh bias and NME and increase correlation than the calibration alone of r_{smin}. This is achieved by partially addressing the excessive evaporative drought in Blodget, Espirra, Palang and Tumba stations. A joint optimization of both r_{smin} and maximum rooting depth is likely to further improve the model simulations. However, it was not the aim of this work to optimize/calibrate CHTESSEL for these stations, but to investigate in the current model formulation which aspects require further attention. The use of subset of FLUXNET stations to evaluate Land Surface Models performance is a common practice (Best et al., 2015; Haverd et al., 2016; Leonardini et al., 2020; Stöckli, Lawrence, et al., 2008; Ukkola et al., 2016).

2.5 Conclusions

This chapter focused on the impact of the representation of canopy resistance on the simulations of latent and sensible heat fluxes by the CHTESSEL model. Observed data from 17 FLUXNET towers were used to carry out offline simulations with a particular emphasis on the representation of evaporation and its relationship with water stress conditions. Three constraints of canopy resistance were evaluated: (i) the role of vegetation characteristics via the use of high spatial resolution LAI representing local station conditions; (ii) the impact of the minimum canopy resistance and (iii) the impact of a uniform roots distribution on soil moisture stress. The replacement of the current LAI climatology used by CHTESSEL, based on an older MODIS climatology with coarse resolution, by a new high-resolution climatology representative of the stations locations did not significantly affect the simulated surface fluxes. The close relationship between LAI and the minimum canopy resistance was investigated showing some potential to improve the latent heat flux variability via an adjustment of this parameter. However, these changes did not impact the excessive evaporative drought in several stations, as reported by Ukkola et al., 2016. In CHTESSEL, we found that this limitation was tightly associated with the depletion of the top meter soil moisture, while water was still available in deeper layers. However, the current model formulation for root distribution was not capable of reaching this deeper reservoir, resulting in an early reduction of evaporation, when compared with observations. The replacement of the current exponential roots profile by a uniform roots distribution and associated maximum rooting depth reduced the underestimation of evaporation during water stress conditions. Despite the limitations associated with a reduced number of stations, our results highlight the importance of roots distribution in controlling soil

moisture resistance in water stress conditions. However, roots distribution are weakly constrained observationally on the global scale. Therefore, research is necessary to understand the implications of these changes on the global water and energy budgets as well as in the coupling with the atmosphere. The proposed uniform roots distribution with a single associated parameter, the maximum rooting depth, is also appealing for a parameter optimization. These could be further addressed along with the revision of land cover and vegetation recently proposed for CHTESSEL (Nogueira et al., 2020), that identified the necessity to calibrate vegetation related parameters (Nogueira et al., 2021). Considering the coupled nature of the surface water and energy cycles and the relevance of land-atmosphere coupling a calibration methodology considering multiple observational datasets, covering different water/energy components and temporal time-scales should be favoured (Orth et al., 2016), also to possibly include some indirect information of poorly constrained parameters through variables coupled with them.

Chapter 3

CTESSEL and CHTESSEL heat fluxes and carbon exchanges offline evaluation against flux tower measurements

3.1 Introduction

The earth land surface processes mediate the majority of the climate impacts on human societies and ecosystems. Industrial and technological developments are having such a big influence on the land surface that today scientists debate whether we have entered a new geological era called Anthropocene. Global warming and weather extreme intensification are part of the risk that our society must currently deal with (Lenton et al., 2019; Steffen et al., 2018). In this context, an accurate representation of land surface processes is critical for our understanding of how climate change will affect the biosphere and how societies could anticipate extreme events.

Land surface models solve the coupled fluxes of water, energy, and carbon between the land surface and atmosphere. LSMs are considered as the most sophisticated tools for predicting how the conditions for life on the Earth will change in the coming years, decades, and centuries. LSMs provide a set of prognostic variables to numerically represent and mediate feedback on biogeochemical cycles, such as the terrestrial carbon cycles. By estimating changes in the biophysical function of the land surface as climate and ecosystems change, LSMs provide information on risks to human societies and natural ecosystems associated with future climate scenarios, including crop productivity, heat waves,urban climate, fire risk, flooding, ecosystem productivity, permafrost and land ice status, and freshwater availability and conditions (Fisher and Koven, 2020).

Through time, LSMs evolved in the representation of processes that are known to impact earth system dynamics. Today, considering global climate change problems, two key model results set the LSM community on its current trajectory: (i) the plant biophysical responses to elevated CO_2 atmospheric concentration and its effect on global climate (Sellers et al., 1996), and (ii) that coupling of climate and carbon cycle could substantially strengthen global warming rates (Cox et al., 2000).

Carbon exchanges were introduced in LSMs in the 1990s, and dynamical carbon processes (linked with vegetation physiology and soil biogeochemistry) were introduced in the early 2000s as the modelling groups started to focus on the response of climate to the carbon cycle (Blyth et al., 2021). Canopy water losses and carbon uptake rates are determined in LSMs by the stomatal conductance, establishing a fundamental link between the carbon and water balances. The modeled photosynthesis calculates the carbon assimilation by the plants considering environment variables (radiation, CO2 concentration, temperature and humidity) (Balsamo et al., 2011; Blyth et al., 2021). Land surface schemes typically use empirical relations or stress functions to reduce canopy gas exchange in response to declining soil moisture (Blyth et al., 2021; Egea et al., 2011).

This chapter extends the work presented on the previous chapter, by extending it to include two versions of the ECMWF land surface model, as well as considering the carbon Net Ecosystem Exchanges (NEE). Reliable estimates of NEE and Qle at the land surface require a correct representation of the CO_2 and H_2O exchange between the vegetation and the atmosphere since those fluxes are linked by the stomatal conductance. Two main formulations of the stomatal conductance are used in the two different ECMWF land surface models, (i) CHTESSEL includes a carbon module but calculates evaporation using a stomatal conductance based on the original Jarvis approach (Boussetta et al., 2012; Jarvis, 1976) and (ii) the Carbon Tiled ECMWF Scheme for Surface Exchange over Land (CTESSEL) were stomatal conductance is parametrized by the plant physiological approach. This plant-physiological approach also called Ags photosynthetic scheme, is based on the observed correlation between net carbon assimilation by the plant and the stomatal conductance as the CO_2 taken up for photosynthesis largely uses the same pathway as water transpired from the plants (C. M. Jacobs et al., 1996). This photosynthetic scheme called A - gs, links the leaf photosynthesis rate and thereby the stomatal conductance to external, surface and atmospheric factors. It describes the main response of ecosystem-scale CO_2 fluxes to atmospheric forcing parameters (e.g., temperature, humidity, radiation, soil moisture) and to a fixed vegetation state via the LAI. This chapter is motivated by the result obtained in part 2, which focused on the impact of an updated monthly LAI climatology and a revised uniform roots distribution on CHTESSEL offline point simulations. Stevens et al., 2020 showed that an updated MODIS derived LAI had a slightly positive effect on CHTESSEL latent and sensible heat flux simulation, while the revised root profile reduced the underestimation of evaporation during water stress conditions. Here we compare the impact of those model parameters change on CTESSEL (Boussetta et al., 2012). Given the coupled nature of the water, carbon and energy cycle each stomatal conductance formulation will provide different fluxes estimations. Pairing the new MODIS monthly climatology and the uniform root distribution with the plant physiological approach, which is partially based on experiment and observations (C. M. Jacobs et al., 1996), could bring model estimates closer to observations.

3.2 Data and Methods

3.2.1 Data

As in the previous chapter (part 2), the same observed data from the 17 selected FLUXNET towers and MODIS derived monthly LAI and Albedo climatology are used.

3.2.2 CTESSEL land surface model

CTESSEL combines CHTESSEL tiling parameterization with the A-gs ISBA-Ags model. The previous study of Stevens et al., 2020 used CHTESSEL and therefore the Jarvis approach where empirical stress function depending on environmental conditions modulate a preset stomatal conductance maximum (Boussetta et al., 2012). The ISBA-Ags model is a modified version of the Jacobs model (Boussetta et al., 2012; C. Jacobs, 1994; C. M. Jacobs et al., 1996), considering the effect of soil water stress on the photosynthesis and canopy resistance (Boussetta et al., 2012; Calvet et al., 2003). This so-called photosynthesis-conductance approach used in CTESSEL, is based on plant physiological considerations, and describes the plant photosynthesis process and its dependence on CO_2, temperature and soil moisture. A detailed description of both CTESSEL and CHTESSEL can be found in the Integrated Forecasting System (IFS) documentation (ECMWF, 2019) and here, the main details of the differences between the CTESSEL and CHTESSEL evaporation and carbon cycle calculation are presented due to their relevance in the results' interpretation and discussion.

In both CHTESSEL and CTESSEL, for high and low vegetation, the turbulent flux of water is given by:

$$E = \frac{\rho_a}{r_a + g_s}(q_L - q_{sat}(T_{sk})), \quad r_a = (|U_L|C_H)^{-1} \tag{3.1}$$

where ρ_a is the air density, U_L and q_L are the wind speed and humidity at the lowest atmospheric model level, $q_{sat}(T_{sk})$ the saturation humidity at skin temperature ((T_{sk}) and CH the turbulent exchange coefficient (depending on the atmospheric stability), the canopy or stomatal conductance (g_s) and the aerodynamic resistance (r_a).

The main difference between the two model versions resides in the calculation of stomatal conductance. In CHTESSEL, the following formulation of the canopy conductance (g_s) is adopted:

$$g_s = g_{s,max} * LAI * [f_1(R_s) * f_2(\theta) * f_3(D_a)] \tag{3.2}$$

with $g_{s,max}$ the vegetation type-dependent maximum stomatal conductance, LAI the leaf area index and $f1$, $f2$, $f3$, three stress functions expressing effects on gs of shortwave radiation, soil moisture stress and atmospheric humidity deficit, respectively.

In CTESSEL, the stomatal conductance is active for regulating both water vapor and CO_2 fluxes. The gross CO_2 assimilation by the canopy (Ag) is calculated using a photosynthesis module developed by Goudriaan et al., 1985. The net flow of CO_2 through the stomata or net assimilation (A_n) is A_g minus the dark respiration (R_d). The canopy or stomatal conductance for CO_2 (g_{sc}), can be derived by Kirchhoff's resistance/conductance analogy from the net flow of CO_2 through the stomata and the difference between the CO_2 concentration outside the leaves (C_s) and the concentration in the intercellular cavities (C_i) (Boussetta et al., 2012).

$$g_{sc} = \frac{A_n(Env)}{C_s - C_i(env)} \tag{3.3}$$

where the functions (Env) indicate the dependence of A_n and C_i on the different environment factors. The stomatal conductance to CO_2, g_{sc} is estimated using a flux-gradient relationship, modified to account for the effect of a specific humidity deficit on stomatal aperture. The first guess g^*_{sc} is given by:

$$g^*_{sc} = \frac{A_n - A_{min}(\frac{D_s}{D_{max}}\frac{A_n+R_d}{A_m+R_d}) + R_d(1 - \frac{A_n+R_d}{A_m+R_d})}{C_s - C_i} \tag{3.4}$$

where A_{min} represents the residual photosynthesis rate (at full light intensity) associated with cuticular transfers when the stomata are closed because of a high specific humidity deficit. A_m is the net CO_2 assimilation and $R-d$ is the dark respiration. The diffusion of CO_2 interacts with that of water vapour. The first guess of the stomatal conductance to CO_2 is corrected for this interaction and calculated interactively to refine the estimation.

The stomatal conductance to water vapour g_s is then given by:

$$g_s = 1.6g_{sc} + g_c \tag{3.5}$$

with the cuticular conductance (g_c) as a vegetation dependent parameter. The factor 1.6 represents the ratio between the diffusivities of water vapour and CO_2. The soil moisture stress response is driven in a complex way through the mesophyll conductance (g_m). The same soil moisture stress factor $f2$, as in CHTESSEL, is used to calculate a separate solution for high and low vegetation (Boussetta et al., 2012):

$$f_2 = \frac{\overline{\theta} - \theta_{pwp}}{\theta_{cap} - \theta_{pwp}} \tag{3.6}$$

where the soil moisture at permanent wilting θ_{pwp} and at field capacity θ_{cap}, are defined by fixed values in lock-up tables. $\overline{\theta}$ is a weighted average of the unfrozen soil water in the soil column. . If $\overline{\theta}$ decreases to values below field capacity, the value of $f2$ becomes smaller than 1 and water stress condition occurs (van den Hurk et al., 2000; Voogt et al., 2006).

3.2.3 Simulation setup

CTESSEL LSM is used to perform offline point simulations, driven by the meteorological data observed at each tower location. The procedure to guarantee enough spin up time and vegetation types allocation is the same as described in section 2.2.3.

Several model configurations were tested and are presented in Table 3.1. Here using the CTESSEL version of the ECMWF LSM we want to investigate the role of high-resolution LAI and Albedo climatologies in model performances and formulations with an interest toward the representation of the carbon cycle. The first model configuration, "C_CTR" for CTESSEL CONTROL, used CTESSEL original input data with the ECMWF IFS. In CTESSEL again, monthly climatologies of snow-free albedo and LAI were extracted from the nearest grid-point of operational NWP fields with a 9km resolution using previous MODIS products (MOD15A2). This model is a reference against which the other setups/configurations will be compared. The experiments labelled as "C_MALB " apply the MODIS extracted Albedo monthly climatology over each station on CTESSEL. "C_MLAI" setup uses the MODIS extracted high-resolution LAI monthly climatology over the stations on CTESSEL. For the last two model setups the albedo and LAI monthly climatologies are extracted to the nearest five pixels from the station using the latest MODIS products (section 2.2.1).

An additional model configuration "C_MLAI_ROOT" was tested to investigate the role of root distribution combined with the MODIS LAI high-resolution data using CTESSEL model. The

procedure to select for each station the optimal rooting depth is mostly the same as the one described in section 2.2.3 and 2.2.4, further details are given in the following section.

Table 3.1: Model simulations acronyms and detailed configuration

Simulation	**Details**
C_CTR	Control simulation with default CTESSEL parameters and input LAI and Albedo
C_MALB	As C_CTR but replacing the input Albedo climatology by the new high resolution MODIS climatology
C_MLAI	As C_CTR but replacing the input LAI climatology by the new high resolution MODIS climatology
C_MLAI_ROOT	As C_MLAI but using an uniform root distribution (Eq. 2.5) and selecting the optimal R_{DMAX} for each station from a set of simulations with R_{DMAX} of 0.5, 1, 2, and 3 m.

3.2.4 Evaluation

Net Ecosystem Exchange, latent and sensible fluxes are evaluated against FLUXNET tower measurements using four metrics (i) the mean bias error (MBE), standard deviation difference (SD), Pearson correlation coefficient r, and normalized mean error (NME). Those metrics follow Best et al., 2015 and were used in the previous CHTESSEL flux study (see Appendix (equation A.1 to equation A.4) for a more detailed description). Calculations were performed on daily simulated and measured fluxes.

For the selection of the optimal rooting depth simulation, a ranking approach considering the four metrics were performed. We performed three evaluations of the optimal root scheme, (i) considering Qle and Qh, (ii) only considering NEE and (iii) considering Qle, Qh and NEE at the same time. By doing so, we can assess the sensitivity of the optimal rooting depth to both the water and carbon cycles. For each metric and fluxes considered, each simulation was ranked from 1 to 4 since we have four different RDMAX (see Table 3.2). The simulation with the lowest rank was selected as the optimal rooting depth station wise. This approach could be considered as limited since it does not consider the actual metric values or the differences between simulations. However the aim of this approach was not to provide a model calibration but to show the effect of a different root distribution on model fluxes regarding the water and carbon cycles.

Table 3.2: Station vegetation types (L define low and H high vegetation types), and optimal rooting depth considering one variable (NEE), two varibales (Qle and Qh) and three variables (NEE, Qle, Qh).

Station	**Plant Functional Type**	**RDMAX optimal (considering Qh-Qle-NEE)**	**RDMAX optimal (considering NEE)**	**RDMAX optimal (considering Qh-Qle)**
Amplero	L,short grass	2	0.5	2
Bugac	L,short grass	1	1	0.5
Fort Peck	L,short grass	2	1	2
Howard	L,tall grass	2	2	2
Kruger	L,tall grass	2	2	3
Mopane	L,tall grass	3	3	3
Blodgett	H, evergreen needleleaf	3	3	3
Espirra	H, evergreen broadleaf	3	3	2
Harvard	H, deciduous broadleaf	2	2	2
Hesse	H, deciduous broadleaf	2	2	0.5
Howlandm	evergreen needleleaf	2	3	0.5
Hyytiala	evergreen needleleaf	0.5	0.5	0.5
Loobos	evergreen needleleaf	2	3	0.5
Palang	evergreen broadleaf	2	2	2
Sylvania	H, interrupted forest	3	1	3
Tumbarumba	evergreen broadleaf	3	0.5	3
University of Michigan	H, deciduous broadleaf	2	2	2

3.3 Results

3.3.1 CTESSEL sensible and latent heat flux evaluation

As for the fluxes evaluation made with CHTESSEL, in section 2.3.2, the use of the high-resolution MODIS albedo has a negligible impact on the model performance, since the original IFS albedo climatology is very close to the MODIS derived albedo climatology.

The new MODIS albedo climatology is similar to the one used in the CTR model setup (see section 2.3.2), therefore this new albedo dataset also has a negligible impact on model performances. Considering the four metrics (MBE, SD, NME, pcorr) over both latent and sensible heat fluxes, C_MALB model performances are almost equal to the CTR ones in terms of scores. The only notable difference in model behavior brought by the use of the new MODIS albedo is a reduction in the sensible heat flux standard deviation of the errors.

The C_MLAI model setup shows a more intense model response to the new MODIS LAI climatology. However, the new LAI has a negative impact on model performance, in both latent and sensible heat fluxes. There is an overall worsening of model performance with the use of C_MLAI In the C_MLAI, Qle MBE is increased from a median value of -6.43 W/m^2 in C_CTR to -10.99 W/m^2 (panel A, Figure 3.1). Qle standard deviation (SD) is increased from 0.15 W/m^2 with C_CTR to 0.16 W/m^2 with C_MLAI (panel B, Figure 3.1). Qle normalized mean error (NME) surged from $0.67W/m^2$ with C_CTR to 0.71 W/m^2 with C_MLAI (panel C, Figure 3.1). The C_MLAI model also lowered the Pearson correlation from 0.81 to 0.8 (panel D, Figure 3.1). The new MODIS LAI also worsened sensible heat flux model performances with an increased MBE from 11.50 W/m^2 with C_CTR to 13.5 W/m^2 with C_MLAI (panel E, Figure 3.1) and SD from 0.2 W/m^2 with C_CTR to 0.21 W/m^2 with C_MLAI (panel F, Figure 3.1). The Qh Pearson correlation is the only met-

ric showing a positive response to C_MLAI model setup with an increase from 0.79 (C_CTR) to 0.81(C_MLAI) (panel H, Figure 3.1).

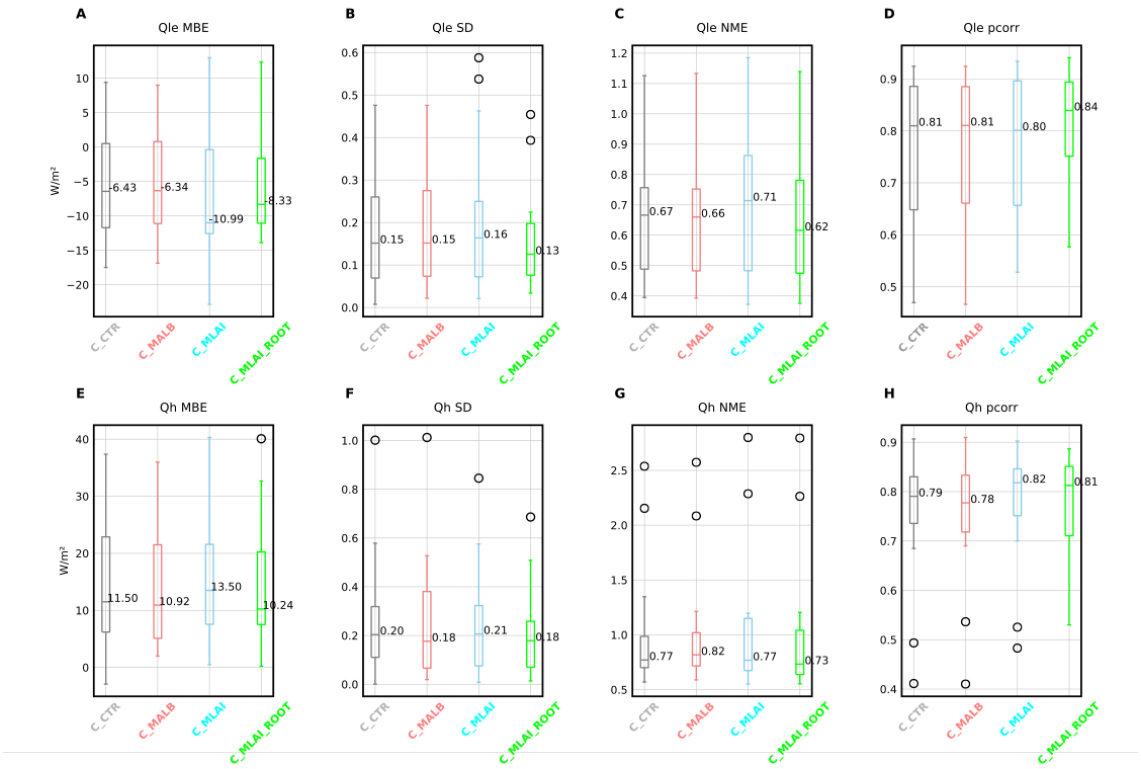

Figure 3.1: Latent (a-d top panels) and sensible (bottom panels) heat flux evaluation in terms of MBE, SD, NME and r for C_CTR, C_MLAI and C_MLAI_ROOT. The boxplots represent each metric's distribution for the 17 towers showing the percentiles 25, 50 and 75. Symbols denote outliers for values further than 1.5 times the interquartile range from the nearest 25th or 75th percentile.

The use of high resolution MODIS LAI and albedo did not bring any systematic improvement in model performance. Stations were grouped by plant functional types, vegetation characteristics and each station within the same group reacted differently to the use of the new climatology's. The 17 Fluxnet stations were also classified and grouped following the Budyko framework (Budyko, 1974) which prescribes the dependence of actual evapotranspiration on energy availability (represented by potential evaporation) and water availability (represented by precipitation). Here again, model responses are randomly distributed amongst the stations which could be distributed on both sides of the Budyko curve (see Figure 3.2). The impact of the MODIS LAI on CTESSEL model performance is irregular in space and time. Most of the stations that presented weak agreement with observations using the C_CTR setup present a degradation of model result with the use of MODIS LAI (Blodgett, Espirra, Hesse , Kruger, Mopane). The C_CTR model setup metrics distribution shows the presence of outliers (Figure 3.1), suggesting irregular model performances over each station. The detailed results for each station and score are presented in the appendix B (Figure B.1 to B.18).

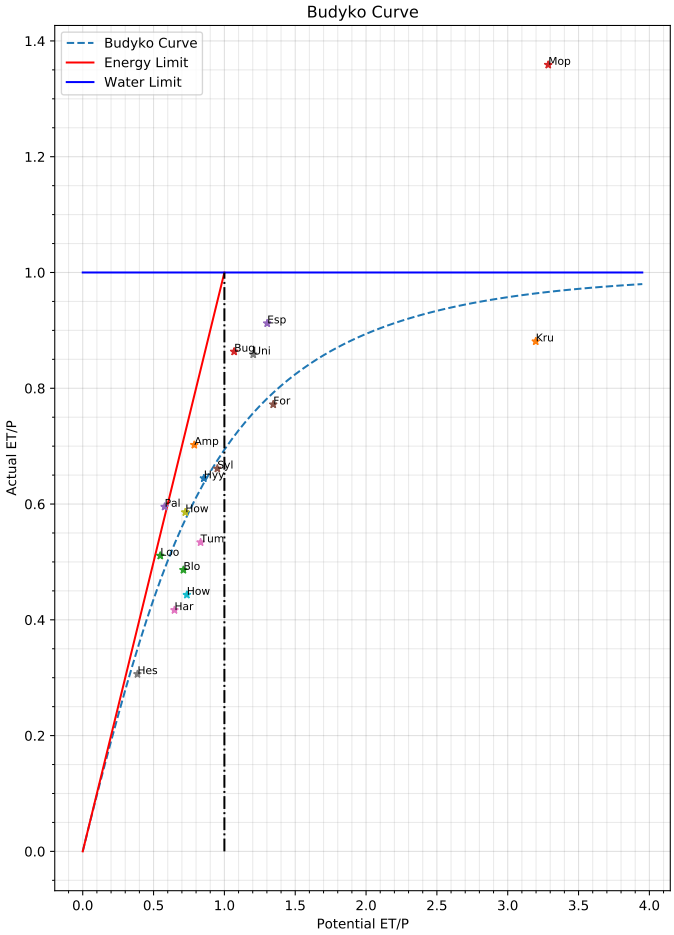

Figure 3.2: Budyko classification of the 17 Fluxnet stations.

The previous study identified several stations showing early evaporation reduction or evaporative drought (Amplero, Blodgett, Espirra, Howard, Mopane, Palang and Tumba), an interesting finding here is that the simple use of the C_CTR (CTESSEL model) version instead of CHTESSEL model (MLAI) has a positive effect with a clear reduction of the early evaporative reduction intensity (see Figure 3.3 and 3.4). The use of the A-gs evaporation scheme reduces summer evaporative droughts at those stations, the model shows a more conservative soil water use strategy than the Jarvis approach. The C_MLAI_NOSMS simulation represents the best achievable model output if evaporation is not constrained by soil moisture. Those model runs are unrealistic since it also strongly depletes soil water content. However, those simulations suggest that the evaporative drought in CTESSEL (like in CHTESSEL) is tightly linked with the soil moisture stress formulation. The discrepancy between the soil water content between the model different soil layers during the dry-down and evaporative drought (Figure 3.3) motivated the exploratory revision of the model root system.

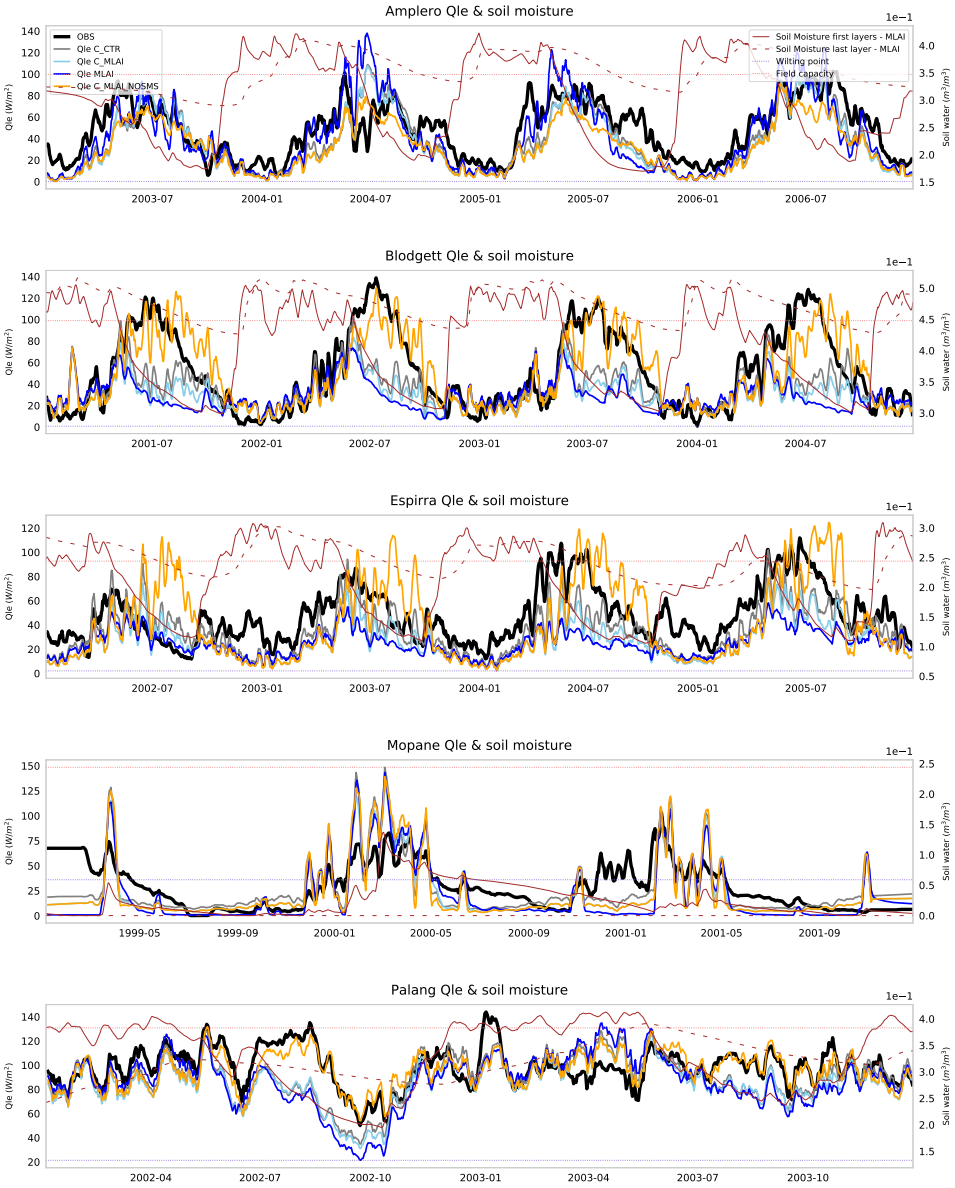

Figure 3.3: Latent heat flux (Qle) and soil moisture in Amplero (a), Blodgett (b), Espirra (c), Mopane (d), and Palang (e). For the Qle (left axis), the observations are in black and the simulation for CTESSEL CTR (C_CTR) in grey, for CTESSEL MODIS LAI (C_MLAI) in light blue, for CHTESSEL MODIS LAI (MLAI) in blue and for CTESSEL without soil moisture stress (C_MLAI_NOSMS) in orange. The soil moisture (right axis) for MLAI simulation is shown for the top 3 layers (red solid) and deep layer (red dashed). The light dotted red and blue lines represent soil moisture at field capacity and the wilting point, respectively.

The optimal rooting depth for each station depends on the variables considered. When only NEE is considered the optimal rooting depth is adjusted to fit carbon cycle observation. When considering Qle and Qh the model tries to adjust the rooting depth in regard to the water and energy cycles. Therefore there is a big contrast between the optimal rooting depth depending on the variables considered (see Table 3.2). The values of the optimal rooting depth adapted to NEE are close to observations found in the literature, with low vegetation having generally a shallower rooting system than high vegetation plant functional types. The NEE adapted roots distribution is close to commonly accepted ranges with low vegetation such a grassland having a shallow rooting system and high vegetation trees having deeper roots. When considering Qle and Qh the rooting depth of low vegetation is somehow exaggerated (3m for Kruger and Mopane) to compensate for evaporation underestimation and some high vegetation trees have an optimal rooting depth of 0.5m to compensate for evaporation overestimation. Since the use of the A-gs already reduces model summer evaporative drought, the addition of a deeper rooting scheme at the stations suffering from early drydown (Amplero, Blodgett, Espirra, Howard, Tumbarumba, Palang) considerably reducing model evaporation underestimation. Amplero early drydown is reduced while winter overestimation is avoided as it was the case with the use of CHTESSEL. The other stations suffering from early drydown also see a clear reduction of model bias with the use of this optimal rooting depth (Figure 3.4).

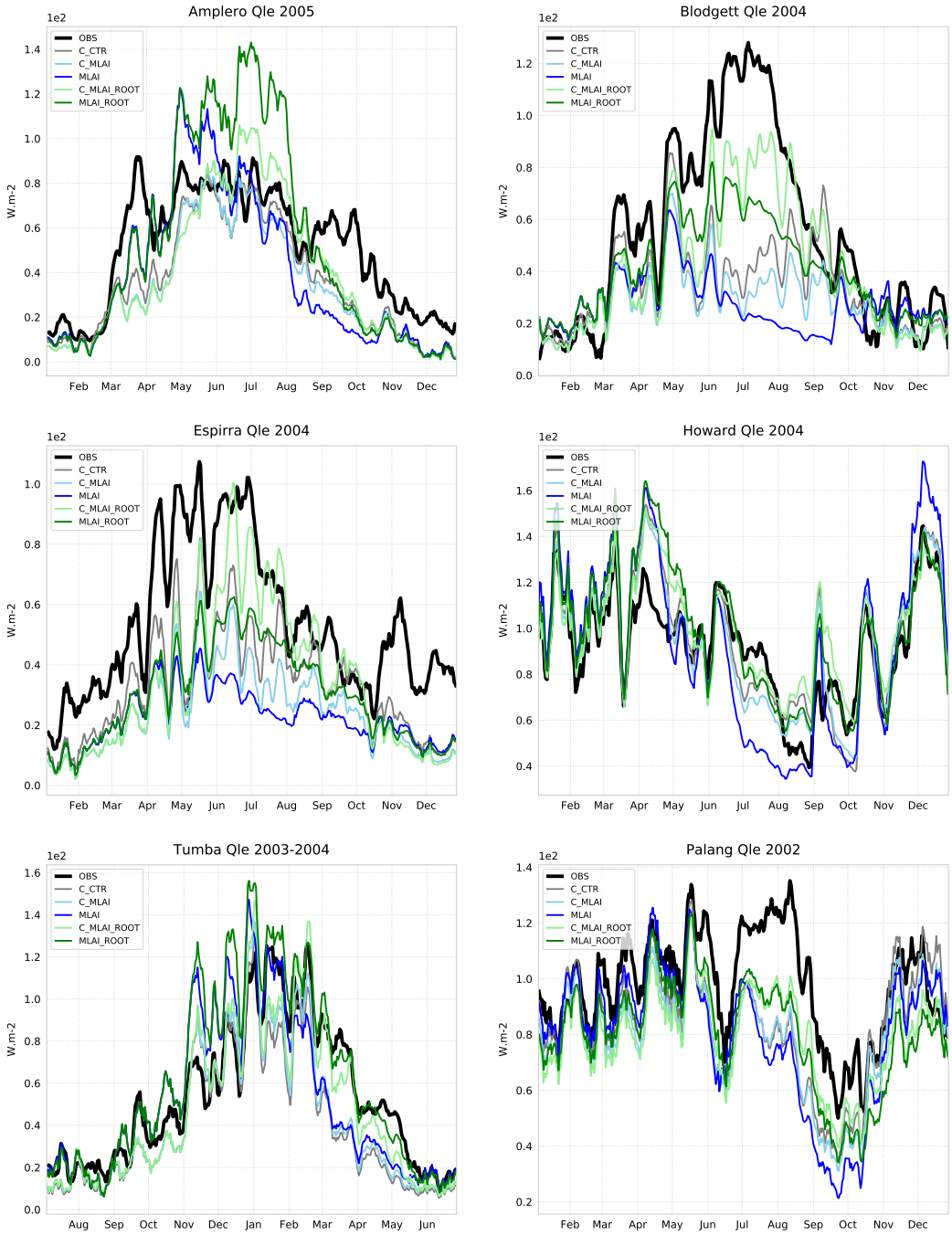

Figure 3.4: Simulated and observed latent heat flux during one example year of summer evaporative drought (14 day running mean smoothing average). Observations are in black, C_CTR in grey, C_MLAI in light blue, MLAI in blue and C_MLAI_ROOT in light green and MLAI_ROOT in dark green.

3.3.2 Carbon fluxes in CHTESSEL and CTESSEL

Net Ecosystem Exchanges model response to the different model setups is more pronounced than the one observed with latent and sensible heat flux. The A-gs photosynthesis scheme used in CTESSEL seems to be more accurate than Jarvis (CHTESSEL) in predicting carbon fluxes, with all the CTESSEL model setups having lower MBE, SD and higher correlation than their CHTESSEL counterpart model setups. However, the goal of this study is not to compare CTESSEL against CHTESSEL performance but to evaluate the impact of high-resolution climatology and deeper root distribution on model behavior.

The MODIS climatology has a slightly positive effect on CTESSEL and a more neutral effect on CHTESSEL carbon fluxes (Figure 3.5). MODIS LAI lower CTESSEL NEE mean bias error and the normalized mean error while improving correlation with observations from 0.53 to 0.56. On the other hand the new MODIS derived monthly LAI improved CHTESSEL correlation while having a negligible impact on MBE, SD and NME. The new root distribution has a strong positive impact on model correlation with an increase from 0.53 with C_CTR to 0.67 with CMLAI_ROOT. The introduction of this new root scheme also lowered model MBE and NME of the net ecosystem exchanges. Most of the stations suffering from early drydown improved their representation of NEE fluxes with the use of the new root distribution with a reduction of model overestimates (Amplero, Blodgett, Espirra, Palang). As seen on the appendix B figures, a correct representation of model NEE fluxes is tightly linked with the soil moisture state. And for several stations, as soon as the soil moisture of the first three layers falls below field capacity threshold then NEE estimates start to diverge more from observations (Blodgett, Espirra, Hesse). As seen in the previous evaluation of Qle/Qh stations for which the C_CTR model setup is already showing good agreement with observation, does not really get affected by any of the model setup changes (Fort Peck, Harvard, Howlandm, Hyytiala, Loobos, University of Michigan). When looking at the metrics and station time series, the tested experimental formulation of uniform rooting depth with the optimal RDMAX has a clear positive impact on NEE model performance and model response intensity is even stronger than the one observed in the evaluation of latent and sensible heat fluxes.

3.3.3 Discussion

The main goal of this chapter was to assess the impact of high-resolution LAI on the ECMWF land surface model with two configurations, considering both water (Qle), energy (Qle & Qh) and carbon (NEE) fluxes over several flux-tower sites. Forecasting atmospheric fluxes at the global scale with good accuracy like it is done for the weather is a challenging task. However, it is also one of the key areas of development to bridge the gaps between weather, air quality and climate models.

High resolution LAI climatology did not affect significantly model performance regarding Qle and Qh, a small degradation of model performance is even observable on the metrics with an increased MBE, SD, NME and a decrease correlation for Qle (Figure 3.1). However, as seen on Figure 3.1, the introduction of a uniform and deeper root scheme brings positive changes to model performance with a reduction of SD, NME and an increased correlation for both Qle and Qh. The LSMs used here present a four-layer soil representation with each vegetation type having a roots distribution in % over the four layers. For all the plant functional types more than 80% of the roots are located within the first 3 layers. This representation seems to be a limiting factor as survivorship

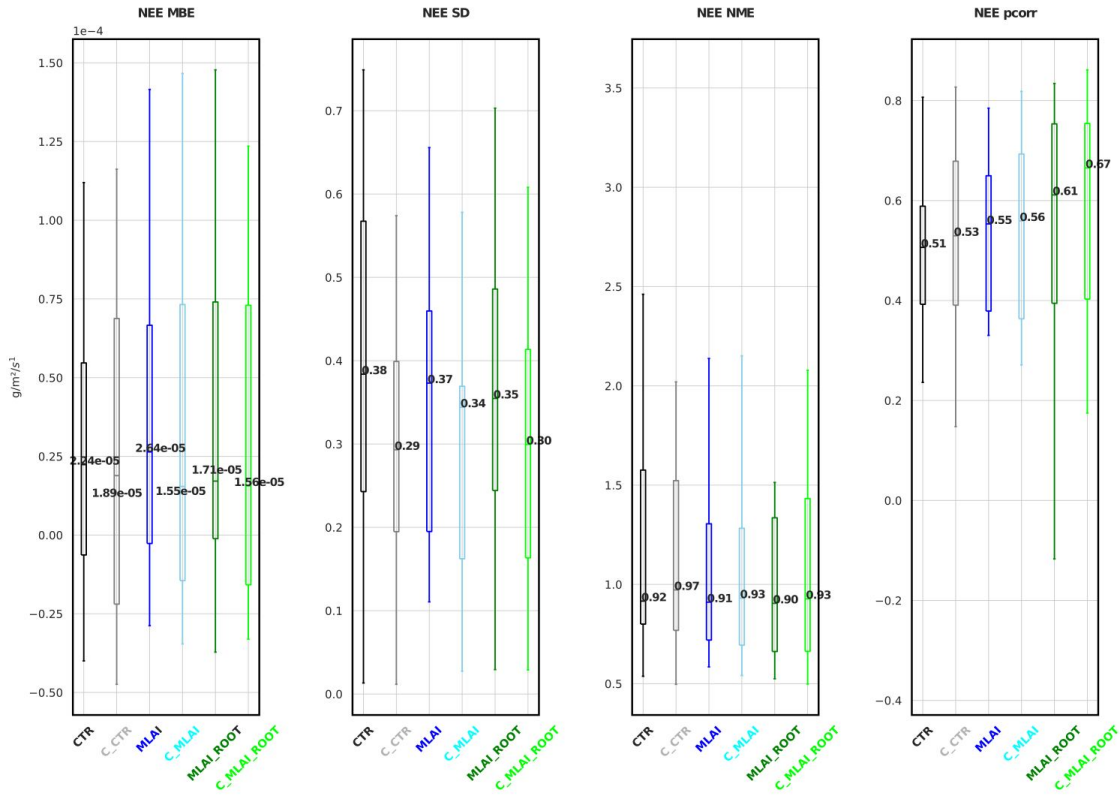

Figure 3.5: Net Ecosystem Exchange evaluation in terms of mean bias error (MBE), standard deviation (SD), normalized mean error (NME) and correlation (r) for CHTESSEL CTR (CTR), CTESSEL CTR (C_CTR), CHTESSEL MODIS LAI (MLAI), CTESSEL MODIS LAI (C_MLAI), CHTESSEL MODIS LAI with root optimization (MLAI_ROOT) and CTESSEL MODIS LAI with root optimization (C_MLAI_ROOT)

of some species in arid systems has been shown to depend completely on a plant's ability to tap water from permanent aquifers (Gardner, 1983). Although a small fraction of the root biomass might be found at depths below 1m, the functional significance of those roots may nevertheless be most important for ecosystem water, carbon fluxes and nutrient cycles (Canadell et al., 1996). Those land surface model limitations are highlighted here by the fact that the new experimental root scheme triggers a more pronounced response from the model as compared with the new LAI climatology. Moreover Qle and Qh model performance benefits from the experimental formulation of uniform rooting depth with the optimal RDMAX bringing C_MLAI_ROOT model outputs closer to observations, since the different model PFTs now have access to deeper soil water. The same outcome is seen on the carbon cycle evaluation where model performances scores are positively impacted in simulations using the new root scheme, which have a better agreement with flux towers observations. However, this improvement in NEE model representation should be taken cautiously since the model still has several limitations, both in terms of estimating gross primary production and respiration (which is not addressed here). The distribution of source and sinks of carbon over land surface is dominated by changes in land use (Houghton, 2000). Human land use and land cover changes have a significant impact on earth climate through changes in the carbon cycle, through altered biogeochemical processes (Houghton, 2003) and through changes in energy and moisture fluxes to

the atmosphere by altering biogeophysical processes (R. A. Betts et al., 2007; P. J. Lawrence et al., 2012). Therefore, Land Use and Land Use Changes (LULUC) have an impact on flux tower observations that are not accounted for by LSMs. Considering that more than 34% of the global land surface is subject to direct alteration by human activities (R. A. Betts et al., 2007), several studies already highlighted the need for a transient land use forcing for both long term climate projection as well as short to medium term weather forecast (P. J. Lawrence et al., 2012; Vinet and Zhedanov, 2011). In this analysis, Bugac and Fort Peck stations located in the middle of cattle farms, the NEE time series show strong carbon released during the summer months, that the model fails to represent. Those carbon release peaks might be due to animal grazing in the vicinity of the stations that the model could not account for in the NEE simulations.

CTESSEL land surface model links evaporation with carbon exchanges. Evaporation and therefore carbon fluxes are in part determined by the soil water content which is defined by two components: (i) the derivation of the root zone soil moisture content (using an exponential root distribution) and (ii) a linear transformation between field capacity (unstressed vegetation) and the wilting point. Here, by testing an experimental uniform root distribution and associated maximum rooting depth, we showed that the derivation of the root zone soil moisture content has the potential to improve model performances and reduce the gap between model outputs and observations. It was also showed that the use of the A-gs photosynthesis scheme (use in CTESSEL), has a strong positive effect on land surface early summer evaporative drought, over the Jarvis scheme used in CHTESSEL and divergence between model and observation might be due to the lack of flexibility in land surface model parameterization given by look-up table values.

3.3.4 Conclusions

In this chapter, FLUXNET tower observations were used to assess the impact of an updated LAI and albedo climatology and a deeper uniform root distribution, on CTESSEL latent and sensible heat fluxes and Net Ecosystem Exchanges. In a previous chapter, it was found that the use of high-resolution MODIS LAI slightly improved CHTESSEL latent heat fluxes model outputs. CTESSEL, which uses a different photosynthesis scheme than CHTESSEL, presents a small degradation of model performances following the use of high resolution LAI climatology. By looking at the model soil moisture outputs it was found that CTESSEL shares the same limitation as CHTESSEL with a depletion of the top meter soil moisture while water is still available in deeper soil layers. Since the current model formulation of root distribution does not allow plants to tap water in the deeper soil layer, the model setup with a deeper and uniform root distribution is able to bring Net Ecosystem Exchanges, latent and sensible heat fluxes model outputs closer to flux tower observations. The results also show that the A-gs formulation used in CTESSEL has a positive impact on the station suffering from evaporative drought and the underestimation of evaporation during water stress conditions. There is a strong model response to the new root scheme which seems to be intensified by the photosynthesis-conductance approach used in CTESSEL. Despite the limitations associated with a reduced number of stations, the results highlighted the importance of a revised land surface model vegetation parameterization optimization, especially in the model root distribution. The roots are key regulators of the water, energy and carbon cycles within the earth system and the land surface models. Therefore, a correct parameterization of the root responses to changes in resources availability or environmental conditions could lower discrepancies between models and observations.

Chapter 4

Confronting different ECMWF land surface model configurations against global scale machine learning gridded datasets

4.1 Introduction

Land Surface Models (LSM) represent the water and energy exchanges at the land-atmosphere interface. The multi component nature of the underlying processes driving those exchanges hampers the attribution of model errors to particular processes. Ongoing modelling developments, supported by increased computational power, have resulted in an increased complexity of LSMs, relying on an expanding source of evaluation data, driven by new emerging methodologies (e.g. machine learning) (Pal and Sharma, 2021) and Earth Observations (Balsamo et al., 2018)

The increased level of model complexity is not necessarily translated into enhanced model performance. Large uncertainties remain in the understanding and modelling of the interactions between atmospheric and terrestrial branches of the hydrologic cycle, due to non-trivial mechanisms at the land surface (Pal and Sharma, 2021). Previous studies have shown that physically based LSMs can be outperformed by statistical data-only-driven models (Best et al., 2015; Haughton et al., 2016; O and Orth, 2020). Intercomparisons of global LSMs suggest large uncertainties on the magnitude, intensity and spatial pattern of land-atmosphere energy fluxes (Jiménez et al., 2011; Jung et al., 2019; Mueller et al., 2013; Schellekens et al., 2017), making it difficult to assess and close the energy and water budgets (Jung et al., 2019; L'Ecuyer et al., 2015; Wild et al., 2015).

Land surface models present significant uncertainty when trying to replicate the land-atmosphere interactions. One of the main reasons behind this is the use of parameterizations to simulate complex processes. Johannsen et al., 2019 identified a cold bias of land surface temperature in the ERA5 reanalysis (Hersbach et al., 2020) over the Iberian Penínsila, suggesting that it could be related with

vegetation cover. Following those findings, Nogueira et al., 2020; Nogueira et al., 2021 showed that the use of satellite derived leaf area index (LAI) and land cover had an added value in constraining and improving land surface temperature simulations in the European Centre for Medium-range Weather Forecast (ECMWF) land surface model (the Carbon-Hydrology Tiled Scheme for Surface Exchanges over Land - CHTESSEL). These findings clearly showed the relevance of vegetation cover in the representation of land surface temperature, which had been also identified in other models and regions (Gou et al., 2019; Trigo et al., 1995; Zheng et al., 2012).

Different vegetation types have several hydraulic functional traits that allow them to modulate their water-use strategy, such as the ability to grow away from dry sites toward deeper or wetter soil patches (Takahashi and Scott, 1991). However, it is still poorly understood how these strategies vary in respect to climate and land cover types and how they respond globally, while intense drought can still trigger vegetation mortality at regional and continental scale (Allen et al., 2010; Y. Liu et al., 2021). In a recent study, Stevens et al., 2020 evaluated the impact of a uniform plant root distribution on CHTESSEL land surface model. Surface fluxes were evaluated against several eddy covariance flux tower measurements. This simplified root scheme had a positive impact on the excessive evaporative drought at several stations, as reported by Ukkola et al., 2016. The replacement of the exponential roots profile, currently in CHTESSEL, by a uniform root scheme and associated maximum rooting depth clearly reduced the underestimation of evaporation during water stress conditions.

In this chapter the previous works of Nogueira et al., 2020 and Stevens et al., 2020 is further extended by focusing on the impact of the different model configurations on the land surface water budget. By integrating remote sensing vegetation characteristics and a uniform and deeper roots distribution, we confront the CHTESSEL model with three independent global datasets derived through machine learning trained with in-situ measurements: (i) gridded global runoff (GRUN, Ghiggi et al., 2019); gridded global soil moisture (SoMo, O and Orth, 2021) and (iii) gridded global evaporation (FLUXCOM, Jung et al., 2019). The model simulations are confronted with the machine learning datasets following a similar methodology as in the International Land Model Benchmarking (ILAMB) system (Collier et al., 2018). The following section presents the datasets, model and evaluation strategy, followed by the results and discussion with the final conclusions in the last section.

4.2 Data and Methods

4.2.1 Data

The datasets used in this chapter are derived from observations, remote sensing and machine learning algorithms. Machine learning algorithms are able to "learn" the complex relationship between a desired "target"and "predictors" from training data (O and Orth, 2020). Machine learning based techniques have gained significant relevance in data-driven research in earth sciences considering their aptitude to upgrade the performance, reduce the uncertainties and benchmark land surface models (Pal and Sharma, 2021). In this chapter the ECMWF land surface models is confronted with three independent datasets, described in the following subsections (i) GRUN runoff, (ii) SOMO soil moisture and (iii) FLUXCOM evaporation.

GRUN

GRUN is an observationally driven global gridded reconstruction of monthly runoff rates derived using a machine learning algorithm, covering the period from 1902 to 2014, with a 0.5^{o} x 0.5^{o} spatial resolution (Ghiggi et al., 2019). This dataset is based on the Global Streamflow Indices and Metadata Archive (GSIM) (Do et al., 2018; Gudmundsson et al., 2018) and on the Global Soil Wetness Project Phase 3 (GSWP3) dataset (Kim, 2017). After further data selection and preprocessing Ghiggi et al., 2019 trained it with the random forest (RF) machine learning algorithm (Breiman, 2001), to produce a global gridded monthly runoff reconstruction. The accuracy of the GRUN dataset was, (i) assessed by cross-validation and compared with an independent set of discharge observations for large river basins taken from the Global Runoff Data Centre (GRDC) Reference Dataset, and (ii) benchmarked against global hydrological models' (GHM) simulations from the Inter-Sectoral Impact Model Intercomparison Project (ISIMIP). After validation and benchmarking, GRUN presents higher predictive skills than the ensemble of state-of-the-art GHMs, especially in the reproduction of seasonality, dynamics and runoff anomalies (Ghiggi et al., 2019).

SoMo

Soil moisture is quantified by the volumetric fraction of soil occupied by water. It controls various environmental and ecosystem processes such as photosynthesis, evapotranspiration, runoff, soil respiration, flooding and most other land-atmosphere interactions (Dirmeyer et al., 2021; Dong et al., 2020). SOMO (O and Orth, 2020) is a novel global-scale gridded soil moisture dataset generated through a data-driven approach. The dataset is based on a Long Short-Term Memory neural network (LSTM) machine learning algorithm to build a soil moisture simulation model. LSTM could be comparable to a recurrent network that is capable of learning long-term dependencies across time steps in sequential data (Hochreiter and Schmidhuber, 1997). It is widely used in land surface modelling for simulations of runoff and soil moisture (Adeyemi et al., 2018; K. Fang and Shen, 2020; Kratzert et al., 2019; O and Orth, 2020). Daily meteorological time series and static features , obtained from both reanalysis and remote sensing are used as predictor variables. As a target variable, O and Orth, 2020 used adjusted in-situ soil moisture measurements from different depths obtained from the International Soil Moisture Network (ISMN) and the National Center for Monitoring and Early Warning of Natural Disasters of Brazil (CEMADEN). The resulting global dataset, provides soil moisture at three different depths: 0-10 cm, 10-30 cm and 30-50 cm, corresponding to Layer 1, Layer 2, and Layer 3 respectively. The daily data has a spatial-resolution of 0.25^{o}, covering the period from 2000 until 2019. SOMO dataset is cross-validated with direct grid-to-point comparison with in-situ measurements, against which this ML datasets shows comparable to better performances than state-of-the-art references (O and Orth, 2020). A global-scale comparison with existing gridded datasets was also performed with a satisfactory consistency between global patterns of SOMO and the reference datasets. However, SoMo has limitations in arid regions, associated with a lack of training data (O and Orth, 2020).

FLUXCOM

Jung et al., 2019 used the validated and trained machine learning techniques for the energy fluxes developed by Tramontana et al., 2016. Machine learning methods were trained using observations

from 224 flux tower sites following the specifications described in (Jung et al., 2019) and generated FLUXCOM, a large ensemble of gridded global flux products. The cross consistency of the different FLUXCOM products was evaluated against the Model Tree Ensemble (Jung et al., 2012), the Global Land Evaporation Amsterdam Model (Martens et al., 2016) and LandFlux-EVAL (Mueller et al., 2013). From the different FLUXCOM products it was decided to use the FLUXCOM Remote Sensing (RS) . The RS setup is based on a collection of MODIS land products and therefore is less subject to uncertainty in meteorological inputs. As stated by Jung et al., 2019, the RS product is preferable for energy and water budget studies or for evaluating the choice of climate input driver on LSM simulations. This dataset has a spatial resolution of 0.0833^{o}, a temporal resolution of 8 days over the time period from 2011 until 2015. Patterns and magnitudes of fluxes were validated against previous state-of-the-art estimates, and as well expectations from theory and literature (Jung et al., 2019).

CCI-CGLS land cover and leaf area index

This work evolved from Nogueira et al., 2021 that updated the ECMWF model land cover characterization leveraged on state-of-the-art EOs - the European Space Agency Climate Change Initiative (ESA-CCI) land cover dataset and the Copernicus Global Land Service (CGLS) Leaf Area Index (LAI). The ESA-CCI provides consistent maps of land cover, based on the classification system developed by the United Nations Food and Agriculture Organization. The 22 land cover classes are derived by combining remotely sensed surface reflectance and in-situ observations. The dataset has a spatial resolution of 300m and is updated on an annual basis from 1992 to 2015. Maps for 2015 were used here. LAI estimates were obtained at 1km resolution covering the entire globe. The LAI product is estimated from the SPOT-VEGETATION and PROBA-V satellite observations using the algorithm described by Verger et al., 2014. Further details on land cover and LAI data pre-processing before it's use in the mode can be found in Nogueira et al., 2021.

Data selection and pre-processing

For all three datasets (GRUN, SoMo, FLUXCOM), we selected points with valid data. This excluded some regions such as large deserts and mountainous regions. The FLUXCOM dataset just considered data from vegetation, therefore permanent unvegetated regions were not considered. Regarding soil moisture, the SoMo dataset does not consider freezing/thawing (O and Orth, 2021). Therefore, we restricted this evaluation to regions and months with simulated temperature above 5^{o}C to exclude any potential contamination from soil freezing/thawing. Finally, only points presenting valid data for more than half of the considered time series are selected. The resulting data masking is shown on Figure 4.1.

4.2.2 Model and simulation setup

CHTESSEL land surface model

The Carbon-Hydrology Tiled Scheme for Surface Exchanges over Land (CHTESSEL) is an integral part of the European Centre for Medium-range Weather Forecast (ECMWF) Integrated Forecasting System (IFS). It computes the land surface response to atmospheric forcing, estimating the surface energy and water fluxes, as well as the evolution of soil temperature, moisture, and snowpack. This

LSM uses the tiling approach, where each grid-box is divided into up to 7 land fractions representing vegetation, soil, snow and interception. Surface fluxes are calculated separately for the different subgrid surface fraction (or "tile"), leading to a separate solution of the surface energy balance, surface water budget and skin temperature for each of these tiles, which are then aggregated. In each grid-box, two vegetation types can coexist (high and low vegetation) controlled by four parameters: dominant high and low vegetation type and the fraction area for the high and low vegetation. Each vegetation type is characterized by a series of fixed parameters: (i) minimum canopy resistance $Rsmin$, (ii) vegetation coverage density $Cveg$, (iii) coefficient GD for the dependence of the canopy resistance on water vapour pressure deficit, and (iv) the root distribution over the soil layers, specified by an exponential profile modulated by two coefficients Ar and Br. The numerical values for the parameters are based on literature (Bonan, 1994; Dorman and Sellers, 1989; Giard and Bazile, 2000; Mahfouf et al., 1995; Manzi and Planton, 1994; A. Pitman, 1991; Zeng et al., 1998). CHTESSEL uses the Biosphere Atmosphere Transfer Scheme vegetation classes (Dickinson et al., 1993).

In CHTESSEL, the vegetation state is given by the Leaf Area Index. In the current operational NWP configuration, a satellite observation (Collection 5 of MODIS MOD15A2) based climatology is considered for the representation of the LAI. The climatology was derived from 9 years of data (2000 to 2008) and rescaled to the previous LAI static field used at ECMWF before 2012 (Boussetta, Balsamo, Beljaars, Panareda, et al., 2013).

Balsamo et al., 2009 implemented in CHTESSEL a new runoff and infiltration parameterizations that are related to the standard deviation of orography and to the soil texture (Balsamo et al., 2009; Boussetta et al., 2021). The rainfall is partitioned in fractions collected by an interception layer and the snow mantle, and a remaining throughfall fraction contributing to surface runoff and infiltration. The snowmelt contributes to surface runoff and infiltration by depleting the snow mantle. A multi-layer soil discretization which is shared for heat and water budget equations is used to solve Darcy's law that governs the subsurface water fluxes (Boussetta et al., 2021). A complete description of CHTESSEL can be found in ECMWF (ECMWF, 2019) and in Boussetta et al., 2021.

Simulation setup

CHTESSEL global offline simulations were carried out driven by ERA5 hourly fields, with a horizontal resolution of about 35 km (cubic octahedral TcO319 grid), for the 40-year period 1979-2018. The first year is excluded to avoid spin-up issues, retaining the 1980-2018 period for the model evaluation.

Several model configurations were tested (Table 4.1). These different configurations aim at investigating the role of (i) changes in land cover and LAI on the global/regional surface water budget in CHTESSEL, (ii) the regional and global impact of a uniform and deeper roots distribution and (iii) the impact of both changes (vegetation and roots distribution) on the surface water budget considering runoff, evaporation and soil moisture.The first model configuration, labelled as "CTR" for control, used CHTESSEL original input data with the ECMWF Integrated Forecast system (IFS). This model configuration serves as a reference against which other model configurations will be compared with. The first revised simulation, labelled as "CLAI", focused on vegetation characteristics (cover fraction, type, leaf area index). In this revised model setup, high and low vegetation fractions and types were replaced for all grid points by data of the updated ECMWF model land cover from Nogueira et al., 2021 described here in section 2.a.4. Leaf area index monthly

climatology is also replaced by values from the CGLS product. A detailed description of this setup is presented in Nogueira et al., 2021, and the changes in land cover and LAI, in respect to control, are presented in the appendix C. In a third model setup, denoted as "CTR_RD", a simpler, deeper and uniform root distribution was adopted with a maximum depth up to 2 meters for low vegetation and 2.89 meter for high vegetation. A fourth setup, referred to as "CLAI_RD" combines ESA_CCI vegetation fractions and types, CGLS leaf area index and the uniform and deeper root distribution. The last model setup, labelled "CTR_RS", explores the impact of a simpler, shallower and uniform root distribution, with a maximum depth up to 1 meter for low vegetation and 2 meter for high vegetation.

Table 4.1: Model simulations acronyms and detailed configuration for grid-scale evaluation

Experiment	**Characteristics**
CTR	Control simulation with default CHTESSEL parameters and input LAI and Albedo
CLAI	Implementation of CCI land cover and vegetation types and CGLS new monmthly LAI climatology
CTR_RD	Same as CTR but with deep uniform roots distribution with a maximum depth of $2m$ for low vegetation and $2.89m$ for high vegetation
CLAI_RD	Same as CLAI with implementation of deep uniform root distribution
CTR_RS	Same as CTR but with shallow and uniform roots distribution with a maximum depth of $1m$ for low vegetation and $2m$ for high vegetation

4.2.3 Evaluation

CHTESSEL simulations were evaluated against GRUN for runoff, FLUXCOM for evaporation and SOMO for soil moisture. Considering the number of different model setups, a systematic and consistent approach to investigate results and changes in simulation responses was necessary. It was decided to use metrics based on the method developed in the International Land Model Benchmarking (ILAMB) package (Collier et al., 2018). This benchmarking method is particularly useful for verification and validation when comparing different model setups. The simulated and machine learning runoff, evaporation and soil moisture are compared using six metrics from the ILAMB package, briefly described in the following points:

- (i) a spatially integrated bias score S_{bias}, which normalize the bias by the variability at any given special location,
- (ii) a spatial centralized root mean square error S_{rmse}. The centralized $RMSE$ removes the

bias from the $RMSE$,

- (iii) phase shift S_{phase}, compare the timing of the maximum of the annual cycle of a variable,

- (iv) interannual variability S_{iav}, computed by removing the annual cycle from both the reference and the model and then computing a score as a function of space,

- (v) spatial distribution S_{dist}, which compares the normalized standard deviation with the spatial correlation,

- (vi) overall score $S_{overall}$ (Eq.4.1) for a given variable and data product, as a composite of the suite of metrics defined above. It offers a general overview of the model setup performance by combining all the other metrics, where the S_{rmse} score is doubly weighted to emphasize its importance (Collier et al., 2018).

$$S_{overall} = \frac{S_{bias} + (2 * S_{rmse}) + S_{phase} + S_{iav} + S_{dist}}{1 + 2 + 1 + 1 + 1} \tag{4.1}$$

The $S_{overall}$ score, allows us to compare the performances of the different model setup, by the mean of a single score grouping different metrics. This single score method highlights which changes, in vegetation characteristics, lead to improvements in terms of a variable (e.g. ET) without deteriorating another one (e.g. soil moisture).

Considering this spatial extent, we decided to group results using the Köppen-Geiger climate classification from Beck et al., 2018. The Köppen-Geiger system classifies climate into five main classes and 30 sub-types, based on threshold values and seasonality of monthly air temperature and precipitation (Beck et al., 2018). This climate classification is suitable to aggregate complex climate gradients into a simple but ecologically meaningful classification scheme (Beck et al., 2018). Here we aim to explore the results of the different CHTESSEL configuration in order to facilitate the assessment of changes and impacts on model response. We decided to use four main climate Köppen-Geiger classes, (i) arid, (ii) temperate, (iii) tropical, (iv) cold (see Figure 4.1). The polar class was not considered as most of the region was already excluded (absence of vegetation and frozen soil).

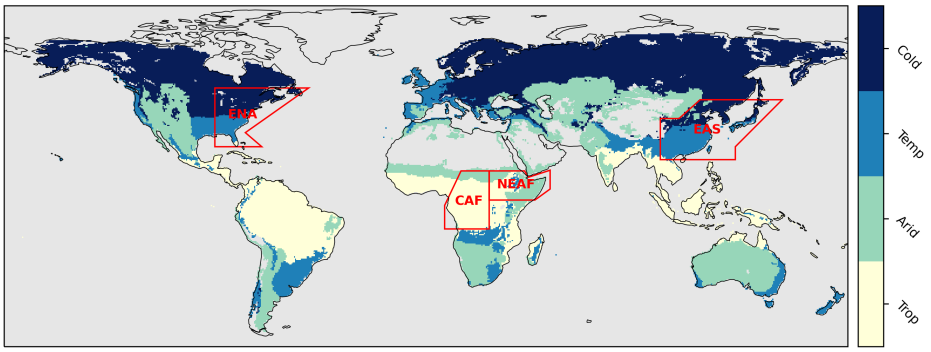

Figure 4.1: Köppen-Geiger four main climate classifications used. The IPCC regions selected are framed with red polygons and light grey area represents masked regions

Although specific locations can share the same Koppen-Geïger classification, they could at the same time present very different annual cycles (Iturbide et al., 2020). Therefore, in addition to the climate regions, several regional domains were selected to investigate in more detail the different model configurations. The four Intergovernmental Panel on Climate Change (IPCC) regions selected are identified in 4.1, and were taken from the regions definitions in Iturbide et al., 2020: (i) East Asia (EAS); (ii) Central África (CAF); (iii) East North America (ENA); and North East Africa (NEAF).

4.3 Results

4.3.1 Performance of CHTESSEL control configuration

The original model configuration (CTR) presents an $S_{overall}$ score of 0.66 (panel (f) Figure 4.2). Higher latitudes tend to have a high $S_{overall}$ score as opposed to southern latitudes location where heterogeneity in model response is marked by low $S_{overall}$ scores at certain specific locations (Brazil, Central Africa, Western Australia). The Köppen-Geiger "cold" and "temperate" classes show better agreement with the machine learning derived observation datasets with $S_{overall}$ scores of 0.72 and 0.67 respectively (Figure 4.3). All Köppen-Geïger groups have a fairly high S_{dist} scoring against all observations datasets (panel D Figure 4.3), which suggest a good correlation and weak deviation of the CTR setup from the observations. The four climatic classes have a relatively low $S_{overall}$ score against GRUN runoff. The Köppen-Geïger "Cold" class has the maximum $S_{overall}$ score of 0.65, "tropical", "temperate" and "arid" classes lag a little bit behind with an $S_{overall}$ score of 0.59, 0.57 and 0.54 respectively (see panel A Figure 4.3). The other metrics (see Appendix Figure C.1) replicate the same response shown by $S_{overall}$ score. The CTR setup succeeded to replicate the S_{phase} with a score of 0.93 for all Köppen Geiger classes considered, showing that the model timing of the maximum of the annual cycle fits with observation. However this model setup fails to correctly simulate the interannual variability especially in the "arid" class with a score as low as

0.54 (see Appendix Figure C.1 and C.4). The Köppen-Geïger “cold” class has a better agreement with GRUN dataset on all metrics with a stronger scoring on the spatial distribution with a score of 0.88.

A duality of result is seen on evaporative fluxes, when CTR is compared against FLUXCOM (see panel B Figure 4.3). The northern hemisphere presents systematic high $S_{overall}$ scores while the southern hemisphere has a strong heterogeneity in results. The Köppen-Geiger ”tropical” class has an $S_{overall}$ score of 0.56 and the “cold” class has a $S_{overall}$ of 0.83. “Temperate” and “cold” regions have a good agreement with the FLUXCOM dataset, with good performances in S_{Bias}, S_{rmse} and S_{phase} (see Appendix Figure C.1 and C.3). However the four köppen Geïger climate classes have difficulties to replicate FLUXCOM on the interannual variability S_{iav} (see Appendix C.3), while succeeding in timing the maximum of the annual cycle S_{phase}.

The four Köppen Geiger classes perform similarly when compared against the SoMo dataset (see panel C Figure 4.3). The CTR model setup interannual variability (S_{iav}) and timing of the mean annual cycle maximum (S_{phase}) is consistent with the SoMo machine learning observation. Only the “arid” class presents a stronger dry bias against observation (see Appendix Figure C.2 and C.3). The “temperate” class presents the stronger agreement with SoMo with an $S_{overall}$ of 0.71 and an S_{dist} of 0.91.

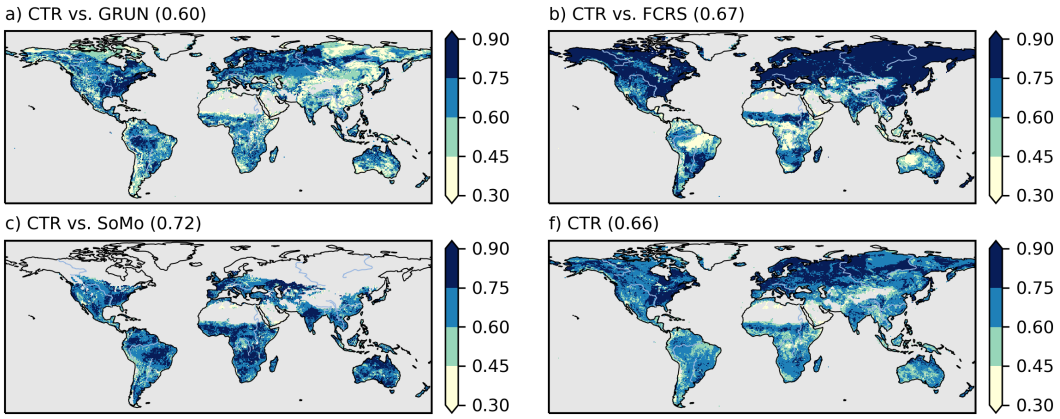

Figure 4.2: Evaluation of the CTR setup against GRUN (a), FLUXCOM (b), SoMo (c) and CTR mean Soverall score (f).

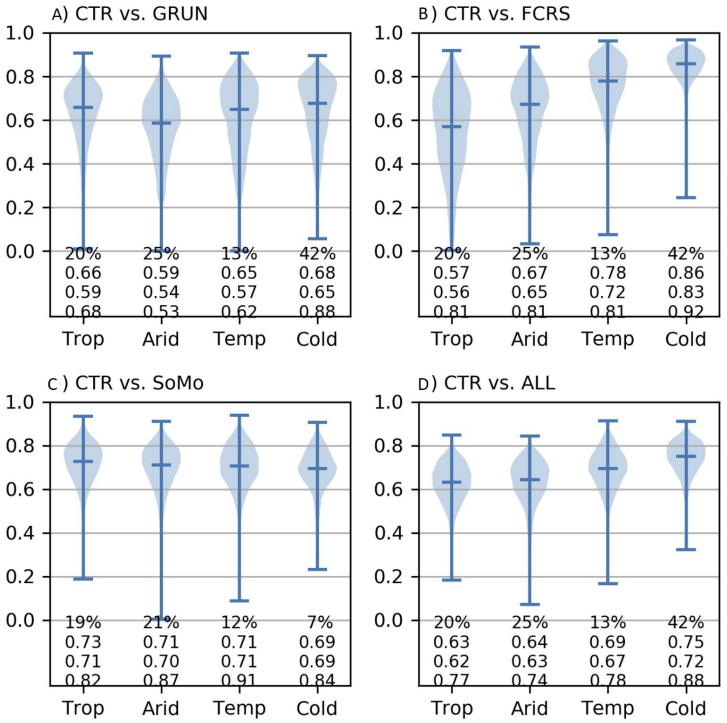

Figure 4.3: 4 Köppen-Geiger classes evaluation of the CTR setup. The first number below the barplots represents the % of points in each Köppen-Geiger region. The score below is the median of the grid-points score. The third number is the spatial score ($S_{overall}$). The fourth number is the distance score (S_{dist}).

4.3.2 Impact of land cover, LAI and rooting depth

The impact of the CCI vegetation cover and CGLS LAI is mostly neutral with a Soverall score almost unchanged, due to high heterogeneity of model responses within the same Köppen-Geïger classification.

The positive changes within the "cold" and "temperate" Köppen-Geïger classes are tapered down by a more negative model response to vegetation changes within the same classes (panel a Figure 4.4).

The CLAI model setup modestly reduced the evaporative bias of the "arid" Köppen-Geïger class. There is such a high degree of heterogeneity in model response to this new land scheme that even the Köppen-Geïger classification has difficulties to highlight any systematic improvement or degradation in model results. Köppen-Geïger "Tropical" class see both improvements (around Central Africa and the Amazonian) and degradation around the same locations giving an unchanged model score (panel b Figure 4.6). The same Köppen-Geïger class was already showing low $S_{overall}$ with the CTR setup (panel e Figure 4.5), therefore changes observed, at those Köppen-Geïger "tropical" zones, do not necessarily mean that the model performed better.

The new vegetation scheme setup deteriorates model soil moisture representation with a worsening of the dry bias.

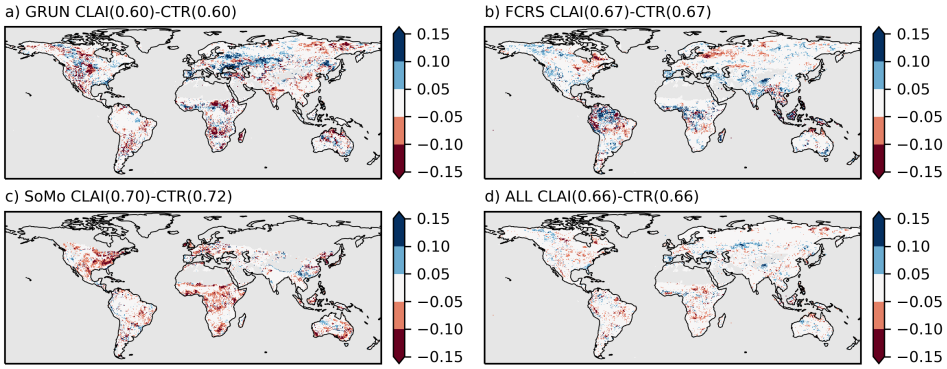

Figure 4.4: $S_{overall}$ score evaluation of the CLAI setup against CTR. (a) GRUN CLAI $S_{overall}$ vs GRUN CTR $S_{overall}$, (b) FLUXCOM CLAI $S_{overall}$ vs FLUXCOM CTR $S_{overall}$, (c) SoMo CLAI $S_{overall}$ vs SoMo CTR $S_{overall}$ and (f) CLAI mean $S_{overall}$ vs CTR mean $S_{overall}$ score (f).

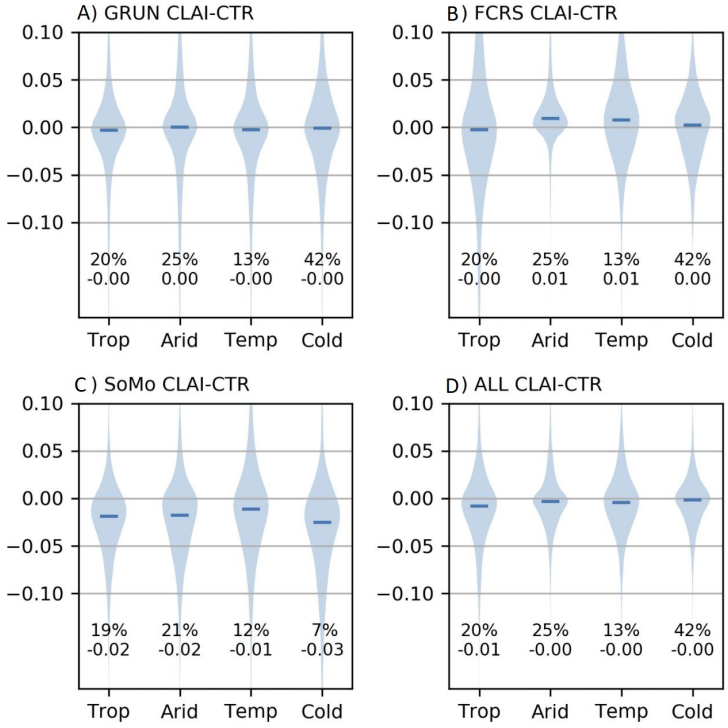

Figure 4.5: 4 Köppen-Geïger classes evaluation of the CLAI setup. The first number below the barplots represents the % of points in each Köppen-Geïger region. The score below is the median of the grid-points $S_{overall}$ score.

Model responses to changes in root distribution are more pronounced than vegetation changes. A deeper and uniform root scheme allows plants to access more volume of soil water by tapping directly into some deeper layer that is not yet water depleted in case of drought. The changes

are not fully reflected in the $S_{overall}$ score (figure 4.6) with small improvements resulting from the new root scheme. The deeper and uniform root distribution brings systematic improvements to the Köppen-Geïger "tropical" class, with an improved runoff, evaporation and soil moisture representation (Figure 4.6 and 4.7). The new root scheme considerably improves the model soil moisture response (panel c, figure 4.6) with a reduction of the dry bias for the "temperate", "cold" and "tropical" Köppen-Geïger classes. Evaporation model output does not benefit from the deeper and uniform root scheme with a degradation of the $S_{overall}$ score for both "temperate" and "cold" classes. The "tropical" and "arid" class present a strong heterogeneity in model evaporative fluxes, as such the $S_{overall}$ score against FLUXCOM remains unchanged for those Köppen-Geïger classes.

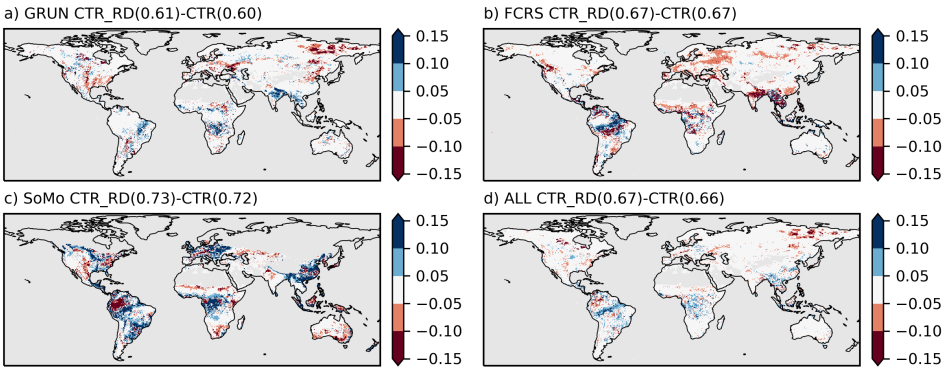

Figure 4.6: $S_{overall}$ score evaluation of the CTR_RD setup against CTR. (a) GRUN CTR_RD $S_{overall}$ vs GRUN CTR $S_{overall}$, (b) FLUXCOM CTR_RD $S_{overall}$ vs FLUXCOM CTR $S_{overall}$, (c) SoMo CTR_RD $S_{overall}$ vs SoMo CTR $S_{overall}$ and (f) CTR_RD mean $S_{overall}$ vs CTR mean $S_{overall}$ score (f).

The model setup combining both the new land cover and the deeper and uniform root distribution presents a model response driven by the new root scheme, with a model response similar to the one of the root distribution (figure 4.8 is similar to figure 4.6). As seen on figure 4.9 this model setup brings systematic positive changes in the "tropical" Köppen-Geïger class as seen with the CTR_{RD} setup (figure 4.7), however those changes are more pronounced using the model setup which combines CCI-CGLS and the new root scheme.

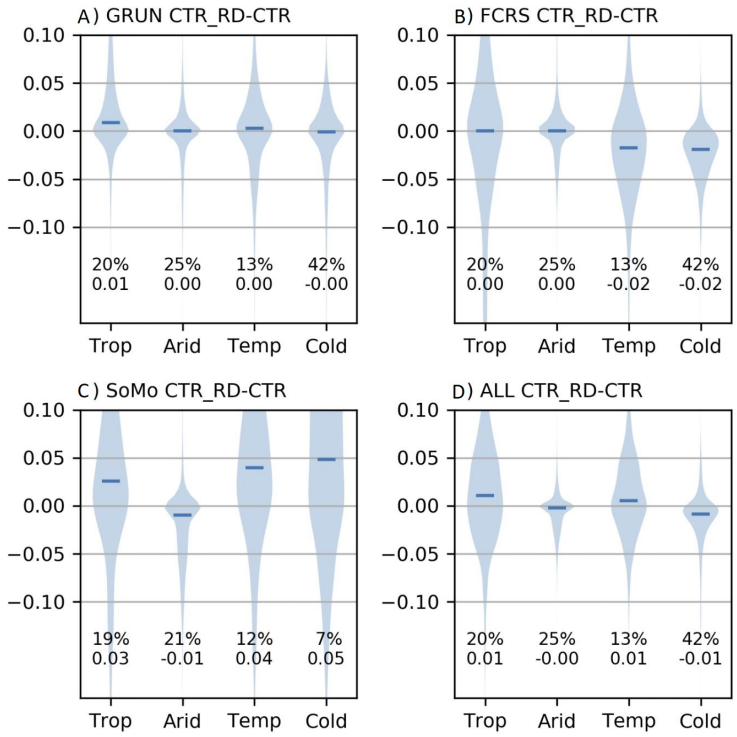

Figure 4.7: 4 Köppen-Geïger classes evaluation of the CTR_RD setup. The first number below the barplots represents the % of points in each Köppen-Geïger region. The score below is the median of the grid-points $S_{overall}$ score.

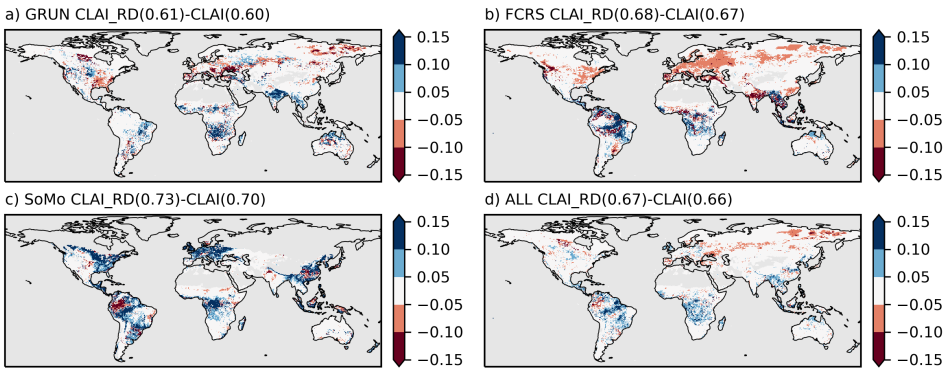

Figure 4.8: $S_{overall}$ score evaluation of the CLAI_RD setup against CTR. (a) GRUN CLAI_RD $S_{overall}$ vs GRUN CLAI $S_{overall}$, (b) FLUXCOM CLAI_RD $S_{overall}$ vs FLUXCOM CLAI $S_{overall}$, (c) SoMo CLAI_RD $S_{overall}$ vs SoMo CLAI $S_{overall}$ and (f) CLAI_RD mean $S_{overall}$ vs CLAI mean $S_{overall}$ score (f).

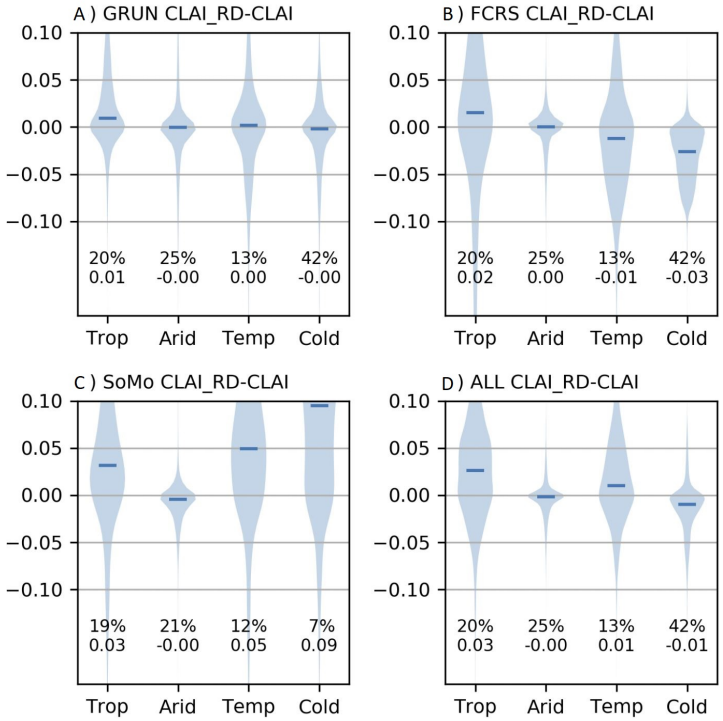

Figure 4.9: 4 Köppen-Geïger classes evaluation of the CLAI_RD setup. The first number below the barplots represents the % of points in each Köppen-Geïger region. The score below is the median of the grid-points $S_{overall}$ score.

4.3.3 Regional evaluation

A regional evaluation gives more information in terms of soil moisture response to model changes and highlights differences that are not fully shown by grid-scale analysis.

The 4 IPCC regions react differently to the different model setups, making it challenging to highlight any systematic improvements or degradation. Some of the annual cycles combine both runoff and evaporation overestimation (Figure 4.10), as we were expecting that an overestimation in runoff would be translated into an underestimation of evaporation. All 4 different model setups overestimate runoff, evaporation and soil moisture for the EAS region. The same response of the model is seen for the CAF where all the model setups underestimate both runoff and evaporation (Figure 4.10). Model response to vegetation changes, in respect to the CTR setup, is not as intense as the one following rooting changes. The deeper and uniform root distribution tends to overestimate shallow soil moisture as plants get access to more water, however the seasonality is not affected by those model changes. It seems that GRUN and FLUXCOM are not consistent with ERA5, which could explain why they present more runoff and evaporation while using the same amount of precipitation, for the CAF region. ENA and NEAF regions have a more consistent signal against ERA5, with less runoff followed by a runoff overestimation (Figure 4.11). When the model is generating too much runoff (as compared with observations) an underestimation of evaporation follows, and reciprocally.

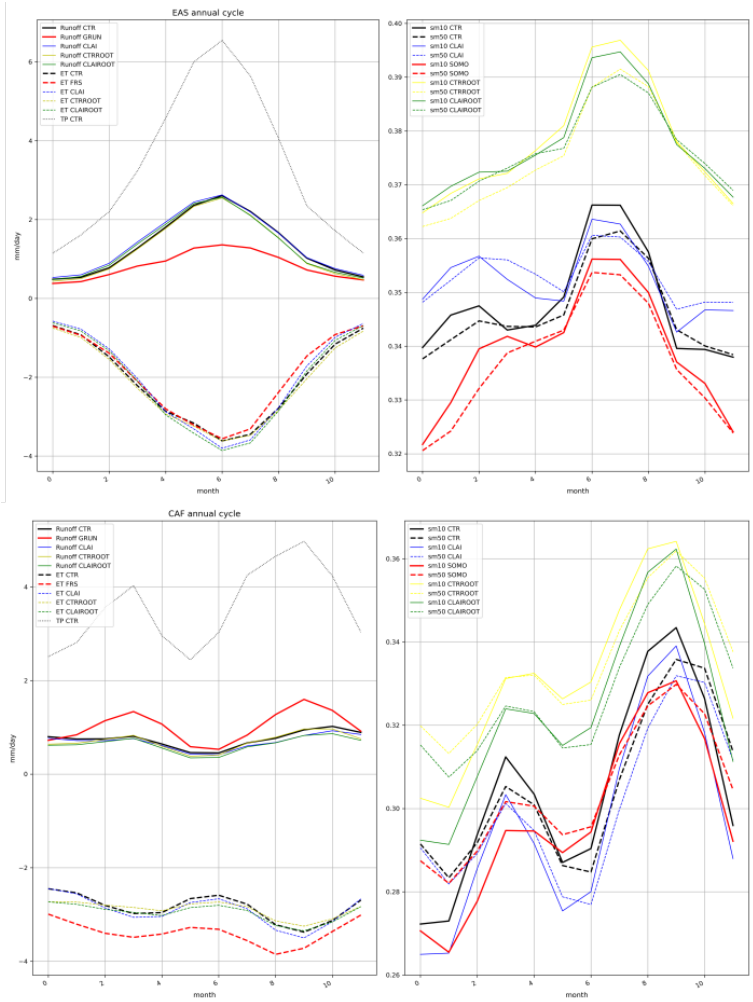

Figure 4.10: IPCC region evaluation Southeast Asia (EAS) and Central Africa (CAF) runoff, evaporation, precipitation and soil moisture (10cm and 50cm depth) mean annual cycle.

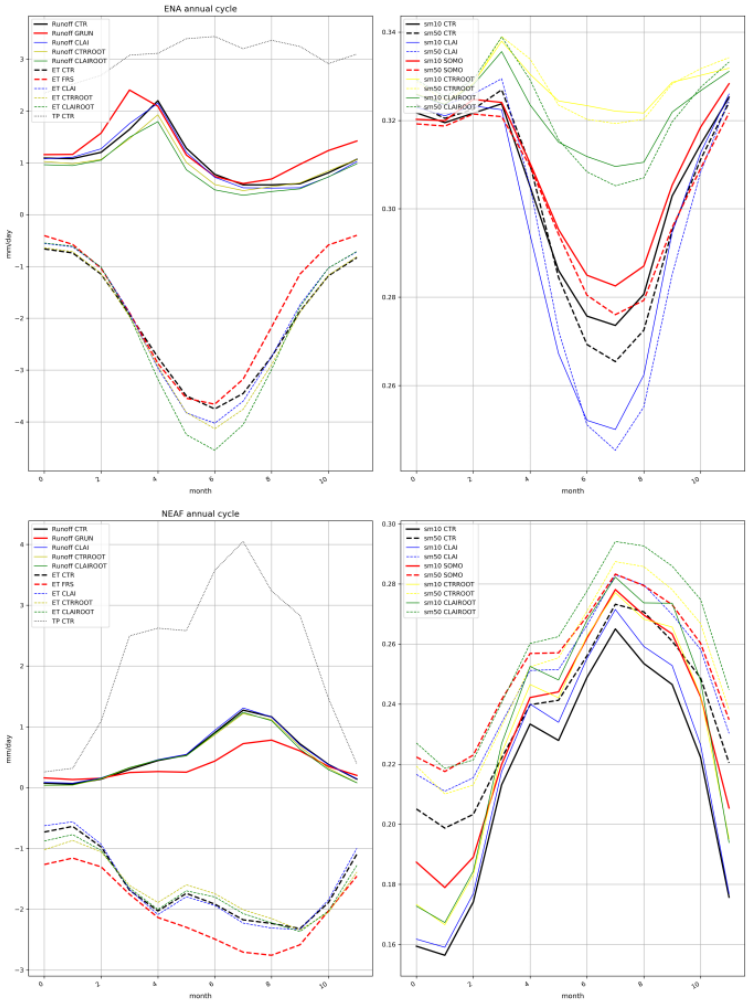

Figure 4.11: IPCC region evaluation Northeast America (ENA) and Northeast Africa (NEAF) runoff, evaporation, precipitation and soil moisture (10cm and 50cm depth) mean annual cycle.

4.4 Discussion

From strictly metrics perspective, the updated land cover and vegetation setup do not induce significant changes in CHTESSEL surface water budget. A worsening of model performances is seen on soil moisture using this updated vegetation datasets. Changes in model performances replicate vegetation modification. Therefore heterogeneities in vegetation changes, from CTR to CLAI, create heterogeneity in model response which is not fully shown and reproduced by the scores (e.g. Amazonian basin, Central Africa). This overall neutral impact, of ESA-CCI and CGLS LAI updated vegetation types and fractions, on offline CHTESSEL surface water budget follows the finding of Nogueira et al., 2021) who also reported a neutral impact on LST and surface fluxes simulation. Nogueira et al., 2021 also show a surface warming over Central Africa and Eastern Brazil, related to uncertainties in vegetation classes cross-walking tables (from ESA-CCI vegetation types into the BATS vegetation classes used in CHTESSEL) which could also explain the heterogeneity in the CLAI model setup surface water budget, observed in the results.

Plants use a wide range of strategies and abilities to handle and manage the impact of water stress, including changes in rooting depth (A. J. Pitman, 2003). The water extracted by plants during the wet season comes from shallow layers where the root density is higher. However, as those layers dry out there is a progressive shift towards using deeper soil water. Survivorship of some species in arid systems has been shown to depend completely on plants' abilities to tap water from permanent aquifers (Gardner, 1983). Different studies show the importance of the deeper root biomass in alleviating water stress in many crops and vegetation types (Canadell et al., 1996; Gardner, 1983; Gregory et al., 1978; Nepstad et al., 1994; A. J. Pitman, 2003. In CHTESSEL, the soil moisture resistance or water stress factor, is parameterized by two components: (i) the derivation of the root zone soil moisture content (using) an exponential root distribution and (ii) a linear transformation between field capacity (unstressed vegetation) and the wilting point (Jarvis, 1976). Here with the CTR_RD and CLAI model setup, we focused only on the first component of the water stress factor. This new uniform root distribution and the associated maximum rooting depth triggers a strong model response considering grid-scale surface water budget. It brings CHTESSEL closer to the machine learning derived observation datasets by setting off plants to access soil water more efficiently. This generates a new surface water budget with a more accurate representation of the shallow soil moisture at the depend of the evaporative fluxes.

Plants have different adaptive strategies in case of drought. They could either access water by growth of the root biomass or limit water loss using physiological regulation (Bartletta et al., 2016; Y. Liu et al., 2021; Nepstad et al., 1994; Sperry and Love, 2015). The Jarvis representation of the sensitivity of stomatal conductance (gs) to water stress, used in LSMs like CHTESSEL, does not consider the role of plant hydraulics and associated changes in leaf and xylem water potential that have a more intrinsic relation with stomatal conductance regulating plants evapotranspiration (Bartletta et al., 2016; Y. Liu et al., 2021; Sperry and Love, 2015). The degradation of the evaporative fluxes, mainly seen on the "temperate" and "cold" Köppen-Geïger classes, might be linked with this incomplete model parameterization/representation of vegetation diverse responses to both soil and atmospheric water deficits situations. Plant water stress values are unfortunately restricted to in-situ and laboratory measurements only considering few vegetation species. Plants' abilities to cope with drought are deployed at a regional and global scale and could differ locally depending on the climate and ecosystem regimes (Y. Liu et al., 2021). The difficulties in representing the diversities of plant responses to water stress might weaken the effect of the deeper and uniform root distribution in representing evaporative fluxes at several locations. The CLAI_RD model setups confirms this idea, with an improvement of the evaporative flux's representation, due to a lower LAI which could act as a proxy for evaporation resistance in the model. A land surface model vegetation parameterization that could include a spatial distribution of ecosystems average behavior instead of the one of the dominant species at each location, could enhance model abilities to simulate the diversity in plant water stress responses. The results of Y. Liu et al., 2021 show that northern latitudes vegetation deploys a stronger physiological regulation over deep rooting strategy to overcome water stress situations. This could explain why the CTR_RD model setup deteriorates evaporative fluxes for the "temperate" and "cold" Köppen-Geïger classes while having a positive effect for the "tropical" and "arid" zones (Figure 4.6 and Figure 4.7).

The "tropical" Köppen-Geïger class benefits the most from the deeper and uniform root distribution (Figure 4.7 and Figure 4.9). This corroborates the findings of Y. Liu et al., 2021 who

found that deep rooting systems are mainly located in tropical regions as opposed to shallow rooting zones which occur in the northern latitudes. An interesting point to note is that despite observation of very deep root biomass in arid regions (Schenk and Jackson, 2002), arid climates tend to have shallow rooting depth (Y. Liu et al., 2021; Yang et al., 2006). This could explain why the "arid" Köppen-Geïger class reacted negatively to the deeper and uniform root distribution.

Ukkola et al., 2016, identified a systematic overestimation of evaporative droughts in several LSMs, including CHTESSEL. An unusually low soil water content generates moisture limitations on surface latent heat fluxes, suppressing cloud formation and thus increasing surface net radiation driving temperatures higher during the duration of extreme heat (Dirmeyer et al., 2021). Here we show that a deeper and uniform root distribution, presents a more conservative approach for shallow soil layer water extraction. These results could have a significant impact by moderating the systematic land surface model evaporative drought overestimation.

4.5 Conclusion

In this chapter, runoff, evaporation and soil moisture global long-term dataset, generated from in-situ measurements are used to assess the impact, of an updated land cover and vegetation seasonality and a deeper and uniform root distribution, on CHTESSEL surface water budget. The replacement of the current vegetation types, cover, characteristics and leaf area index, by a new high resolution remote sensing derived global vegetation dataset did not significantly affect the different simulated water budgets. However, the introduction of a simple deeper and uniform root scheme, allowing plants to use soil water more efficiently, sparks a more pronounced and positive response from ECMWF land surface model. This outcome has several implications. First, this work shows that machine learning derived observation datasets can help the land surface model community, by filling the gap between in-situ observation points and the grid-scale of the model outputs. Those new state-of-the-art data could efficiently be used to evaluate, constrain and finally optimize land surface model parameterization. The second finding goes against the expectations that more accurate, remote sensing derived vegetation characteristics could greatly enhance model performance. The results in this chapter goes against that idea since a simple and deeper root distribution triggers more model responses than the satellite derived updated vegetation cover and seasonality. Another outcome of this work, and nevertheless the most meaningful, is that land surface model parameterization should be more focused on global assessment of plant water strategies at the ecosystem level instead of the current dominant tree parameter affectation. Therefore, even if an increase in model resolution could slightly improve simulation, the core of LSMs discrepancies lay in the parameterization uncertainty to represent and capture smaller-scale unresolved processes and integrate them at any given scale.

Chapter 5

Conclusion

In this thesis, several relevant land surface processes were reviewed aiming to advance our understanding of the coupling between the energy, water, and carbon cycles and their numerical representation in the ECMWF land surface model. The focus was put on the impact of LSM's vegetation representation and its ability to bring water budgets and carbon estimates closer to observations. In the first chapters I focused on the impact of the representation of the canopy resistance and stomatal conductance on the simulations of Net Ecosystem Exchanges (NEE), latent and sensible heat fluxes using different configurations of ECMWF land surface model (CHTESSEL and CTESSEL). Observed data from 17 flux towers representative of different Plant Functional Types (PFTs) were used to carry out offline point simulations with an emphasis on the representation of evaporation and NEE fluxes in water stress conditions. Two different formulations of the stomatal conductance were used here: (i) Jarvis, used in CHTESSEL, where empirical stress function depending on environmental conditions regulate water exchanges and (ii) the A-gs scheme based on plant physiological considerations, used in CTESSEL. Three constraints of the canopy resistance parameter were also evaluated using those two models: (i) the role of accurate vegetation characteristics with the use of high spatial resolution Leaf Area Index (LAI); (ii) the impact of an optimized minimum canopy resistance and (iii) the impact of a deeper and uniform roots distribution. MODIS derived LAI presents different values and more inter-annual variability than the original model inputs and were expected to enhance model performance with a site-specific climatology. Contrary to this expectation, both CHTESSEL and CTESSEL reacted moderately to the high-resolution LAI as NEE, and latent and sensible heat fluxes simulations remained mainly unchanged. The adjustment of the canopy showed some potential to improve CHTESSEL latent and sensible heat fluxes estimates. However, this parameter adjustment was detrimental once the stations were in a water limited regime with an increase of the evaporative drought already reported at several stations. We found that one of the model's limitations was tightly associated with the depletion of the soil moisture in the shallower soil layer while the original roots profile could not access the water available in the deeper layer. Therefore, the replacement of CHTESSEL and CTESSEL exponential roots profile by a deeper and uniform roots profile triggers a strong model response with a reduction of evaporation underestimation during water stress conditions. The A-gs scheme of the stomatal conductance also had a positive impact on model output with an increased accuracy of NEE estimates and a further reduction of the evaporation gap between model and observation under water stress conditions. The plant

physiological approach replicates the release of water vapor when plant stomata open to assimilate carbon. This approach tends to provide the model with a more conservative use of the soil moisture by the plants under water limited regime. This proposed uniform and deeper roots distribution is appealing for LSMs optimization therefore we spatially extended this work to the model grid-scale to understand the implications of these changes on the global surface water budgets. Using different CHTESSEL model configurations I further investigated two canopy resistance constraints: (i) the role of vegetation characteristics by using state-of-the-art Earth Observations land cover and LAI dataset; and (ii) the impact of the simplified roots scheme on evaporation, runoff and soil moisture. Grid-scale model outputs were compared against independent observationally based machine learning datasets using Köppen-Geïger and IPCC climate classifications through the land surface model benchmarking method (ILAMB). The weak model response to high resolution vegetation characteristics dataset is also shown at the global scale with model outputs relatively unchanged. Scores were like those obtained by the original model setup with only a small deterioration of soil moisture representation seen across the different climate classes and zones. The uniform roots distribution triggered also a more pronounced model response at the global scale. Model soil moisture benefits the most from the new roots' distribution with more accurate estimates in each climate class and zones. The Köppen-Geïger tropical class shows better agreement with machine learning datasets. However, results are mixed and it's hard to guarantee that model runoff, evaporation and soil moisture are positively impacted by this new root scheme. Plants have different adaptive strategies to environment conditions. The degradation or even the improvement of the land water budget might be linked with the model inability to correctly set-up that diversity in vegetation responses to external factors. A land surface model vegetation parameterization that could include a spatial distribution of the ecosystem behavior instead of the dominant Plant Functional Types might further enhance model performance. However, considering the limitation of encountering such data and the already weak model response from the high-resolution LAI it seems that a different roots scheme could be a viable parameter optimization which needs further evaluation within the land surface model community.

Appendix A

Supporting material of Chapter 2.

The statistical metrics used following Best et al., 2015: the mean bias error (MBE), normalized mean error (NME), standard deviation difference (SD) and correlation coefficient (r) were computed using daily values with M, O and n representing the model data, observed flux tower data and the number of days, respectively.

$$MBE = \frac{\sum_{i=1}^{n}(M_i - O_i)}{n} \tag{A.1}$$

$$NME = \frac{\sum |M_i - O_i|}{\sum |O - O_i} \tag{A.2}$$

$$SD = |1 - \frac{\sqrt{\frac{\sum M_i - M^2}{n-1}}}{\sqrt{\frac{\sum O_i - O^2}{n-1}}}| \tag{A.3}$$

$$r = \frac{\sum_{i=1}^{n}(M_i - M)(O_i - O)}{\sqrt{\sum_{i=1}^{n}(M_i - M)^2}\sqrt{\sum_{i=1}^{n}(O_i - O)^2}} \tag{A.4}$$

Table A.1: CHTESSEL vegetation types and associated parameters. R_1 to R_4 denote the root fraction in layers 1 to 4 (with depths of 0.07, 0.21, 0.72 and 1.89 m). The Final 4 lines indicate the root fraction when considering an uniform rooting depth with maximum rooting depth R_{DMAX} of 0.5, 1, 2 and 2.89 meters.

Land cover type	H/L	Cveg	R_{smin}	a_r	b_r	R_1	R_2	R_3	R_4
Crops	L	0.90	100	5.55	2.61	24	41	31	4
Short grass	L	0.85	100	10.74	2.61	35	38	23	4
Tall grass	L	0.70	100	8.24	1.63	27	27	27	9
Tundra	L	0.50	80	8.99	8.99	47	45	8	0
Irrigated Crops	L	0.90	180	5.56	2.61	24	41	31	4
Semi desert	L	0.1	150	4.37	0.98	17	31	33	19
Bogs and marshes	L	0.6	240	7.34	1.30	25	34	27	11
Evergreen shrubs	L	0.50	225	6.34	1,57	23	36	30	11
Deciduous shrubs	L	0.50	225	6.33	1.16	23	36	30	11
Evergreen needeleaf trees	H	0.90	250	6.71	2.18	26	39	29	6
Deciduous needleleaf trees	H	0.90	250	7.07	1.95	26	38	29	7
Deciduous broadleaf trees	H	0.90	175	5.99	1.96	24	38	31	7
Evergreen broadleaf trees	H	0.99	240	7.34	1.30	25	34	27	14
Mixed forest	H	0.90	250	4.45	1.63	19	35	36	10
Interrupted forest	H	0.90	175	4.45	1.63	19	35	36	10
R_{DMAX}=0.5						14	42	44	0
R_{DMAX}=1						7	21	72	0
R_{DMAX}=2						4	11	36	50
R_{DMAX}=3						2	7	25	65

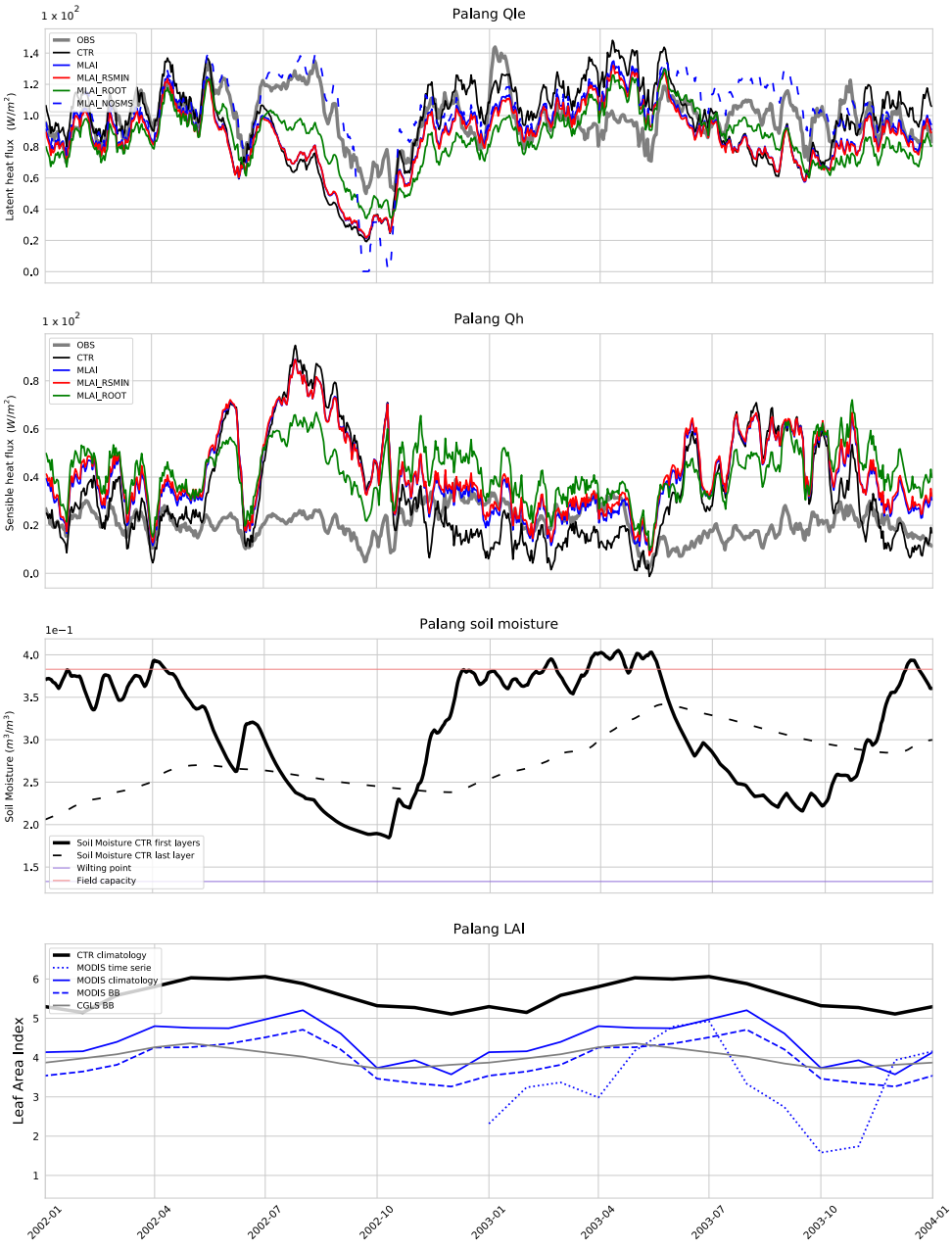

Figure A.1: Time series of Sensible heat flux, latent heat flux, soil moisture and LAI in Palang. The turbulent fluxes time series compare the observations (gray) with the simulations: CTR (black), MLAI (blue), MLAI_RSMIN (red), MLAI_ROOT (green) and MLAI_NOSMS (dashed blue). The soil moisture time series shows the CTR top 3 layers meter soil moisture (top meter solid back) and the bottom layer soil moisture (dashed black) as well as the soil moisture at wilting point (blue) and field capacity (red). The LAI time series compares CTR (black) with the high resolution MODIS LAI time series (dotted blue), the high resolution MLAI (blue), the climatology of MODIS considering the 0.25° bounding box (dashed blue) and CGLS LAI climatology (grey).

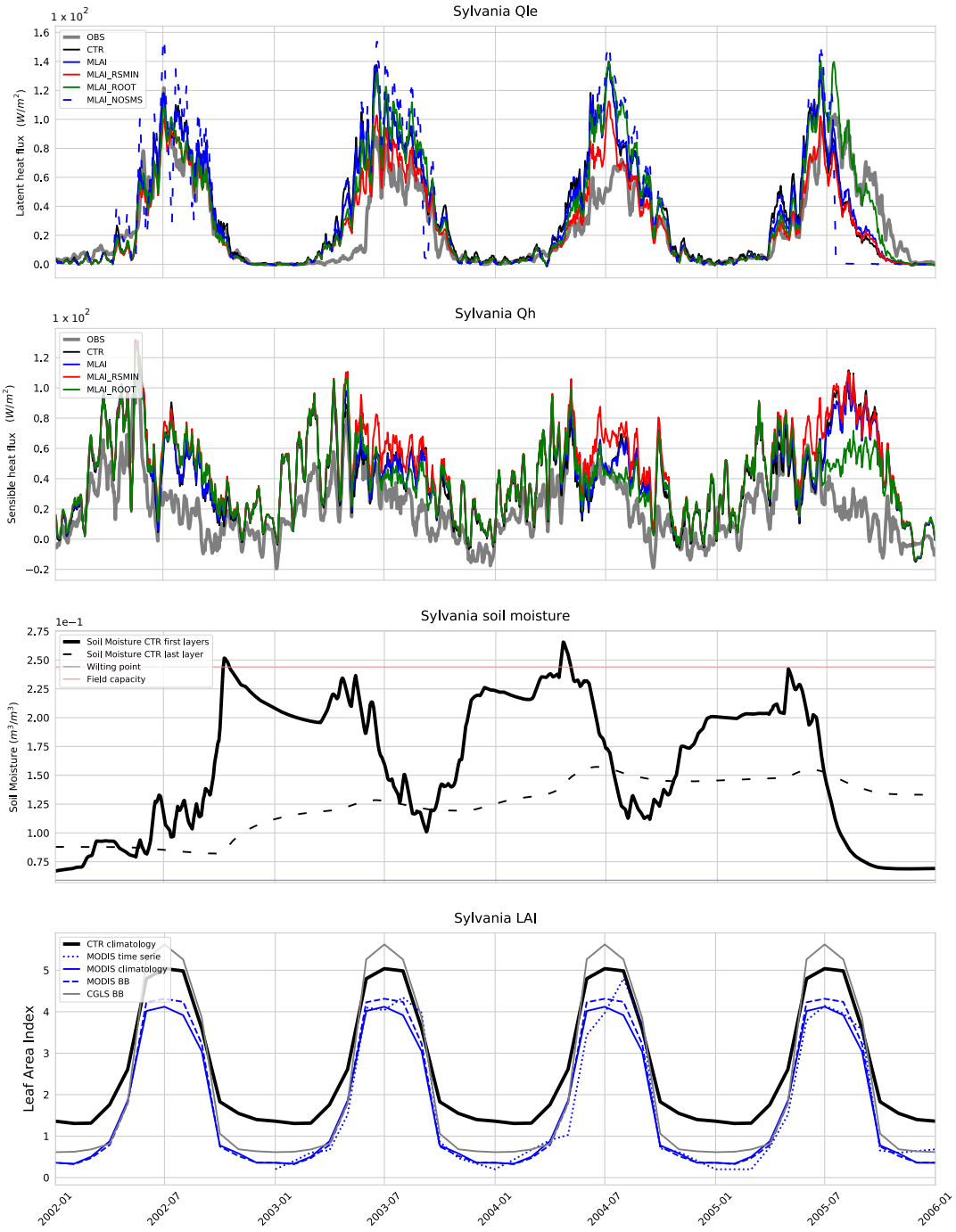

Figure A.2: As Figure A.1 but for Sylvania station.

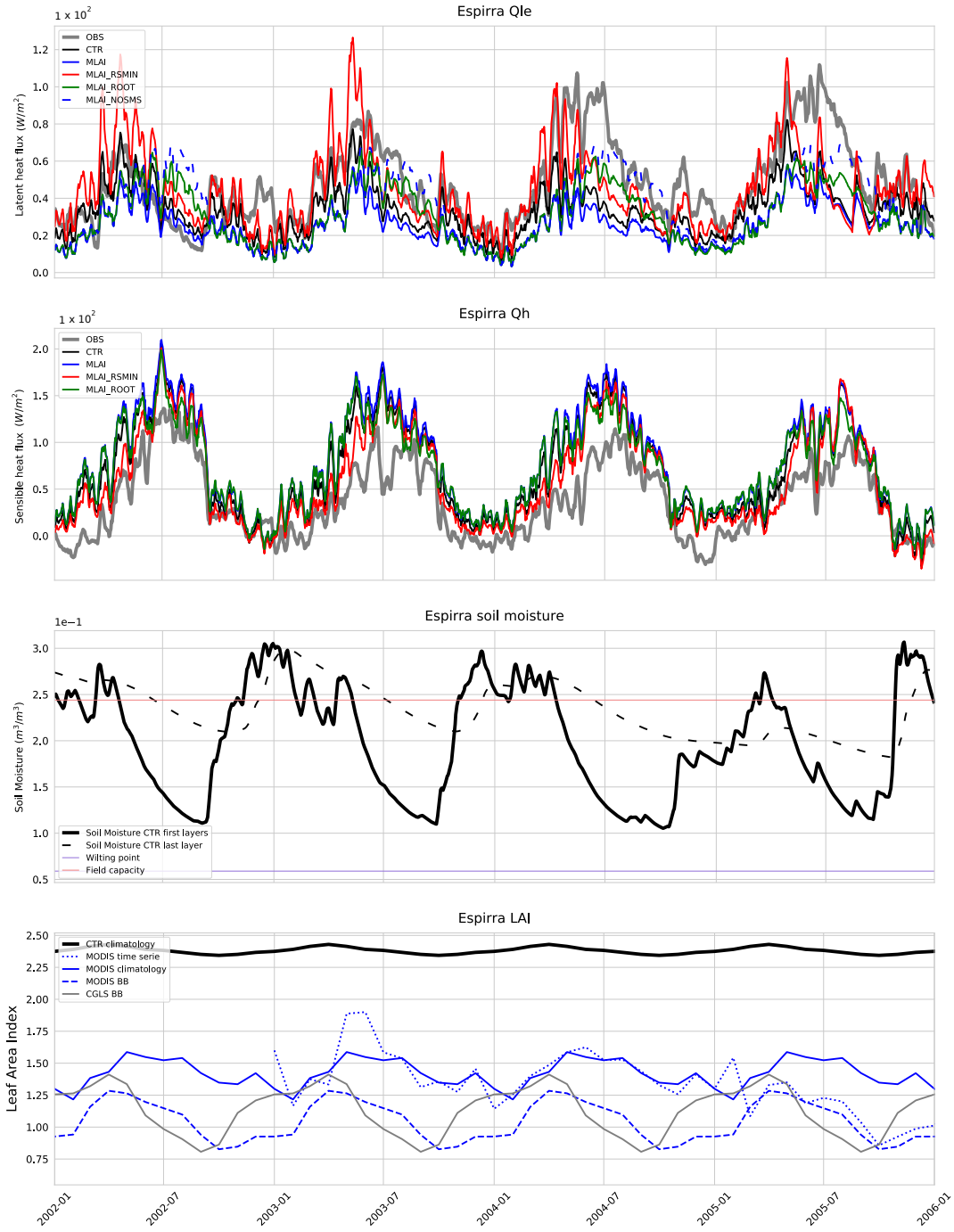

Figure A.3: As Figure A.1 but for Espirra station.

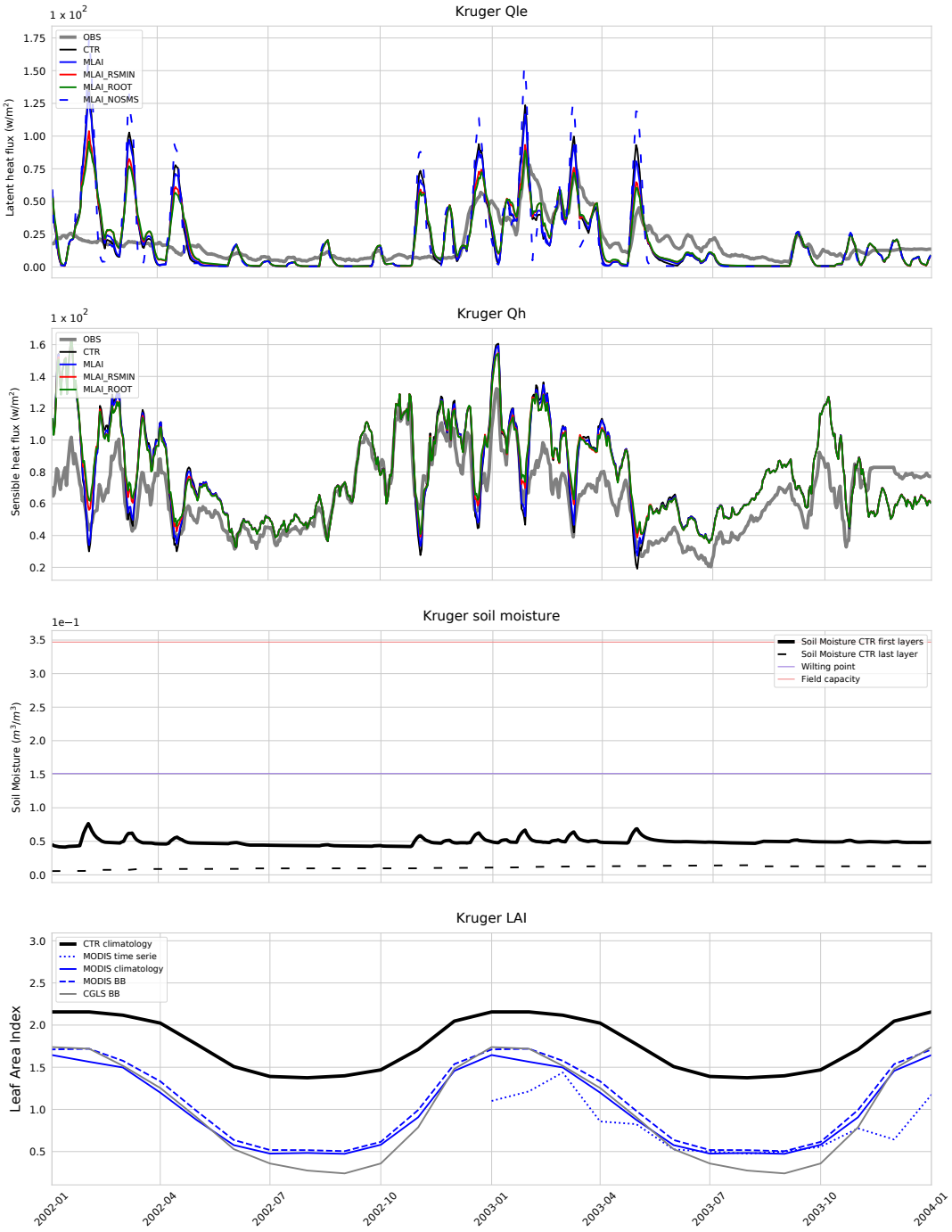

Figure A.4: As Figure A.1 but for Kruger station.

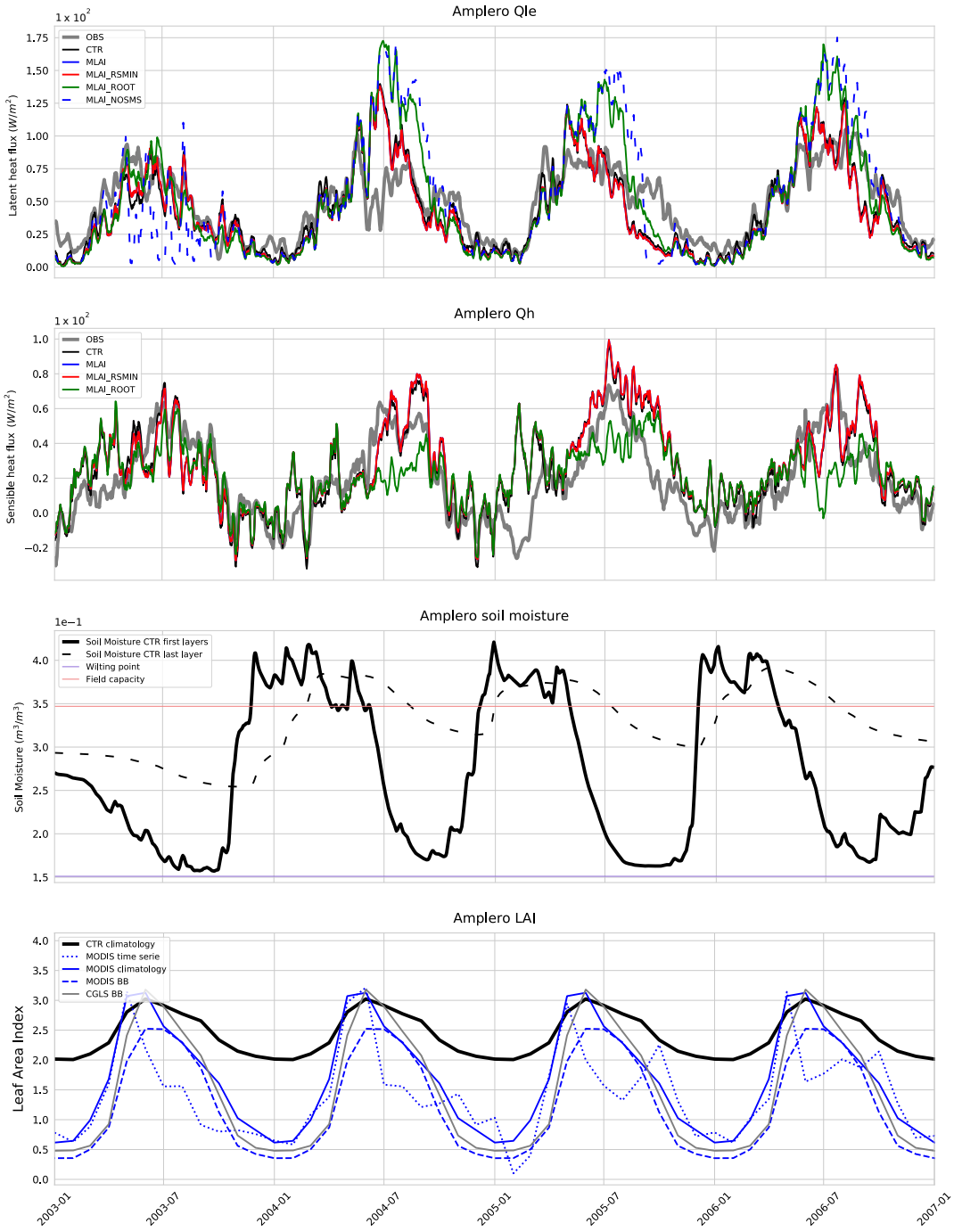

Figure A.5: As Figure A.1 but for Amplero station.

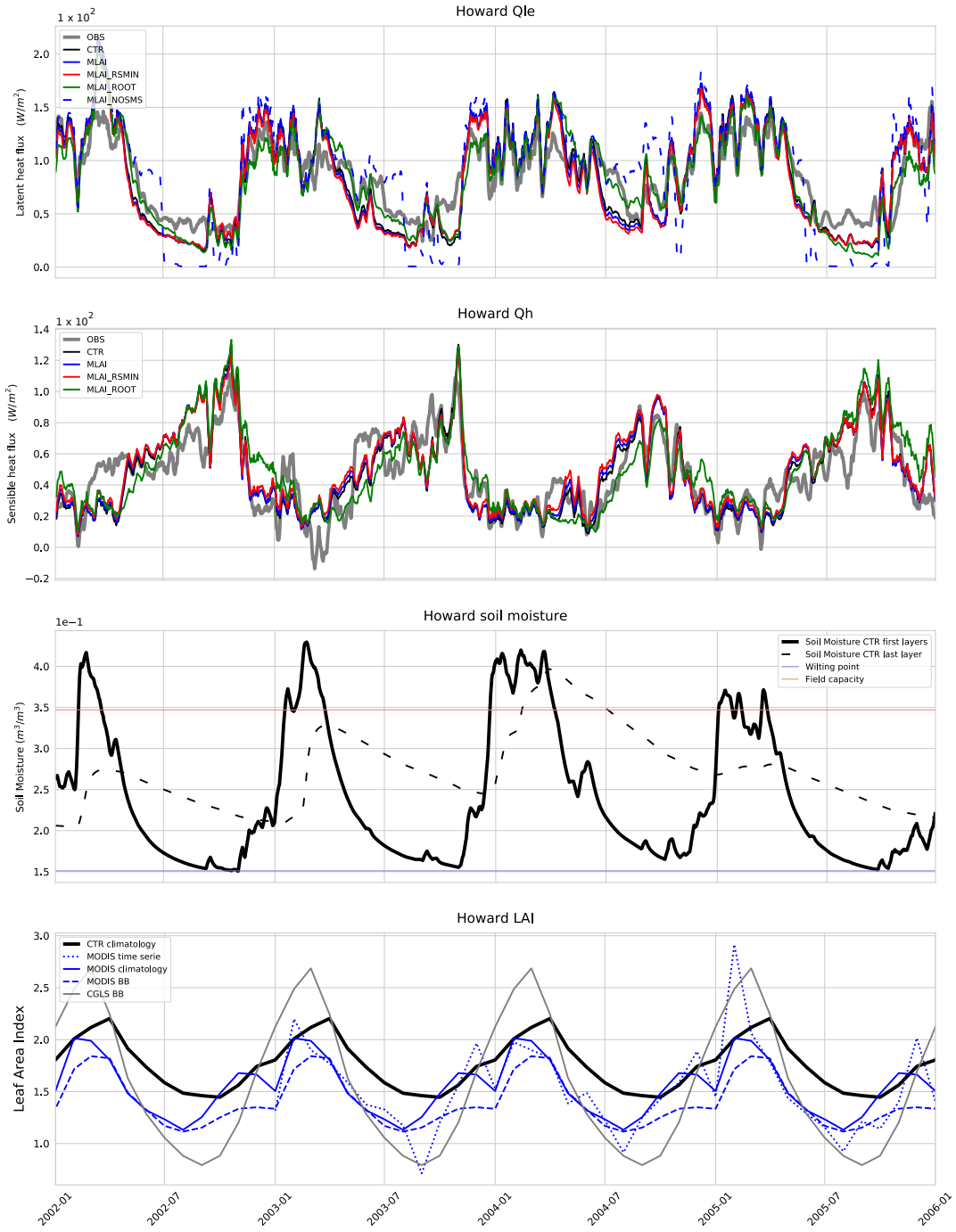

Figure A.6: As Figure A.1 but for Howard station.

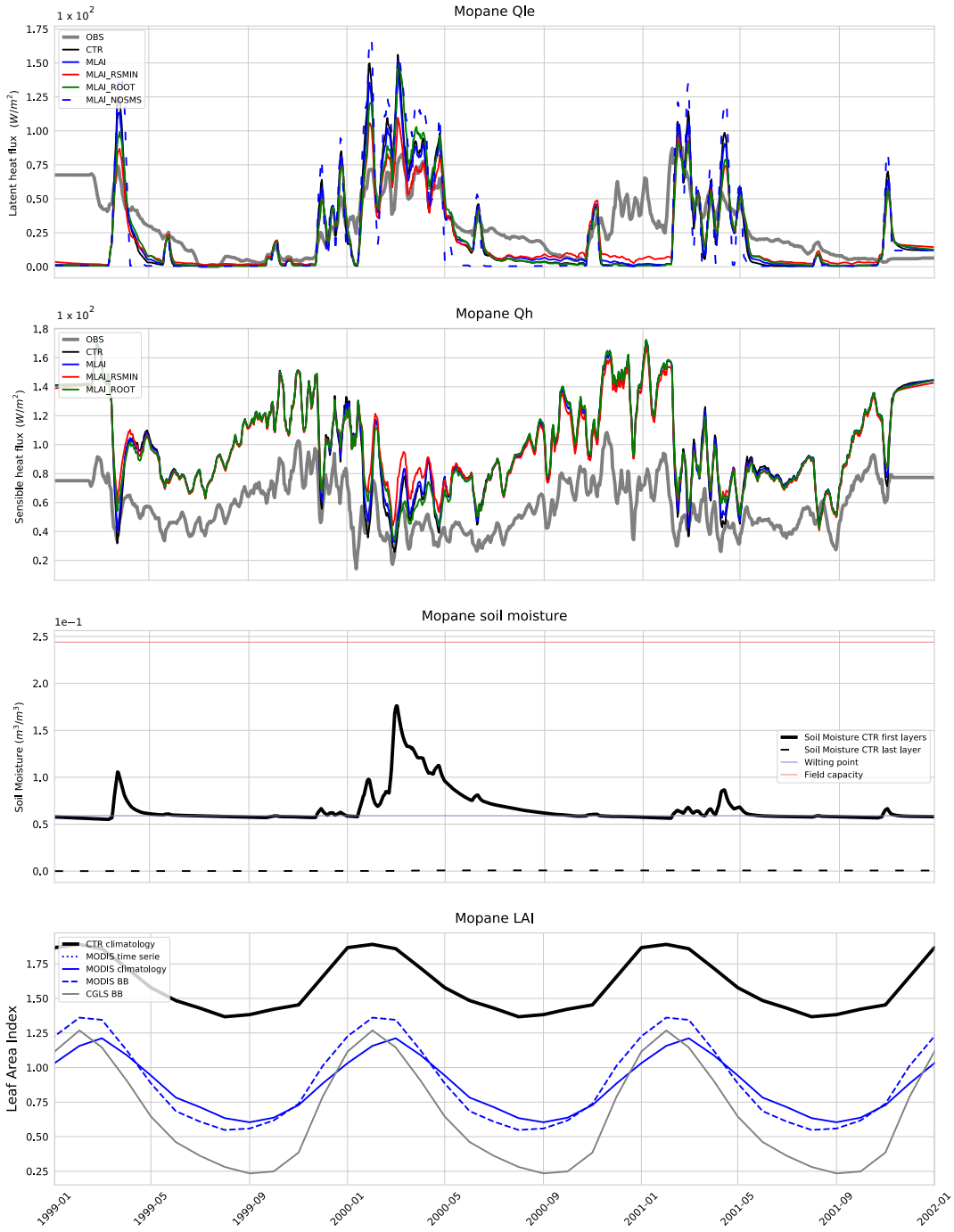

Figure A.7: As Figure A.1 but for Mopane station.

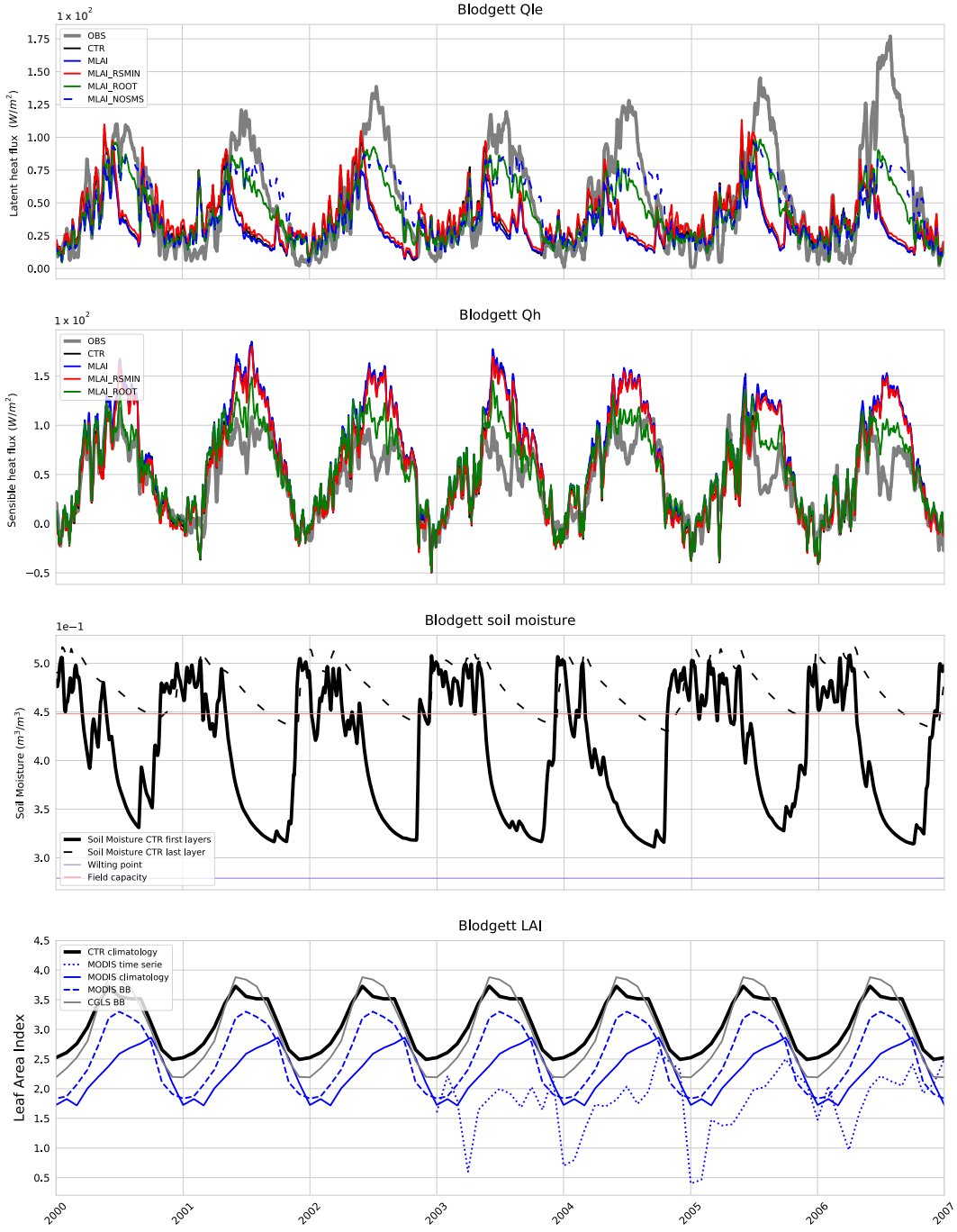

Figure A.8: As Figure A.1 but for Blodgett station.

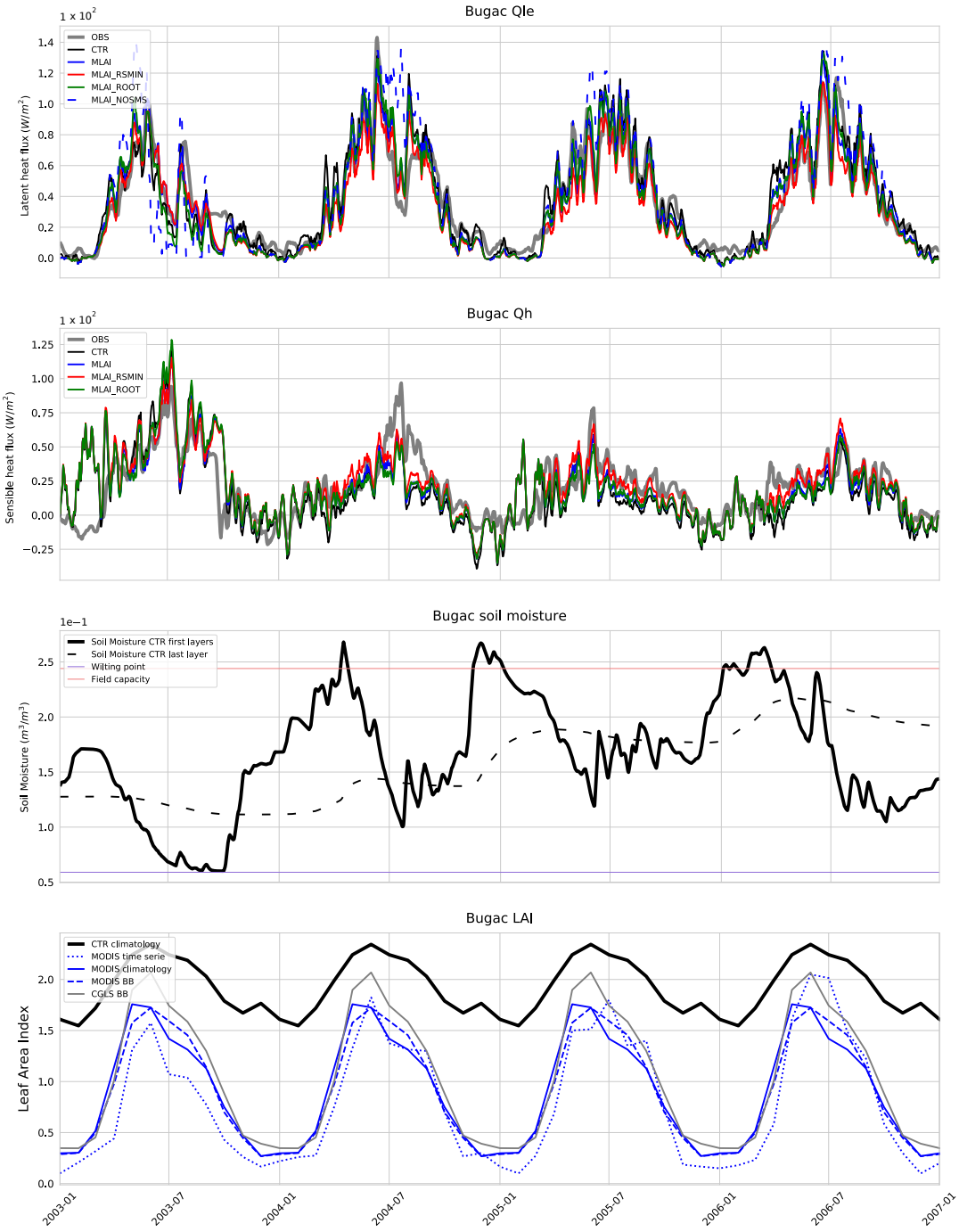

Figure A.9: As Figure A.1 but for Bugac station.

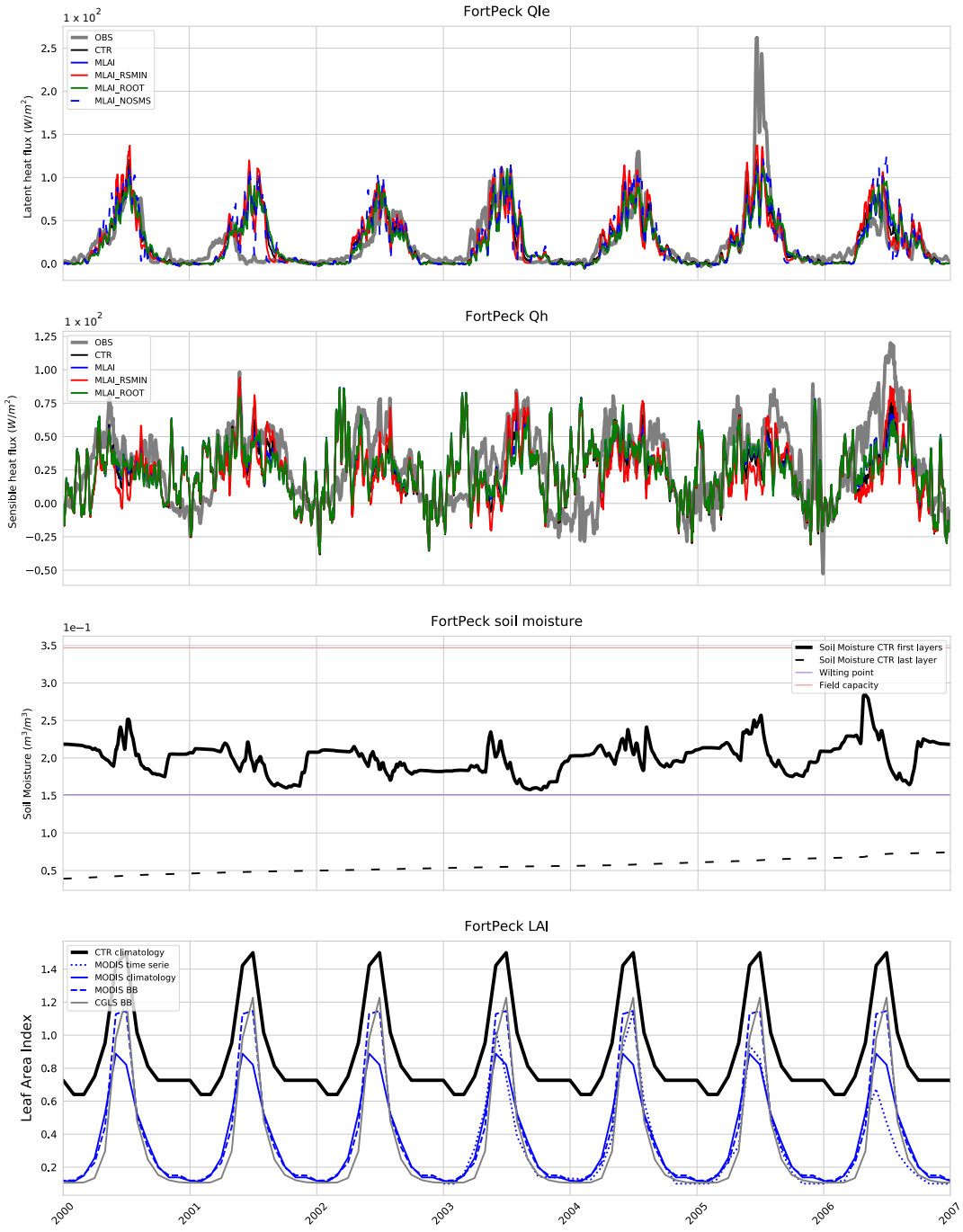

Figure A.10: As Figure A.1 but for Fort Peck station.

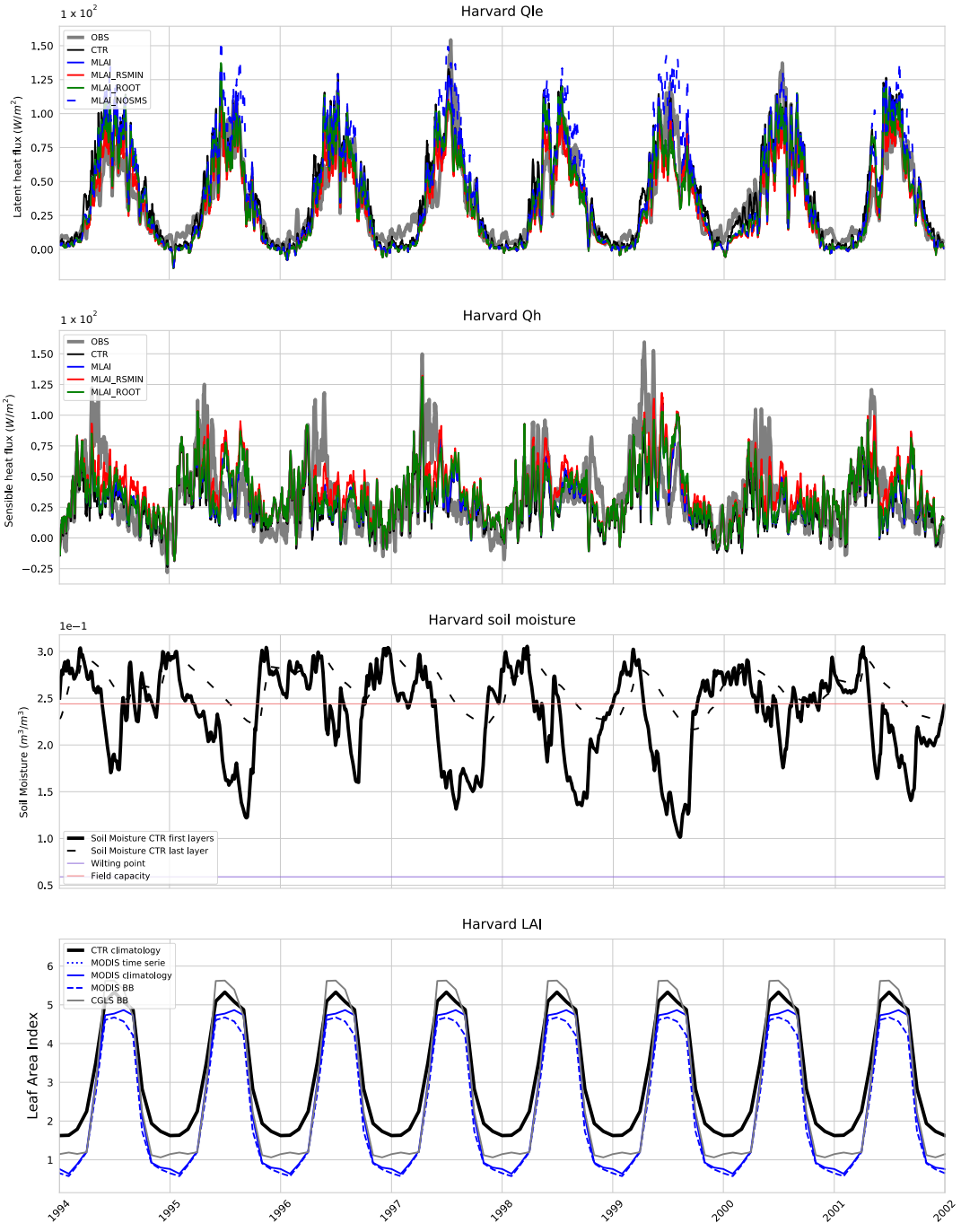

Figure A.11: As Figure A.1 but for Harvard station.

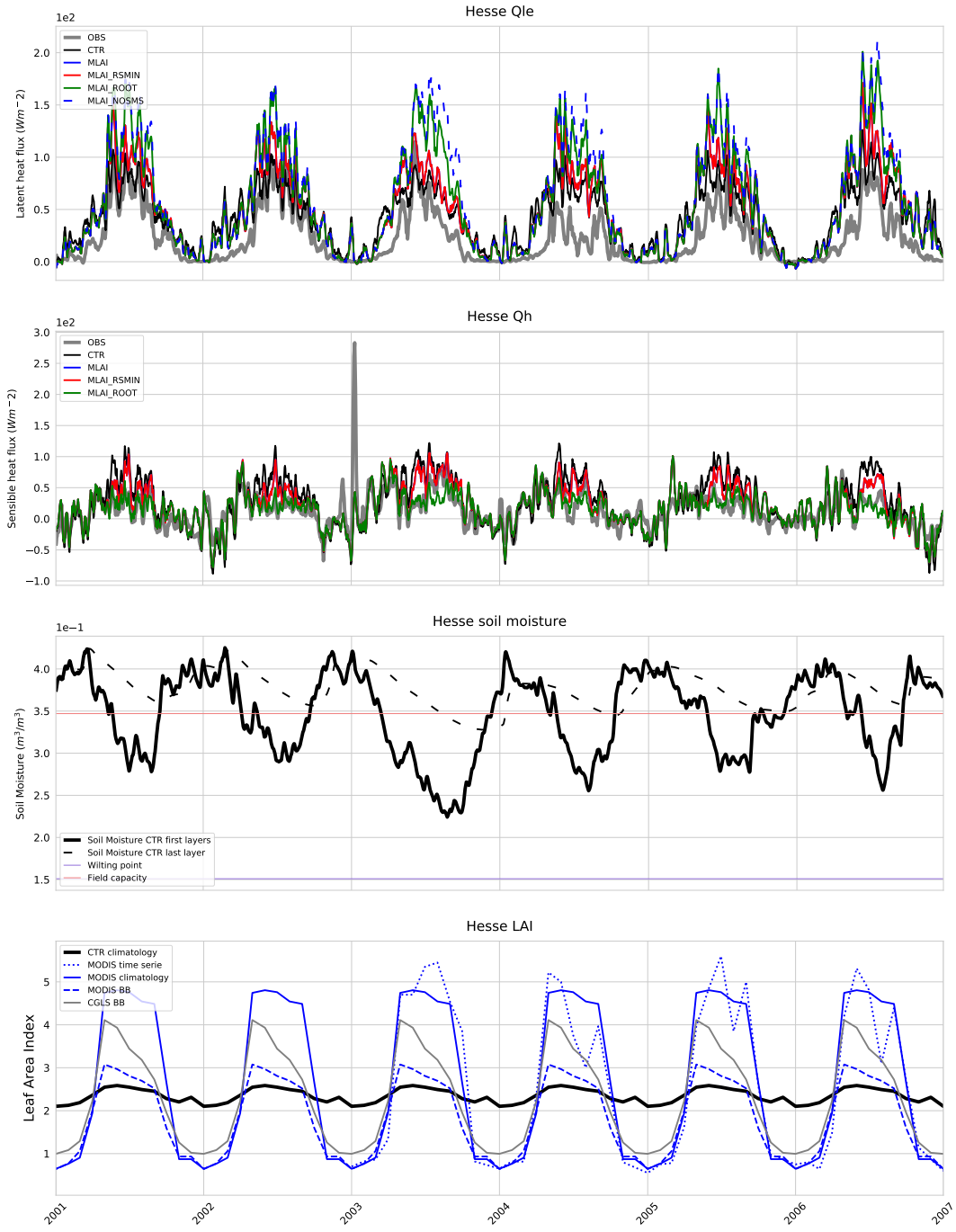

Figure A.12: As Figure A.1 but for Hesse station.

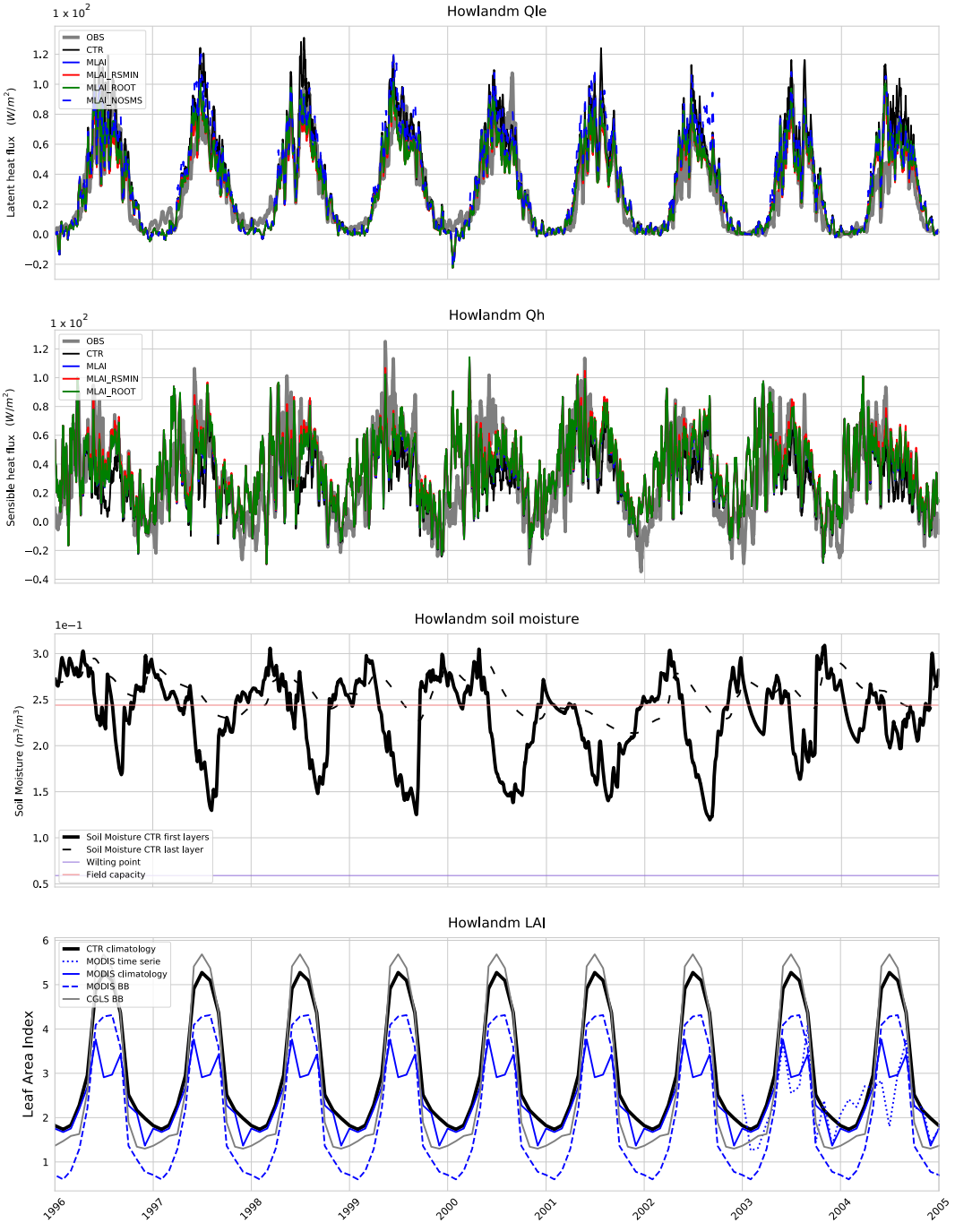

Figure A.13: As Figure A.1 but for Howlandm station.

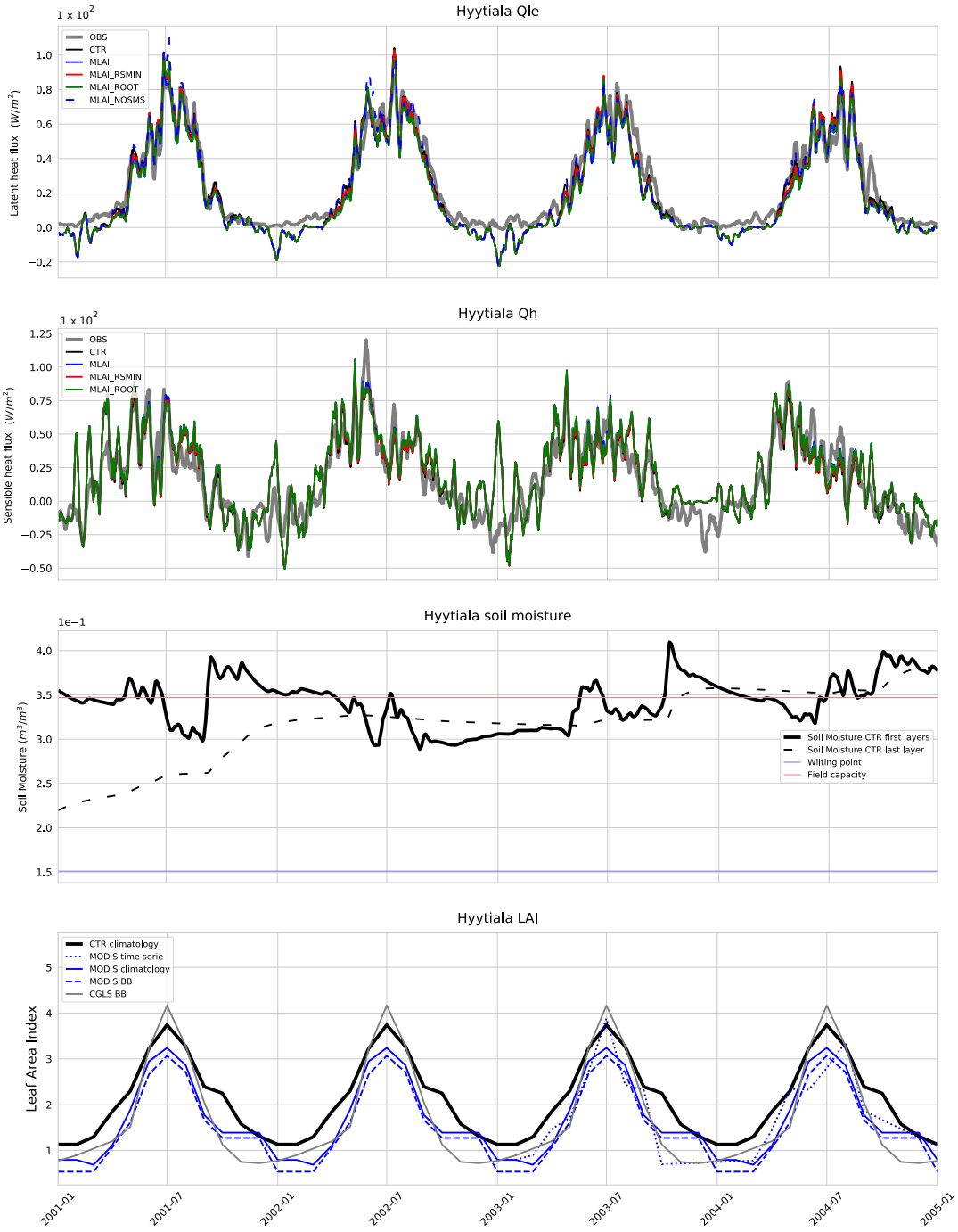

Figure A.14: As Figure A.1 but for Hyytiala station.

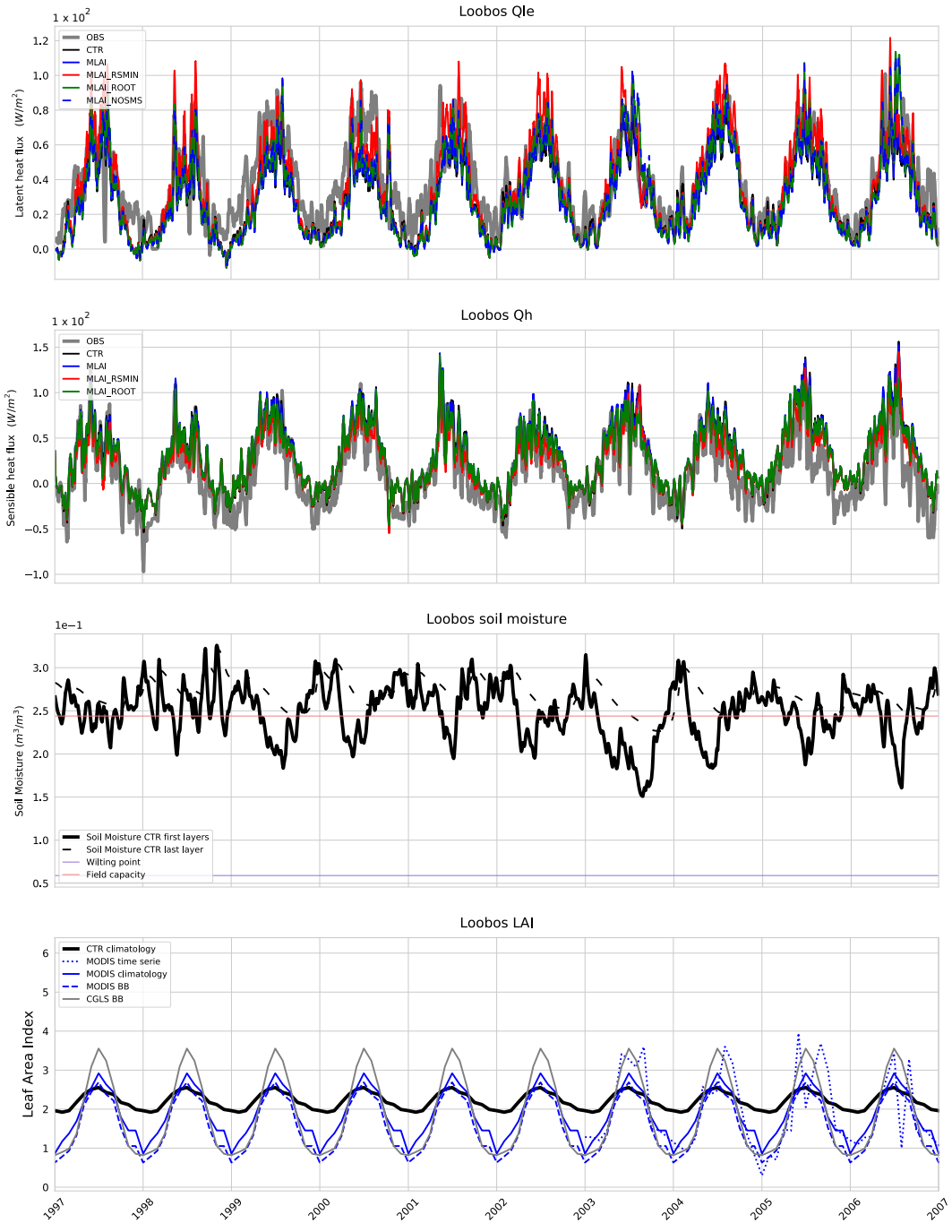

Figure A.15: As Figure A.1 but for Loobos station.

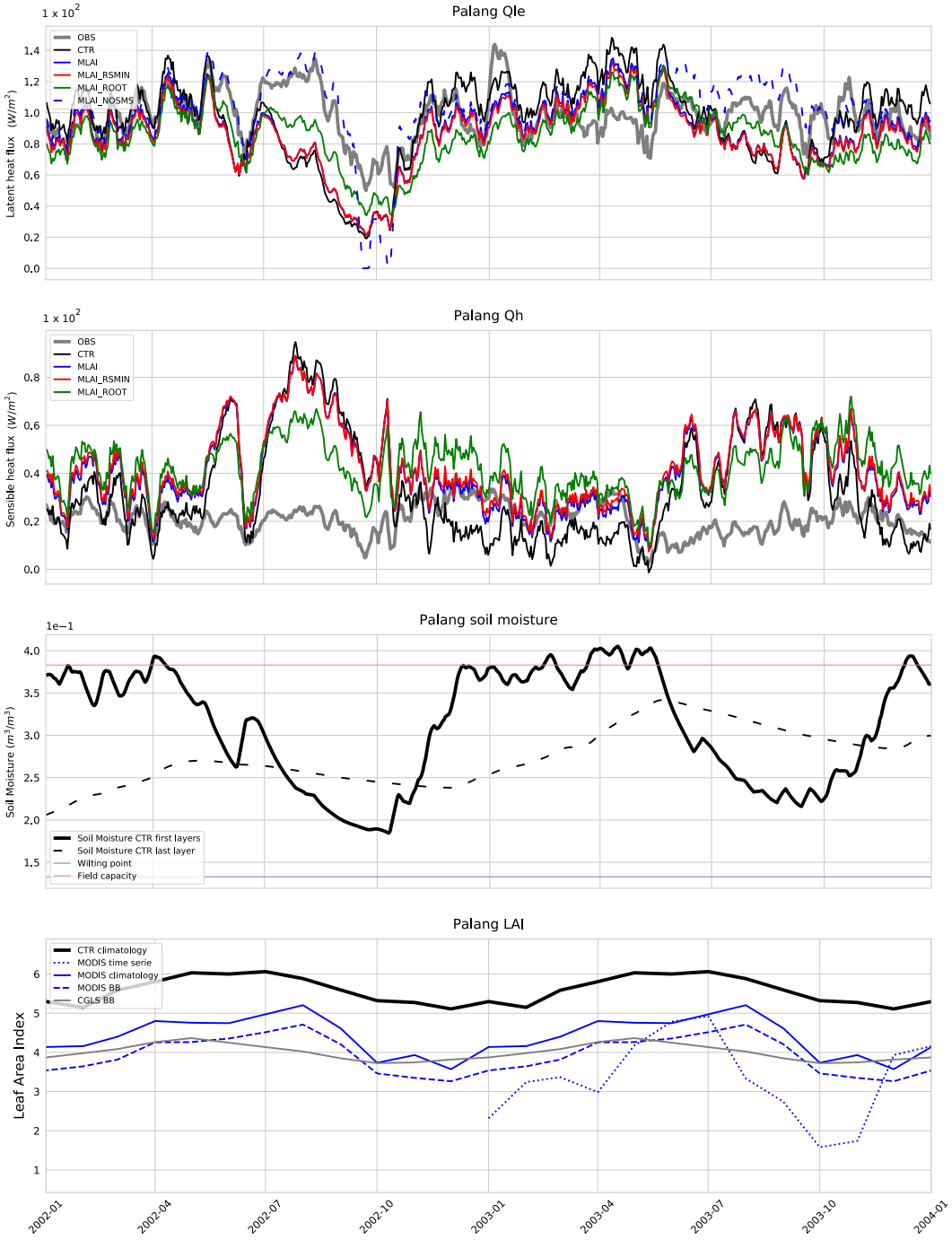

Figure A.16: As Figure A.1 but for Palang station.

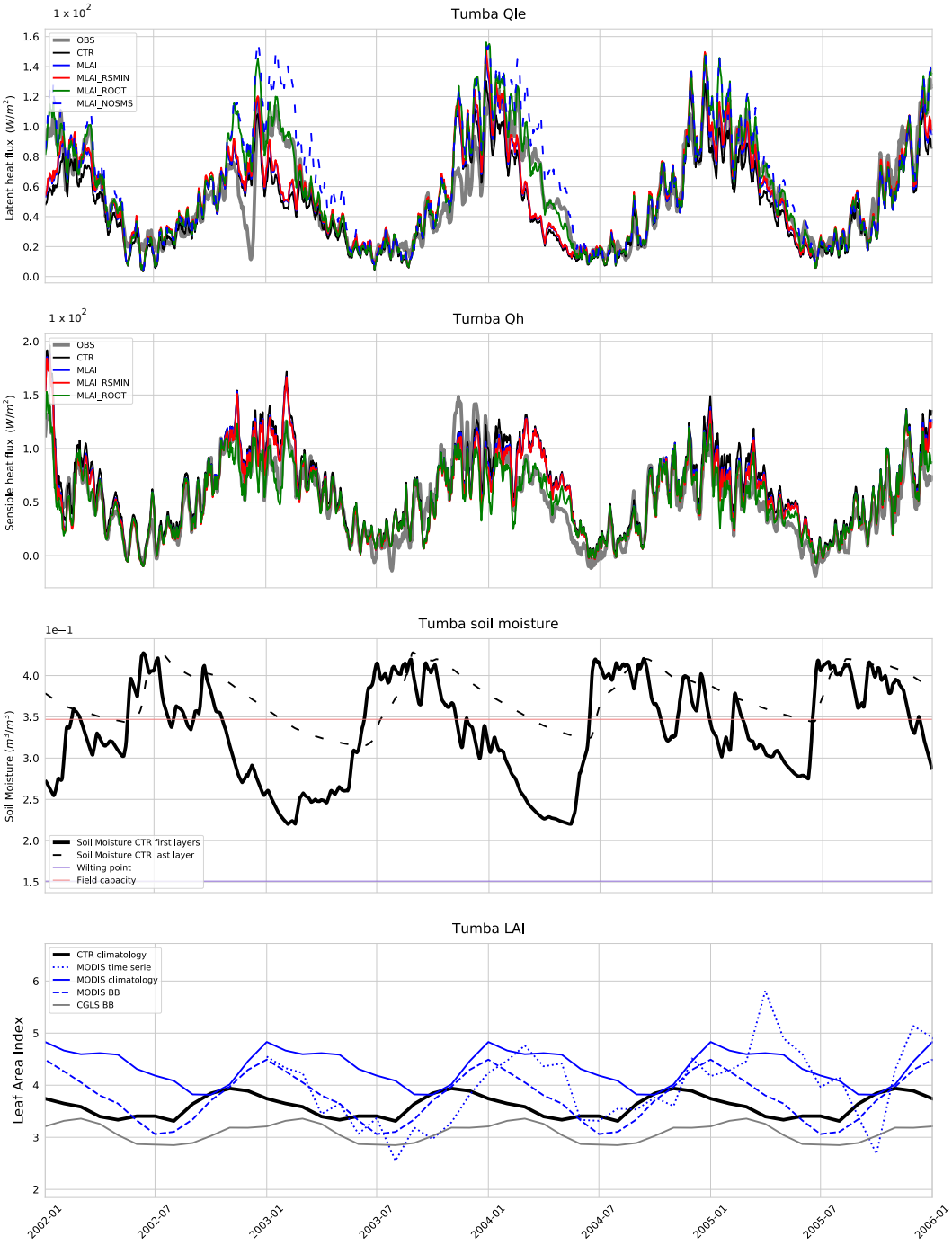

Figure A.17: As Figure A.1 but for Tumbarumba station.

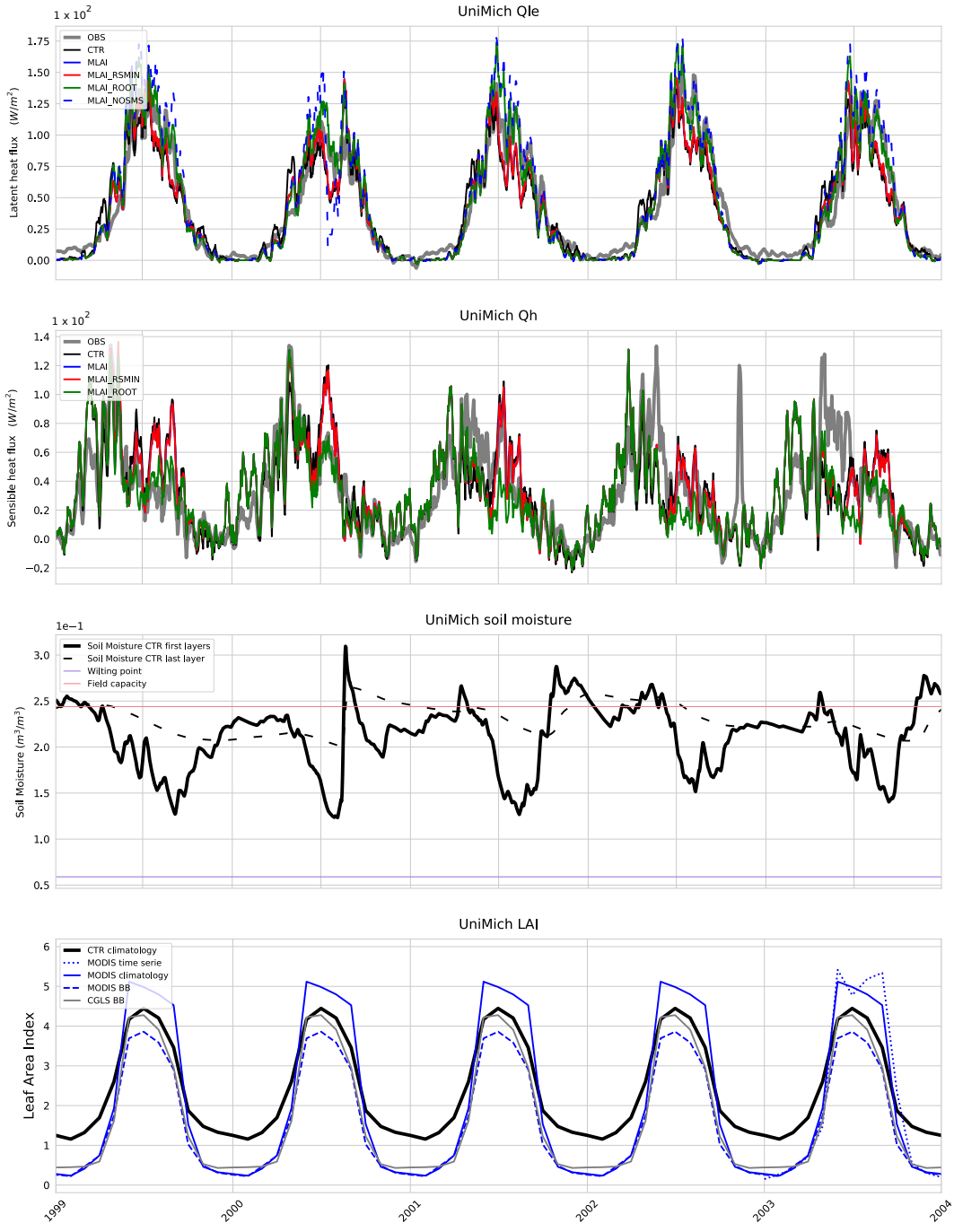

Figure A.18: As Figure A.1 but for University of Michigan station.

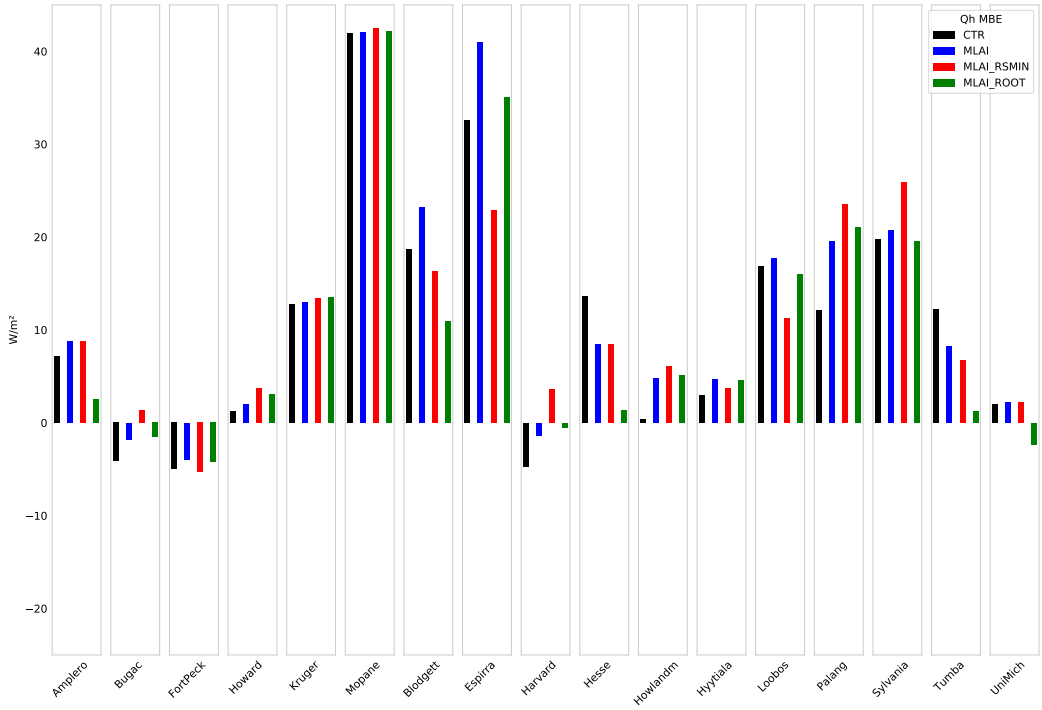

Figure A.19: Sensible heat flux MBE in the 17 stations for each simulation: CTR, MLAI, MLAI_RSMIN and MLAI_ROOT.

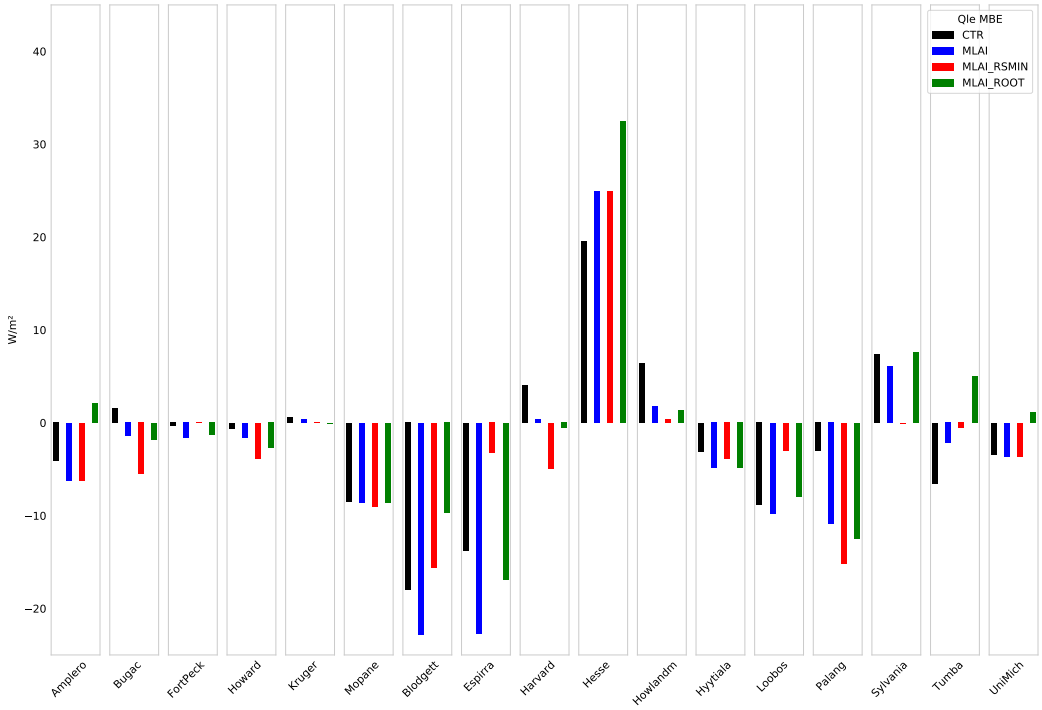

Figure A.20: Latent heat flux MBE in the 17 stations for each simulation: CTR, MLAI, MLAI_RSMIN and MLAI_ROOT.

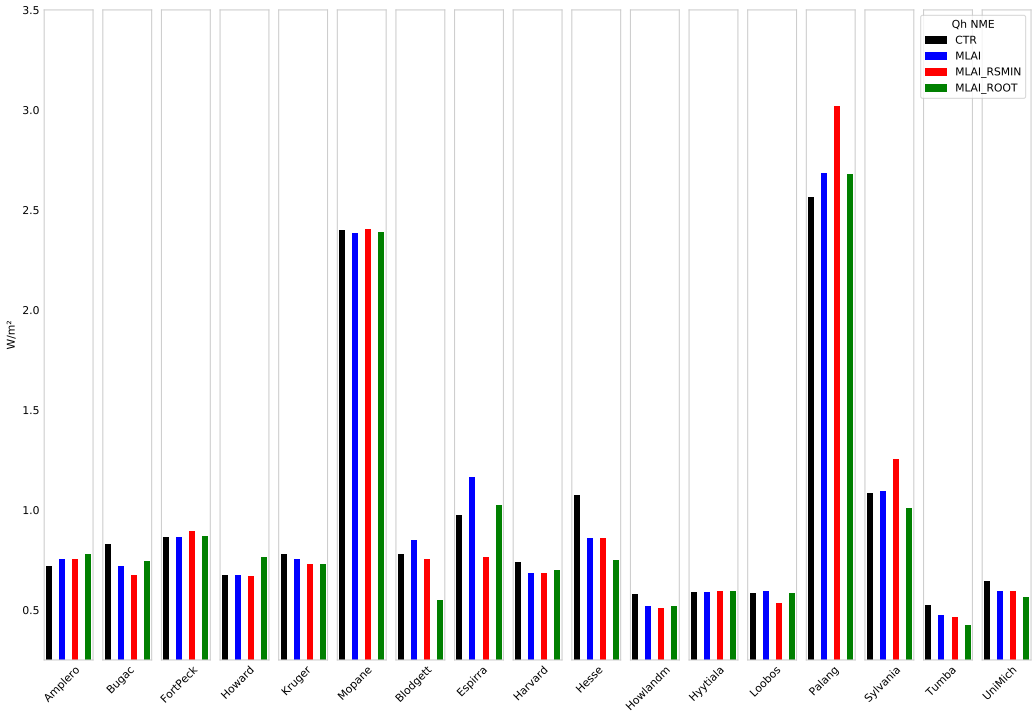

Figure A.21: Sensible heat flux NME in the 17 stations for each simulation: CTR, MLAI, MLAI_RSMIN and MLAI_ROOT.

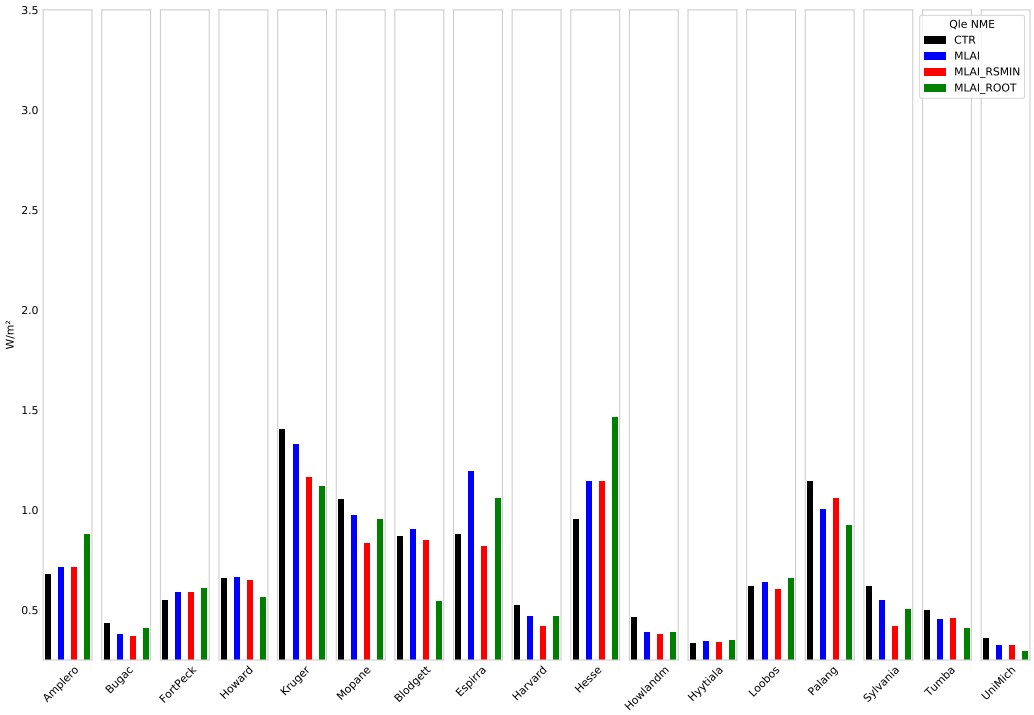

Figure A.22: Latent heat flux NME in the 17 stations for each simulation: CTR, MLAI, MLAI_RSMIN and MLAI_ROOT.

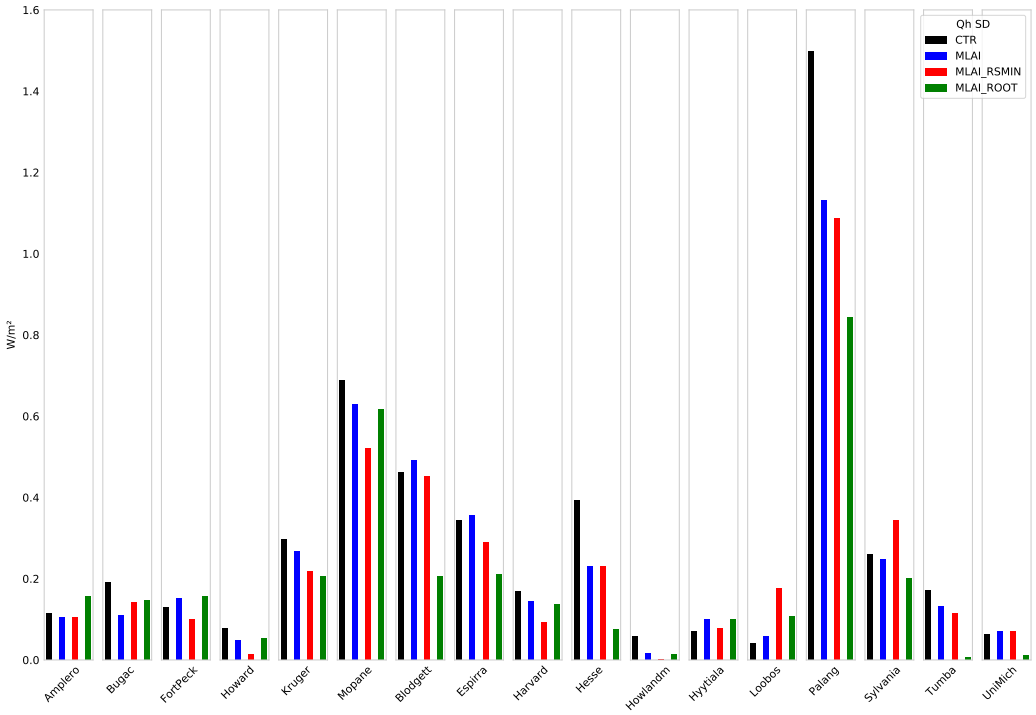

Figure A.23: Sensible heat flux SD in the 17 stations for each simulation: CTR, MLAI, MLAI_RSMIN and MLAI_ROOT.

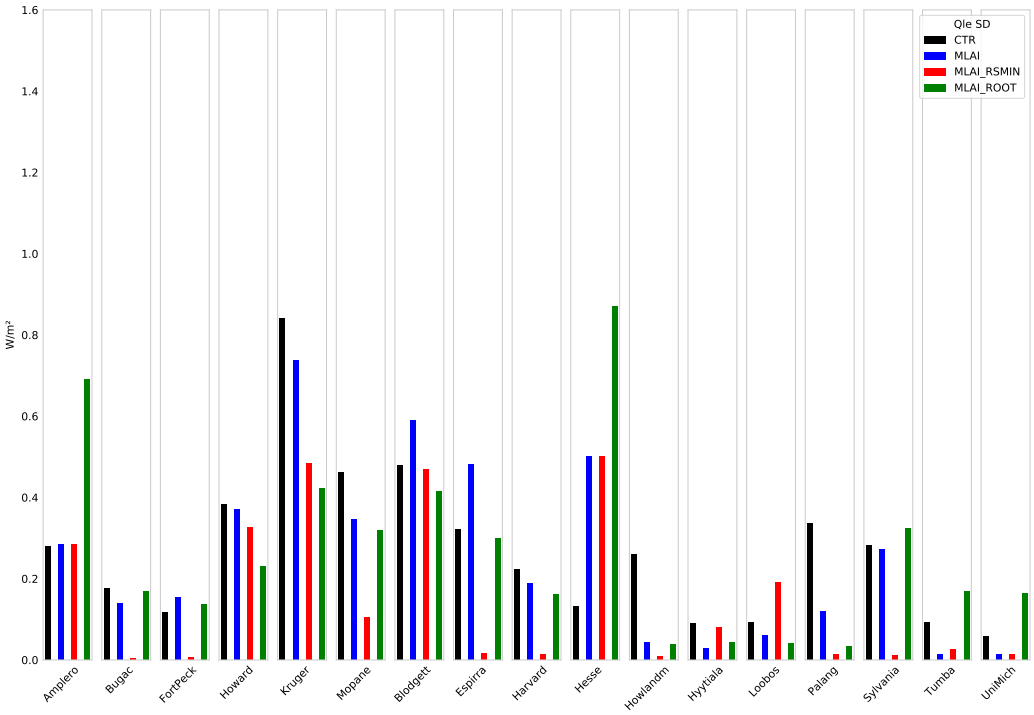

Figure A.24: Sensible heat flux SD in the 17 stations for each simulation: CTR, MLAI, MLAI_RSMIN and MLAI_ROOT.

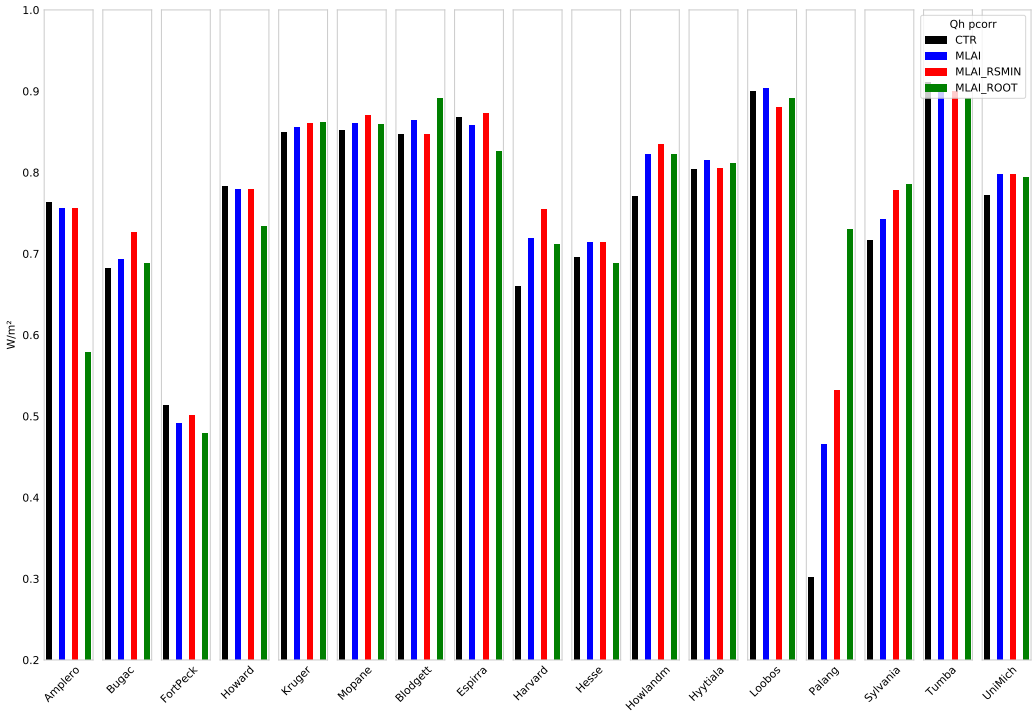

Figure A.25: Sensible heat flux correlation in the 17 stations for each simulation: CTR, MLAI, MLAI_RSMIN and MLAI_ROOT.

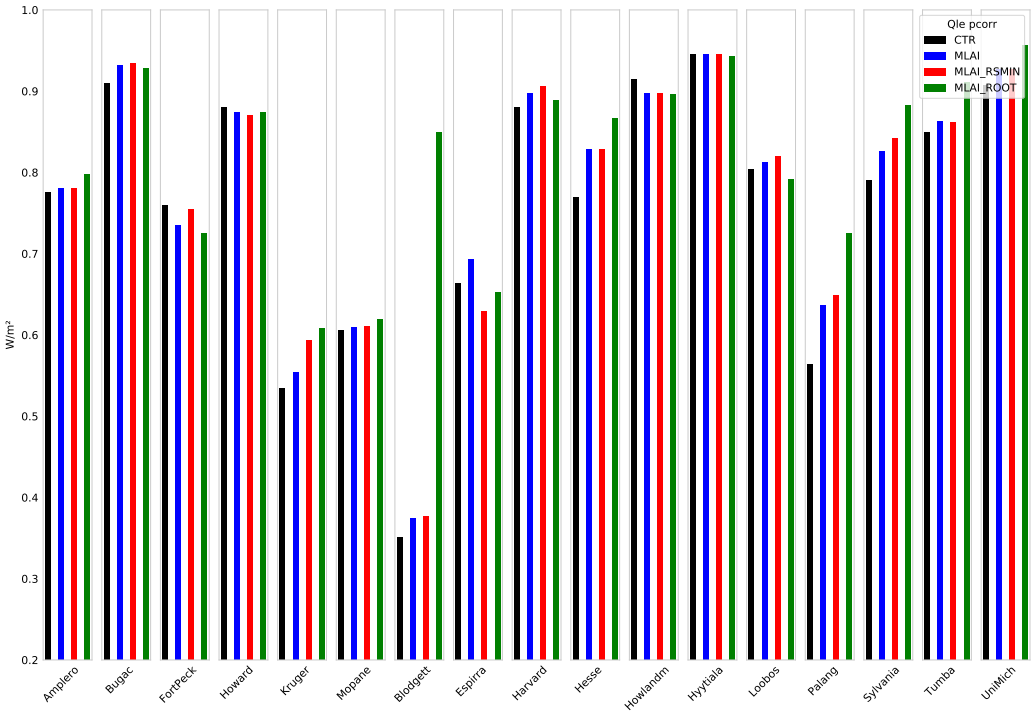

Figure A.26: Latent heat flux correlation in the 17 stations for each simulation: CTR, MLAI, MLAI_RSMIN and MLAI_ROOT.

Appendix B

Supporting material of Chapter 3.

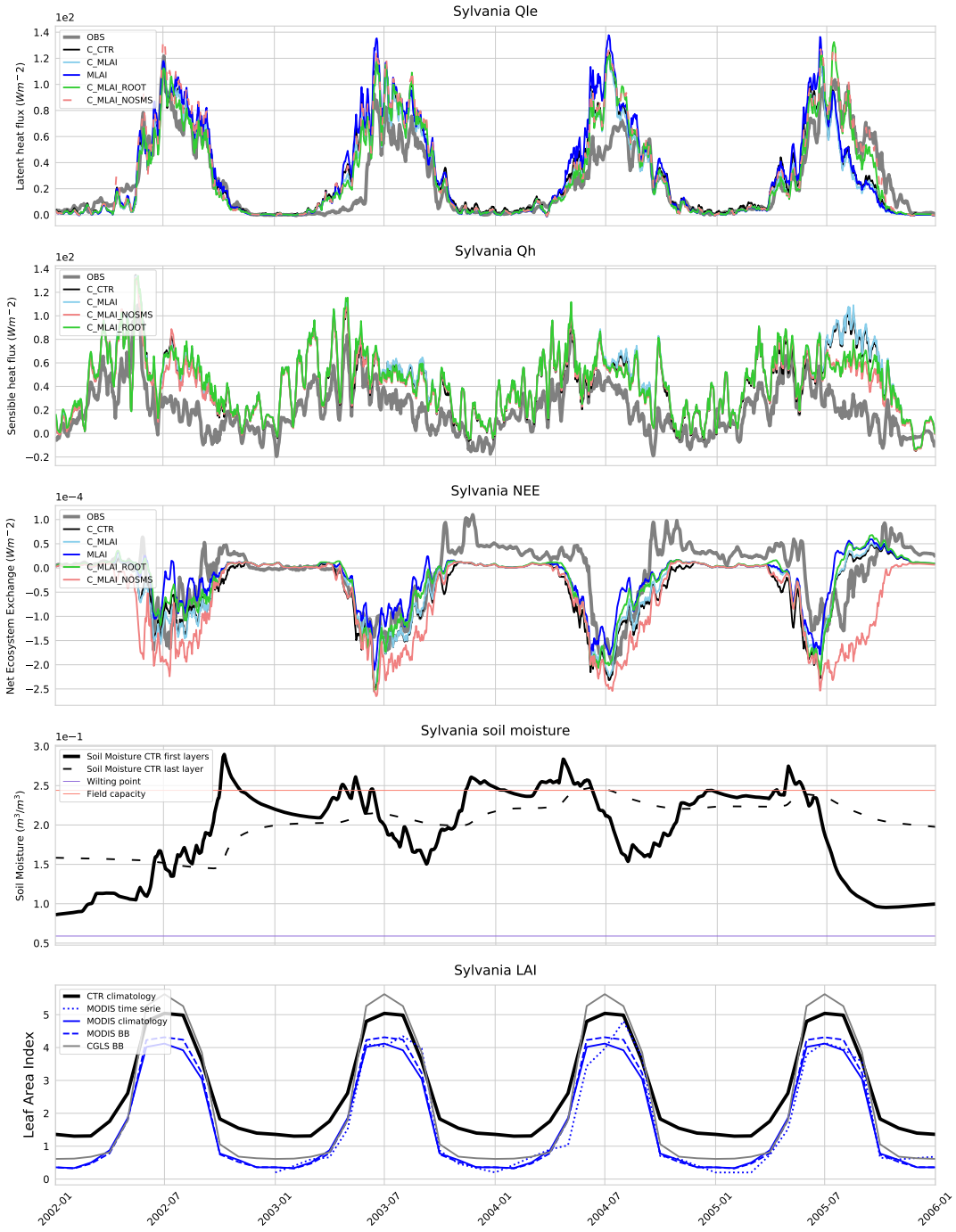

Figure B.2: As Figure B.1 but for Sylvania station.

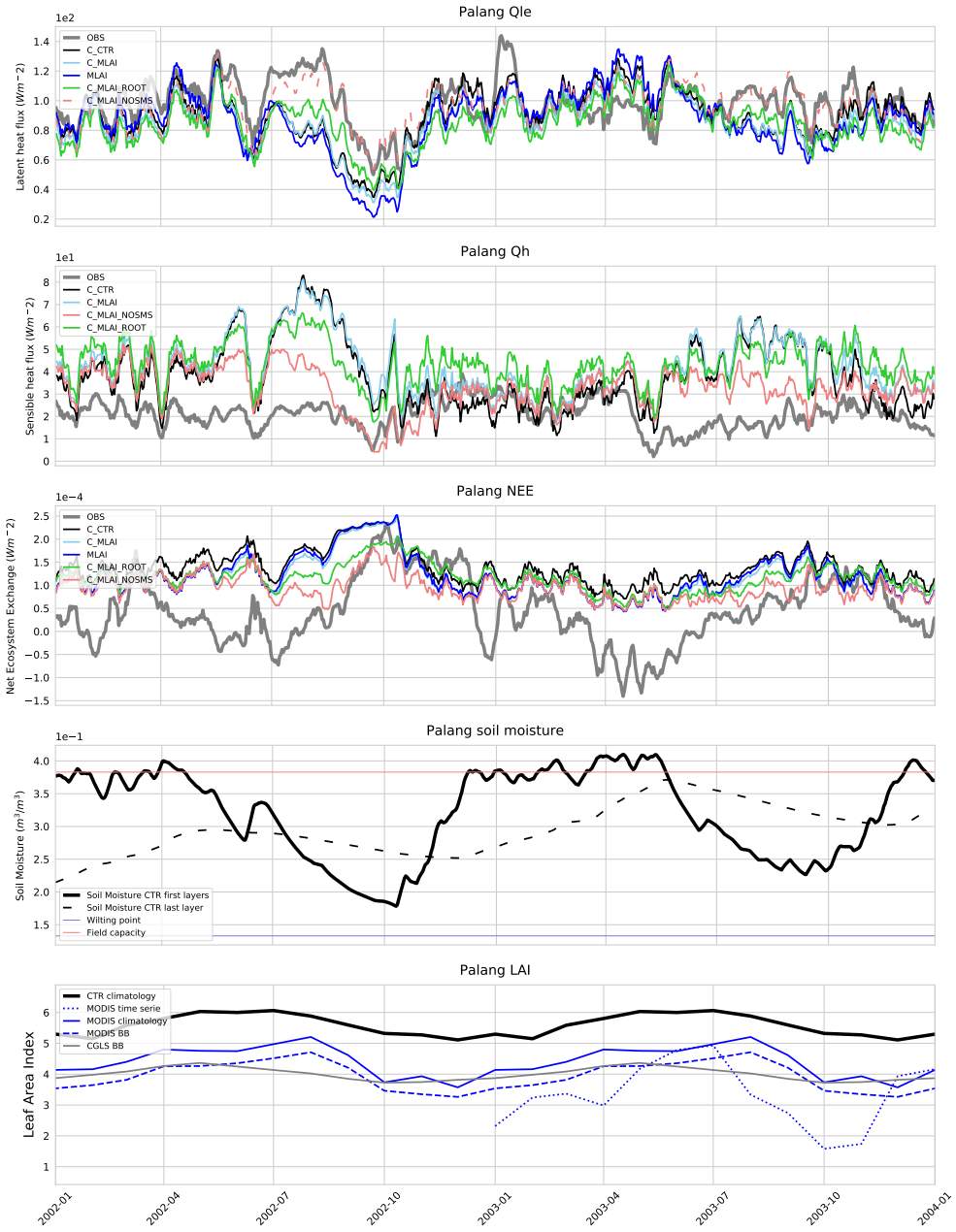

Figure B.1: Time series of Sensible heat flux, latent heat flux, soil moisture and LAI in Palang. The turbulent fluxes time series compare the observations (grey) with the simulations: C_CTR (black), C_MLAI (light blue), MLAI (blue), C_MLAI_ROOT (green) and C_MLAI_NOSMS (dashed red). The soil moisture time series shows the CTR top 3 layers meter soil moisture (top meter solid back) and the bottom layer soil moisture (dashed black) as well as the soil moisture at wilting point (blue) and field capacity (red). The LAI time series compares CTR (black) with the high resolution MODIS LAI time series (dotted blue), the high resolution MLAI and C_MLAI (blue), the climatology of MODIS considering the 0.25° bounding box (dashed blue) and CGLS LAI climatology (grey).

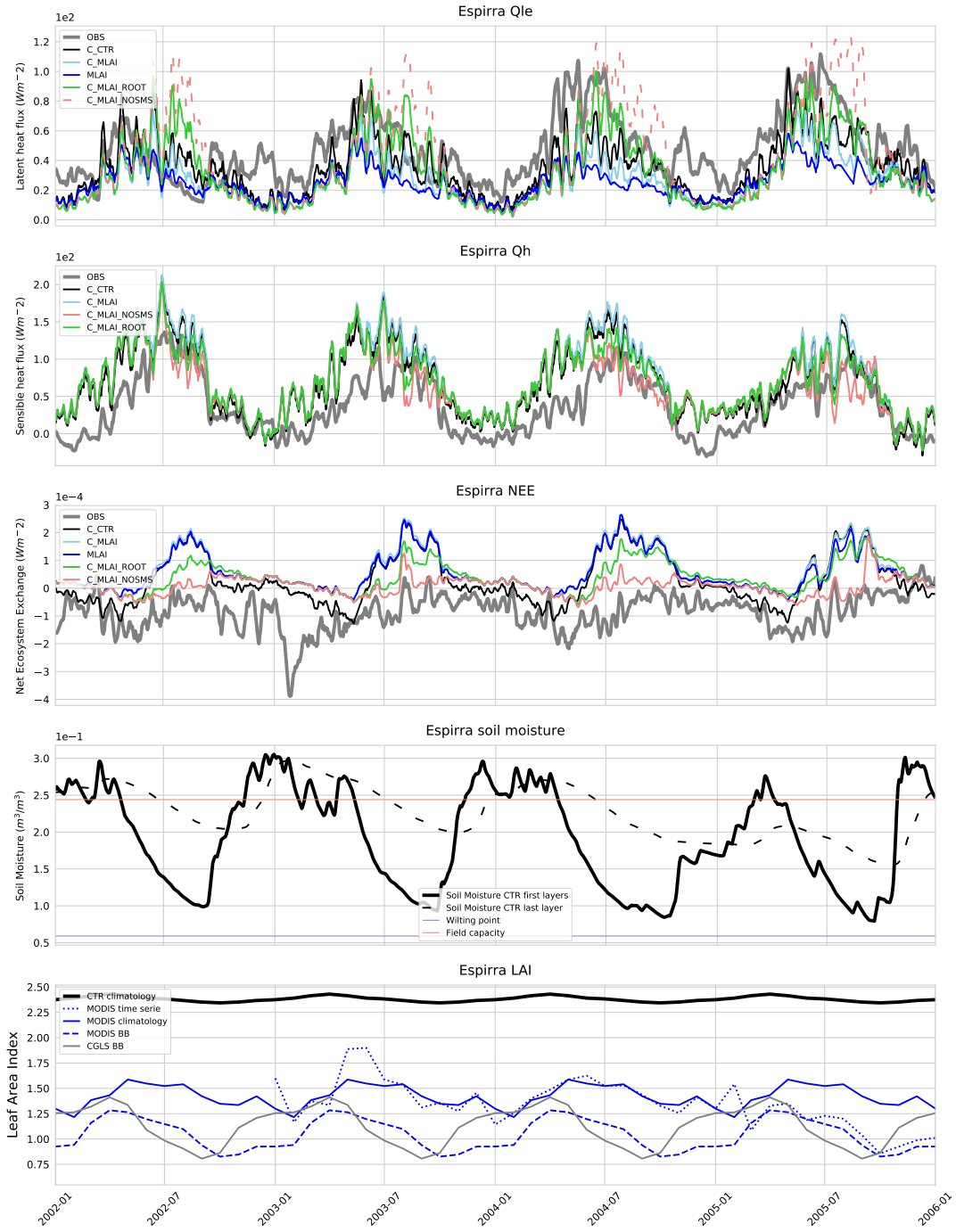

Figure B.3: As Figure B.1 but for Espirra station.

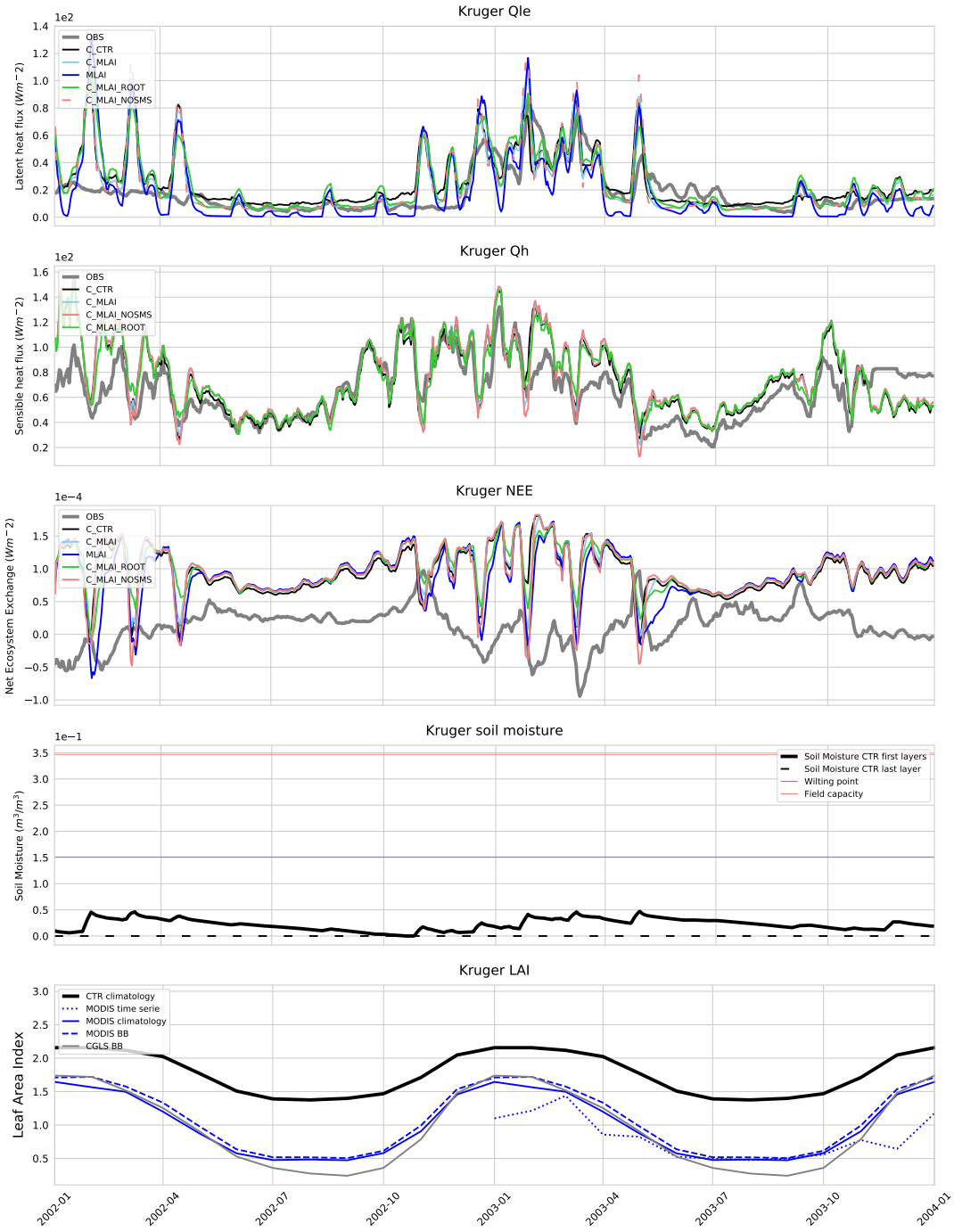

Figure B.4: As Figure B.1 but for Kruger station.

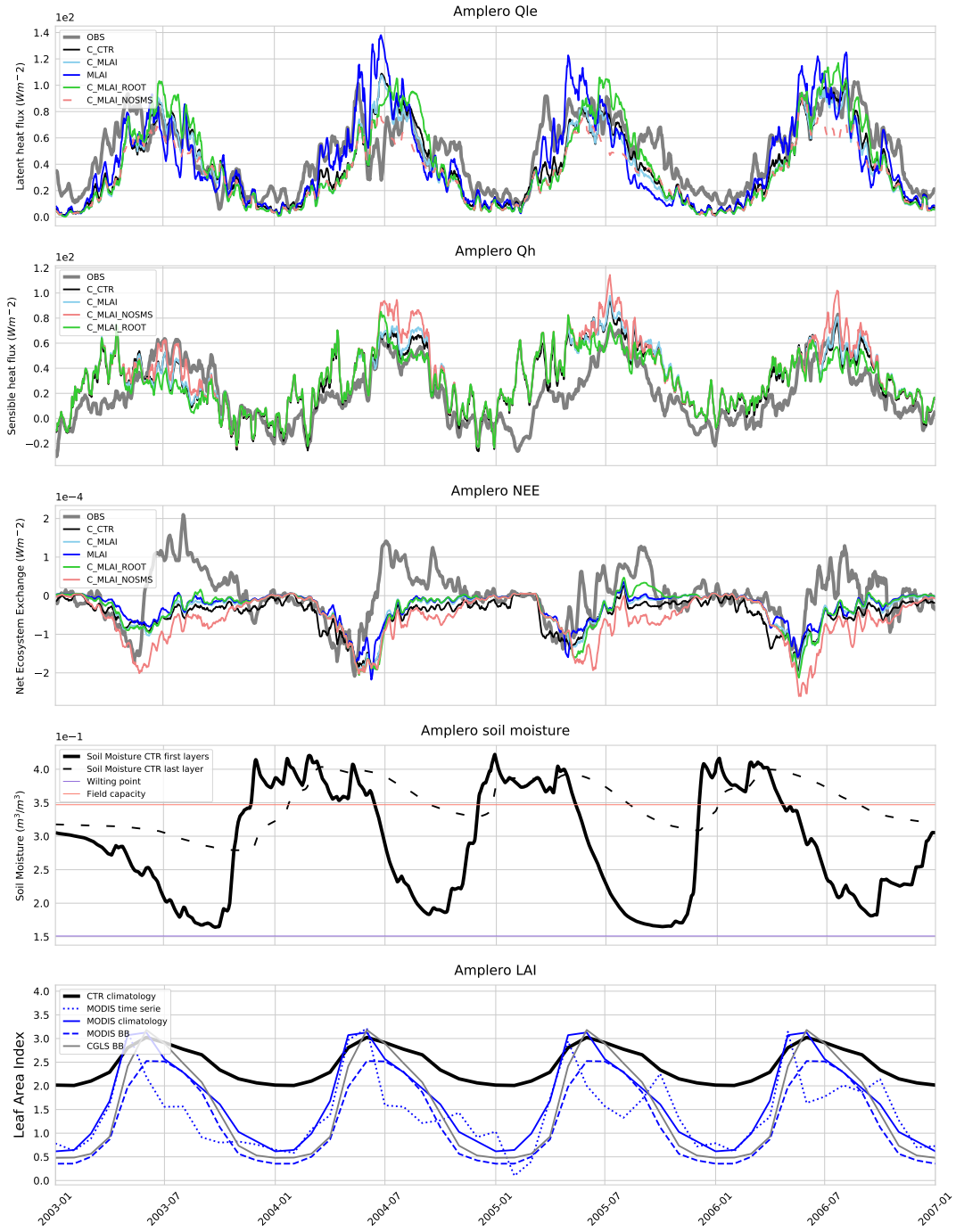

Figure B.5: As Figure B.1 but for Amplero station.

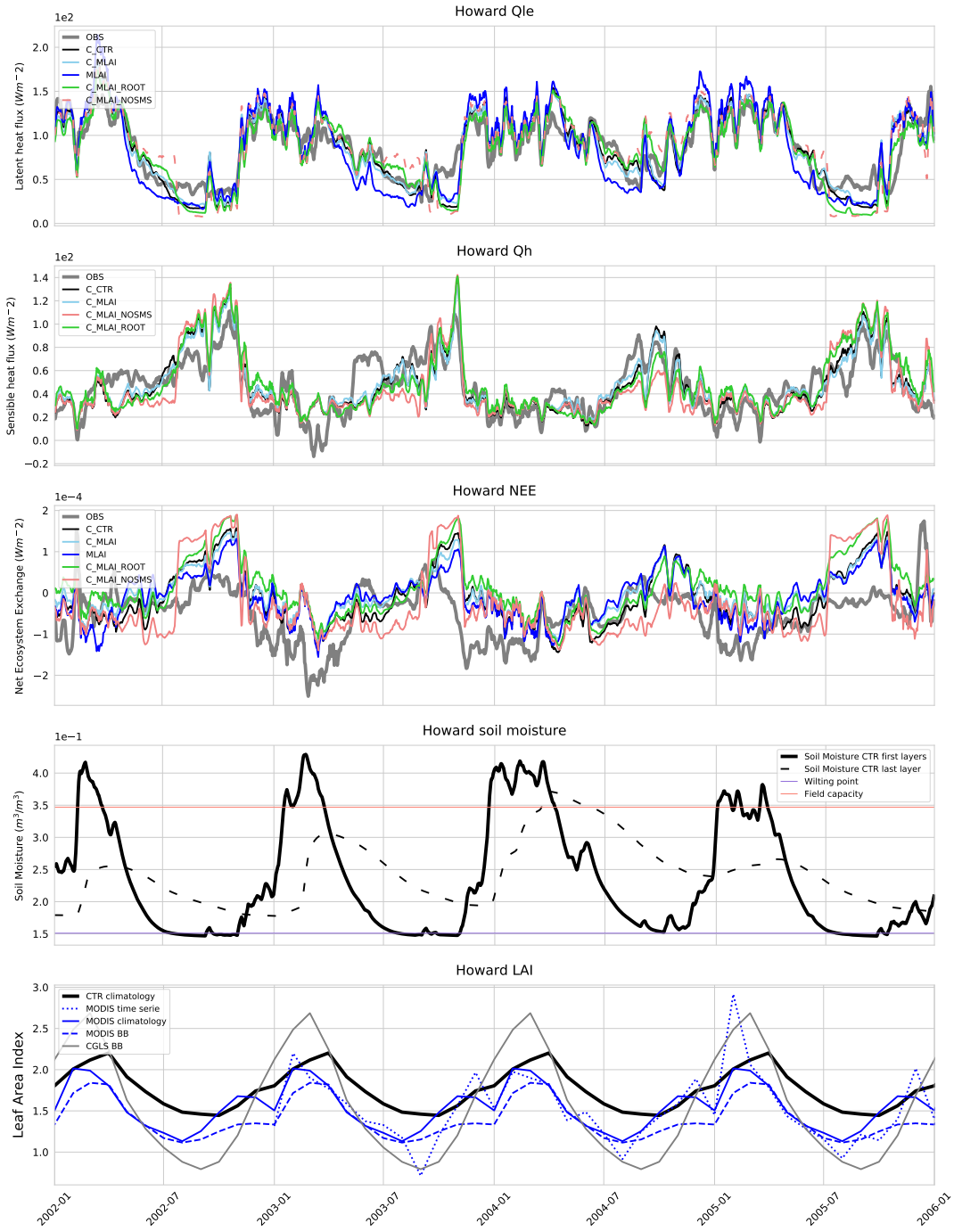

Figure B.6: As Figure B.1 but for Howard station.

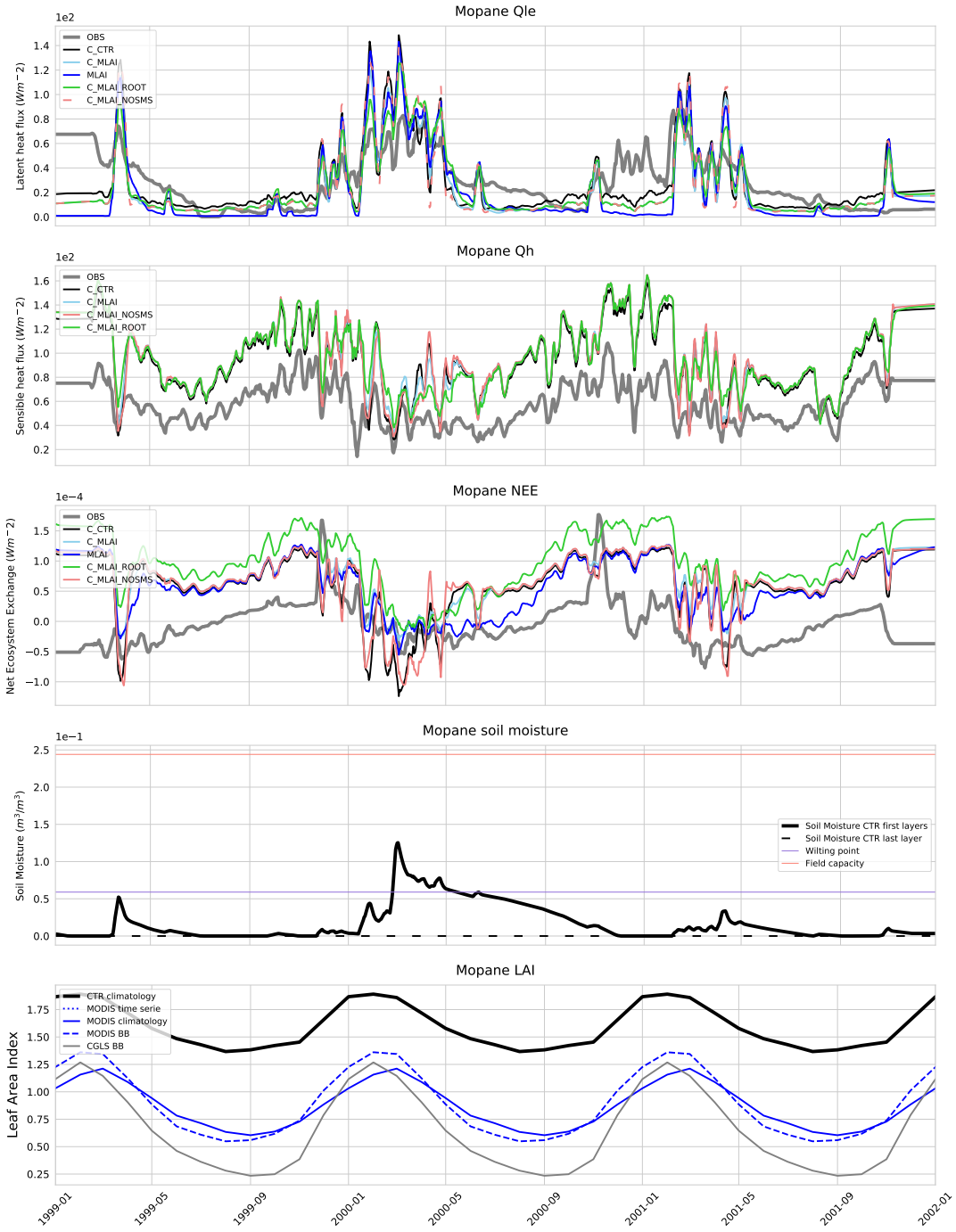

Figure B.7: As Figure B.1 but for Mopane station.

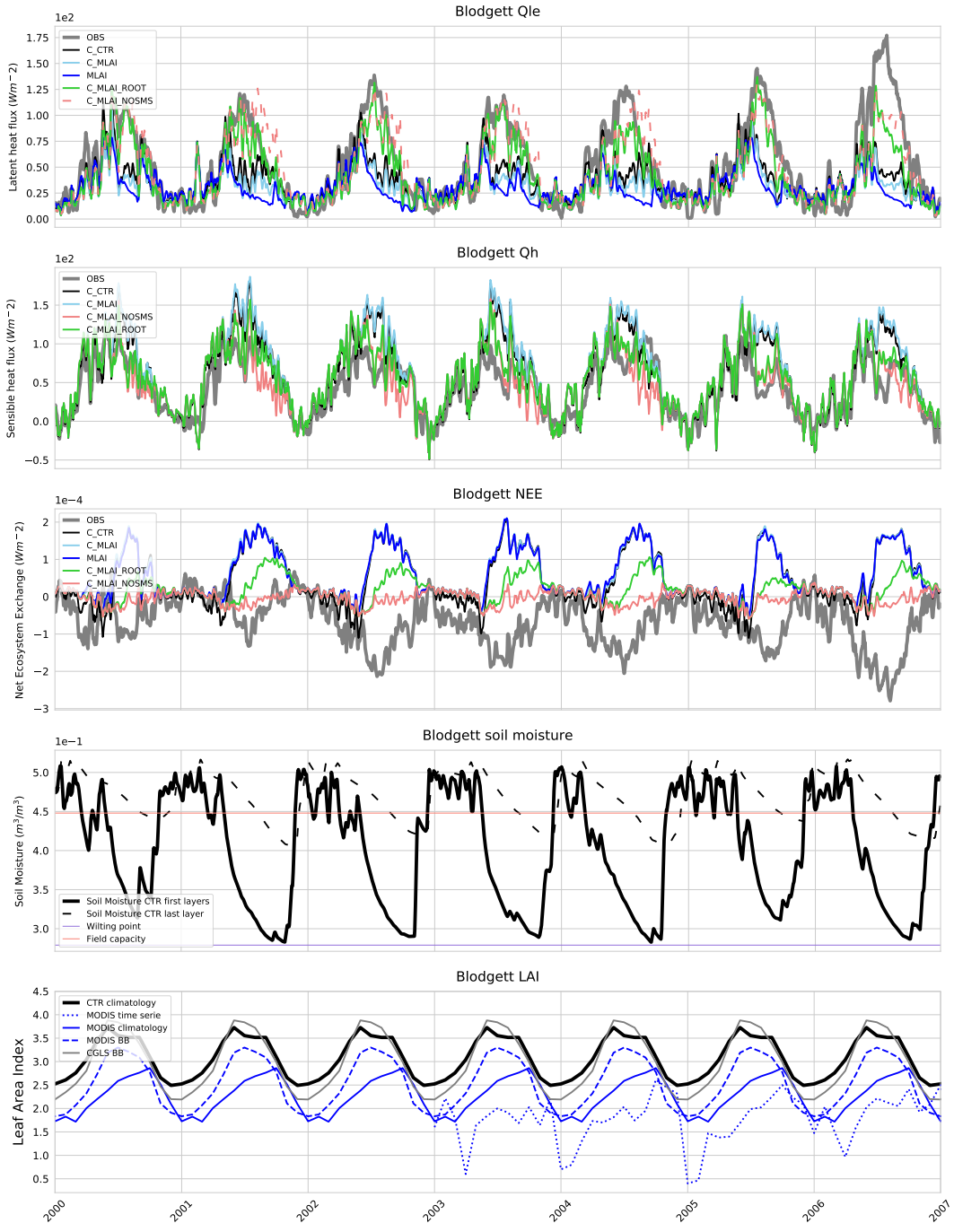

Figure B.8: As Figure B.1 but for Blodgett station.

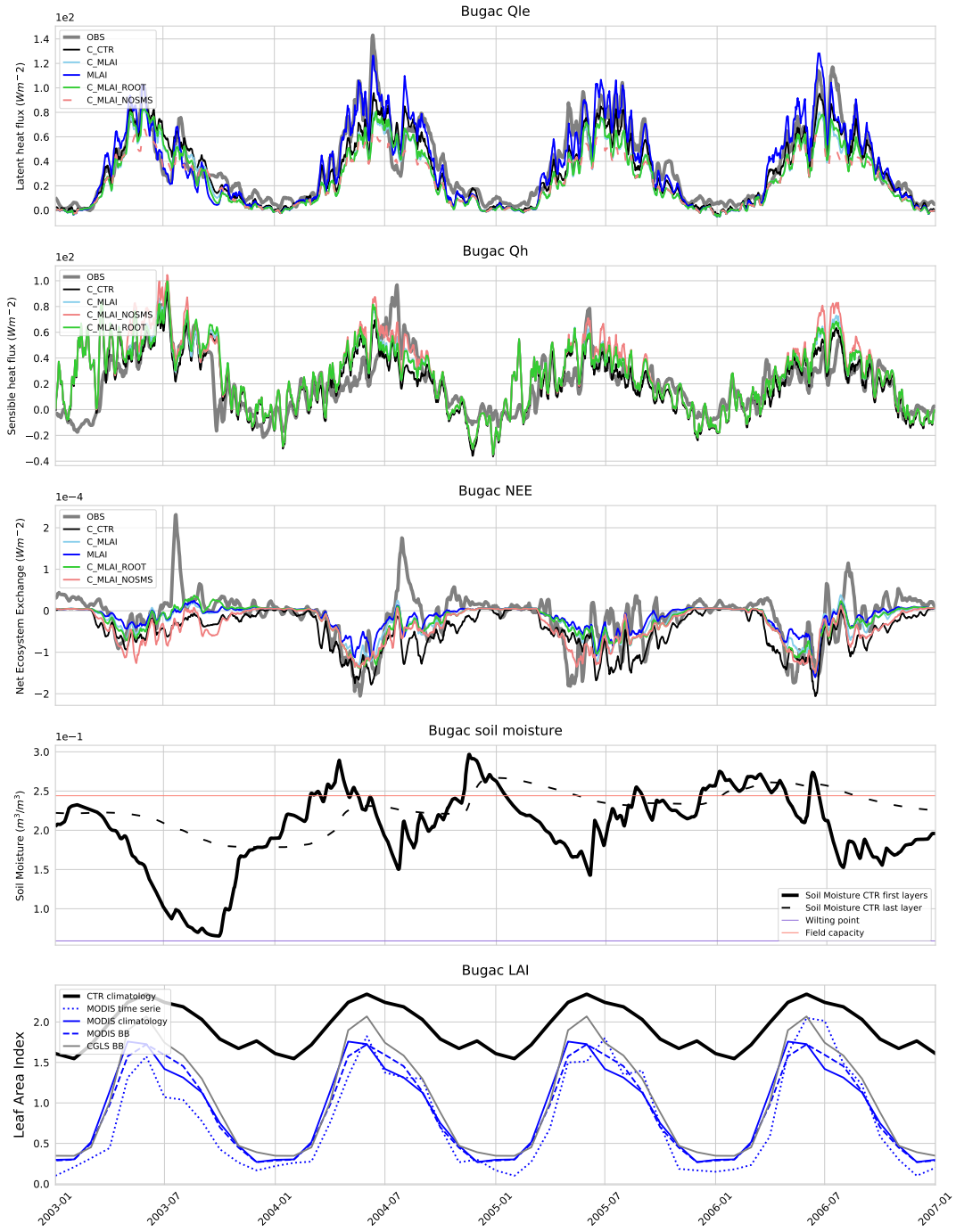

Figure B.9: As Figure B.1 but for Bugac station.

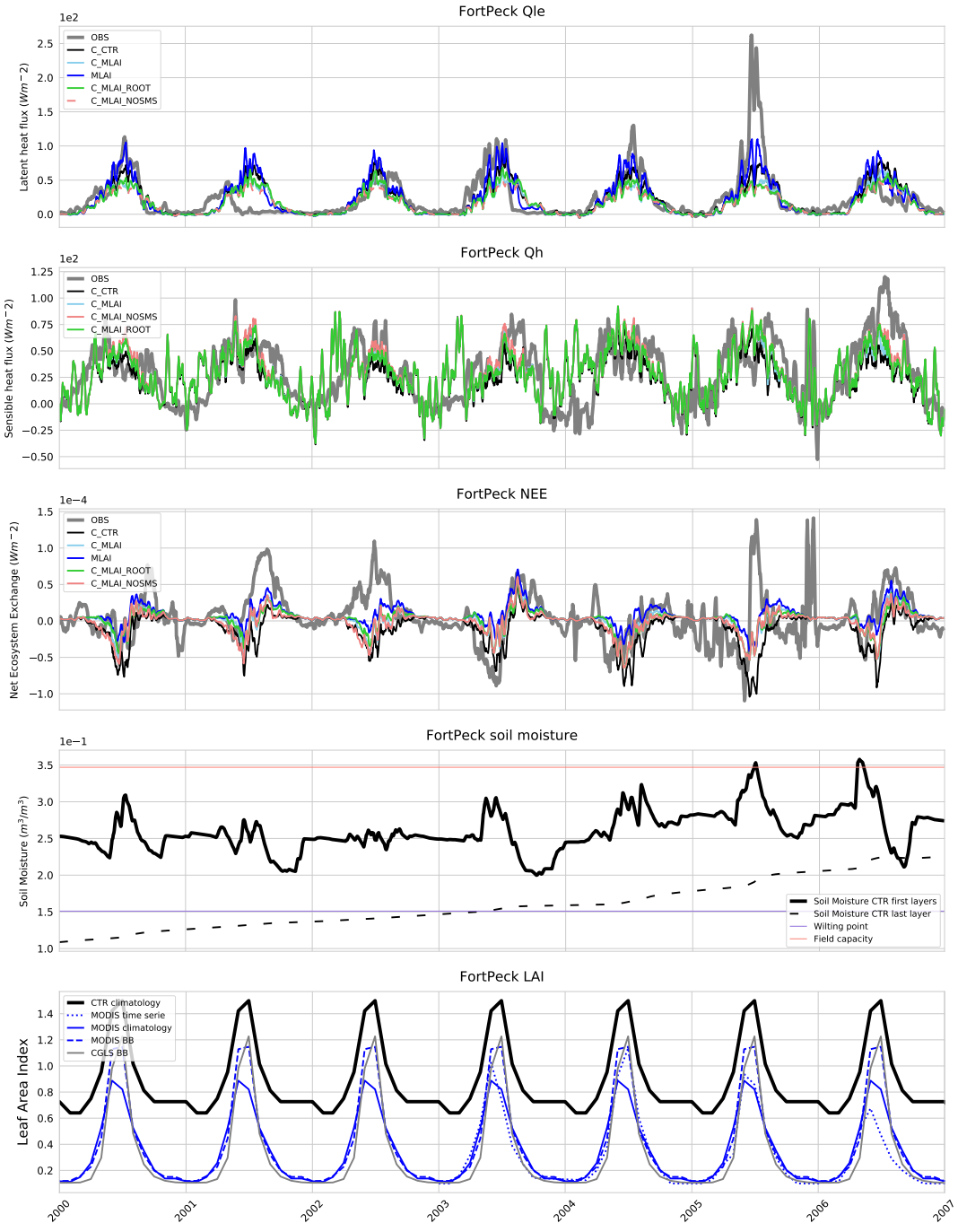

Figure B.10: As Figure B.1 but for Fort Peck station.

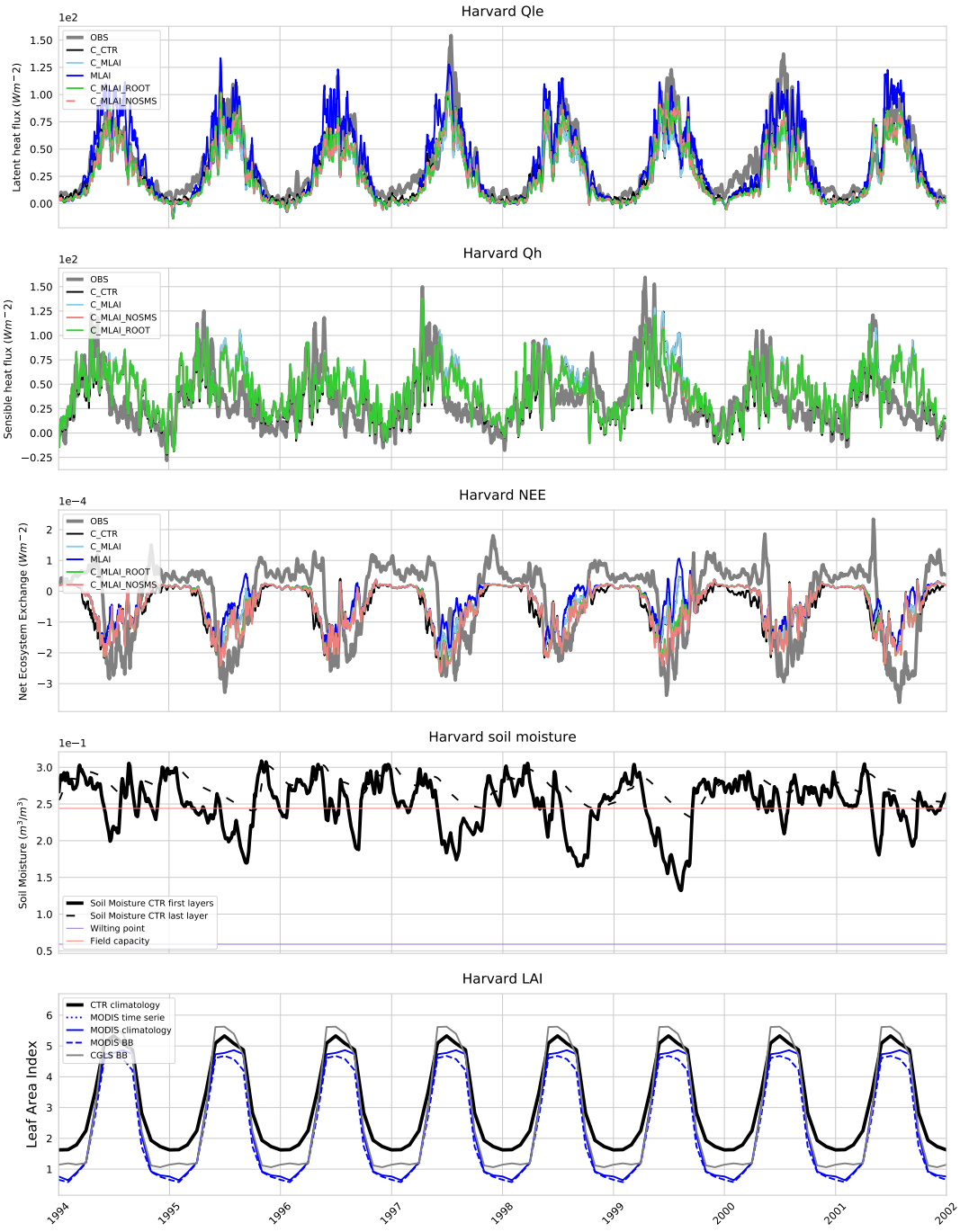

Figure B.11: As Figure B.1 but for Harvard station.

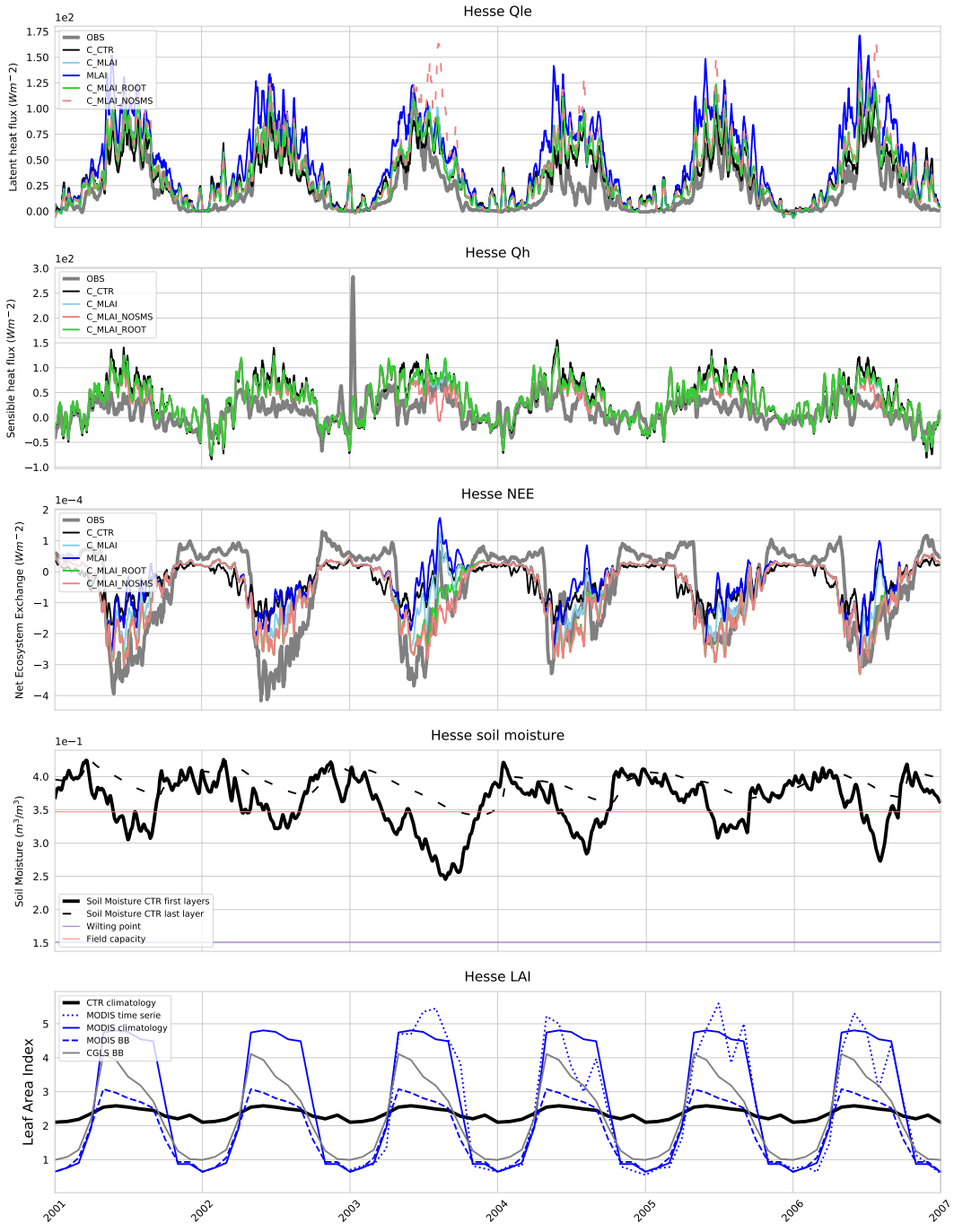

Figure B.12: As Figure B.1 but for Hesse station.

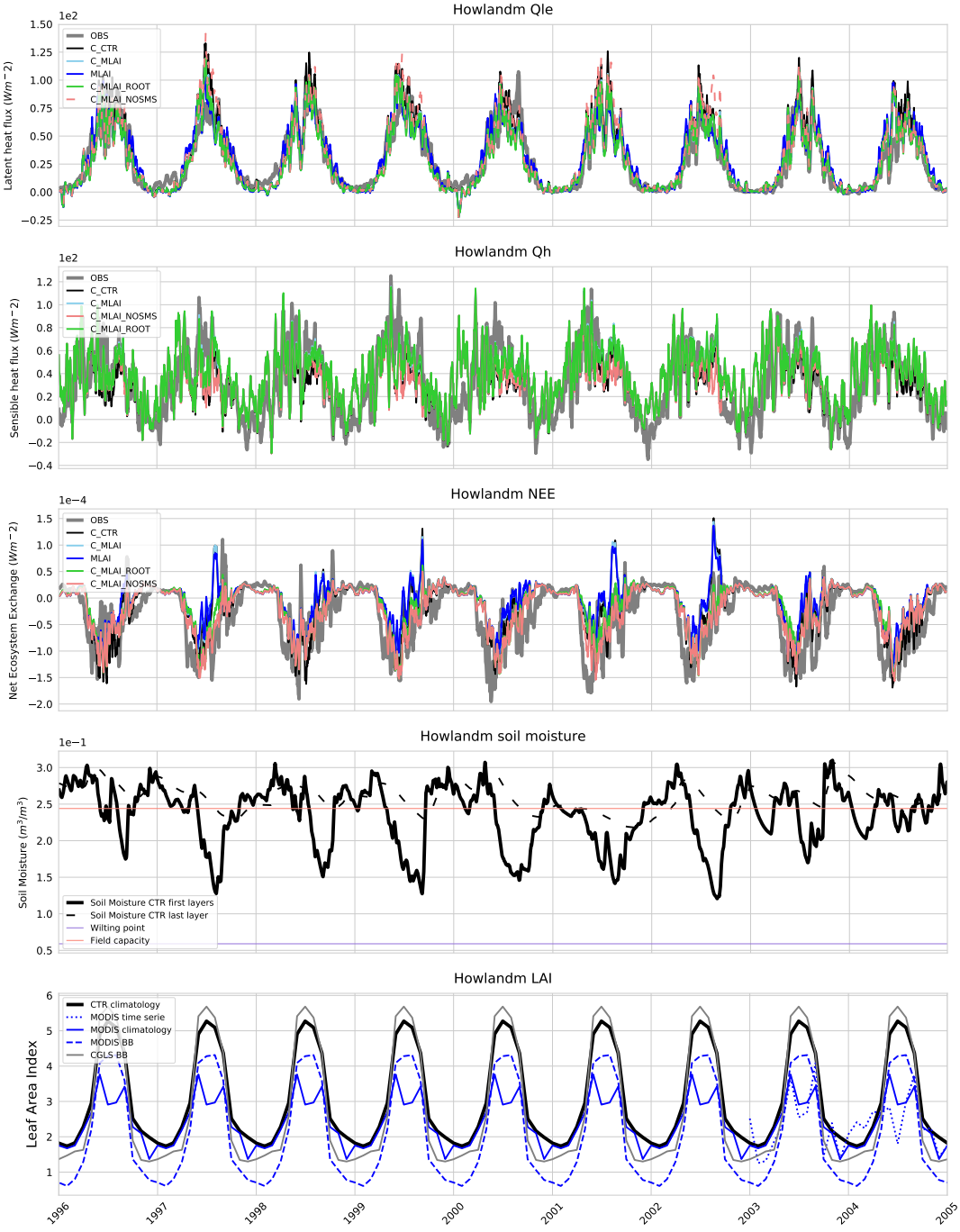

Figure B.13: As Figure B.1 but for Howlandm station.

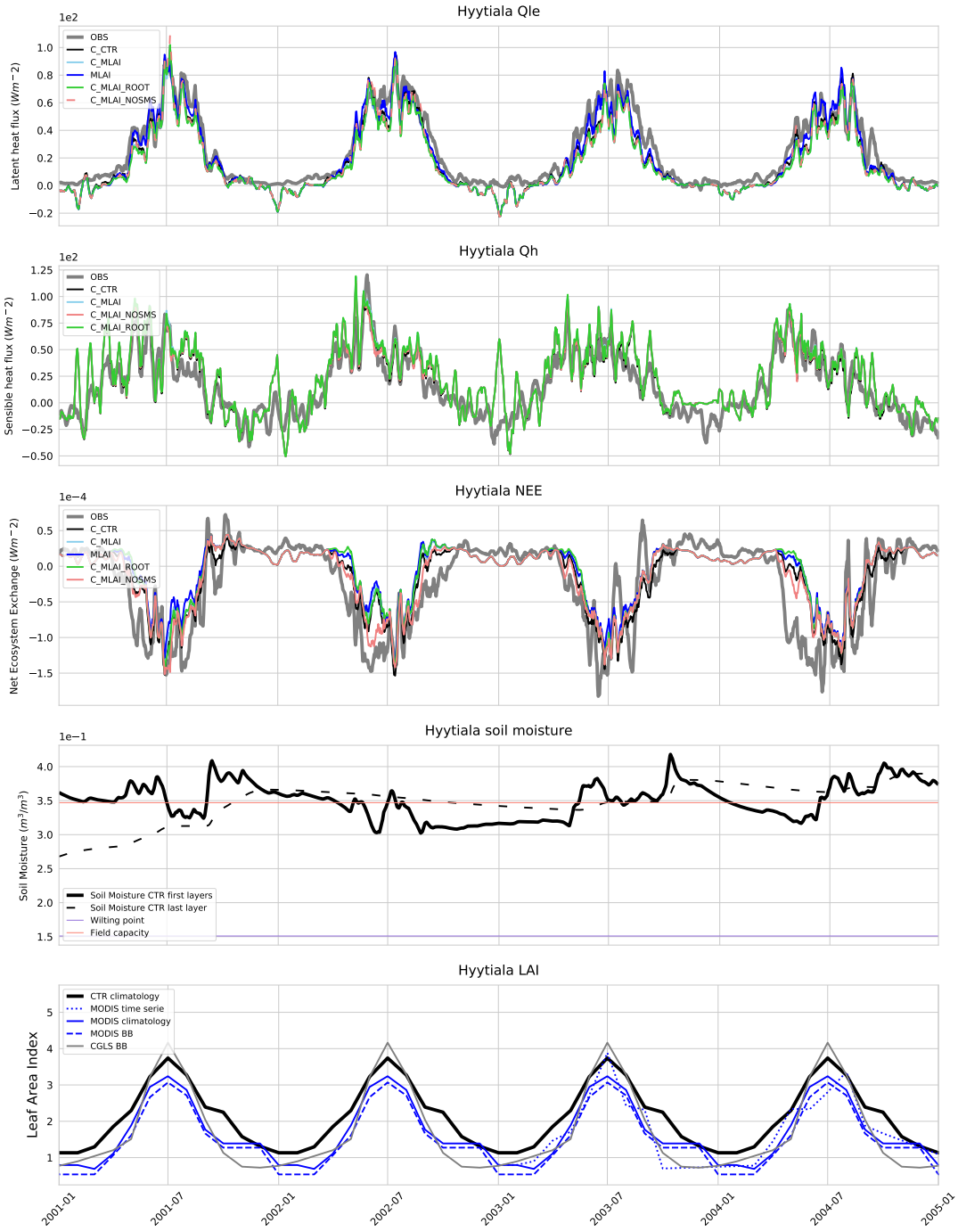

Figure B.14: As Figure B.1 but for Hyytiala station.

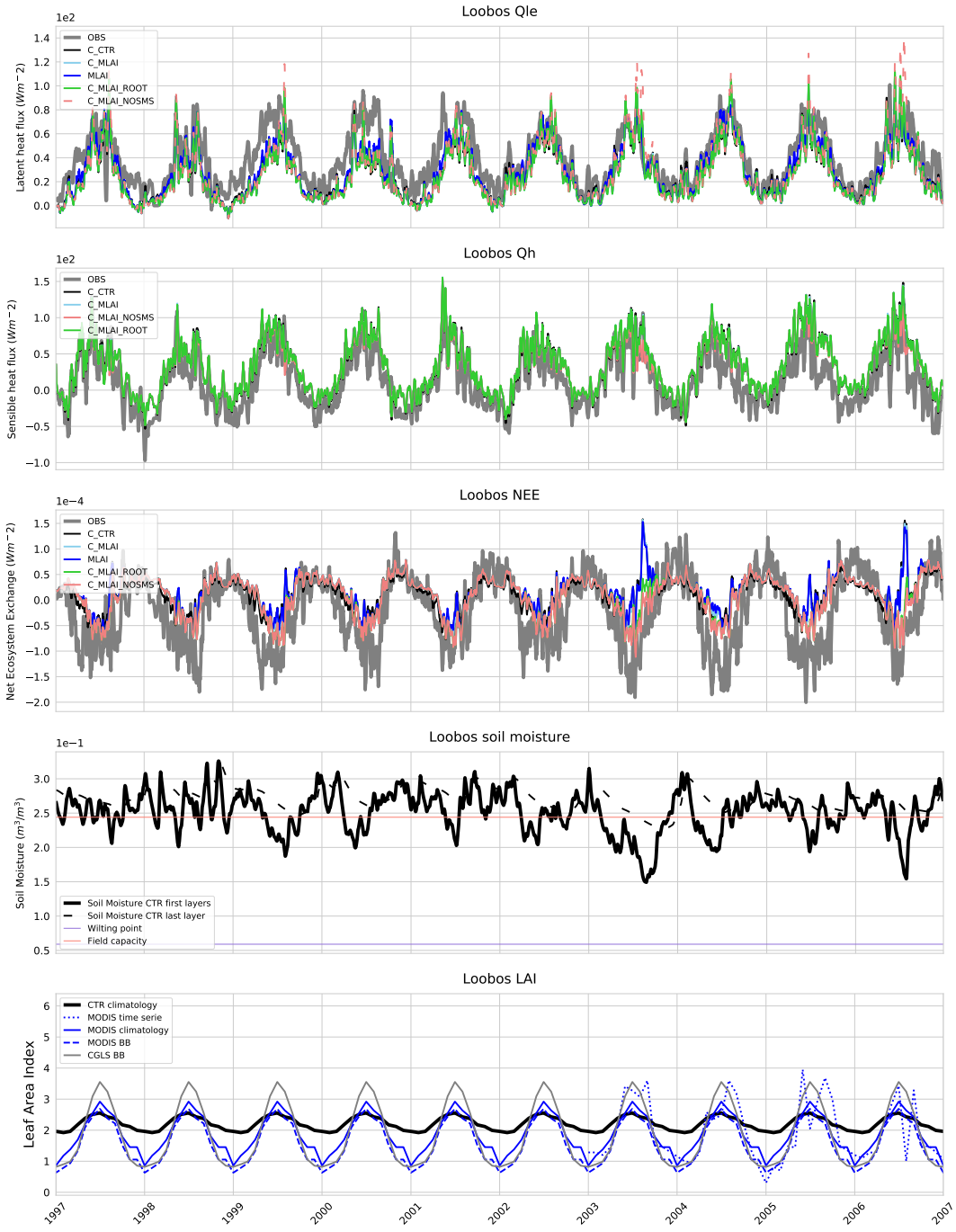

Figure B.15: As Figure B.1 but for Loobos station.

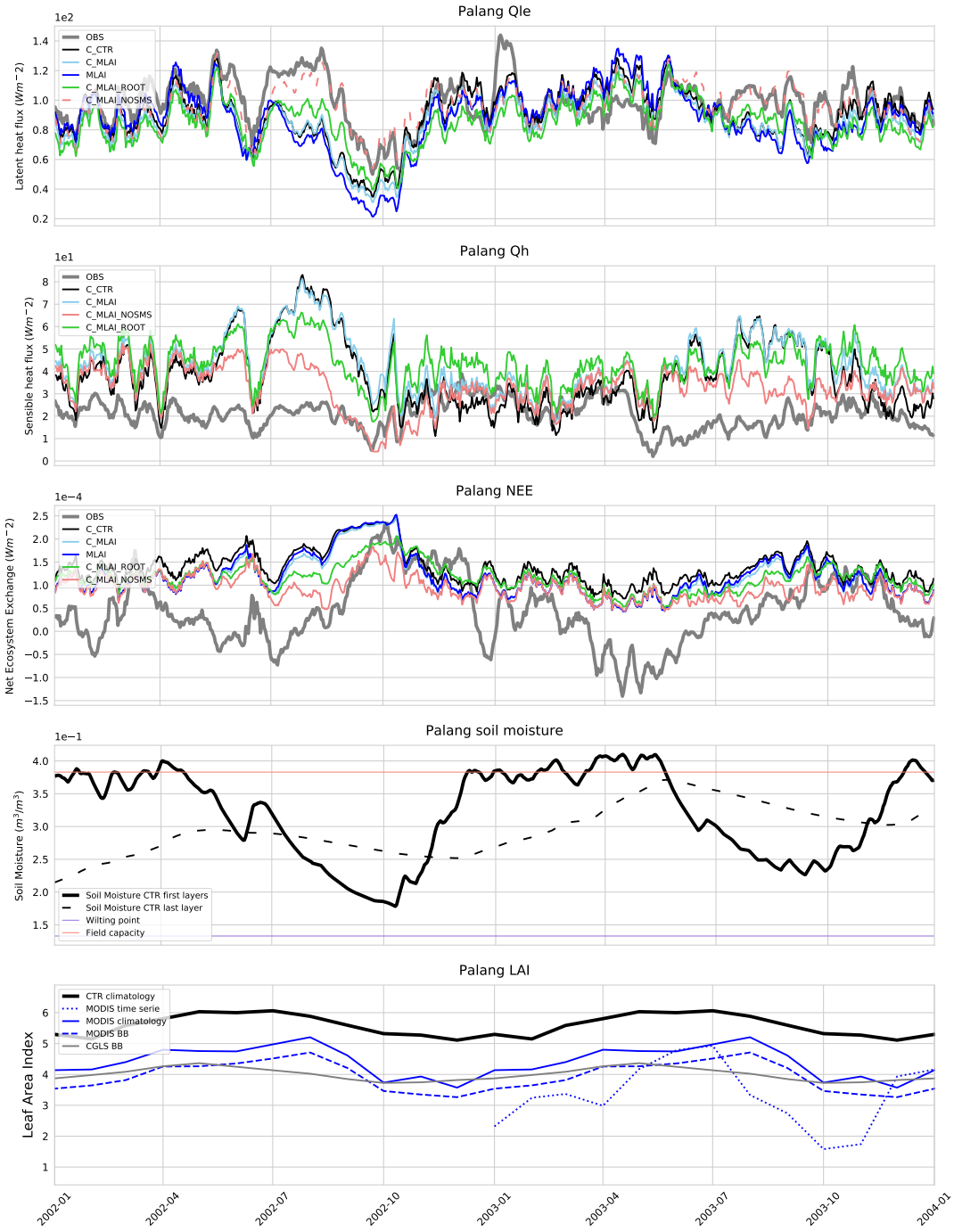

Figure B.16: As Figure B.1 but for Palang station.

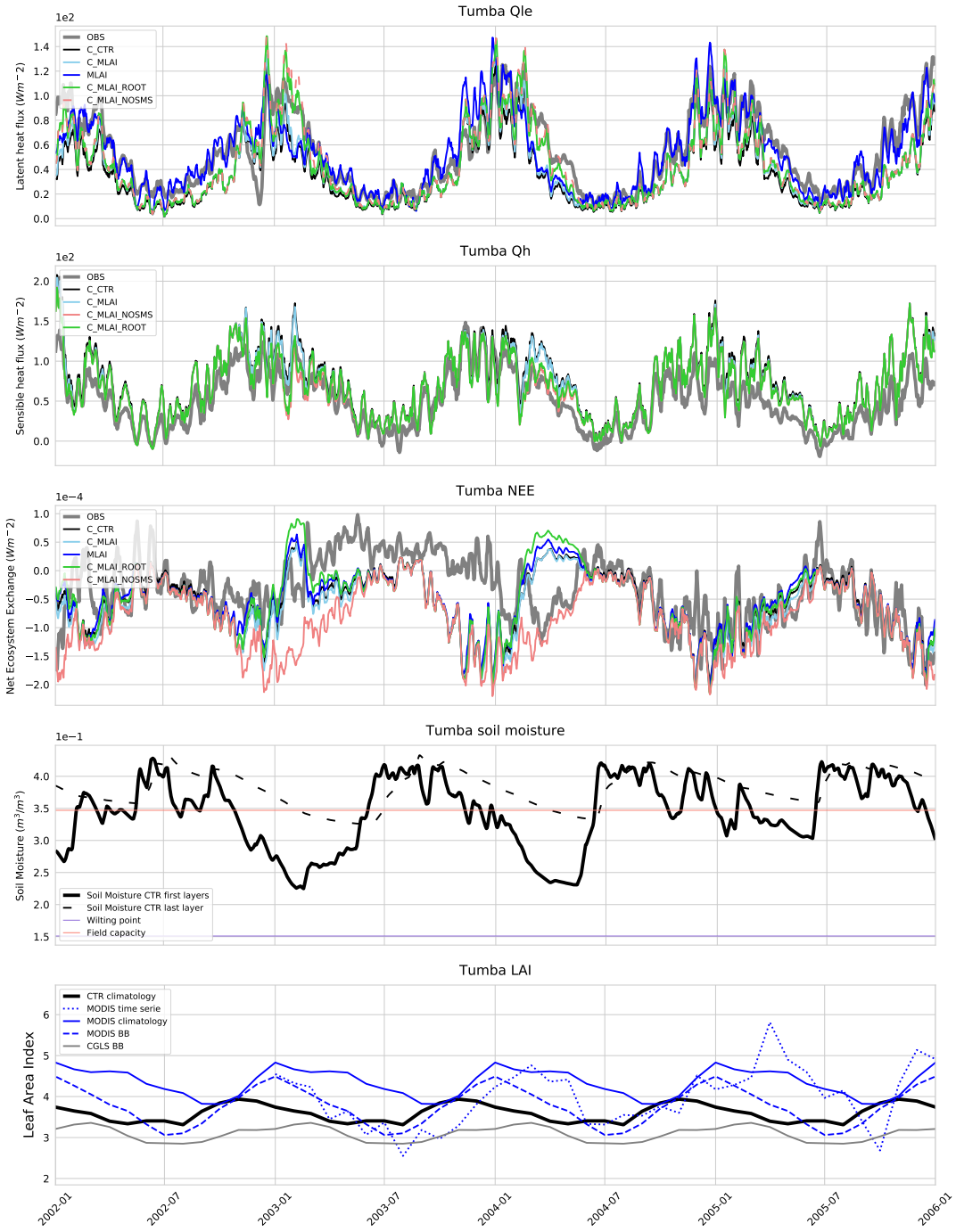

Figure B.17: As Figure B.1 but for Tumbarumba station.

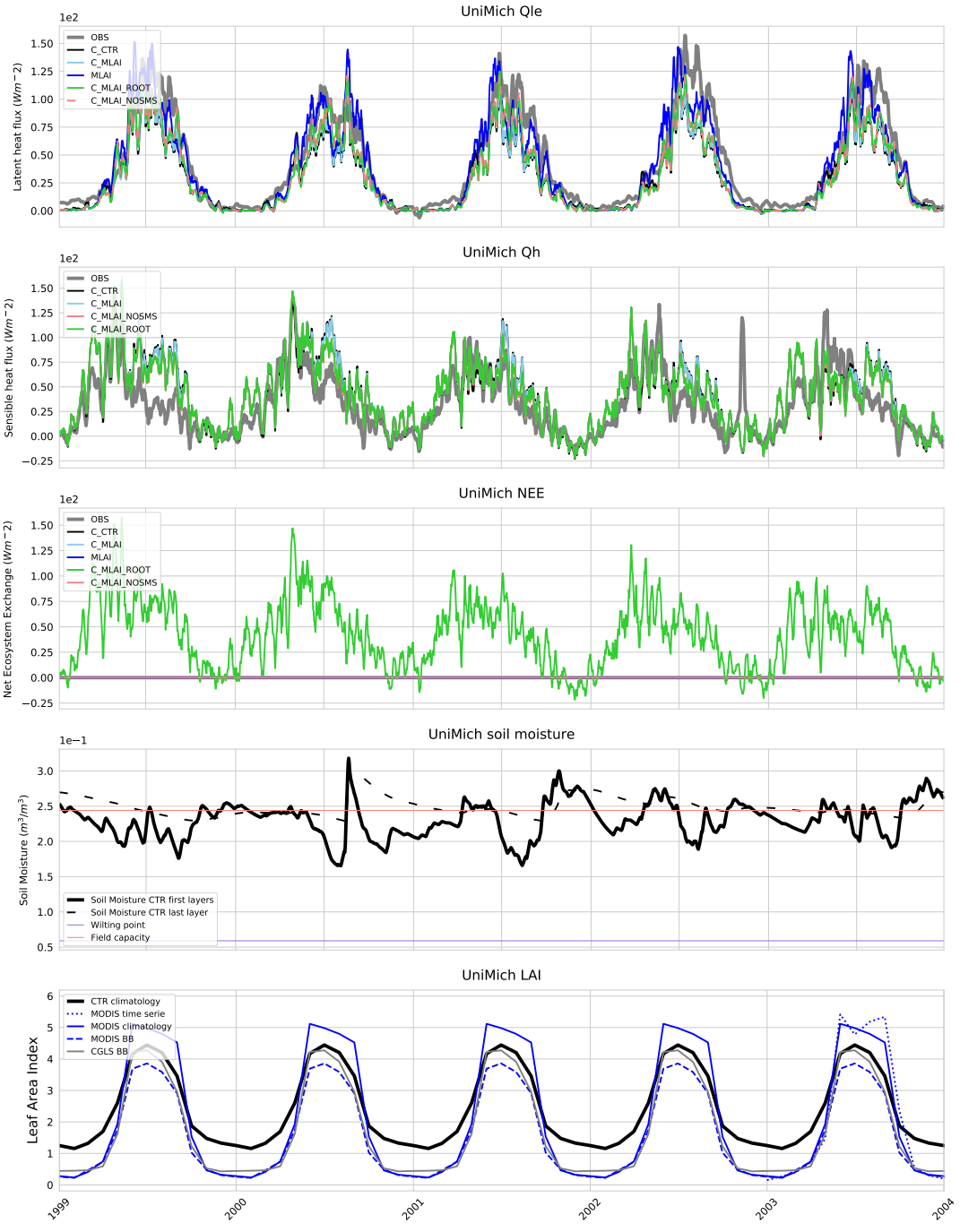

Figure B.18: As Figure B.1 but for University of Michigan station.

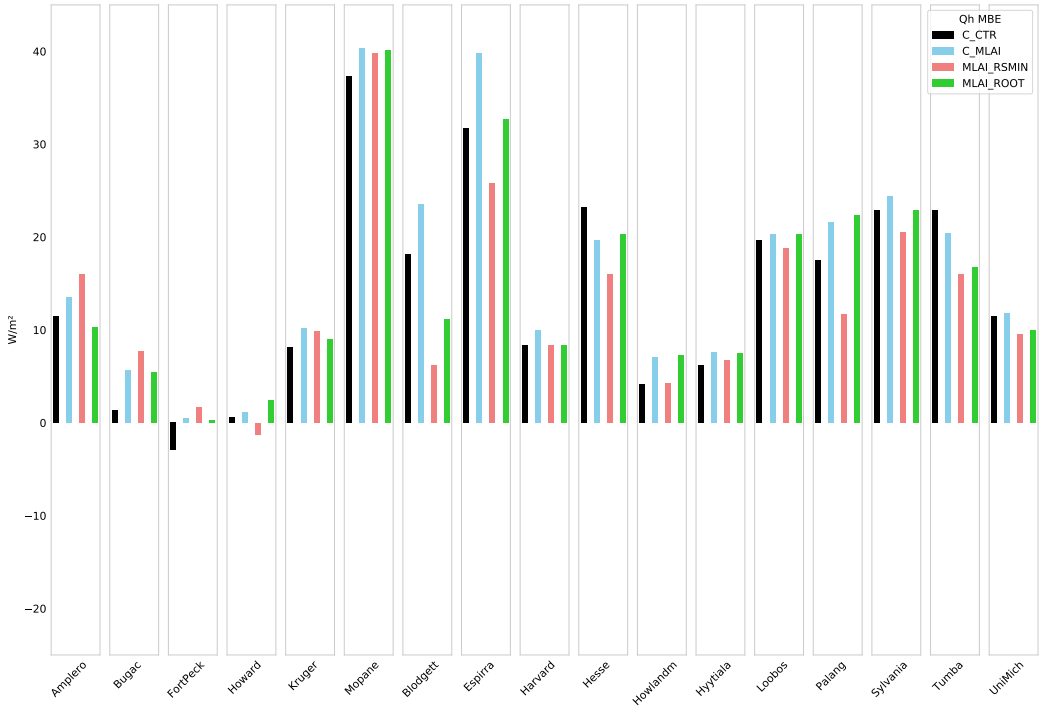

Figure B.19: Sensible heat flux MBE in the 17 stations for each simulation: CTR, MLAI, MLAI_RSMIN and MLAI_ROOT.

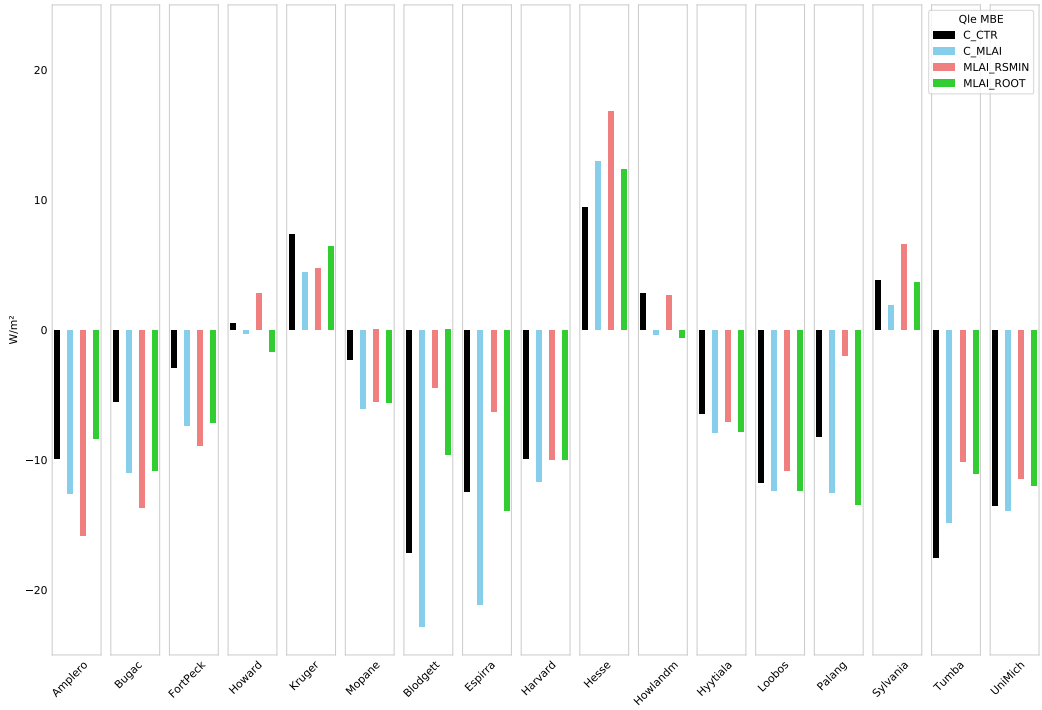

Figure B.20: Latent heat flux MBE in the 17 stations for each simulation: CTR, MLAI, MLAI_RSMIN and MLAI_ROOT.

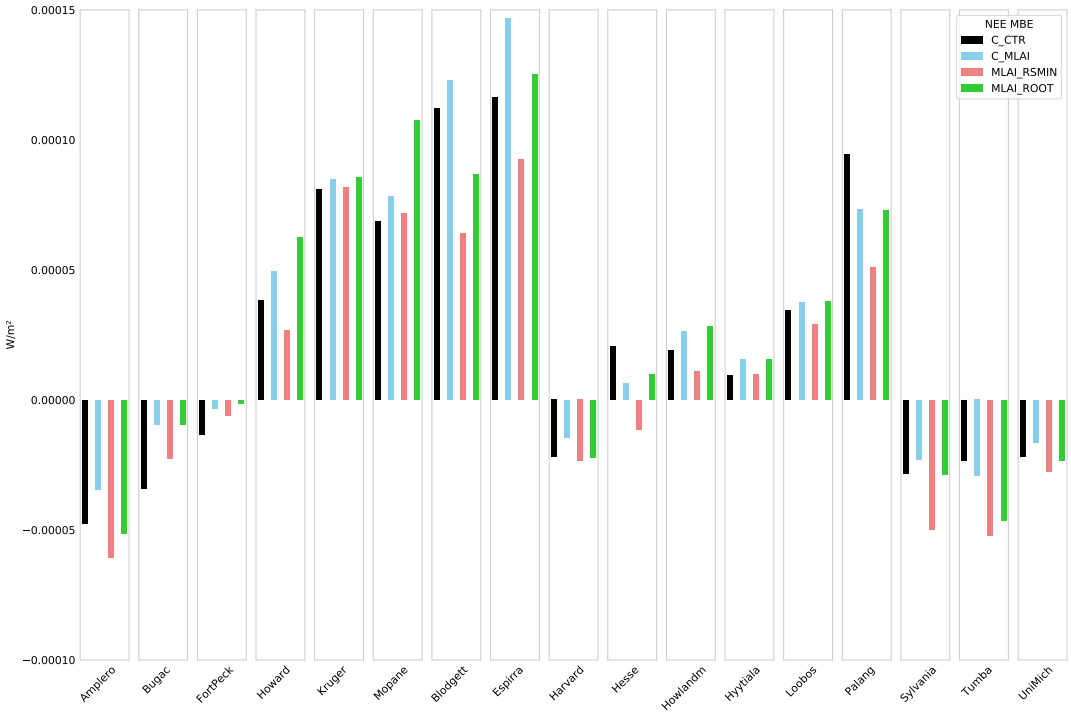

Figure B.21: Sensible heat flux SD in the 17 stations for each simulation: CTR, MLAI, MLAI_RSMIN and MLAI_ROOT.

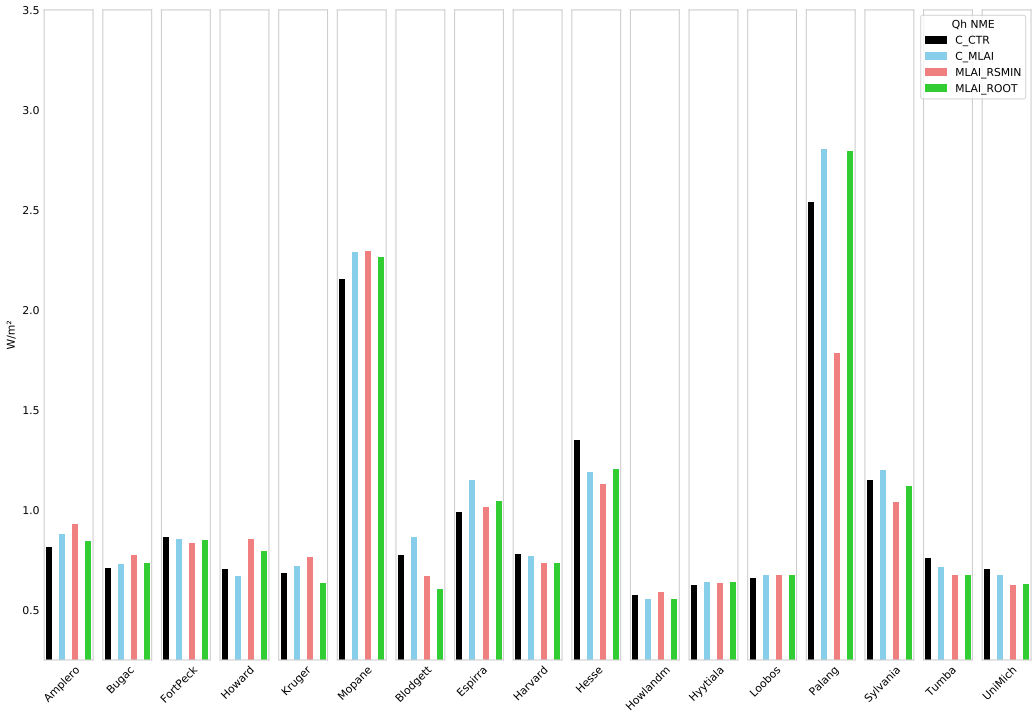

Figure B.22: Sensible heat flux NME in the 17 stations for each simulation: CTR, MLAI, MLAI_RSMIN and MLAI_ROOT.

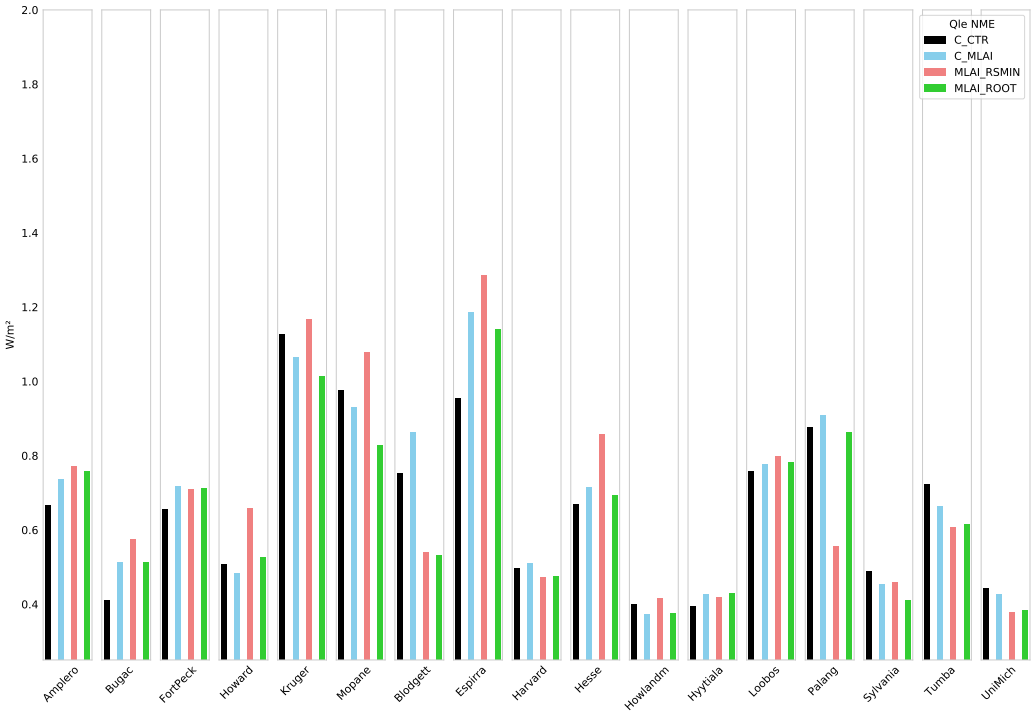

Figure B.23: Latent heat flux NME in the 17 stations for each simulation: CTR, MLAI, MLAI_RSMIN and MLAI_ROOT.

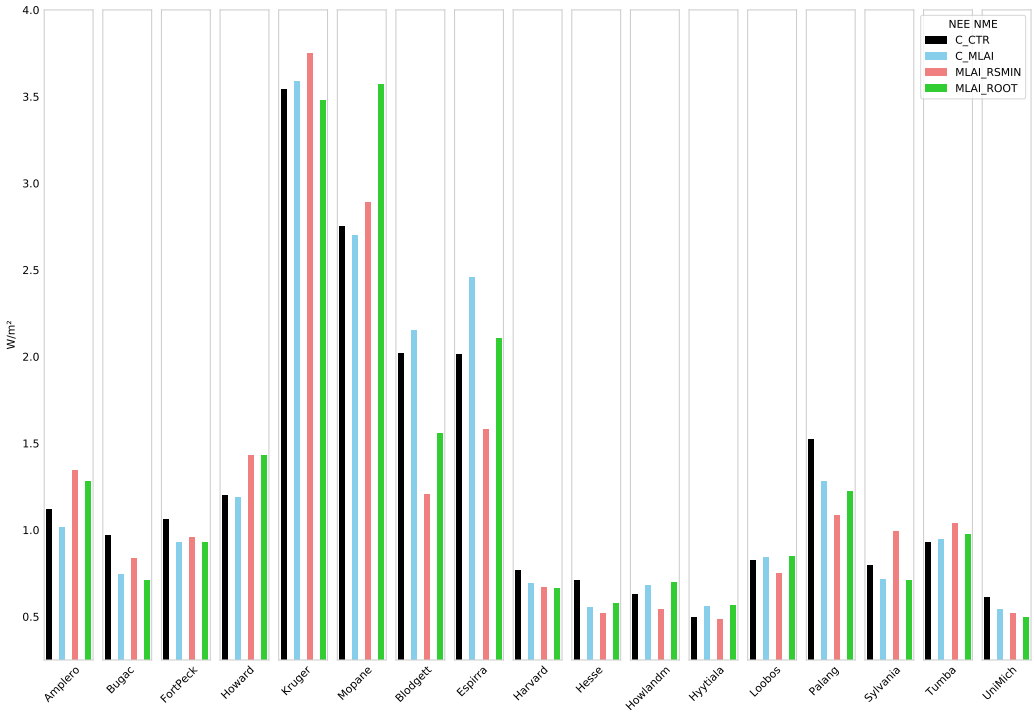

Figure B.24: Latent heat flux correlation in the 17 stations for each simulation: CTR, MLAI, MLAI_RSMIN and MLAI_ROOT.

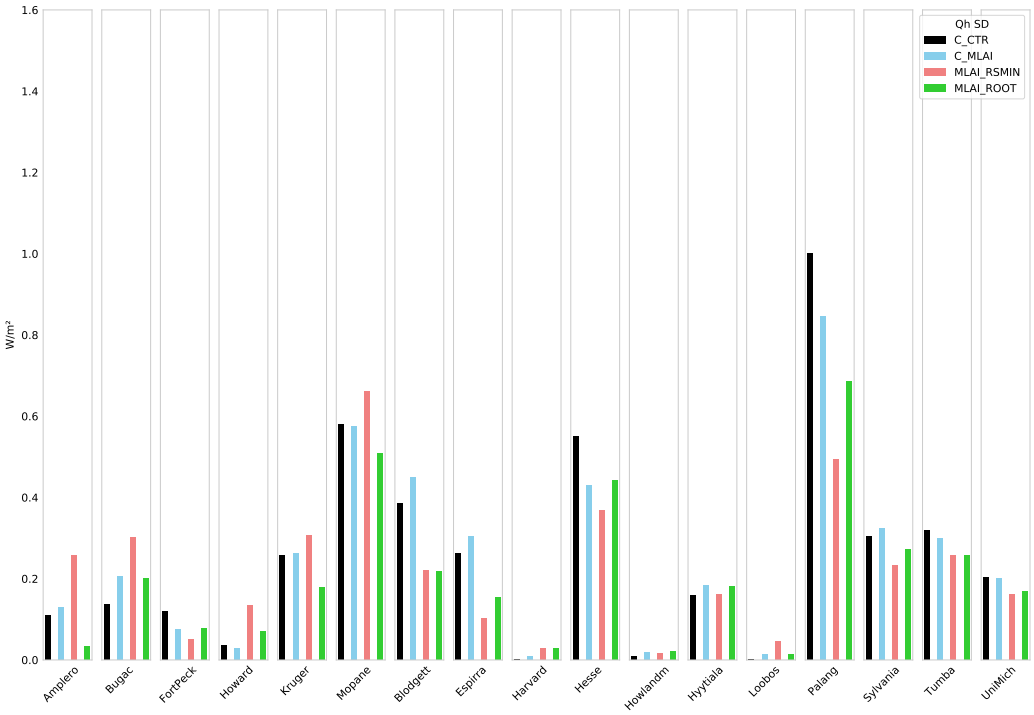

Figure B.25: Sensible heat flux SD in the 17 stations for each simulation: CTR, MLAI, MLAI_RSMIN and MLAI_ROOT.

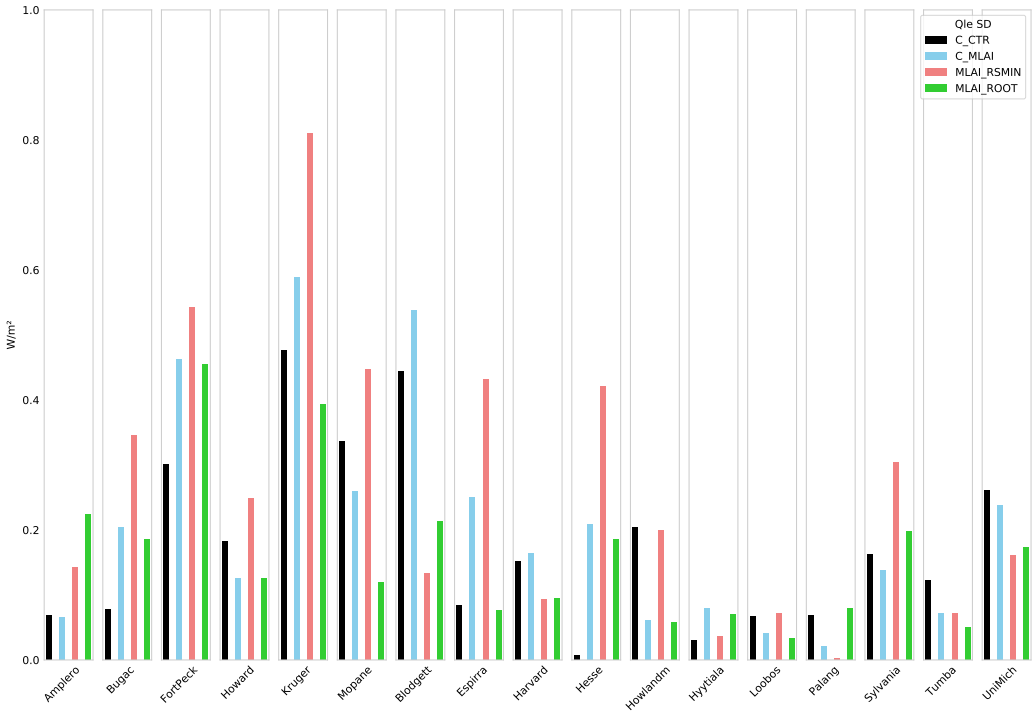

Figure B.26: Sensible heat flux SD in the 17 stations for each simulation: CTR, MLAI, MLAI_RSMIN and MLAI_ROOT.

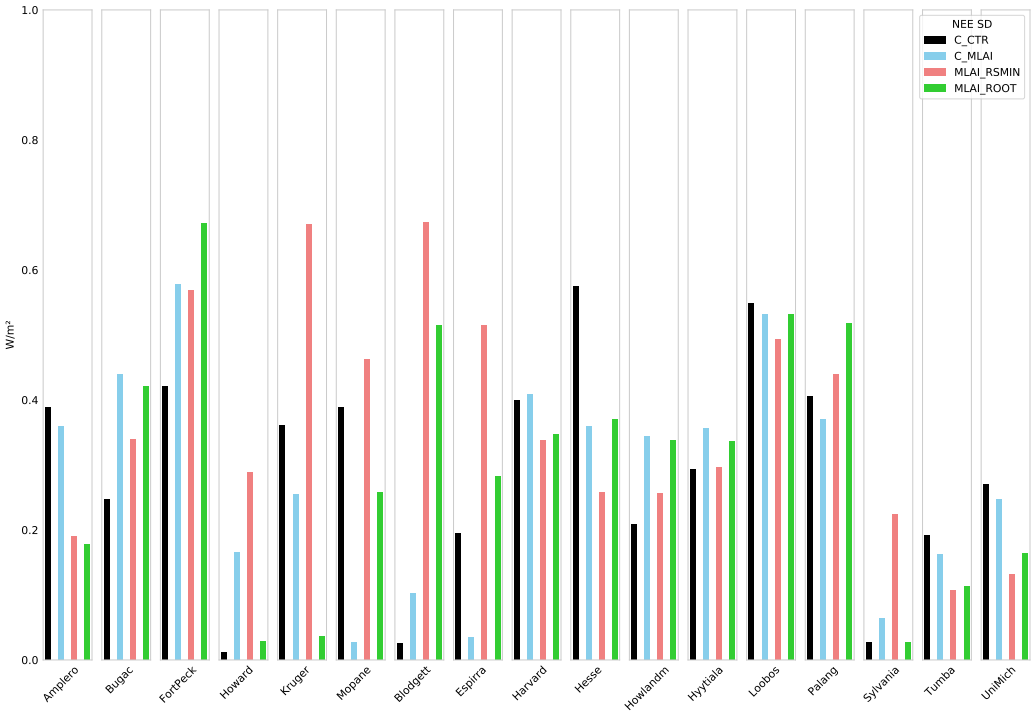

Figure B.27: Sensible heat flux SD in the 17 stations for each simulation: CTR, MLAI, MLAI_RSMIN and MLAI_ROOT.

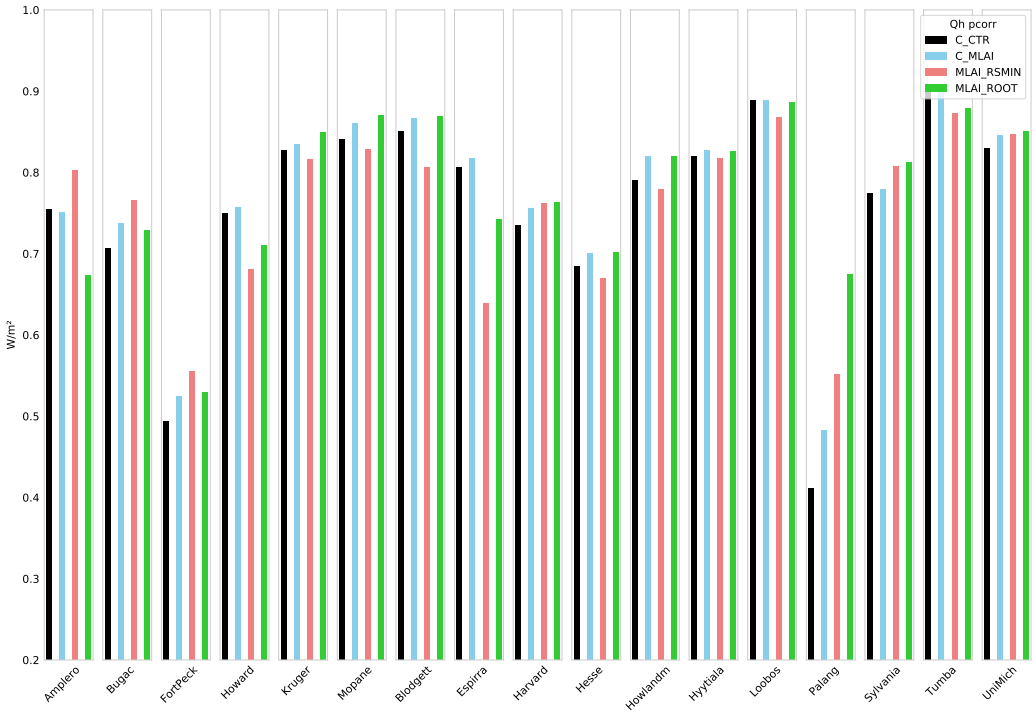

Figure B.28: Sensible heat flux correlation in the 17 stations for each simulation: CTR, MLAI, MLAI_RSMIN and MLAI_ROOT.

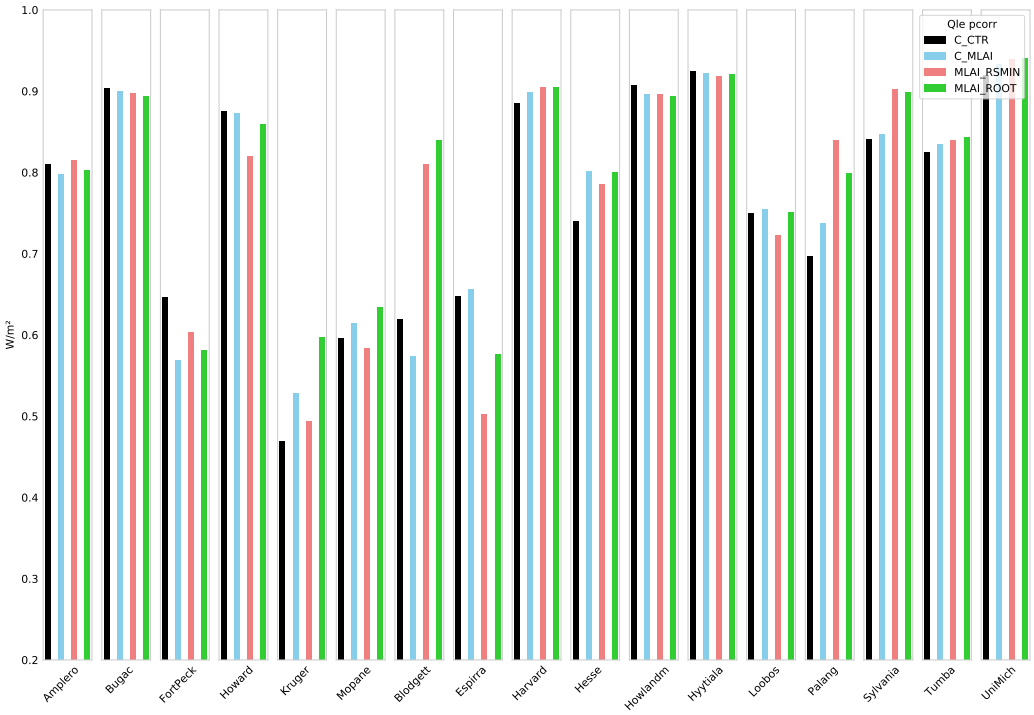

Figure B.29: Latent heat flux correlation in the 17 stations for each simulation: CTR, MLAI, MLAI_RSMIN and MLAI_ROOT.

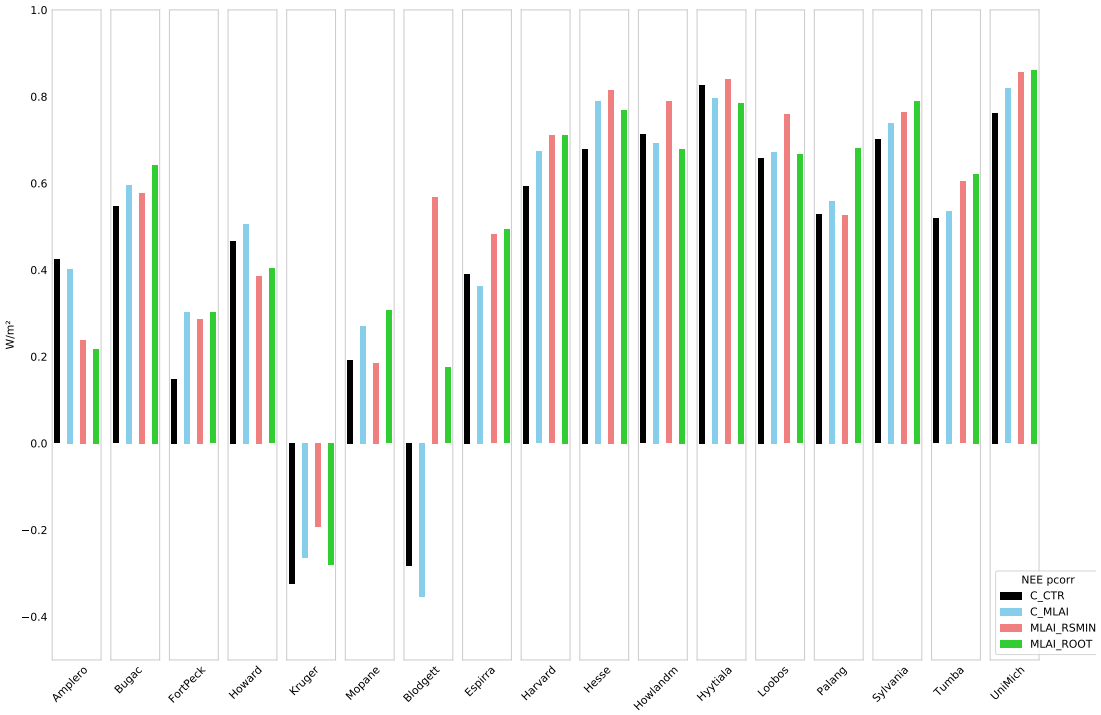

Figure B.30: Sensible heat flux correlation in the 17 stations for each simulation: CTR, MLAI, MLAI_RSMIN and MLAI_ROOT.

Appendix C

Supporting material of Chapter 4.

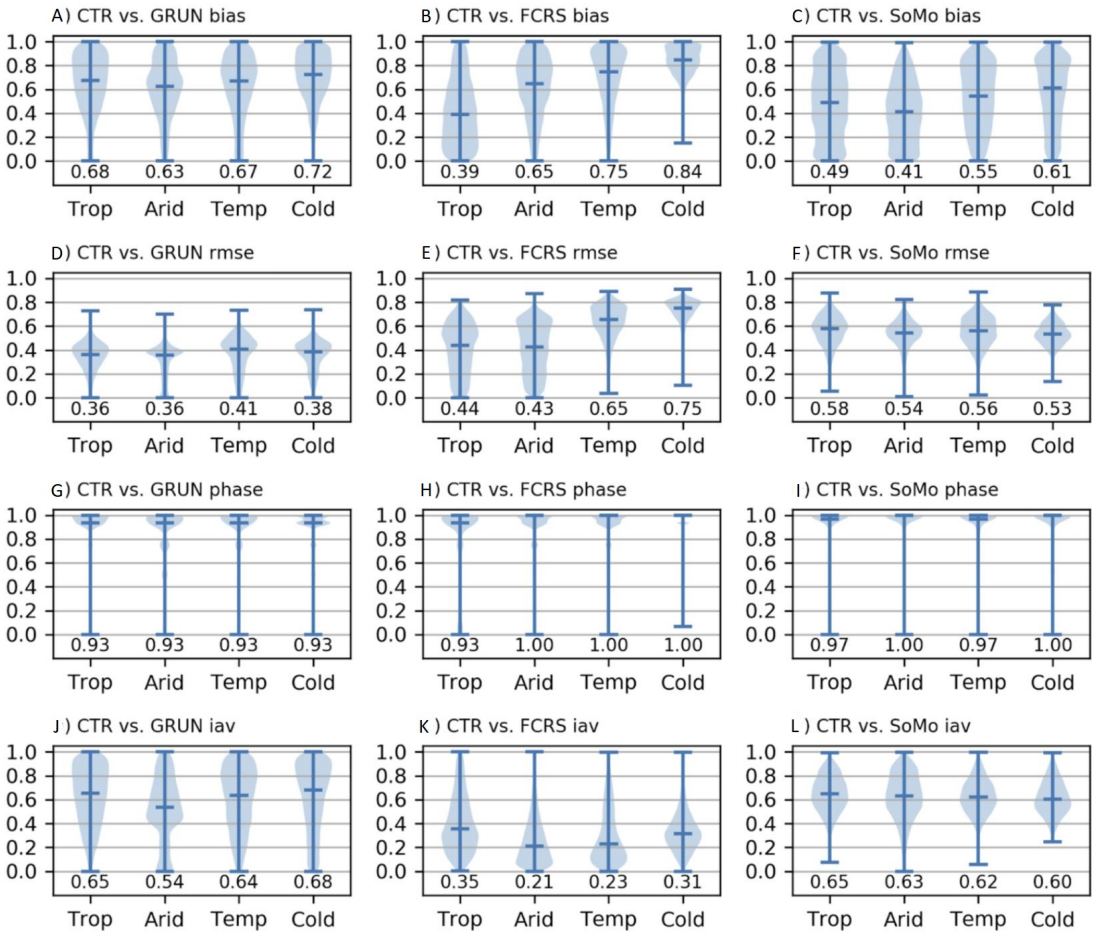

Figure C.1: Ilamb metrics evaluation of the CTR model setup.

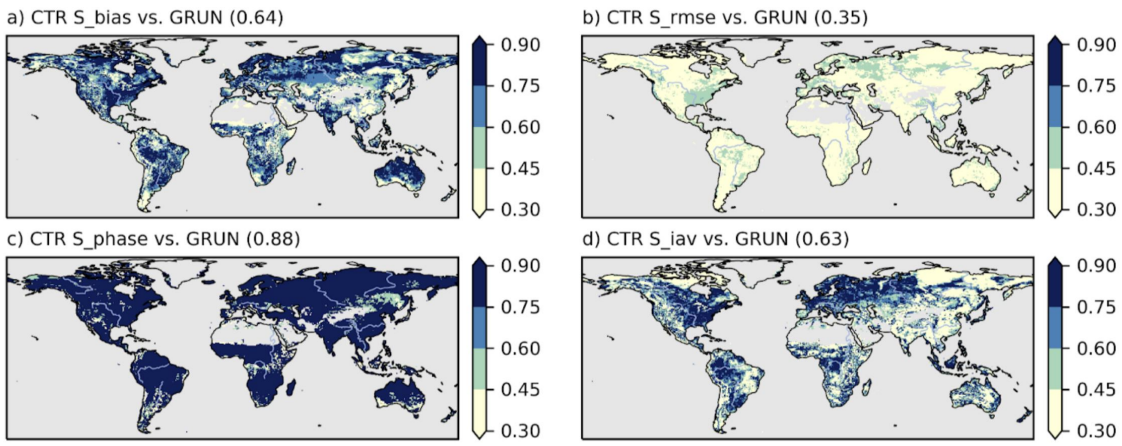

Figure C.2: Evaluation of the CTR setup against GRUN. (a) Sbias, (b) Srmse, (c) Sphase, (d) Siav.

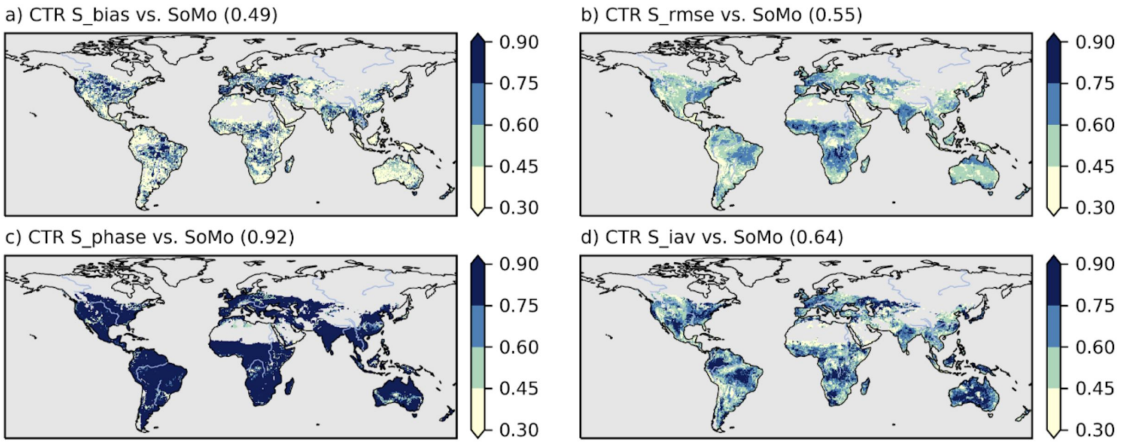

Figure C.3: Evaluation of the CTR setup against SoMo. (a) Sbias, (b) Srmse, (c) Sphase, (d) Siav.

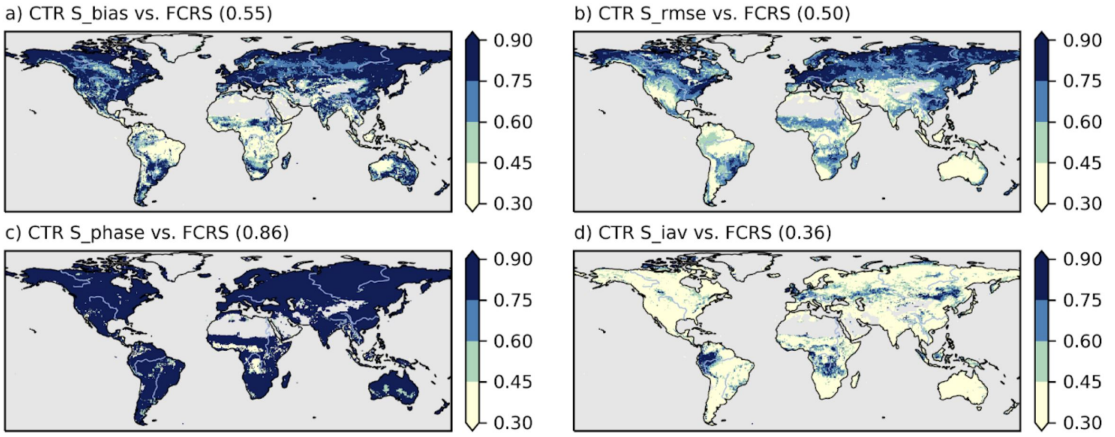

Figure C.4: Evaluation of the CTR setup against Fluxcom. (a) Sbias, (b) Srmse, (c) Sphase, (d) Siav.

Bibliography

Adeyemi, O., Grove, I., Peets, S., Domun, Y., & Norton, T. (2018). Dynamic neural network modelling of soil moisture content for predictive irrigation scheduling. *Sensors (Switzerland)*, *18*(10). https://doi.org/10.3390/s18103408

Albergel, C., Dutra, E., Bonan, B., Zheng, Y., Munier, S., Balsamo, G., de Rosnay, P., Muñoz-Sabater, J., & Calvet, J. C. (2019). Monitoring and forecasting the impact of the 2018 summer heatwave on vegetation. *Remote Sensing*, *11*(5). https://doi.org/10.3390/rs11050520

Albergel, C., Zheng, Y., Bonan, B., Dutra, E., Rodríguez-Fernández, N., Munier, S., Draper, C., De Rosnay, P., Muñoz-Sabater, J., Balsamo, G., Fairbairn, D., Meurey, C., & Calvet, J. C. (2020). Data assimilation for continuous global assessment of severe conditions over terrestrial surfaces. *Hydrology and Earth System Sciences*, *24*(9), 4291–4316. https://doi.org/10.5194/hess-24-4291-2020

Allen, C. D., Macalady, A. K., Chenchouni, H., Bachelet, D., McDowell, N., Vennetier, M., Kitzberger, T., Rigling, A., Breshears, D. D., Hogg, E. H., Gonzalez, P., Fensham, R., Zhang, Z., Castro, J., Demidova, N., Lim, J. H., Allard, G., Running, S. W., Semerci, A., & Cobb, N. (2010). A global overview of drought and heat-induced tree mortality reveals emerging climate change risks for forests. *Forest Ecology and Management*, *259*(4), 660–684. https://doi.org/10.1016/j.foreco.2009.09.001

Balsamo, G., Agusti-Panareda, A., Albergel, C., Arduini, G., Beljaars, A., Bidlot, J., Bousserez, N., Boussetta, S., Brown, A., Buizza, R., Buontempo, C., Chevallier, F., Choulga, M., Cloke, H., Cronin, M. F., Dahoui, M., Rosnay, P. D., Dirmeyer, P. A., Drusch, M., ... Zeng, X. (2018). Satellite and in situ observations for advancing global earth surface modelling: A review. *Remote Sensing*, *10*(12), 1–72. https://doi.org/10.3390/rs10122038

Balsamo, G., Dutra, E., Beljaars, A., & Viterbo, P. (2011). Evolution of land surface processes in the Integrated Forecast System. *ECMWF Newsletter No. 127*, *127*, 17–22. All%20Papers/B/Balsamo%20et%20al.%202011%20-%20Evolution%20of%20land%20surface%20processes%20in%20the%20IFS.pdf

Balsamo, G., Viterbo, P., Beijaars, A., van den Hurk, B., Hirschi, M., Betts, A. K., & Scipal, K. (2009). A revised hydrology for the ECMWF model: Verification from field site to terrestrial water storage and impact in the integrated forecast system. *Journal of Hydrometeorology*, *10*(3), 623–643. https://doi.org/10.1175/2008JHM1068.1

Bartletta, M. K., Klein, T., Jansen, S., Choat, B., & Sack, L. (2016). The correlations and sequence of plant stomatal, hydraulic, and wilting responses to drought. *Proceedings of the National Academy of Sciences of the United States of America*, *113*(46), 13098–13103. https://doi.org/10.1073/pnas.1604088113

Beck, H. E., Zimmermann, N. E., McVicar, T. R., Vergopolan, N., Berg, A., & Wood, E. F. (2018). Present and future köppen-geiger climate classification maps at 1-km resolution. *Scientific Data*, *5*, 1–12. https://doi.org/10.1038/sdata.2018.214

Best, M. J., Abramowitz, G., Johnson, H. R., Pitman, A. J., Balsamo, G., Boone, A., Cuntz, M., Decharme, B., Dirmeyer, P. A., Dong, J., Ek, M., Guo, Z., Haverd, V., van Den Hurk, B. J., Nearing, G. S., Pak, B., Peters-Lidard, C., Santanello, J. A., Stevens, L., & Vuichard, N. (2015). The plumbing of land surface models: Benchmarking model performance. *Journal of Hydrometeorology*, *16*(3), 1425–1442. https://doi.org/10.1175/JHM-D-14-0158.1

Betts, A. K., Ball, J. H., Beljaars, A. C., Miller, M. J., & Viterbo, P. A. (1996). The land surface-atmosphere interaction: A review based on observational and global modeling perspectives. *Journal of Geophysical Research Atmospheres*, *101*(D3), 7209–7225. https://doi.org/10.1029/95JD02135

Betts, R. A., Falloon, P. D., Goldewijk, K. K., & Ramankutty, N. (2007). Biogeophysical effects of land use on climate: Model simulations of radiative forcing and large-scale temperature change. *Agricultural and Forest Meteorology*, *142*(2-4), 216–233. https://doi.org/10.1016/j.agrformet.2006.08.021

Blyth, E. M., Arora, V. K., Clark, D. B., Dadson, S. J., De Kauwe, M. G., Lawrence, D. M., Melton, J. R., Pongratz, J., Turton, R. H., Yoshimura, K., & Yuan, H. (2021). Advances in Land Surface Modelling. *Current Climate Change Reports*, *7*(2), 45–71. https://doi.org/10.1007/s40641-021-00171-5

Bonan, G. B. (1994). Comparison of two land surface process models using prescribed forcings. *Journal of Geophysical Research*, *99*(D12). https://doi.org/10.1029/94jd02188

Boussetta, S., Balsamo, G., Arduini, G., Dutra, E., McNorton, J., Choulga, M., Agustí-Panareda, A., Beljaars, A., Wedi, N., Munõz-Sabater, J., de Rosnay, P., Sandu, I., Hadade, I., Carver, G., Mazzetti, C., Prudhomme, C., Yamazaki, D., & Zsoter, E. (2021). Ecland: The ecmwf land surface modelling system. *Atmosphere*, *12*(6), 1–40. https://doi.org/10.3390/atmos12060723

Boussetta, S., Balsamo, G., Beljaars, A., Agusti-panareda, A., Calvet, J.-c., Jacobs, C., Hurk, B. V. D., Viterbo, P., Lafont, S., Dutra, E., Jarlan, L., Balzarolo, M., Papale, D., & Werf, G. V. D. (2012). Natural land carbon dioxide exchanges System : Implementation and Offline validation. (May).

Boussetta, S., Balsamo, G., Beljaars, A., Kral, T., & Jarlan, L. (2013). Impact of a satellite-derived leaf area index monthly climatology in a global numerical weather prediction model. *International Journal of Remote Sensing*, *34*(9-10), 3520–3542. https://doi.org/10.1080/01431161.2012.716543

Boussetta, S., Balsamo, G., Beljaars, A., Panareda, A. A., Calvet, J. C., Jacobs, C., Van Den Hurk, B., Viterbo, P., Lafont, S., Dutra, E., Jarlan, L., Balzarolo, M., Papale, D., & Van Der Werf, G. (2013). Natural land carbon dioxide exchanges in the ECMWF integrated forecasting system: Implementation and offline validation. *Journal of Geophysical Research Atmospheres*, *118*(12), 5923–5946. https://doi.org/10.1002/jgrd.50488

Boussetta, S., Balsamo, G., Dutra, E., Beljaars, A., & Albergel, C. (2015). Assimilation of surface albedo and vegetation states from satellite observations and their impact on numerical weather prediction. *Remote Sensing of Environment*, *163*, 111–126. https://doi.org/10.1016/j.rse.2015.03.009

Breiman, L. (2001). Random Forests. *Machine Learning*, *45*(5-32). https://doi.org/10.1007/978-3-030-62008-0_35

Brown, L. A., Meier, C., Morris, H., Pastor-Guzman, J., Bai, G., Lerebourg, C., Gobron, N., Lanconelli, C., Clerici, M., & Dash, J. (2020). Evaluation of global leaf area index and fraction of absorbed photosynthetically active radiation products over North America using Copernicus Ground Based Observations for Validation data. *Remote Sensing of Environment*, *247*(January), 111935. https://doi.org/10.1016/j.rse.2020.111935

Budyko, M. I. (1974). *Climate and Life* (D. H. Miller, Ed.; Academic P).

Cabelguenne, M., & Debaeke, P. (1998). Experimental determination and modelling of the soil water extraction capacities of crops of maize, sunflower, soya bean, sorghum and wheat. *Plant and Soil*, *202*(2), 175–192. https://doi.org/10.1023/A:1004376728978

Calvet, J.-c., Viterbo, P., Ciais, P., Hurk, B. V. D., Moors, E., Kaptein, A., & Leroy, M. (2003). Integrated Project (2004-2007) co- funded by the European Commission, aims at addressing European and global environment issues, based on the use of remote sensing data. The carbon observatory of. *Carbon*.

Canadell, J., Jackson, R. B., Ehleringer, J. R., Mooney, H. A., Sala, O. E., & Schulze, E. D. (1996). Maximum rooting depth of vegetation types at the global scale. *Oecologia*, *108*(4), 583–595. https://doi.org/10.1007/BF00329030

Carvalhais, N., Forkel, M., Khomik, M., Bellarby, J., Jung, M., Migliavacca, M., Mu, M., Saatchi, S., Santoro, M., Thurner, M., Weber, U., Ahrens, B., Beer, C., Cescatti, A., Randerson, J. T., & Reichstein, M. (2014). Global covariation of carbon turnover times with climate in terrestrial ecosystems. *Nature*, *514*(7521), 213–217. https://doi.org/10.1038/nature13731

Cescatti, A., Marcolla, B., Santhana Vannan, S. K., Pan, J. Y., Román, M. O., Yang, X., Ciais, P., Cook, R. B., Law, B. E., Matteucci, G., Migliavacca, M., Moors, E., Richardson, A. D., Seufert, G., & Schaaf, C. B. (2012). Intercomparison of MODIS albedo retrievals and in situ measurements across the global FLUXNET network. *Remote Sensing of Environment*, *121*, 323–334. https://doi.org/10.1016/j.rse.2012.02.019

Coenders-Gerrits, A. M., Van Der Ent, R. J., Bogaard, T. A., Wang-Erlandsson, L., Hrachowitz, M., & Savenije, H. H. (2014). Uncertainties in transpiration estimates. *Nature*, *506*(7487), E1–E2. https://doi.org/10.1038/nature12925

Collier, N., Hoffman, F. M., Lawrence, D. M., Keppel-Aleks, G., Koven, C. D., Riley, W. J., Mu, M., & Randerson, J. T. (2018). The International Land Model Benchmarking (ILAMB) System: Design, Theory, and Implementation. *Journal of Advances in Modeling Earth Systems*, *10*(11), 2731–2754. https://doi.org/10.1029/2018MS001354

Cox, P. M., Betts, R. A., Jones, C. D., Spall, S. A., & Totterdell, I. J. (2000). Acceleration of global warming due to carbon-cycle feedbacks in a coupled climate model. *Nature*, *408*(November), 184–187.

Damour, G., Simonneau, T., Cochard, H., & Urban, L. (2010). An overview of models of stomatal conductance at the leaf level. *Plant, Cell and Environment*, *33*(9), 1419–1438. https://doi.org/10.1111/j.1365-3040.2010.02181.x

Denissen, J. M., Teuling, A. J., Reichstein, M., & Orth, R. (2020). Critical Soil Moisture Derived From Satellite Observations Over Europe. *Journal of Geophysical Research: Atmospheres*, *125*(6), 0–3. https://doi.org/10.1029/2019JD031672

Desborough, C. E. (1997). The impact of root weighting on the response of transpiration to moisture stress in land surface schemes. *Monthly Weather Review*, *125*(8), 1920–1930. https://doi.org/10.1175/1520-0493(1997)125⟨1920:TIORWO⟩2.0.CO;2

Dickinson, E., Henderson-Sellers, A., & Kennedy, J. (1993). Biosphere-atmosphere Transfer Scheme (BATS) Version 1e as Coupled to the NCAR Community Climate Model. *NCAR Tech. Rep. NCAR/TN-3871STR, 72*, (August), 77. https://opensky.ucar.edu/islandora/object/technotes%5C%5C%3A154/

Dirmeyer, P. A., Balsamo, G., Blyth, E. M., Morrison, R., & Cooper, H. M. (2021). Land-Atmosphere Interactions Exacerbated the Drought and Heatwave Over Northern Europe During Summer 2018. *AGU Advances*, *2*(2), 1–16. https://doi.org/10.1029/2020av000283

Do, H. X., Gudmundsson, L., Leonard, M., & Westra, S. (2018). The Global Streamflow Indices and Metadata Archive (GSIM)-Part 1: The production of a daily streamflow archive and metadata. *Earth System Science Data*, *10*(2), 765–785. https://doi.org/10.5194/essd-10-765-2018

Dong, J., Dirmeyer, P. A., Lei, F., Anderson, M. C., Holmes, T. R., Hain, C., & Crow, W. T. (2020). Soil Evaporation Stress Determines Soil Moisture-Evapotranspiration Coupling Strength in Land Surface Modeling. *Geophysical Research Letters*, *47*(21), 1–11. https://doi.org/10.1029/2020GL090391

Dorman, J. L., & Sellers, P. J. (1989). A global climatology of albedo, roughness length and stomatal resistance for atmospheric general circulation models as represented by the Simple Biosphere Model (SiB). *Journal of Applied Meteorology*, *28*(9), 833–855. https://doi.org/10.1175/1520-0450(1989)028⟨0833:AGCOAR⟩2.0.CO;2

ECMWF. (2019). IFS Cy46r1: Part IV: Physical Processes. *IFS documentation*, (January), 1–171.

Egea, G., Verhoef, A., & Vidale, P. L. (2011). Towards an improved and more flexible representation of water stress in coupled photosynthesis-stomatal conductance models. *Agricultural and Forest Meteorology*, *151*(10), 1370–1384. https://doi.org/10.1016/j.agrformet.2011.05.019

Ershadi, A., McCabe, M. F., Evans, J. P., Chaney, N. W., & Wood, E. F. (2014). Multi-site evaluation of terrestrial evaporation models using FLUXNET data. *Agricultural and Forest Meteorology*, *187*, 46–61. https://doi.org/10.1016/j.agrformet.2013.11.008

Fang, H., Wei, S., Jiang, C., & Scipal, K. (2012). Theoretical uncertainty analysis of global MODIS, CYCLOPES, and GLOBCARBON LAI products using a triple collocation method. *Remote Sensing of Environment*, *124*, 610–621. https://doi.org/10.1016/j.rse.2012.06.013

Fang, K., & Shen, C. (2020). Near-real-time forecast of satellite-based soil moisture using long short-term memory with an adaptive data integration kernel. *Journal of Hydrometeorology*, *21*(3), 399–413. https://doi.org/10.1175/JHM-D-19-0169.1

Fisher, R. A., & Koven, C. D. (2020). Perspectives on the Future of Land Surface Models and the Challenges of Representing Complex Terrestrial Systems. *Journal of Advances in Modeling Earth Systems*, *12*(4). https://doi.org/10.1029/2018MS001453

Gardner, W. R. (1983). Soil properties and efficient water use: An overview. *1*(2496), 73–85.

Gentine, P., Holtslag, A. A., D'Andrea, F., & Ek, M. (2013). Surface and atmospheric controls on the onset of moist convection over land. *Journal of Hydrometeorology*, *14*(5), 1443–1462. https://doi.org/10.1175/JHM-D-12-0137.1

Ghiggi, G., Humphrey, V., Seneviratne, S. I., & Gudmundsson, L. (2019). GRUN: An observation-based global gridded runoff dataset from 1902 to 2014. *Earth System Science Data*, *11*(4), 1655–1674. https://doi.org/10.5194/essd-11-1655-2019

Giard, D., & Bazile, E. (2000). Implementation of a new assimilation scheme for soil and surface variables in a global NWP model. *Monthly Weather Review*, *128*(4), 997–1015. https://doi.org/10.1175/1520-0493(2000)128⟨0997:IOANAS⟩2.0.CO;2

Gou, J., Wang, F., Jin, K., Mu, X., & Chen, D. (2019). More realistic land-use and vegetation parameters in a regional climate model reduce model biases over China. *International Journal of Climatology*, *39*(12), 4825–4837. https://doi.org/10.1002/joc.6110

Goudriaan, J., van Laar, H. H., van Keulen, H., & Louwerse, W. (1985). Photosynthesis, CO2 and plant production. *Life Sciences*, *86*. https://doi.org/10.1201/9781482279993-9

Gregory, P. J., McGowan, M., & Biscoe, P. V. (1978). Water relations of winter wheat: 2. Soil water relations. *The Journal of Agricultural Science*, *91*(1), 103–116. https://doi.org/10.1017/S0021859600056665

Gudmundsson, L., Do, H. X., Leonard, M., & Westra, S. (2018). The Global Streamflow Indices and Metadata Archive (GSIM)-Part 2: Quality control, time-series indices and homogeneity assessment. *Earth System Science Data*, *10*(2), 787–804. https://doi.org/10.5194/essd-10-787-2018

Guswa, A. J. (2008). The influence of climate on root depth: A carbon cost-benefit analysis. *Water Resources Research*, *44*(2), 1–11. https://doi.org/10.1029/2007WR006384

Hall, A. (2004). The role of surface albedo feedback in climate. *Journal of Climate*, *17*(7), 1550–1568. https://doi.org/10.1175/1520-0442(2004)017⟨1550:TROSAF⟩2.0.CO;2

Haughton, N., Abramowitz, G., Pitman, A. J., Or, D., Best, M. J., Johnson, H. R., Balsamo, G., Boone, A., Cuntz, M., Decharme, B., Dirmeyer, P. A., Dong, J., Ek, M., Guo, Z., Haverd, V., van den Hurk, B. J., Nearing, G. S., Pak, B., Santanello, J. A., … Vuichard, N. (2016). The plumbing of land surface models: Is poor performance a result of methodology or data quality? *Journal of Hydrometeorology*, *17*(6), 1705–1723. https://doi.org/10.1175/JHM-D-15-0171.1

Haverd, V., Cuntz, M., Nieradzik, L. P., & Harman, I. N. (2016). Improved representations of coupled soil-canopy processes in the CABLE land surface model (Subversion revision 3432). *Geoscientific Model Development*, *9*(9), 3111–3122. https://doi.org/10.5194/gmd-9-3111-2016

Hersbach, H., Bell, B., Berrisford, P., Hirahara, S., Horányi, A., Muñoz-Sabater, J., Nicolas, J., Peubey, C., Radu, R., Schepers, D., Simmons, A., Soci, C., Abdalla, S., Abellan, X., Balsamo, G., Bechtold, P., Biavati, G., Bidlot, J., Bonavita, M., … Thépaut, J. N. (2020). The ERA5 global reanalysis. *Quarterly Journal of the Royal Meteorological Society*, *146*(730), 1999–2049. https://doi.org/10.1002/qj.3803

Hochreiter, S., & Schmidhuber, J. (1997). Long Short-Term Memory. *Neural Computation*, *9*(8), 1735–1780. https://doi.org/10.1162/neco.1997.9.8.1735

Houghton, R. A. (2000). Interannual variability in the global carbon cycle. *Journal of Geophysical Research Atmospheres*, *105*(D15), 20121–20130. https://doi.org/10.1029/2000JD900041

Houghton, R. A. (2003). Revised estimates of the annual net flux of carbon to the atmosphere from changes in land use and land management 1850-2000. *Tellus, Series B: Chemical and Physical Meteorology*, *55*(2), 378–390. https://doi.org/10.1034/j.1600-0889.2003.01450.x

Iturbide, M., Gutiérrez, J. M., Alves, L. M., Bedia, J., Cerezo-Mota, R., Cimadevilla, E., Cofiño, A. S., Luca, A. D., Faria, S. H., Gorodetskaya, I. V., Hauser, M., Herrera, S., Hennessy, K., Hewitt, H. T., Jones, R. G., Krakovska, S., Manzanas, R., Martínez-Castro, D., Narisma, G. T., ... Vera, C. S. (2020). An update of IPCC climate reference regions for subcontinental analysis of climate model data: definition and aggregated datasets. *Earth System Science Data*, *12*(4), 2959–2970. https://doi.org/10.5194/essd-12-2959-2020

Jacobs, C. (1994). *Direct Impacts of Atmospheric CO2 Enrichment on Regional Transpiration.*

Jacobs, C. M., Van Den Hurk, B. J., & De Bruin, H. A. (1996). Stomatal behaviour and photosynthetic rate of unstressed grapevines in semi-arid conditions. *Agricultural and Forest Meteorology*, *80*(2-4), 111–134. https://doi.org/10.1016/0168-1923(95)02295-3

Jarvis, P. G. (1976). The interpretation of the variations in leaf water potential and stomatal conductance found in canopies in the field. *Philosophical Transactions of the Royal Society of London. B, Biological Sciences*, *273*(927), 593–610. https://doi.org/10.1098/rstb.1976.0035

Jiménez, C., Prigent, C., Mueller, B., Seneviratne, S. I., McCabe, M. F., Wood, E. F., Rossow, W. B., Balsamo, G., Betts, A. K., Dirmeyer, P. A., Fisher, J. B., Jung, M., Kanamitsu, M., Reichle, R. H., Reichstein, M., Rodell, M., Sheffield, J., Tu, K., & Wang, K. (2011). Global intercomparison of 12 land surface heat flux estimates. *Journal of Geophysical Research Atmospheres*, *116*(2), 1–27. https://doi.org/10.1029/2010JD014545

Johannsen, F., Ermida, S., Martins, J. P., Trigo, I. F., Nogueira, M., & Dutra, E. (2019). Cold bias of ERA5 summertime daily maximum land surface temperature over Iberian Peninsula. *Remote Sensing*, *11*(21). https://doi.org/10.3390/rs11212570

Jung, M., Koirala, S., Weber, U., Ichii, K., Gans, F., Camps-Valls, G., Papale, D., Schwalm, C., Tramontana, G., & Reichstein, M. (2019). The FLUXCOM ensemble of global land-atmosphere energy fluxes. *Scientific Data*, *6*(1), 1–14. https://doi.org/10.1038/s41597-019-0076-8

Jung, M., Reichstein, M., Margolis, H. A., Cescatti, A., Richardson, A. D., Arain, M. A., Arneth, A., Bernhofer, C., Bonal, D., Chen, J., Gianelle, D., Gobron, N., Kiely, G., Kutsch, W., Lasslop, G., Law, B. E., Lindroth, A., Merbold, L., Montagnani, L., ... Williams, C. (2012). Erratum: Global patterns of land-atmosphere fluxes of carbon dioxide, latent heat, and sensible heat derived from eddy covariance, satellite, and meteorological observations (Journal of Geophysical Research G: Biogeosciences (2011) 116 (G00J07) DOI: 10.10. *Journal of Geophysical Research G: Biogeosciences*, *117*(4), 1–16. https://doi.org/10.1029/2012JG002190

Kim, H. (2017). Global Soil Wetness Project Phase 3 Atmospheric Boundary Conditions (Experiment 1) [Data set]. https://doi.org/10.20783/DIAS.501

Konings, A. G., Williams, A. P., & Gentine, P. (2017). Sensitivity of grassland productivity to aridity controlled by stomatal and xylem regulation. *Nature Geoscience*. https://doi.org/DOI:10.1038/ngeo2903

Koster, R. D., Mahanama, S. P., Yamada, T. J., Balsamo, G., Berg, A. A., Boisserie, M., Dirmeyer, P. A., Doblas-Reyes, F. J., Drewitt, G., Gordon, C. T., Guo, Z., Jeong, J. H., Lawrence, D. M., Lee, W. S., Li, Z., Luo, L., Malyshev, S., Merryfield, W. J., Seneviratne, S. I., ... Wood, E. F. (2010). Contribution of land surface initialization to subseasonal forecast

skill: First results from a multi-model experiment. *Geophysical Research Letters*, *37*(2), 1–6. https://doi.org/10.1029/2009GL041677

Koster, R. D., Mahanama, S. P., Yamada, T. J., Balsamo, G., Berg, A. A., Boisserie, M., Dirmeyer, P. A., Doblas-Reyes, F. J., Drewitt, G., Gordon, C. T., Guo, Z., Jeong, J. H., Lee, W. S., Li, Z., Luo, L., Malyshev, S., Merryfield, W. J., Seneviratne, S. I., Stanelle, T., … Wood, E. F. (2011). The second phase of the global land-atmosphere coupling experiment: Soil moisture contributions to subseasonal forecast skill. *Journal of Hydrometeorology*, *12*(5), 805–822. https://doi.org/10.1175/2011JHM1365.1

Koster, R. D., & Walker, G. K. (2015). Interactive vegetation phenology, soil moisture, and monthly temperature forecasts. *Journal of Hydrometeorology*, *16*(4), 1456–1465. https://doi.org/10.1175/JHM-D-14-0205.1

Kratzert, F., Klotz, D., Shalev, G., Klambauer, G., Hochreiter, S., & Nearing, G. (2019). Towards learning universal, regional, and local hydrological behaviors via machine learning applied to large-sample datasets. *Hydrology and Earth System Sciences*, *23*(12), 5089–5110. https://doi.org/10.5194/hess-23-5089-2019

Lawrence, D. M., Thornton, P. E., Oleson, K. W., & Bonan, G. B. (2007). The partitioning of evapotranspiration into transpiration, soil evaporation, and canopy evaporation in a GCM: Impacts on land-atmosphere interaction. *Journal of Hydrometeorology*, *8*(4), 862–880. https://doi.org/10.1175/JHM596.1

Lawrence, P. J., Feddema, J. J., Bonan, G. B., Meehl, G. A., O'Neill, B. C., Oleson, K. W., Levis, S., Lawrence, D. M., Kluzek, E., Lindsay, K., & Thornton, P. E. (2012). Simulating the biogeochemical and biogeophysical impacts of transient land cover change and wood harvest in the Community Climate System Model (CCSM4) from 1850 to 2100. *Journal of Climate*, *25*(9), 3071–3095. https://doi.org/10.1175/JCLI-D-11-00256.1

L'Ecuyer, T. S., Beaudoing, H. K., Rodell, M., Olson, W., Lin, B., Kato, S., Clayson, C. A., Wood, E., Sheffield, J., Adler, R., Huffman, G., Bosilovich, M., Gu, G., Robertson, F., Houser, P. R., Chambers, D., Famiglietti, J. S., Fetzer, E., Liu, W. T., … Hilburn, K. (2015). The observed state of the energy budget in the early twenty-first century. *Journal of Climate*, *28*(21), 8319–8346. https://doi.org/10.1175/JCLI-D-14-00556.1

Lenton, T. M., Rockström, J., Gaffney, O., Rahmstorf, S., Richardson, K., Steffen, W., & Schellnhuber, H. J. (2019). An aeroplane flies over a glacier in the Wrangell St Elias National Park in Alaska. *Nature*, *575*, 592–595.

Leonardini, G., Anctil, F., Abrahamowicz, M., Gaborit, É., Vionnet, V., Nadeau, D. F., & Fortin, V. (2020). Evaluation of the soil, vegetation, and snow (svs) land surface model for the simulation of surface energy fluxes and soil moisture under snow-free conditions. *Atmosphere*, *11*(3). https://doi.org/10.3390/atmos11030278

Liu, X., Chen, F., Barlage, M., & Niyogi, D. (2020). Implementing Dynamic Rooting Depth for Improved Simulation of Soil Moisture and Land Surface Feedbacks in Noah-MP-Crop. *Journal of Advances in Modeling Earth Systems*, *12*(2), 1–15. https://doi.org/10.1029/2019MS001786

Liu, Y., Konings, A. G., Kennedy, D., & Gentine, P. (2021). Global Coordination in Plant Physiological and Rooting Strategies in Response to Water Stress. *Global Biogeochemical Cycles*, *35*(7), 1–23. https://doi.org/10.1029/2020GB006758

Mahfouf, J. F., Manzi, A. O., Noilhan, J., Giordani, H., & Deque, M. (1995). The land surface scheme ISBA within the Meteo-France climate model ARPEGE. Part I: implementation and preliminary results. *Journal of Climate*, *8*(8), 2039–2057. https://doi.org/10.1175/1520-0442(1995)008⟨2039:TLSSIW⟩2.0.CO;2

Manabe, S. (1969). Climate and the Ocean Circulation 1. *Monthly Weather Review*, *97*(11), 739–774. https://doi.org/10.1175/1520-0493(1969)097⟨0739:catoc⟩2.3.co;2

Manrique-Suñén, A. (2016). *The treatment of vegetation in land surface models: implications for predictions of land-atmosphere exchange* (Doctoral dissertation). University of Reading.

Manzi, A. O., & Planton, S. (1994). Implementation of the ISBA parametrization scheme for land surface processes in a GCM - an annual cycle experiment. *Journal of Hydrology*, *155*(3-4), 353–387. https://doi.org/10.1016/0022-1694(94)90178-3

Martens, B., Miralles, D., Lievens, H., van der Schalie, R., de Jeu, R., Férnandez-Prieto, D., Beck, H., Dorigo, W., & Verhoest, N. (2016). GLEAM v3: satellite-based land evaporation and root-zone soil moisture. *Geoscientific Model Development Discussions*, (August), 1–36. https://doi.org/10.5194/gmd-2016-162

Martens, B., Schumacher, D. L., Wouters, H., Muñoz-Sabater, J., Verhoest, N. E., & Miralles, D. G. (2020). Evaluating the land-surface energy partitioning in ERA5. *Geoscientific Model Development*, *13*(9), 4159–4181. https://doi.org/10.5194/gmd-13-4159-2020

Massmann, A., Gentine, P., & Lin, C. (2019). When Does Vapor Pressure Deficit Drive or Reduce Evapotranspiration? *Journal of Advances in Modeling Earth Systems*, *11*(10), 3305–3320. https://doi.org/10.1029/2019MS001790

Mueller, B., Hirschi, M., Jimenez, C., Ciais, P., Dirmeyer, P. A., Dolman, A. J., Fisher, J. B., Jung, M., Ludwig, F., Maignan, F., Miralles, D. G., McCabe, M. F., Reichstein, M., Sheffield, J., Wang, K., Wood, E. F., Zhang, Y., & Seneviratne, S. I. (2013). Benchmark products for land evapotranspiration: LandFlux-EVAL multi-data set synthesis. *Hydrology and Earth System Sciences*, *17*(10), 3707–3720. https://doi.org/10.5194/hess-17-3707-2013

Nepstad, D. C., De Carvalho, C. R., Davidson, E. A., Jipp, P. H., Lefebvre, P. A., Negreiros, G. H., Da Silva, E. D., Stone, T. A., Trumbore, S. E., & Vieira, S. (1994). The role of deep roots in the hydrological and carbon cycles of Amazonian forests and pastures. https://doi.org/10.1038/372666a0

Nielsen, D. C., & Vigil, M. F. (2018). Soil water extraction for several dryland crops. *Agronomy Journal*, *110*(6), 2447–2455. https://doi.org/10.2134/agronj2018.05.0335

Nogueira, M., Albergel, C., Boussetta, S., Johannsen, F., Trigo, I. F., Ermida, S. L., Martins, J. P., & Dutra, E. (2020). Role of vegetation in representing land surface temperature in the CHTESSEL (CY45R1) and SURFEX-ISBA (v8.1) land surface models: A case study over Iberia. *Geoscientific Model Development*, *13*(9), 3975–3993. https://doi.org/10.5194/gmd-13-3975-2020

Nogueira, M., Boussetta, S., Balsamo, G., Albergel, C., Trigo, I. F., Johannsen, F., Miralles, D. G., & Dutra, E. (2021). Upgrading Land-Cover and Vegetation Seasonality in the ECMWF Coupled System: Verification With FLUXNET Sites, METEOSAT Satellite Land Surface Temperatures, and ERA5 Atmospheric Reanalysis. *Journal of Geophysical Research: Atmospheres*, *126*(15), 1–26. https://doi.org/10.1029/2020JD034163

O, S., & Orth, R. (2020). Global soil moisture from in-situ measurements using machine learning – SoMo.ml, 1–12. http://arxiv.org/abs/2010.02374

O, S., & Orth, R. (2021). Global soil moisture data derived through machine learning trained with in-situ measurements. *Scientific Data*, *8*(1), 1–14. https://doi.org/10.1038/s41597-021-00964-1

Orth, R., & Seneviratne, S. I. (2012). Analysis of soil moisture memory from observations in Europe. *Journal of Geophysical Research Atmospheres*, *117*(15), 1–19. https://doi.org/10.1029/2011JD017366

Orth, R., Dutra, E., Trigo, I., & Balsamo, G. (2016). Advancing land surface model development with satellite-based Earth observations. *Hydrology and Earth System Sciences Discussions*, (December), 1–21. https://doi.org/10.5194/hess-2016-628

Pal, S., & Sharma, P. (2021). A Review of Machine Learning Applications in Land Surface Modeling. *Earth*, *2*(1), 174–190. https://doi.org/10.3390/earth2010011

Pielke, R. A., Avissar, R., Raupach, M., Dolman, A. J., Zeng, X., & Denning, A. S. (1998). Interactions between the atmosphere and terrestrial ecosystems: influence on weather and climate. *Global Change Biology*, *4*(5), 461–475. https://doi.org/10.1046/j.1365-2486.1998.00176.x

Pinto, C. A., Nadezhdina, N., David, J. S., Kurz-Besson, C., Caldeira, M. C., Henriques, M. O., Monteiro, F. G., Pereira, J. S., & David, T. S. (2014). Transpiration in Quercus suber trees under shallow water table conditions: The role of soil and groundwater. *Hydrological Processes*, *28*(25), 6067–6079. https://doi.org/10.1002/hyp.10097

Pitman, A. (1991). Description of the bare essentials of Surface transfer. *Annual Review of Materials Research*, *32*(1), 77–111. http://www.annualreviews.org/doi/abs/10.1146/annurev.matsci.32.110101.155324

Pitman, A. J. (2003). The evolution of, and revolution in, land surface schemes designed for climate models. *International Journal of Climatology*, *23*(5), 479–510. https://doi.org/10.1002/joc.893

Prentice, I. C., Dong, N., Gleason, S. M., Maire, V., & Wright, I. J. (2014). Balancing the costs of carbon gain and water transport: Testing a new theoretical framework for plant functional ecology. *Ecology Letters*, *17*(1), 82–91. https://doi.org/10.1111/ele.12211

Prentice, I. C., Farquhar, G. D., Fasham, M. J. R., Goulden, M., Heimann, M., Jaramillo, V. J., Kheshgi, H. S., Le Quéré, C., Scholes, R. J., Wallace, D. W. R., & Al., E. (2001). The carbon cycle and atmospheric carbon dioxide. *Climate Change 2001: The Scientific Basis*, (IPCC), 183–237. http://eprints.ifm-geomar.de/3422/%5C%5Cnhttp://www.grida.no/climate/ipcc_tar/wg1/pdf/tar-03.pdf%5C%5Cnhttp://www.grida.no/climate/ipcc_tar/wg1/095.htm%5C%5Cnhttp://www.grida.no/publications/other/ipcc_tar/?src=/climate/ipcc_tar/wg1/index.htm

Rodrigues, A., Pita, G., Mateus, J., Kurz-Besson, C., Casquilho, M., Cerasoli, S., Gomes, A., & Pereira, J. (2011). Eight years of continuous carbon fluxes measurements in a Portuguese eucalypt stand under two main events: Drought and felling. *Agricultural and Forest Meteorology*, *151*(4), 493–507. https://doi.org/10.1016/j.agrformet.2010.12.007

Schaaf, C. B., Gao, F., Strahler, A. H., Lucht, W., Li, X., Tsang, T., Strugnell, N. C., Zhang, X., Jin, Y., Muller, J.-p., Lewis, P., Barnsley, M., Hobson, P., Disney, M., Roberts, G., Dunderdale, M., Doll, C., Robert, P., Hu, B., ... Roy, D. (2002). Schaaf et al 2002 First

operational BRDF, albedo nadir reflectance products from MODIS.pdf. *Remote Sensing of Environment*, *83*, 135–148.

Schellekens, J., Dutra, E., Martínez-De La Torre, A., Balsamo, G., Van Dijk, A., Sperna Weiland, F., Minvielle, M., Calvet, J. C., Decharme, B., Eisner, S., Fink, G., Flörke, M., Peßenteiner, S., Van Beek, R., Polcher, J., Beck, H., Orth, R., Calton, B., Burke, S., … Weedon, G. P. (2017). A global water resources ensemble of hydrological models: The eartH2Observe Tier-1 dataset. *Earth System Science Data*, *9*(2), 389–413. https://doi.org/10.5194/essd-9-389-2017

Schenk, H. J., & Jackson, R. B. (2002). The global biogeography of roots. *Ecological Monographs*, *72*(3), 311–328. https://doi.org/10.1890/0012-9615(2002)072[0311:TGBOR]2.0.CO;2

Schlesinger, W. H., & Jasechko, S. (2014). Transpiration in the global water cycle. *Agricultural and Forest Meteorology*, *189-190*, 115–117. https://doi.org/10.1016/j.agrformet.2014.01.011

Sea, W. B., Choler, P., Beringer, J., Weinmann, R. A., Hutley, L. B., & Leuning, R. (2011). Documenting improvement in leaf area index estimates from MODIS using hemispherical photos for Australian savannas. *Agricultural and Forest Meteorology*, *151*(11), 1453–1461. https://doi.org/10.1016/j.agrformet.2010.12.006

Sellers, P. J., Bounoua, L., Collatz, G. J., Randall, D. A., Dazlich, D. A., Los, S. O., Berry, J. A., Fung, I., Tucker, C. J., Field, C. B., & Jensen, T. G. (1996). Comparison of radiative and physiological effects of doubled atmospheric CO2 on climate. *Science*, *271*(5254), 1402–1406. https://doi.org/10.1126/science.271.5254.1402

Seneviratne, S. I., Corti, T., Davin, E. L., Hirschi, M., Jaeger, E. B., Lehner, I., Orlowsky, B., & Teuling, A. J. (2010). Investigating soil moisture-climate interactions in a changing climate: A review. *Earth-Science Reviews*, *99*(3-4), 125–161. https://doi.org/10.1016/j.earscirev.2010.02.004

Sperry, J. S., & Love, D. M. (2015). What plant hydraulics can tell us about responses to climate-change droughts. *New Phytologist*, *207*(1), 14–27. https://doi.org/10.1111/nph.13354

Sprintsin, M., Chen, J. M., Desai, A., & Gough, C. M. (2012). Evaluation of leaf-to-canopy upscaling methodologies against carbon flux data in North America. *Journal of Geophysical Research: Biogeosciences*, *117*(1), 1–17. https://doi.org/10.1029/2010JG001407

Steffen, W., Rockström, J., Richardson, K., Lenton, T. M., Folke, C., Liverman, D., Summerhayes, C. P., Barnosky, A. D., Cornell, S. E., Crucifix, M., Donges, J. F., Fetzer, I., Lade, S. J., Scheffer, M., Winkelmann, R., & Schellnhuber, H. J. (2018). Trajectories of the Earth System in the Anthropocene. *Proceedings of the National Academy of Sciences of the United States of America*, *115*(33), 8252–8259. https://doi.org/10.1073/pnas.1810141115

Stevens, D., Miranda, P. M., Orth, R., Boussetta, S., Balsamo, G., & Dutra, E. (2020). Sensitivity of surface fluxes in the ECMWF land surface model to the remotely sensed leaf area index and root distribution: Evaluation with tower flux data. *Atmosphere*, *11*(12), 1–19. https://doi.org/10.3390/atmos11121362

Stöckli, R., Lawrence, D. M., Niu, G.-Y., Oleson, K. W., Thornton, P. E., Yang, Z.-L., Bonan, G. B., Denning, A. S., & Running, S. W. (2008). Use of FLUXNET in the Community Land Model development. *Journal of Geophysical Research: Biogeosciences*, *113*(G1), n/a–n/a. https://doi.org/10.1029/2007jg000562

Stöckli, R., Rutishauser, T., Dragoni, D., O'Keefe, J., Thornton, P. E., Jolly, M., Lu, L., & Denning, A. S. (2008). Remote sensing data assimilation for a prognostic phenology model. *Journal of Geophysical Research: Biogeosciences*, *113*(4), 1–19. https://doi.org/10.1029/2008JG000781

Sun, Q., Wang, Z., Li, Z., Erb, A., & Schaaf, C. B. (2017). Evaluation of the global MODIS 30 arc-second spatially and temporally complete snow-free land surface albedo and reflectance anisotropy dataset. *International Journal of Applied Earth Observation and Geoinformation*, *58*, 36–49. https://doi.org/10.1016/j.jag.2017.01.011

Sungmin, O., Dutra, E., & Orth, R. (2020). Robustness of process-based versus data-driven modeling in changing climatic conditions. *Journal of Hydrometeorology*, *21*(9), 1929–1944. https://doi.org/10.1175/JHM-D-20-0072.1

Takahashi, H., & Scott, T. K. (1991). Hydrotropism and its interaction with gravitropism in maize roots. *Plant Physiology*, *96*(2), 558–564. https://doi.org/10.1104/pp.96.2.558

Teuling, A. J., Van Loon, A. F., Seneviratne, S. I., Lehner, I., Aubinet, M., Heinesch, B., Bernhofer, C., Grünwald, T., Prasse, H., & Spank, U. (2013). Evapotranspiration amplifies European summer drought. *Geophysical Research Letters*, *40*(10), 2071–2075. https://doi.org/10.1002/grl.50495

Tramontana, G., Jung, M., Schwalm, C. R., Ichii, K., Camps-Valls, G., Ráduly, B., Reichstein, M., Arain, M. A., Cescatti, A., Kiely, G., Merbold, L., Serrano-Ortiz, P., Sickert, S., Wolf, S., & Papale, D. (2016). Predicting carbon dioxide and energy fluxes across global FLUXNET sites with regression algorithms. *Biogeosciences*, *13*(14), 4291–4313. https://doi.org/10.5194/bg-13-4291-2016

Trigo, I. F., Boussetta, S., Viterbo, P., Balsamo, G., Beljaars, A., & Sandu, I. (1995). Journal of geophysical research. *Nature*, *175*(4449), 238. https://doi.org/10.1038/175238c0

Ukkola, A. M., De Kauwe, M. G., Pitman, A. J., Best, M. J., Abramowitz, G., Haverd, V., Decker, M., & Haughton, N. (2016). Land surface models systematically overestimate the intensity, duration and magnitude of seasonal-scale evaporative droughts. *Environmental Research Letters*, *11*(10). https://doi.org/10.1088/1748-9326/11/10/104012

van den Hurk, B. J., Viterbo, P., Beljaars, A., & Betts, A. K. (2000). *Offline validation of the ERA40 surface scheme* (tech. rep.). European Center for Medium-Range Weather Forecasts.

Verger, A., Baret, F., & Weiss, M. (2014). Near real-time vegetation monitoring at global scale. *IEEE Journal of Selected Topics in Applied Earth Observations and Remote Sensing*, *7*(8), 3473–3481. https://doi.org/10.1109/JSTARS.2014.2328632

Verhoef, A., & Egea, G. (2014). Modeling plant transpiration under limited soil water: Comparison of different plant and soil hydraulic parameterizations and preliminary implications for their use in land surface models. *Agricultural and Forest Meteorology*, *191*, 22–32. https://doi.org/10.1016/j.agrformet.2014.02.009

Vinet, L., & Zhedanov, A. (2011). *A 'missing' family of classical orthogonal polynomials* (J. G. Canadell, D. E. Pataki, & L. F. Pitelka, Eds.; Springer-V, Vol. 44). IGBP - Global Change. https://doi.org/10.1088/1751-8113/44/8/085201

Vogel, M. M., Orth, R., Cheruy, F., Hagemann, S., Lorenz, R., van den Hurk, B. J., & Seneviratne, S. I. (2017). Regional amplification of projected changes in extreme temperatures strongly controlled by soil moisture-temperature feedbacks. *Geophysical Research Letters*, *44*(3), 1511–1519. https://doi.org/10.1002/2016GL071235

Voogt, M., van den Hurk, B. J., & Jacobs, C. (2006). The ECMWF land surface scheme extended with a photosynthesis and LAI module tested for a coniferous forest site Article.

Wang, Z., Schaaf, C. B., Strahler, A. H., Chopping, M. J., Román, M. O., Shuai, Y., Woodcock, C. E., Hollinger, D. Y., & Fitzjarrald, D. R. (2014). Evaluation of MODIS albedo product (MCD43A) over grassland, agriculture and forest surface types during dormant and snow-covered periods. *Remote Sensing of Environment*, *140*, 60–77. https://doi.org/10.1016/j.rse.2013.08.025

Wild, M., Folini, D., Hakuba, M. Z., Schär, C., Seneviratne, S. I., Kato, S., Rutan, D., Ammann, C., Wood, E. F., & König-Langlo, G. (2015). The energy balance over land and oceans: an assessment based on direct observations and CMIP5 climate models. *Climate Dynamics*, *44*(11-12), 3393–3429. https://doi.org/10.1007/s00382-014-2430-z

Wilson, K. (2002). EnWilson, K. (2002). Energy balance closure at FLUXNET sites. Agricultural and Forest Meteorology, 113(1–4), 223–243. https://doi.org/10.1016/S0168-1923(02)00109-0ergy balance closure at FLUXNET sites. *Agricultural and Forest Meteorology*, *113*(1-4), 223–243. http://www.sciencedirect.com/science/article/pii/S0168192302001090

Woodward, F. I. (1998). Vegetation-climate feedbacks in a greenhouse world. *Philosophical Transactions of the Royal Society B: Biological Sciences*, *353*(1365), 29–39. https://doi.org/10.1098/rstb.1998.0188

Yang, W., Tan, B., Huang, D., Rautiainen, M., Shabanov, N. V., Wang, Y., Privette, J. L., Huemmrich, K. F., Fensholt, R., Sandholt, I., Weiss, M., Ahl, D. E., Gower, S. T., Nemani, R. R., Knyazikhin, Y., & Myneni, R. B. (2006). MODIS leaf area index products: From validation to algorithm improvement. *IEEE Transactions on Geoscience and Remote Sensing*, *44*(7), 1885–1896. https://doi.org/10.1109/TGRS.2006.871215

Zeng, X., Dai, Y. J., Dickinson, R. E., & Shaikh, M. (1998). The role of root distribution for climate simulation over land. *Geophysical Research Letters*, *25*(24), 4533–4536. https://doi.org/10.1029/1998GL900216

Zhao, W., & Li, A. (2015). A Review on Land Surface Processes Modelling over Complex Terrain. *Advances in Meteorology*, *2015*. https://doi.org/10.1155/2015/607181

Zheng, W., Wei, H., Wang, Z., Zeng, X., Meng, J., Ek, M., Mitchell, K., & Derber, J. (2012). Improvement of daytime land surface skin temperature over arid regions in the NCEP GFS model and its impact on satellite data assimilation. *Journal of Geophysical Research Atmospheres*, *117*(6), 1–14. https://doi.org/10.1029/2011JD015901